UNIVERSITÉ DE REIMS CHAMPAGNE-ARDENNE, FRANCE

UNIVERSITÉ NATIONALE DE RECHERCHE D'ÉTAT À TOMSK, RUSSIE

U.F.R. Sciences Exactes et Naturelles

École Doctorale n°620 Sciences du Numérique et de l'Ingénieur

THÈSE EN CO-TUTELLE

Pour obtenir le grade de

DOCTEUR DE L'UNIVERSITÉ DE REIMS CHAMPAGNE-ARDENNE

Discipline : Optique et milieux dilués

Spécialité : Physique

Présentée et soutenue publiquement par

Iana CHIZHMAKOVA

Le 13 Juillet 2022

MODELISATION DE SPECTRES INFRAROUGES POUR LES GAZ A EFFECT DE SERRE A FORT POTENTIEL DE RECHAUFFEMENT PLANETAIRE: CF_4 ET SF_6

Résumé substantiel en français

Avec les publications en anglaise intégrées

Thèse dirigée par **Andrey NIKITIN, à l'Universitè de Tomsk**

Et par **Michael REY et Vladimir TYUTEREV Université de Reims Champagne-Ardenne,**

JURY

L. Manceron	Directeur de recherche CNRS, Université Paris-Sorbonne	Rapporteur
A. Bykov	Professeur à l'IOA, Académie des Sciences, Russie	Rapporteur
M. Rey	Directeur de recherche CNRS, Université Reims Champagne-Ardenne	Directeur de Thèse
A. Nikitin	Professeur à l'Université de Tomsk, Russie	Directeur de Thèse
V. Tyuterev	Professeur émérite à l'Université de Reims Champagne-Ardenne	Co-directeur de Thèse
V. Boudon	Directeur de recherche CNRS, Université de Bourgogne	Examinateur
A. Vigasin	Directeur de recherche à l'IAP de Moscow Acad. Sci., Russie	Examinateur
E. Starikova	Chargée de recherché, IOA, Académie des Sciences, Russie	Examinateur

Table des matières

Introduction

L'une des tâches principales de la spectroscopie moléculaire dans le domaine infrarouge est l'identification de molécules organiques et inorganiques en phase gazeuse ou liquide caractérisées par un ensemble de paramètres spectroscopiques, des fréquences et des intensités de raies, des paramètres d'élargissement, etc. L'analyse spectrale a trouvé de nombreuses applications dans de nombreux domaines, tels que l'étude des propriétés des gaz, la biophysique, l'astrophysique ou encore la physique atmosphérique. Afin d'analyser la composition de l'atmosphère, il est souhaitable d'avoir des informations les plus complètes possibles sur une large gamme spectrale. Le développement de la spectroscopie infrarouge à transformée de Fourier (FTIR) ainsi que des technologies laser a permis de faire des progrès significatifs dans l'identification des gaz. Cependant, les spectres de molécules polyatomiques « toupies sphériques » présente des densité d'états très élevés et par conséquent une grande quantité de données à extraire et à analyser. Cette tâche peut être parfois très difficile à partir de méthodes purement expérimentales. Par exemple, afin d'étudier des spectres à haute température, les listes spectroscopiques doivent inclure une grosse quantité d'information, même pour des raies très faibles. Pour cela, il est nécessaire de pouvoir calculer un nombre important de transitions, allant de quelques millions à plusieurs milliards selon la valeur maximale de J.

Avec le développement de gros calculateurs, des progrès significatifs ont été réalisés en spectroscopie théorique en se basant sur les calculs de chimie quantique. La littérature scientifique récente démontre à quel point que les listes théoriques ont maintenant une grande place dans l'étude et l'analyse de données expérimentales ainsi que dans la modélisation d'atmosphères planétaires. Par exemple, il y a eu grand d'intérêt pour les spectres infrarouges du méthane (CH_4) au cours des dernières décennies pour l'étude des atmosphères des planètes du système solaire et de leurs satellites [1] [2] [3]. Les paramètres de bande du méthane sont alors d'une importance capitale [4] [5] [6] [7] [8]. L'amélioration des programmes *ab initio,* des algorithmes de construction d'une surface d'énergie potentielle (PES) et des méthodes de résolution du problème nucléaire permet de calculer des niveaux (ro)vibrationnels avec une précision toujours plus grande. Les progrès récents dans les calculs variationnels à partir de PES et de surfaces de moment dipolaire (DMS) pour des molécules légères telles que l'eau, l'ozone, l'ammoniac, le méthane ou l'éthylène ont mené à l'identification de nombreuses bandes vibrationnels et conduit à la modélisation des spectres de ces molécules à différentes températures. Pour les molécules plus lourdes possédant des modes vibrationnels de plus basse énergie – ce qui est l'objet de ce travail - de tels calculs deviennent plus compliqués car ils nécessitent la prise en compte de grands nombres quantiques V et J. Pour de tels systèmes, la densité d'états est très élevée, rendant encore plus compliquée les calculs à haute température. Il est donc nécessaire d'avoir à disposition des outils efficaces pour pouvoir effectuer des calculs variationnels de qualité. Notons que les listes *ab initio* contenant plusieurs milliards de transitions sont devenues courantes pour diverses applications planétaires et atmosphériques.

Un des objectifs de cette thèse est d'obtenir des PES et DMS ab initio très précises, permettant de calculer des niveaux rovibrationnels et de modéliser les spectres de molécules qui composent l'atmosphère terrestre. Nous nous focaliserons sur CF_4 et SF_6. Une analyse des spectres expérimentaux à haute résolution de la molécule CF_4 en combinant des modèles effectifs spectroscopiques et les informations obtenues à l'aide de PES et DMS ab initio pour les positions et les intensités est également effectuée

Objet d'étude

L'étude des propriétés spectroscopiques des molécules de type toupie sphérique intéresse particulièrement la communauté scientifique. Tout d'abord, cela est dû à l'utilisation de ces composés dans divers domaines industriels. En même temps, ces molécules jouent un rôle actif dans les processus se produisant dans l'atmosphère terrestre. Cette thèse propose une analyse théorique et expérimentale des gaz à effet de serre fluorés : CF_4et SF_6.

Le tétrafluorométhane CF_4 (tétrafluorure de carbone, CFC-14, PFC-14, R-14) est un gaz incolore, non toxique et ininflammable appartenant au groupe des perfluorocarbures (PFC - Perfluorocarbures). Les PFC sont des gaz à effet de serre (GES) extrêmement puissants et sont considérés comme l'un des gaz traces ayant la plus longue durée de vie dans l'atmosphère. Le tétrafluorométhane est le PFC le plus abondant dans la stratosphère, où sa durée de vie, selon [9], peut atteindre 50 milles ans. Cela est dû au fait que les molécules CF_4 sont les moins actives par rapport aux autres fréons et ne se désintègrent pas très lentement dans l'atmosphère, ce qui conduit à leur accumulation. CF_4 est une molécule hautement absorbante et possède l'un des plus grands potentiels réchauffement mondiaux (GWP) connus [10]. Malgré une source lithosphérique naturelle [11], la principale source de CF_4 est anthropique et est associée à la production d'aluminium [12].

L'hexafluorure de soufre SF_6, qui possède de hautes propriétés d'isolation électrique et d'extinction d'arc, a été largement utilisé dans de nombreux domaines de l'industrie et de la médecine [13] [14] [15]. En raison des fortes bandes d'absorption dans les fenêtres de transparence atmosphérique, le SF_6 est un GES puissant, dont le GWP est 29300 fois supérieur à celui du CO_2[16]. SF_6 est l'un des produits chimiques gazeux les plus stables avec une durée de vie atmosphérique de 3200 ans [9]. Les isotopologues les plus abondants sont $^{32}SF_6$ (95%), $^{34}SF_6$ (4%) et $^{33}SF_6$ (0,7%).

Ces gaz peuvent jouer un rôle actif dans le réchauffement climatique et sont soumis aux directives du Protocole de Kyoto de la Convention-cadre des Nations Unies sur les changements climatiques (CCNUCC) pour les espèces recommandées pour la surveillance environnementale. [17] [18] [19].

Etat de l'art

Les émissions de GES provenant de sources anthropiques ont entraîné une augmentation significative de leur concentration dans l'atmosphère, ce qui peut provoquer des changements climatiques importants en un temps relativement court. Les GES absorbent le rayonnement dans l'infrarouge moyen et lointain dans l'atmosphère terrestre, ce qui conduit à l'effet de serre. Des bases de données spectroscopiques modernes telles que HITRAN [20] et GEISA [21], contiennent des listes « raie par raie » avec de nombreuses attributions (information sur les nombres quantiques ainsi que sur un certain nombre d'autres paramètres spectroscopiques). Cependant, pour la majorité des molécules de cinq et sept atomes, l'identification n'est connue que pour les polyades inférieures, ce qui rend difficile le calcul des spectres à différentes températures.

Ces dernières années, de nombreux travaux ont été consacrés à l'étude des spectres des molécules fluorées considérées dans cette thèse. La première étude expérimentale des spectres infrarouges de CF_4 a été rapportée par Bailey et al.[22] en 1938. Les mesures correspondantes couvraient une gamme de 2 à 19 mm, qui a ensuite été étendue en 1951 par Woltz et al.[23] jusqu'à 2–33 mm. Depuis, d'autres études expérimentales ont été publiées. [24] [25], couvrant l'infrarouge lointain, qui ont ensuite été complétées par une étude théorique [26].

Au cours des quatre dernières décennies, un certain nombre d'études expérimentales et théoriques ont été consacrées ont porté sur l'analyse et la prédiction des spectres de la molécule SF_6 [27]. Dans la Ref. [28] l'état $v_3 = 2$ a été étudié en utilisant deux bandes latérales accordées indépendamment d'un laser CO_2. Les intensités des vibrations fondamentales actives dans le domaine infrarouge ont également été étudiées dans les travaux [29] et [30]. De nombreux d'efforts ont récemment été menés pour analyser les spectres SF_6 à haute résolution en utilisant des hamiltoniens phénoménologiques effectifs dont les paramètres ont été empiriquement ajustés aux données expérimentales [31] [32] [33] [34] [35].

Dans ce travail, nous considérons une méthode variationnelle à partir de PES pour résoudre l'équation de Schrödinger nucléaire. Cette approche a été appliquée avec succès à de nombreuses molécules à quatre et cinq atomes. [36] [37] [38] [39], ainsi que des molécules à six atomes telles que C_2H_4 [40] [41] [42].

Résultats de ce travail.

5 publications scientifiques à comité de lecture ont été publiées, dans lesquelles se trouvent les principaux résultats scientifiques décrits dans ce rapport.

Les résultats inclus dans le travail de thèse ont été discutés et présentés lors de conférences russes et internationales. Les travaux ont été présentés sous forme de présentations orales et posters lors des conférences suivantes :

-XXIV Colloque international « Optique atmosphérique et océanique. Physique de l'atmosphère" 2018

- XIX Symposium international sur la spectroscopie moléculaire à haute résolution 2019

- XXVII conférence "Aérosols de Sibérie"2020

Liste des publications de l'auteur :

1. Michaël Rey, Andrei V. Nikitin, I.S. Chizhmakova, Vladimir G. Tyuterev Understanding global infrared opacity and hot bands of greenhouse molecules with low vibrational modes from first-principles calculations: the case of CF_4// Phys.Chem.Chem.Phys. – 2018. – V. 20. – P.21008 – 21033. **DOI:** 10.1039/c8cp03252a

2. M. Mattoussi, M. Rey, M. Rotger, A.V. Nikitin, I. Chizhmakova, X. Thomas, H. Aroui, S. Tashkun, V.G. Tyuterev Preliminary analysis of the interacting pentad bands ($\nu_2 + 2\nu_4, \nu_2 + \nu_3, 4\nu_2, \nu_1 + 2\nu_2, 2\nu_1$) of CF_4 in the 1600 – 1800 cm^{-1} region // J. Quant. Spectrosc. Radiat. Transfer. – 2019. – V. 226. – P. 92 – 99 **DOI:** 10.1016/j.jqsrt.2019.01.018

3. Chizhmakova I.S., Nikitin A.V. Potential Energy Surface of SF_6 // Atmospheric and Oceanic Optics, 2019, V. 32, No. 6, P. 613–618. DOI: 10.1134/S1024856019060046

4. Nikitin, A.V., Rey, M., Chizhmakova, I.S., Tyuterev, V.G.First Full-Dimensional Potential Energy and Dipole Moment Surfaces of SF_6 // J. Phys.Chem. – 2020. – V. 124. – P. 7014–7023. DOI: 10.1021/acs.jpca.0c02733A

5. Rey M. Towards a complete elucidation of the ro-vibrational band structure in the SF6infrared spectrum from full quantum-mechanical calculations / M. Rey, I. S. Chizhmakova, A. V. Nikitin, V. G. Tyuterev / Phys. Chem. Chem. Phys. – 2021. – Vol. 23. – P. 12115–12126. – DOI: 10.1039/d0cp05727d (Scopus)

Les travaux ont été réalisés avec le soutien financier de :

Travail de recherche dans le cadre du programme d'amélioration de la compétitivité TSU

Bourse du gouvernement français du nom de V. I. Vernadsky pour la rédaction d'un mémoire en cotutelle scientifique (National Research Tomsk State University, Tomsk, Russie - Université de Reims Champagne-Ardenne France, Reims, 2019 - 2022) ;

Subvention RSF n° 19-77-10046 (2018-2022) ;

Subvention RFBR n° 20-35-90075 (2020-2022) ;

Contenu principal du rapport

- L'introduction décrit la pertinence du sujet et présente les objets d'étude ainsi que l'état de l'art.

Chapitre 1. Fondements théoriques et méthodes de calcul

Le premier chapitre est consacré aux méthodes *ab initio* qui sont maintenant utilisées dans beaucoup d'études. Ce chapitre contient une description de l'équation de Schrödinger et des approximations (Section 1.1) ainsi que des principes généraux pour résoudre l'équation du mouvement des noyaux (Section 1.2).
Le choix de la méthode *ab initio* détermine en grande partie la précision des calculs des niveaux et des transitions rovibrationnelles. Afin de résoudre l'équation de Schrödinger électronique, une description de la méthode de Möller-Plesset (MP) [43] et de la méthode « coupled-cluster» (CC) [44] est donnée. Une combinaison de ces méthodes avec des bases de Dunning polarisées [45] permet d'obtenir des niveaux vibrationnels avec une précision de quelques cm^{-1}.
Le développement d'une méthode variationnelle efficace est indispensable pour pouvoir modéliser des spectres à haute résolution tout en permettant de mieux cerner l'organisation des bandes froides et chaudes sur une large gamme spectrale. Des travaux consacrés à l'étude de molécules plus légères, telles que CH_4, SiH_4 ou GeH_4,[46] [47] [48] [49] [39] démontrent à quel point les calculs théoriques récents peuvent être précis.

Chapitre 2. Construction de surfaces d'énergie potentielle (PES) et de moment dipolaire (DMP) précises

Le deuxième chapitre est consacré à la description de l'approche théorique pour le calcul des PES et le DMS de CF_4 et SF_6. Afin de résoudre l'équation de Schrödinger électronique, la méthode CCSD(T) est utilisée [50] avec des bases de Dunning, ce qui permet d'obtenir les niveaux vibrationnels les plus bas avec une précision de quelques cm^{-1} · Pour une molécule polyatomique non-linéaire composée de N noyaux, la PES sera de dimension 3N-6. La représentation géométrique de la surface dans l'espace multidimensionnel des variables qui déterminent la configuration des noyaux a été obtenue à partir des coupes unidimensionnelles le long de chaque coordonnée de symétrie, construites sous la forme d'une fonction polynomiale.

En utilisant l'algorithme décrit dans la Ref. [51], un ensemble de tenseurs irréductibles totalement symétriques jusqu'à un certain ordre a été construit. Chaque tenseur est représenté comme la somme des produits de puissances symétrisées $S(R,A)_C^{p_n}$, où SR correspond aux composantes radiales, SA correspond aux composantes angulaires, C est la représentation irréductible du groupe ponctuel; p_n est le degré de la coordonnée symétrisée $S_n, n = 1,2,3, \ldots$.

Pour chaque groupe $\{p1, p2, \dots, pn\}$, un certain ensemble de puissances symétrisées a été fixé afin de déterminer de manière unique un jeu de constantes de force par ajustement. Ensuite, un ensemble de géométries a été déterminé pour une définition non ambiguë du champ de force.

Les propriétés de symétrie d'une molécule jouent un rôle essentiel en chimie et en physique tels que la construction du moment dipolaire, la détermination des vibrations fondamentales d'une molécule et la détermination des transitions spectroscopiques autorisées. Les sous-sections 2.1.1. et 2.2.1 donnent une description théorique des molécules CF_4 et SF_6 avec une présentation des groupes ponctuels auxquels appartiennent les molécules étudiées regroupant les opérations de symétrie, les éléments de matrice, les tables de caractères ainsi que la forme des vibrations normales.

Le choix d'un ensemble de points *ab initio* dans l'espace des configurations nucléaires et la représentation de la PES sous la forme d'une fonction analytique symétrisée sont donnés dans les sections 2.1.3 et 2.2.4.

La fonction potentielle a été construite à partir d'opérateurs tensoriels irréductibles

$$\mathrm{V(R)} = \sum_{\mathrm{p}} \mathrm{F}_{ip} \prod_{\mathrm{i}\sigma} \left(\mathrm{S}_{\mathrm{i}\sigma}^{(\Gamma_\mathrm{i})}\right)^{\mathrm{p}_{\mathrm{i}\sigma}} \qquad (1)$$

où l'indice i inclut tous les termes possibles jusqu'à une certaine puissance totale p_max, F_{ip} est l'ensemble des paramètres de la PES *ab initio*, et chaque tenseur R_i^p peut être obtenu comme le produit correspondant de coordonnées radiales et angulaires symétrisées.

La molécule CF_4 est décrite par quatre modes vibrationnels et la PES est donc par quatre coordonnées symétrisées selon le schéma de couplage suivant :

$$R_i^p = \left(\left(\left[SR_{A_1}\right]^{p_1} \times \left[SR_A\right]^{p_2}\right)^C \times \left(\left[SR_{F_2}\right]^{p_3} \times \left[SR_{F_2}\right]^{p_4}\right)^C\right)^{A_1} \qquad (2)$$

où $[SR_C]^p$ est la puissance symétrisée ; $p = p_1 + p_2 + p_3 + p_4$ est le degré total. Dans le cas de la molécule CF_4, l'équation (2) inclut tous les paramètres jusqu'au sixième ordre, complétés par 43 paramètres angulaires principaux jusqu'au huitième ordre.

Dans le cas d'une molécule SF_6 à sept atomes, trois modes de vibration radiaux $v_1 - v_4$ se transforment selon les représentations $A_{1g}(774.5\ cm^{-1}), E_g(643.3\ cm^{-1})et\ F_{1u}(\ 948.1\ cm^{-1})$, et les trois modes angulaires $v_4 - v_6$ selon les représentations $F_{1u}(615.0\ cm^{-1}), F_{2g}(524.0\ cm^{-1})et\ F_{2u}(347{,}7\ cm^{-1})$. Ainsi, l'expression (2) peut être obtenue comme suit :

$$\mathrm{R_i^p} = \left(\left(\left[\mathrm{SR_{A1_g}}\right]^{\mathrm{p_1}} \times \left(\left[\mathrm{SR_{E_g}}\right]^{\mathrm{p_2}} \times \left[\mathrm{SR_{F1_u}}\right]^{\mathrm{p_3}}\right)^{\mathrm{C_{23}}}\right)^{\mathrm{C'}} \times \left(\left[\mathrm{SR_{F1_u}}\right]^{\mathrm{p_4}} \times \left(\left[\mathrm{SR_{F2_g}}\right]^{\mathrm{p_5}} \times \left[\mathrm{SR_{F2_u}}\right]^{\mathrm{p_6}}\right)^{\mathrm{C_{56}}}\right)^{\mathrm{C''}}\right)^{\mathrm{A1g}}, \qquad (3)$$

Les points *ab initio* ont été ajustés à partir de cette représentation analytique, en tenant compte de la symétrie (2) et (3) et de la fonction de poids utilisée par Schwenke et Partridge.

$$w(E) = \frac{\tanh(-0.0005(E - E_1) + 1.002002002)}{2.002002002} \quad (4)$$

Des expressions analytiques du moment dipolaire μ_α^{MFF} ont été obtenues à la fois en coordonnées internes curvilignes et en coordonnées rectilignes normales dans le repère d'Eckart lié à la molécule (MFF). Par exemple

$$\mu_\alpha^{MFF} = \sum_i \widetilde{K}_i \tilde{R}_{i\alpha}^p \quad (5)$$

où

$$\tilde{R}_{i\alpha}^p = \left(\left(\left[q_1^{(A_1)} \right]^{p_1} \times \left[q_2^{(E)} \right]^{p_2} \right)^{(C_1)} \times \left(\left[q_3^{(F_2)} \right]^{p_3} \times \left[q_4^{(F_2)} \right]^{p_4} \right)^{(C_2)} \right)^{(F_2)} \quad (6)$$

est défini par les puissances successives $p = \{p_1, p_2, p_3, p_4\}$ de tenseurs irréductibles pour les modes une fois $\left\{q_1^{(A_1)}\right\}$, deux fois $\left\{q_2^{(E)}\right\}$ et trois fois $\left\{q_3^{(F_2)}\right\}$, $\left\{q_4^{(F_2)}\right\}$ dégénérés. C_1 et C_2 désignent les types de symétrie tétraédrique des interactions tensorielles intermédiaires appartenant aux types $\{A_1, A_2, E, F_1, F_2\}$, et $\widetilde{K}_i$sont les paramètres de la DMS.

La section 2.4 résume le chapitre 2 et liste les principaux résultats : les résultats sont également présentés dans les articles joints à ce manuscrit.:
Understanding global infrared opacity and hot bands of greenhouse molecules with low vibrational modes from first-principles calculations: the case of CF_4.
Potential Energy Surface of SF_6.
First Full-Dimensional Potential Energy and Dipole Moment Surfaces of SF_6.

Molécule CF_4

Des PES et DMS à neuf dimensions pour le tétrafluorure de carbone ont été obtenues. Un léger raffinement empirique de la géométrie d'équilibre et de quatre paramètres quadratiques du PES, calculés au niveau de la théorie CCSD(T)/aug-cc-pVQZ-DK, a donné un écart quadratique moyen $de \sim 0{,}001\, cm-1$ pour les énergies de rotation et une très bonne précision pour tous les centres de bandes vibrationnelles connues expérimentalement jusqu'à $3000\ cm^{-1}$.
Au final, 298 paramètres sur les 330 ajustables ont été déterminés. L'ajustement de la PES a été effectué de manière fiable par la méthode des moindres carrés à partir de 19 882 points *ab initio* jusqu'à 15 000 cm^{-1}. En effet, le rapport $\frac{N_{param}}{N_{data}} = \frac{1}{65}$ avec un écart-type de 0,24 cm^{-1} rend cet ajustement assez fiable. Concernant le moment dipolaire calculé au niveau VTZ, 604 paramètres (sur un total de 680 paramètres au sixième ordre) ont été déterminés à partir de la même grille, avec un écart type de 0,00001 Debye.

Molécule SF_6

La PES *ab initio* finale de la molécule SF_6 a été construite à l'ordre 5 à partir de 8708 configurations nucléaires calculées au niveau CCSD(T)/CVQZ-DK. L'écart type est de 0,5 cm^{-1} pour 4283 géométries. Sur les 260 paramètres de la DMS au quatrième ordre, 194 ont été statistiquement bien définis, l'écart type de $1{,}4 \times 10^{-5}$ u.a. . Les résultats obtenus démontrent à quel point une représentation en termes d'opérateurs tensoriels irréductibles permet d'obtenir des expressions analytiques compactes pour les PES et DMS à 9 et 15 dimensions qui seront utilisées dans la modélisation de spectres infrarouges.

Chapitre 3. Construire des listes théoriques

Le troisième chapitre est consacré à la construction de listes *ab initio* pour les molécules (CF_4) et (SF_6). Les calculs quantiques incluant tous les degrés de liberté représentent une tâche extrêmement difficile et nécessitent l'utilisation de méthodes optimisées afin (i) de converger tous le calculs (ii) de diagonaliser de très grandes matrices (iii) de tenir compte de toutes les transitions nécessaires pour des calculs d'opacité fiables.

La section 3.1 décrit le code de calcul TENSOR écrit par M. Rey en FORTRAN90. Ce logiciel est organisé autour de deux axes principaux : NMMod et NMVar. Ce « package » est consacré à l'étude de molécules semi-rigides non-linéaires appartenant à un groupe ponctuel de symétrie quelconque et a récemment été étendu aux systèmes non-rigides.

- NMMod construit l'Hamiltonien de Watson et le moment dipolaire sous forme tensorielle à partir des PES et DMS *ab initio,* et d'un ensemble de coordonnées normales symétrisées $\{q\}$.
- NMVar calcule les solutions propres de l'équation de Schrödinger stationnaire par calcul variationnel. Un jeu de fonctions de bases dites « réduites » est introduit pour résoudre le problème rovibrationnel. La procédure pour construire un spectre moléculaire est décrite schématiquement sur la figure 1

CF_4 : La simulation globale des spectres à haute résolution de CF_4 dans la gamme 0-3000 cm^{-1} est présentée dans Ref. *Understanding global infrared opacity and hot bands of greenhouse molecules with low vibrational modes from first-principles calculations: the case of CF_4* [52]. Une comparaison de l'absorption théorique avec les spectres expérimentaux PNNL [53] à moyenne résolution, enregistrés à des températures de 5, 25 et 50 °C à une pression de 1 atm dans une large gamme spectrale de 570–6500 cm^{-1} a permis de valider les calculs (voir Fig. 2). Les spectres PNNL ne sont pas attribués, donc leurs paramètres de raie ou de bande n'ont pas été extraits, mais ces données brutes fournissent une mine d'informations expérimentales précieuses pour tester les prédictions théoriques. Toutes les comparaisons dans cette section ont été faites à 296 K. On a montré qu'un quasi-continuum formé de raies très faibles pouvait apparaitre dans les spectres

infrarouges de CF_4 même à température ambiante en raison d'une forte augmentation de la densité des transitions. Afin d'effectuer des calculs d'opacité à température ambiante, il a fallu aller jusqu'à $J = 80$, et considérer plus de deux milliards de transitions.

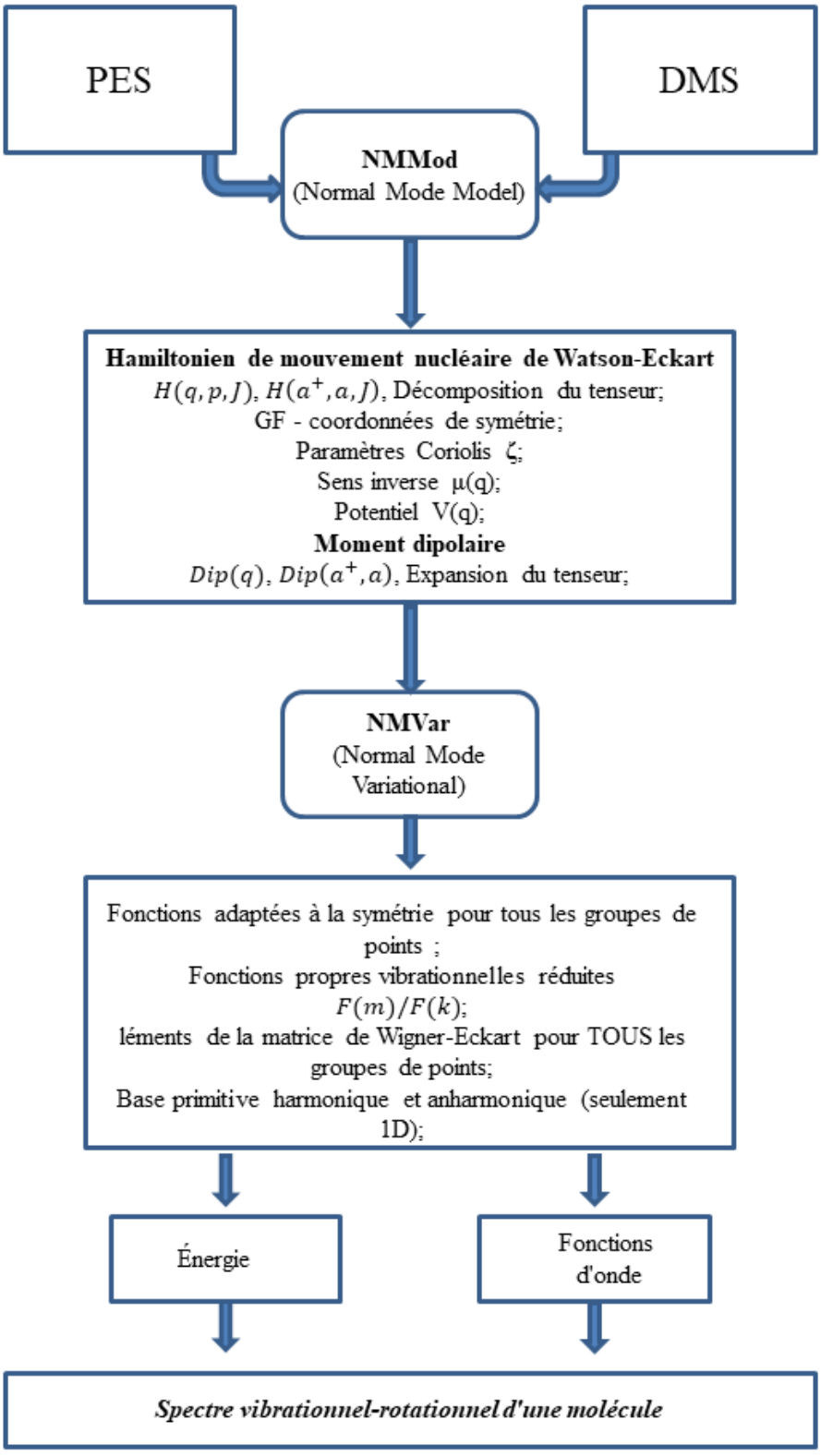

Fig. 1 Description schématique du code TENSOR

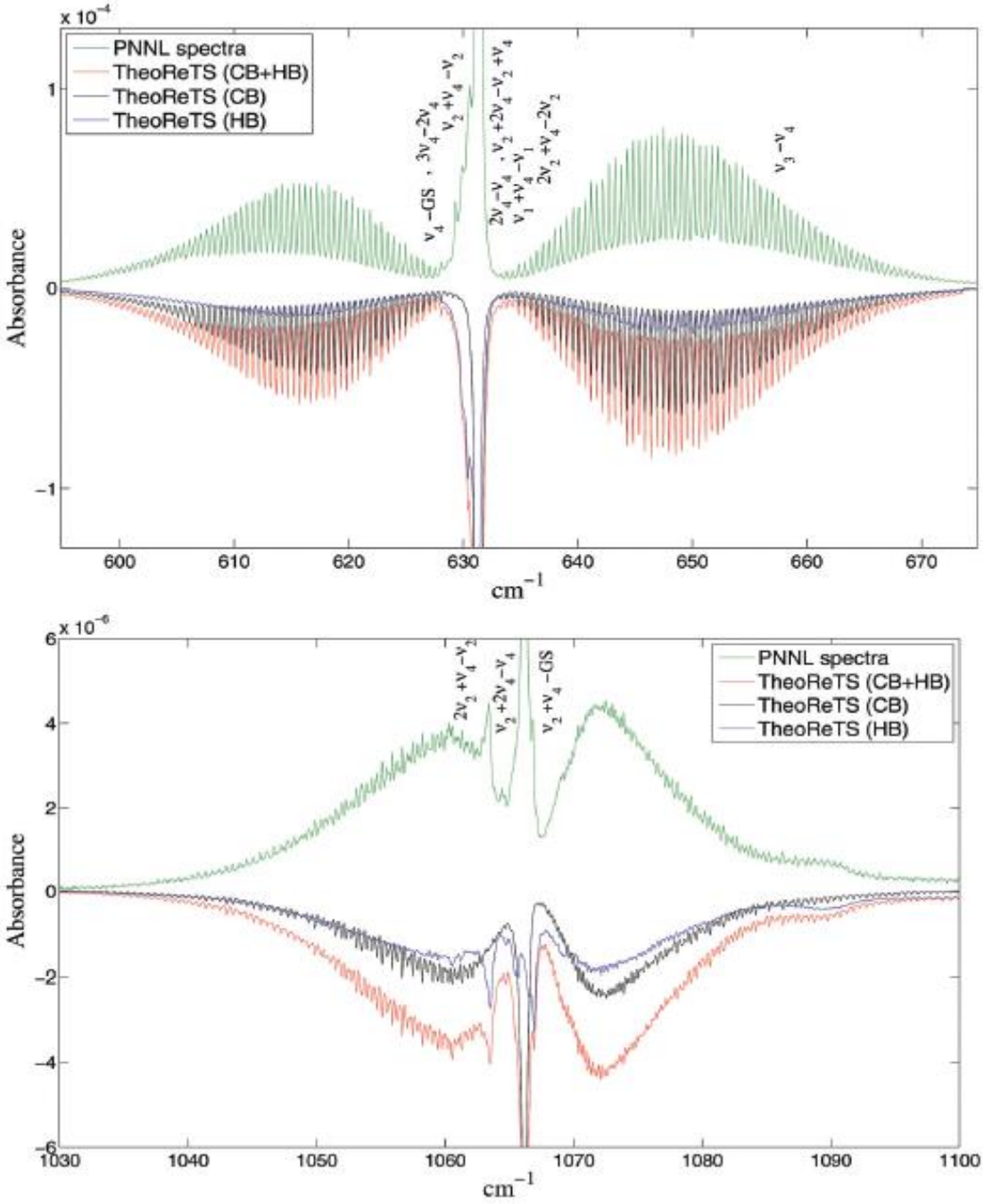

Figure 2 Un exemple de comparaison des spectres d'absorption théorique de CF_4 inclus dans la base de données de Reims-Tomsk (TheoReTS) avec des enregistrements PNNL à température ambiante dans la plage de 1850–2200 cm^{-1} (transitions CB=*cold band*, HB=*hot band* et CB + HB).

SF_6 : Concernant la molécule SF_6, des états rotationnels très excités ont été calculés jusqu'à $J = 121$ dans la Réf. *Towards a complete elucidation of the ro-vibrational band structure in the SF6infrared spectrum from full quantum-mechanical calculations* [54], ce qui a permis de prédire plus de 6 milliards de transitions attribuées à plus de 500 bandes froides et chaudes. La figure 3 donne un exemple de comparaison entre les

spectres PNNL et les calculs théoriques, en séparant les contributions provenant de bandes froides et de bandes chaudes [53]. Ces données seront prochainement incluses dans GEISA sous la forme de sections efficaces. Toutes les simulations de spectres ont été effectuées à une résolution de 0,1 cm^{-1} et une pression de 760 Torr en utilisant une longueur de trajet optique de 20 cm et un profil de Voigt 0,06 cm par atmosphère.

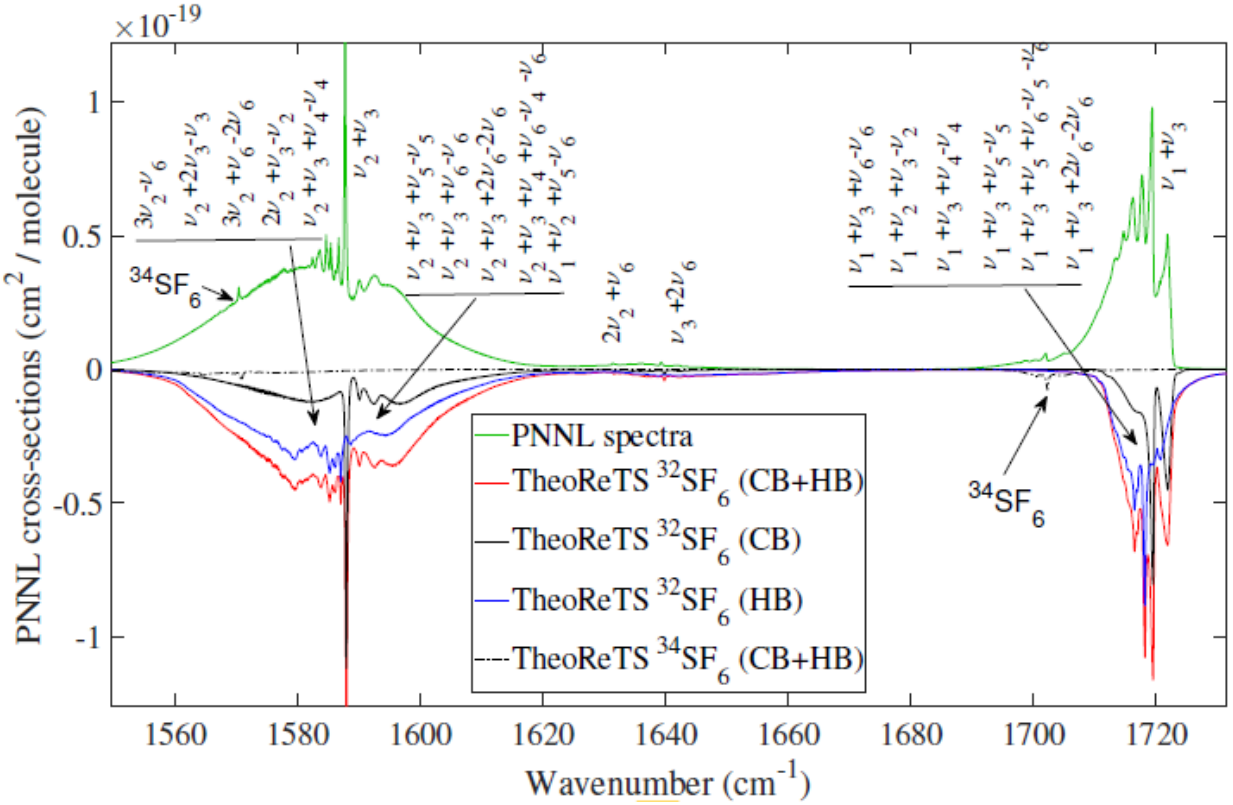

Figure 3 Comparaison des spectres d'absorption théoriques $^{32}SF_6$+$^{34}SF_6$ inclus dans la base de données de Reims-Tomsk (TheoReTS) aux spectres PNNL expérimentaux à moyenne résolution enregistrés à température ambiante dans la gamme 1010-1730 cm^{-1} (transitions CB=*cold band*, HB=*hot band* et CB + HB).

Les intensités absolues des raies ont été calculées et des listes théoriques « globales » construites pour les 3 espèces les plus abondantes :$^{32}SF_6$, $^{33}SF_6$ et $^{34}SF_6$, — en utilisant nos PES et DMS. Nos spectres calculés à température ambiante reproduisent les spectres observés avec une précision jamais atteinte pour une molécule à sept atomes.

Afin d'accélérer les simulations de spectres, les données obtenues ont été divisées en deux parties :

(a) des listes de « raies fortes » avec des niveaux d'énergie inférieurs pour simuler à différentes températures ;

(b) des bibliothèques compressées de "*superlines*" composées de transitions très faibles, facilitant la modélisation du quasi-continuum. Le nombre de transitions est ainsi réduit par 1 ou 2 ordres de grandeur.

Chapitre 4. Analyse du spectre de la molécule CF_4 dans la gamme 2160–2210 cm-1

Le quatrième chapitre est consacré à l'analyse du spectre de la molécule CF_4 dans la gamme 2160–2210 cm^{-1}. La complexité des spectres CF_4 dans la gamme 2160–2210 cm^{-1} est due à la présence des transitions froides et chaudes, ainsi qu'à la présence de bandes à trois, quatre et cinq quanta. L'absorption la plus forte dans cette région est associée à la bande $\nu_1 + \nu_3$ avec une intensité intégrée de $\sim 5{,}0 \times 10^{-19}$cm/molécule. Les bandes $\nu_1 + \nu_2 + \nu_3 - \nu_4 et\ \nu_1 + 2\nu_4$ sont cinq fois plus faibles que cette bande, et $\nu_1 + \nu_3 + \nu_4 - \nu_4, \nu_1 + \nu_2 + 2\nu_4 - \nu_2, \nu_1 + 3\nu_4 - \nu_4, \nu_1 + 2\nu_2 + \nu_3 - 2\nu_2 et\ 2\nu_2 + \nu_3$ est un ordre de grandeur plus faible. Afin d'effectuer une analyse précise des spectres expérimentaux dans cette gamme, une "approche mixte" a été utilisée, combinant Hamiltonien effectif par polyade obtenu à partir de la PES par transformations de contact [99] et intensités *ab initio*. Cette approche permet de caractériser de manière précise les termes de résonnance et par la même occasion de lever certaines ambiguïtés dans la détermination des paramètres des modèles purement empiriques [100].

L'analyse raie par raie du spectre expérimental reste une tâche très difficile. L'Hamiltonien effectif adapté à la structure en polyade de CF_4 est défini comme la somme des contributions correspondant aux différents polyades inférieures $P_k(k = 0,1,\dots,k)$, où P_0 est l'état vibrational fondamental. Le modèle utilisé est défini comme :

$$H = \sum H_k = \tilde{H}_{P_0} + \tilde{H}_{\nu_2} + \tilde{H}_{\nu_4} + \tilde{H}_{Dyad} + \tilde{H}_{\nu_2+\nu_4} + \tilde{H}_{Tetrade} + \tilde{H}_{Dyade2} + \tilde{H}_{Pentade}. \qquad (7)$$

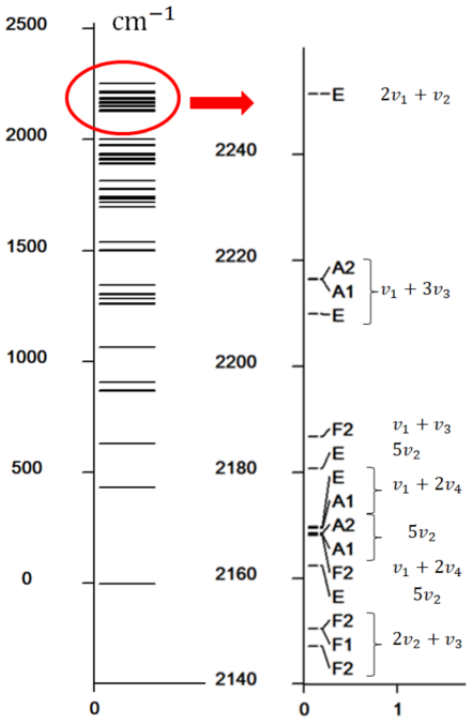

Figure 4 Schéma des niveaux vibrationnels des polyades de la molécule CF_4 (à gauche) et des sous-niveaux vibrationnels (à droite) de l'hexade d'une partie du système correspondant aux bandes vibrationnelles analysées dans ce travail. La bande vibrationnelle $2\nu_1 + \nu_2$ a un sous-niveau de symétrie vibrationnelle de

type E ; la bande $\nu_1 + 3\nu_2$ a trois sous-niveaux (A_1, A_2, E) ; la bande $\nu_1 + \nu_3$ a un sous-niveau (F_2) ; la bande $5\nu_2$ a trois sous-niveaux (A_1, A_2, E) ; la bande $\nu_1 + 2\nu_4$ a trois sous-niveaux (A_1, F_2, E) ; la bande $2\nu_2 + \nu_3$a dix sous-niveaux (F_1, F_2).

Afin d'obtenir des résultats avec une précision comparable à celle expérimentale, l'Hamiltonien effectif a été développé jusqu'au 6ème ordre. La modélisation du spectre, l'attribution des transitions ainsi que le processus d'ajustement ont été effectués à l'aide des logiciels MIRS et SpectraPlot basés sur une comparaison itérative semi-automatique des spectres calculés (bâtons) et expérimentaux. Dans la Réf. *Preliminary analysis of the interacting pentad bands (v +2v ,v +v ,4v ,v +2v ,2v) of CF in the 1600 – 1800 cm^{-1} region* [106], 48 des 2188 paramètres de l'hamiltonien effectif du sixième ordre ont été ajustés sur les spectres dans la gamme 1600–1800 cm^{-1}, dans cette thèse 11 autres paramètres de l'hamiltonien effectif (tableau 2) ont été ajustés sur les spectres dans la plage 2160–2210 cm^{-1}

Tableau 2. Valeurs des paramètres ajustés de l'hamiltonien effectif pour CF_4

	Nomenclature tensorielle		Paramètres ajusté
	Rotation	Vibration	
1	R 0 (0, 0A1)	1010 1010	-1,0529640674E+01
2	R 1 (1, 0F1)	1010 1010	-7,8977801035E-03
3	R 2 (0, 0A1)	1010 1010	-1,5039331401E-05
4	R 1 (1, 0F1)	1010 1002	2,0455767619E-03
5	R 0 (0, 0A1)	1010 1002	5,8729130379E-01
6	R 1 (1, 0F1)	1010 1002	-8,8290674940E-04
7	R 0 (0, 0A1)	1010 0210	8,6692581509E-02
8	R 1 (1, 0F1)	1010 0210	-1,4030889467E-03
9	R 1 (1, 0F1)	1010 0210	-1,0127001972E-04
10	R 0 (0, 0A1)	1010 0210	9,9141412734E-04
11	R 1 (1, 0F1)	1010 0210	-1,6383775845E-07

L'écart type est de 8,6243E-04, ce qui peut être considéré comme un résultat très satisfaisant.
L'ajustement de 8 paramètres du moment dipolaire effectif sur les intensités *ab initio* a permis d'obtenir les intensités pour cinq des six bandes de CF_4 avec une erreur de 1,1 %. Les statistiques de cet ajustement sont présentées dans le tableau 3.

Tableau 3. Valeurs des paramètres de moment dipolaire effectif pour CF_4

	Nomenclature tensorielle		Paramètres ajusté
	Rotation	Vibration	
1	R 0 (0, $0A_1$)	0000 0210	3,0677673220E-04
2	R 0 (0, $0A_1$)	0000 0210	−7,0097729574E-05
3	R 0 (0, $0A_1$)	0000 1002	3,8582053784E-04
4	R 0 (0, $0A_1$)	0000 1010	7,4121145986E-03
5	R 1 (1, $0F_1$)	0000 1010	1,3437943401E-07
6	R 2 (0, $0A_1$)	0000 1010	9,8005076990E-09
7	R 2 (2, 0E)	0000 1010	1,8003881577E-08
8	R 2 (2, $0F_2$)	0000 1010	−3,0670244770E-08

Nous observons dans la figure 5 une vue d'ensemble du spectre expérimental et du spectre calculé dans les mêmes conditions expérimentales avec le logiciel MIRS.

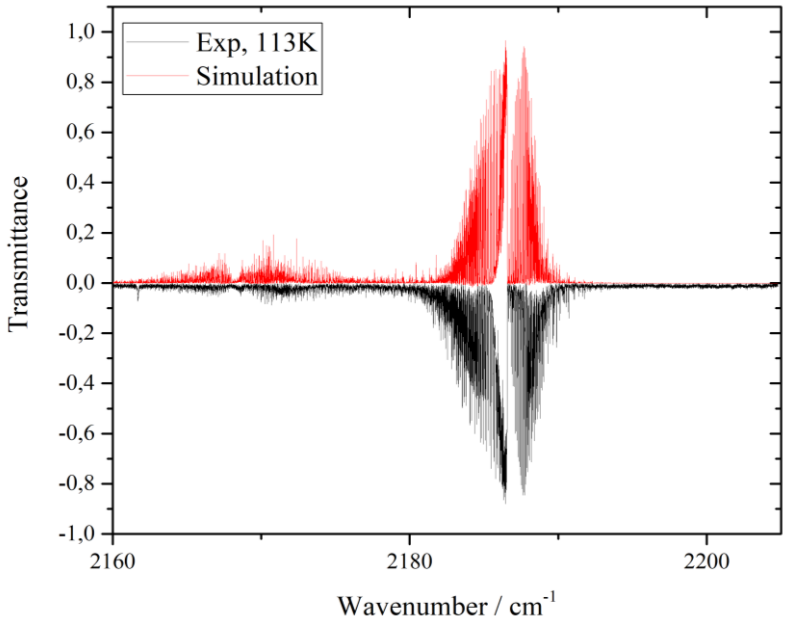

Figure 5 Comparaisons entre les spectres expérimentaux et la simulation theorique de CF_4 à 113K dans la gamme spectrale entre 2160 et 2205 cm^{-1}.

L'objectif principal de ce travail a été de construire des listes très précises pour CF_4 et SF_6 qui seront incluses dans les futures versions des bases de données HITRAN et GEISA.

Conclusion

Cette thèse présente les recherches menées par l'auteur jusqu'en 2022. Voici le travail qui a été effectué : une PES et une DMS à 9 dimensions ont été construites pour CF_4 à l'aide de calculs *ab initio* au niveau CCSD(T) sur une grille composée de 19882 points. De manière similaire, une PES et une DMS à 15 dimensions ont été construites pour la molécule SF_6 dans son état électronique fondamental.

Nous avons obtenu des listes *ab initio* très précises et les plus complètes possibles dans les gammes contenant les bandes d'absorption les plus fortes. Des calculs variationnels poussés basés sur l'introduction de bases réduites ont été effectués et ont permis la prédiction de plusieurs centaines de nouvelles bandes. Par exemple, pour SF_6 les premiers spectres théoriques à haute résolution et à température ambiante dans la gamme 300-3000 cm^{-1} ont été calculés pour les trois isotopologues les plus abondants ($^{32}SF_6$, $^{33}SF_6$ et $^{34}SF_6$). Concernant CF_4, les positions et intensités de transition de l'hexade dans la gamme 2160–2210 cm^{-1} à une température de 113 K ont été analysées. Voici les bandes en question : $2\nu_1 + \nu_2$, $\nu_1 + 3\nu_2$, $\nu_1 + \nu_3$, $5\nu_2$, $\nu_1 + 2\nu_4$ et $2\nu_2 + 2\nu_4$.

Dans tous nos calculs, les intensités *ab initio* calculées permettent de rivaliser avec les meilleures mesures expérimentales. Contrairement aux modèles effectifs, des extrapolations à différentes températures sont beaucoup plus simple et plus fiable à partir de calculs variationnels. Les données théoriques sont incluses dans la base de Reims-Tomsk TheoReTS (http://theorets.univ-reims.fr), (http://theorets.tsu.ru). Ce travail servira de base lors des prochaines analyses de spectres expérimentaux à haute résolution.

Bibliographie

1. Brown L.R., Sung K., Benner D.C., Devi V.M., Boudon V., Gabard T., and et al. Methane line parameters in the HITRAN2012 database. // J. Quant. Spectrosc. Radiat. Transfer. 2013. Vol. 130. pp. 201-219.
2. Bernath P.F. Molecular opacities for exoplanets // Phil. Trans. R Soc. A. 2014. Vol. 372. P. 20130087.
3. Tinetti G., Encrenaz T., and Coustenis A. Spectroscopy of planetary atmospheres in our Galaxy // Astron Astrophys Rev. 2013. Vol. 21. No. 1. P. 63.
4. Buchwitz M., De B.R., Noel S., Burrows J.P., Bovensmann H., Schneising O., Khlystova I., Bruns M., Bremer H., Berga-maschi P., Korner S., and Heimann M. Atmospheric carbon gases retrieved from SCIAMACHY by WFM-DOAS: version 0.5 CO and CH4 and impact of calibration improvements on CO2 retrieval. // Atmos Chem Phys. 2006. Vol. 6. pp. 2907-2918.
5. Frankenberg C., Meirink J.F., Bergamaschi P., Goede A.P.H., Heimann M., Korner S., Platt U., Van W.M., and Wagner T. Satellite chartography of atmospheric methane from SCIAMACHY on board ENVISAT: Analysis of the years 2003 and 2004. // J Geophys Res. 2006. Vol. 111.
6. Bergamaschi P., Frankenberg C., Meirink J.F., Krol M., Den-tener F., Wagner T., Platt U., Kaplan J., Korner S., Heimann M., and et al. Satellite chartography of atmospheric methane from SCIAMACHY on board ENVISAT: 2. Evaluation based on inverse model simulations. // J Geopphys Res. 2007. Vol. 112.
7. Schneising O., Buchwitz M., Burrows J.P., Bovensmann H., Bergamaschi P., and Peters W. Three years of greenhouse gas column-averaged dry air mole fractions retrieved from satellite –Part 2: Methane. // Atmos Chem Phys Discuss. 2008. Vol. 8. pp. 8273-8326.
8. Nisbet E.G., Dlugokencky E.J., Manning M.R., Lowry D., Fisher R.E., France J.L., and al. E. Rising atmospheric methane: 2007–2014 growth // Global Biogeochemical Cycles. 2016. Vol. 30. pp. 1356-1370.
9. Ravishankara A.R., Solomon S., Turnipseed A.A., and Warren R.F. Atmospheric Lifetimes of Long-Lived Halogenated Species // Science, Vol. 259, 1993. pp. 194 - 199.
10. Zander R., Solomon S., Mahicu E., Goldman A., Rinsland C.R., Gunson M.R., Abrams M.C., Chang A.Y., Salawitch R.J., Michelscn H.A., Newchurch M.J., and P. S.G. Increase // Geophys. Res. Lett. 1996. Vol. 23. No. 17. P. 2353 — 2356.
11. Harnisch J., Borchers R., Fabian P., and and Maiss M. Tropospheric trends for CF4 and C2F6 since 1982 derived from SF6 dated stratospheric air // Geophys. Res. Lett. 2000. Vol. 23. pp. 1099 – 1102.
12. Khalil M.A.K., Rasmussen R.A., Culbertson J.A., Prins J.M., Grimsrud E.P., and Shearer M.J.

Atmospheric Perfluorocarbons // Environ. Sci. Technol. 2003. Vol. 37. pp. 4358 – 4361.

13. Malik N.H., Qureshi A.H. A Review of Electrical Breakdown in Mixtures of SF6 and Other Gases // IEEE Trans. Electr. Insul. 1979. Vol. 14. No. 1.
14. Jesse S., Pedraza A.J., and Fowlkes J.D. Etching-enhanced Ablation and the Formation of a Microstructure in Silicon by Laser Irradiation in an SF6 Atmosphere // J. Mater. Res. 2002. No. 17. P. 1002.
15. Johnstone W.M., Newell W.R. Absolute elastic differential cross sections for electron scattering from SF6 // J. Phys. B: At. Mol. Opt. Phys. 1991. No. 24. pp. 473 - 487.
16. Hodnebrog O., Etminan M., Fuglestvedt J.S., Marston G., Myhre G., Nielsen C.J., Shine K.P., and Wallington T.J. Global Warming Potentials and Radiative Efficiencies of Halocarbons and Related Compounds: a Comprehensive Review // Rev. Geophys. 2013. Vol. 51. No. 2. pp. 300 - 378.
17. Harnisch J., N. H. Comparison of Emissions Estimates Derived from Atmospheric Measurements with National Estimates of HFCs, PFCs and SF6 // Environ Sci Pollut Res, Vol. 9, 2002. pp. 315 - 319.
18. Harnisch J., Jager D., Gale J., and Stobbe O. Halogenated Compounds and Climate Change: Future Emission Levels and Reduction Costs // Environ Sci Pollut Res, Vol. 9, 2002. pp. 369 - 374.
19. Boudon V., Champion J.P., Gabard T., Pierre G., Loete M., and Wenger C. Spectroscopic tools for remote sensing of greenhouse CH4, CF4 and SF6 // Environ Chem. Lett., Vol. 1, 2003. pp. 86 - 91.
20. Gordon I.E., Rothman L.S., Hill C., Kochanov R.V., Tan Y., Bernath P.F., Birk M., Boudon V., Campargue A., Chance K., and al. E. The HITRAN 2016 molecular spec- troscopic database // J. Quant. Spectrosc. Radiat. Transf., Vol. 203, 2017. pp. 3 – 69.
21. Jacquinet-Husson N., Armante R., Scott N.A., Chedin A., Crepeau L., Boutammine C., Bouhdaoui A., Crevoisier C., Capelle V., Boonne C., et al. The 2015 edition of the GEISA spectroscopic database // J. Mol. Spectrosc., Vol. 327, 2016. pp. 31 - 72.
22. Bailey C.R., Hale J.B., and Thompson J.W. The molecular structures of carbon and silicon tetrafluorides // Proc. R. Soc. A, Vol. 167, 1938. P. 555.
23. Wolltz P.J.H., Nielsen A.H. The Structure of the Molecules PH3, AsH3, and SbH3 // J. Chem. Phys., Vol. 20, 1952. pp. 307 - 312.
24. Rosenberg A., Brinbaum G. Charge Scavenging vs Hydrogen Atom Scavenging in the Radiolysis of Liquid Saturated Hydrocarbons // J. Chem. Phys., Vol. 48, 1968. pp. 1396 - 1397.
25. Levin I.W., Lewis T.P. Absolute infrared intensities of CF4 // J. Chem. Phys., Vol. 52, 1970. pp. 1608 - 1609.
26. Joslin C.G., Gray C.G., and Singhj S. Far-infrared absorption in gaseous CH4 and CF4 // Mol. Phys., Vol. 54, No. 1469 - 1489, 1985.

27. McDowell R.S., Galbraith H.W., Cantrell C.D., and Nereson N.G. High-J assignments in the 10.5-μm SF6 spectrum: identification of the levels pumped by CO2 P(12) and P(22) // Opt. Letters., Vol. 2, 1978. pp. 97 – 99.

28. McDowell R.S., Krohn B.J., Flicker H., and Vasquez M.C. Sub-Doppler study of the $v3$=2 state of SF6 by infrared–infrared double resonance with a sideband spectrometer // Spectrochimica Acta A., Vol. 42, 1986. pp. 351 – 369.

29. Person W.B., Overend J. Infrared intensities: A model for the quantitative prediction of the vibrational strengths of SF6 and UF6 // J. Chem. Phys., Vol. 66, 1976. pp. 1442 – 1448.

30. Kim K., McDowell R.S., and King W.T. Integrated infrared intensities and transition moments in SF6 // J. Chem. Phys., Vol. 73, 1980. pp. 36 - 41.

31. Boudon V., Hepp M., Herman M., Pak I., and Pierre G. High-Resolution Jet-Cooled Spectroscopy of SF6: The ν2+ ν6Combination Band of32SF6and the ν3Band of the Rare Isotopomers // J. Mol. Spectrosc., Vol. 192, 1998. pp. 359 – 367.

32. Bermejo D., Martínez R.Z., Loubignac E., Boudon V., and Pierre G. High-Resolution spectroscopy and analysis of the fundamental modes of 28 SiF4. Accurate experimental determination of the Si – F bond length // J. Mol. Spectrosc., Vol. 201, 2000. pp. 164 – 171.

33. Faye M., Boudon V., Loëte M., Roy P., and Manceron L. Observation and analysis of the SF6 v2 + v4 + v5 band: Improved parameters for the v5 = 1 state. // J. Mol. Spectrosc., Vol. 325, 2016. pp. 35-41.

34. Faye M., Boudon V., Loëte M., Roy P., and Manceron L. The high overtone and combination levels of SF6 revisited at Doppler limited resolution: A global effective rovibrational model for highly excited vibrational states // J. Quant. Spectrosc. Radiat. Transfer, Vol. 190, 2017. pp. 38-47.

35. Faye M., Manceron L., Roy P., Boudon V., and Loëte M. First analysis of the v3 + v5 combination band of SF6 observed at Doppler limited resolution and effective model for v3 + v5 -v5 hot band. // J. Mol. Spectrosc., Vol. 348, 2018. pp. 37-42.

36. Yurchenko S.N., Carvajal M., Thiel W., and Jensen P. Ab initio dipole moment and theoretical rovibrational intensities in the electronic ground state of PH3 // J. Mol. Spectrosc., Vol. 239, 2006. pp. 71 - 87.

37. Nikitin A.V., Holka F., Tyuterev V.G., and Fremont J. Vibration energy levels of the PH3, PH2D, and PHD2 molecules calculated from high order potential energy surface // J. Chem. Phys., Vol. 130, 2009. P. 244312.

38. Huang X., Schwenke D.W., and Lee T.J. Rovibrational spectra of ammonia. II. Detailed analysis, comparison, and prediction of spectroscopic assignments for 14NH3, 15NH3, and 14ND3 //. Chem. Phys., Vol. 134, 2011. P. 044321.

39. Nikitin A.V., Rey M., Rodina A., Krishna B.M., and Tyuterev V.G. Full-Dimensional Potential Energy and Dipole Moment Surfaces of GeH4 Molecule and Accurate First-Principle Rotationally Resolved Intensity Predictions in the Infrared // Indian J. Chem., Sect. A: Inorg., Bio-inorg., Phys., Theor. Anal. Chem., Vol. 120, 2016. P. 8983 − 8997.
40. Delahaye T., Nikitin A., Rey M., Szalay P.G., and Tyuterev V.G. A new accurate ground-state potential energy surface of ethylene and predictions for rotational and vibrational energy levels. // J. Chem. Phys., Vol. 141, 2014. P. 104301.
41. Delahaye T., Nikitin A.V., Rey M., Szalay P.G., and Tyuterev V.G. Accurate 12D dipole moment surfaces of ethylene // Chem. Phys. Lett., Vol. 639, 2015. P. 275 − 282.
42. Rey M., Delahaye T., Nikitin A.V., and Tyuterev V.G. First theoretical global line lists of ethylene (12C2H4) spectra at various temperatures in the far-infrared range for quantification of absorption and emission in planetary atmospheres // Astron. Astrophys., Vol. 594, 2016. P. A47.
43. Cremer D. Møller–Plesset perturbation theory: from small molecule methods to methods for thousands of atoms, 2011.
44. Bartlett R.J., Musia M. Coupled-cluster theory in quantum chemistry // Rev. Mod. Phys, Vol. 79, 2007. P. 291.
45. Dunning Jr T.H. Gaussian basis sets for use in correlated molecular calculations. I. The atoms boron through neon and hydrogen // J. Chem. Phys., Vol. 90, 1989. pp. 1007 - 1023.
46. Owens A., Yurchenko S.N., Yachmenev A., and Thiel W. A global potential energy surface and dipole moment surface for silane // J. Chem. Phys., Vol. 143, 2015. P. 244317.
47. Owens A., Yurchenko S.N., Yachmenev A., and Tennyson J. A highly accurate ab initio potential energy surface for methane // J. Chem. Phys., Vol. 145, 2016. P. 104305.
48. Rey M., Nikitin A.V., and Tyuterev V.G. Accurate Theoretical Methane Line Lists in the Infrared up to 3000 K and Quasi-continuum Absorption/Emission Modeling for Astrophysical Applications // Astrophys. J., Vol. 847, 2017. P. 1.
49. Rey M., Nikitin A.V., Bezard B., Rannou P., Coustenis A., and Tyuterev V.G. New accurate theoretical line lists of 12CH4 and 13CH4 in the 0–13400 cm−1 range: Application to the modeling of methane absorption in Titan's atmosphere // Icarus, Vol. 303, 2018. pp. 114 – 130.
50. Purvis G.D., Bartlett R.J. A full coupled-cluster singles and doubles model: The inclusion of disconnected triples // J. Chem. Phys., Vol. 76, 1982. P. 1910.
51. Brown L.R., Nikitin A., Chris Benner D., Malathy D.V., Smith M.A.H., Fejard L., Champion J.P., Tyuterev V.G., and Sams R.L. Line intensities of CH3D in the Triad region: 6-10 um // J. Mol. Structure., Vol. 695-696, 2004. pp. 181 - 188.

52. Rey M., Chizhmakova I.S., Nikitin A.V., and Tyuterev V.G. Understanding global infrared opacity and hot bands of greenhouse molecules with low vibrational modes from first-principles calculations: the case of CF4 // Phys.Chem.Chem.Phys. 2018. Vol. 20. pp. 21008--21033.
53. Johnson T.J., Sams R.L., and Sharpe S.W. // Proceedings of SPIE - The International Society for Optical Engineering, Vol. 5269, 2004. pp. 159 – 167.
54. Rey M., Chizhmakova I.S., Nikitin A.V., and Tyuterev G. Towards a complete elucidation of the ro-vibrational band structure in the SF6 infrared spectrum from full quantum-mechanical calculations // Phys. Chem. Chem. Phys., Vol. 21, 2021.
55. Jensen F. Introduction to Computational chemistry. John Wiley and Sons, 2007. 429 pp.
56. Boudon V., Mitchell J., Domanskaya A., Maul C., Georges R., Benidar A., and Harter W.G. High-resolution spectroscopy and analysis of the m3/2m4 dyad of CF4 // Molecular Physics. 2011. Vol. 109. pp. 2273–2290.
57. Carlos M., Gruson O., Richard C., Boudon V., Rotger M., Thomas X., Maul C., Sydow C., Domanskaya A., Georges R., et al. // J. Quant. Spectrosc. Radiat. Transfer, Vol. 201, 2017. pp. 75 - 93.
58. Wang X.G., Sibert III E.L., and Martin J.M.L. // J. Chem. Phys., Vol. 112, 2000. pp. 1353 – 1366.
59. Vogt N., Demaison J., and Rudolph H.D. // Mol. Phys., Vol. 112, 2014. pp. 2873 – 2883.
60. Nikitin A.V., Rey M., and Tyuterev V.G. Rotational and vibrational energy levels of methane calculated from a new potential energy surface // Chem. Phys. Lett. 2011. Vol. 501. pp. 179-186.
61. Eisfeld W. Highly accurate determination of the electron affinity of SF6 and analysis of structure and photodetachment spectrum of SF6 // J. Chem. Phys. 2011. No. 134. P. 054303.
62. Miller B.R., Fink M. Mean amplitudes of vibration of SF6 and intramolecular multiple scattering // J. Chem. Phys. 1981. No. 75. P. 5326.
63. Zhilinskii B.I., Perevalov V.I., and Tyuterev V.G. Method of Irreducible Tensorial Operators in the Theory of Molecular Spectra. Novosibirsk: Nauka, 1987.
64. Tennyson J. Variational calculations of rotation-vibration spectra. Wiley; 1st edition, 2000. 305 - 322 pp.
65. Nikitin A., Champion J.P., and G. T.V. The MIRS computer package for modeling the rovibrational spectra of polyatomic molecules // J. Quant. Spectrosc. Radiat. Transfer., Vol. 82, 2003. pp. 239 - 249.
66. Champion J.P. Complete development of vibration–rotation Hamiltonian adapted to study of interactions in spherical top molecules—application to v2 and v4 bands of 12CH4 // Can. J. Phys., Vol. 55, 1977. pp. 1802 – 1828.
67. Amat G., Nielsen H.H., and Tarrago G. Rotation-vibration of polyatomic molecules. NewYork: Dekker, 1974.

68. Aliev M.R., Watson J.K.G. Higher-order eCects in the vibration-rotation spectra of semirigid molecules. NewYork: Academic Press, 1985. 1 – 67 pp.

69. Никитин А.В., Кочанов Р.В. Визуализация и идентификация спектров программой SpectraPlot // Оптика атмосферы и океана, Т. 24, 2011. С. 936 - 941.

70. Champion J.P., Loete M., and Pierre G. Spectroscopy of the earth's atmosphere and interstellar medium. San Diego: Academic Press, 1992.

71. Rey M., Nikitin A.V., and Tyuterev V.G. Complete nuclear motion Hamiltonian in the irreducible normal mode tensor operator formalism for the methane molecule // J. Chem. Phys., Vol. 136, 2012. P. 244106.

72. Rey M., Nikitin A.V., and Tyuterev V.G. First principles intensity calculations of the methane rovibrational spectra in the infrared up to 9300 cm−1 // Phys. Chem. Chem. Phys., Vol. 15, 2013. pp. 10049 – 10061.

73. Rey M., Nikitin A.V., and Tyuterev V.G. Accurate first-principles calculations for 12CH3D infrared spectra from isotopic and symmetry transformations // J. Chem. Phys., Vol. 141, 2014. P. 044316.

74. Rey M., Nikitin A.V., and Tyuterev V.G. First Predictions of Rotationally Resolved Infrared Spectra of Dideuteromethane (12CH2D2) From Potential Energy and Dipole Moment Surfaces // J. Phys. Chem. A, Vol. 119, 2015. pp. 4763-4779.

75. Ke H., Boudon V., Richard C., Madhur V., Faye M., and Manceron L. Analysis and modeling of combination bands of sulfur hexafluoride 32SF6 based on global fits. Update of the SHeCaSDa database // J. Mol. Spectrosc., Vol. 368, 2020. P. 111251.

76. Rey M., Nikitin A.V., Babikov Y., and Tyuterev V.G. TheoReTS – An information system for theoretical spectra based on variational predictions from molecular potential energy and dipole moment surfaces // J. Molec. Spectrosc. 2016. Vol. 327. pp. 138–158.

77. Fock V. Näherungsmethode zur Lösung des quantenmechanischen Mehrkörperproblems // Zeitschrift für Physik, Vol. 61, 1930. pp. 126 – 148.

78. Hartree D.R., Hartree W. Self-consistent field, with exchange, for beryllium // Proceedings of the royal society A, Vol. 150, 1935.

79. Darling T., Dennison D.M. The Water Vapor Molecule // Phys. Rev., Vol. 57, 1940.

80. Watson J.K.G. Simplification of the molecular vibration-rotation hamiltonian // Mol. Phys., 1968. pp. 479-490.

81. Rey M., Nikitin A.V., and Tyuterev V.G. THEORETICAL HOT METHANE LINE LISTS UP TO T = 2000 K FOR ASTROPHYSICAL APPLICATIONS // Astrophys. J., Vol. 789, 2014.

82. Rey M., Boudon V., and C. W. Orientation of O(3) and SU(2)⊗CI representations in cubic point

groups (Oh,Td) for application to molecular spectroscopy // J. Mol. Spectrosc, Vol. 219, 2003. pp. 313 - 325.

83. Tyuterev V.G., Tashkun S.A., Rey M., Kochanov R.V., Nikitin A.V., and Delahaye T. Accurate spectroscopic models for methane polyads derived from a poten- tial energy surface using high-order contact transformations // J. Phys. Chem. 2013. Vol. 117. pp. 13779–805.
84. Perevalov V.I., Tyuterev V.G., and Zhilinskii B.I. Ambiguity of spectroscopic param- eters in the case of accidental vibration—rotation resonances in tetrahedral molecules. r2J and r2J2 terms for E-F2 interacting state // Chem. Phys. Lett. 1984. Vol. 104. pp. 455–61.
85. Mattoussi M., Rey M., Rotger M., Nikitin A.V., Chizhmakova I., Thomas X., Aroui H., Tashkun S., and Tyuterev V.G. Preliminary analysis of the interacting pentad bands (ν2 + 2 ν4 , ν2 + ν3 , 4 ν2 , ν1 + 2 ν2 , 2 ν1) of CF 4 in the 1600 –1800 cm −1 region // J. Quant. Spectrosc. Radiat. Transfer. 2019. Vol. 226. pp. 92 - 99.
86. Almlof J., Taylor P.R. General contraction of Gaussian basis sets. I. Atomic natural orbitals for first- and second-row atoms // J. Chem. Phys., Vol. 86, 1987. P. 4070.
87. Rey M., Nikitin A.V., and Tyuterev V.G. Convergence of normal mode variational calculations of methane spectra: Theoretical linelist in the icosad range computed from potential energy and dipole moment surfaces // J. Quant. Spectrosc. Radiat. Transf., Vol. 164, 2015. pp. 207 - 220.
88. Nikitin A.V., Rey M., Champion J.P., and G. T.V. Extension of the MIRS com- puter package for modeling of molecular spectra: from effective to full ab ini- tio ro-vibrational hamiltonians in irreducible tensor form // J. Quant. Spectrosc. Radiat. Transf. 2012. Vol. 113. pp. 1034–42.
89. Nikitin A.V., Champion J.P., and Tyuterev V.G. Improved algorithms for the modeling of vibrational polyads of polyatomic molecules: application to Td, Oh, and C3v molecules // J. Molec. Spectrosc, Vol. 182, 1997. pp. 72 - 84.
90. Werner H., Knowles P.J., Lindh R., and al. E. MOLPRO, version 2009.1, a package of ab initio programs; http://www.molpro.net
91. Nikitin A.V., Rey M., and Tyuterev V.G. First fully ab initio potential energy surface of methane with a spectroscopic // J. Chem. Phys., Vol. 145, 2016. P. 114309.
92. Manzhos S., Carrington T., Laverdure L., and Mosey N. Computing the Anharmonic Vibrational Spectrum of UF6 in 15 Dimensions with an Optimized Basis Set and Rectangular Collocation // J. Phys. Chem. A, Vol. 119, 2015. P. 9557 − 9567.
93. Werner H.J., Knowles P.J., Knizia G., Manby F.R., and al. E. Molpro: a general-purpose quantum chemistry program package // WIREs Comput. Mol. Sci., Vol. 2, 2012. pp. 242 - 253.
94. Schütz H.J., Knowles P.J., Lindh R., al. E. MOLPRO, version 2019.1, a package of ab initio programs // http://www.molpro.net.

95. Halonen L., Child M.S. A local mode model for tetrahedral molecules // Molec. Phys. 1982. Vol. 46. pp. 239-255.

96. Schatz P.N., Hornig D.F. Bond Moments and Derivatives in CF4, SiF4, and SF6 from Infrared Intensities // J. Chem. Phys. 1953. Vol. 21. No. 9. P. 1516.

97. Fernandez-Gomez M., Lopez-Gonzalez J.J. Calculation of internal valence force constants for XY6(Oh) Octahedral molecules // J. Mol. Struct. 1990. Vol. 220. pp. 287 - 300.

98. Pistorius T.C.W.F. Potential Field and Force Constants of Octahedral Molecules // J. Chem. Phys. 1958. Vol. 29. No. 6. pp. 1328 - 1332.

99. Gray D.L., Robiette A.G. The anharmonic force field and equilibrium structure of methane // J. Mol. Spectr., Vol. 37, 1979. pp. 1901 – 1920.

100. Boudon V., Champion J.P., Gabard T., Loëte M., Michelot F., Pierre G., Rotger M., Wenger C., and Rey M. Symmetry-adapted tensorial formalism to model rovibrational and rovibronic spectra of molecules pertaining to various point groups // J. Mol. Spectrosc, Vol. 228, 2004. pp. 620 - 634.

101. Ulenikov O.N., Bekhtereva E.S., Albert S., Bauerecker S., Niederer H.M., and Quack M. Survey of the high resolution infrared spectrum of methane (12CH4 and 13CH4): Partial vibrational assignment extended towards 12 000 cm-1 // J. Chem. Phys. 2014. Vol. 141. No. 23. P. 234302.

102. Oldani M., Bauder A., Hilico J.C., Loete M., and Champion J.P. Microwave Fourier Transform Spectroscopy of Rovibrational Transitions in the ν2/ν4 of Methane-12C and -13C // Europhys. Lett. 1987. Vol. 4. pp. 29 – 33.

103. Nikitin A.V., Rey M., and Tyuterev V.G. An efficient method for energy levels calculation using full symmetry and exact kinetic energy operator: tetrahedral molecules // J. Chem. Phys., Vol. 142, 2015. P. 094118.

104. Woon D.E., Dunning T.H. Gaussian basis sets for use in correlated molecular calculations. III. The atoms aluminum through argon // J. Chem. Phys., Vol. 98, 1993. P. 1358.

105. Wilson A.K., Woon D.E., Peterson K.A., and Dunning T.H. Gaussian basis sets for use in correlated molecular calculations. IX. The atoms gallium through krypton // J. Chem. Phys, Vol. 110, 1999. P. 7667.

106. DeYonker N.J., Peterson K.A., and Wilson A.K. Systematically Convergent Correlation Consistent Basis Sets for Molecular Core−Valence Correlation Effects: The Third-Row Atoms Gallium through Krypton // J. Phys. Chem. A, Vol. 111, 2007. P. 11383 − 11393.

107. Jong W.A.D., Harrison R.J., and Dixon D.A.P. Douglas-Kroll energy and gradients in NWChem: Estimating scalar relativistic effects using Douglas-Kroll contracted basis sets- // J. Chem. Phys., Vol. 114, 2001. P. 48.

108. Faye M., Le Ven A., Boudon V., Manceron L., Asselin P., Soulard P., Kwabia Tchana F., and Roy P. High-resolution spectroscopy of difference and combination bands of SF6 to elucidate the ν3 + ν1 − ν1 and ν3 + ν2 − ν2 hot band structures in the ν3 region // Mol. Phys., Vol. 112, 2014. pp. 2504 - 2514.
109. Boudon V., Manceron L., Kwabia Tchana F., Loëte M., Lago L., and Roy P. Resolving the forbidden band of SF6 // Phys. Chem. Chem. Phys, Vol. 16, 2014. pp. 1415 – 1423.

Annexe

Understanding global infrared opacity and hot bands of greenhouse molecules with low vibrational modes from first-principles calculations: the case of CF_4

Michaël Rey, Andrei V. Nikitin, I.S. Chizhmakova, Vladimir G. Tyuterev

Phys.Chem.Chem.Phys., 20, (2018)

PCCP

PAPER

View Article Online
View Journal | View Issue

Cite this: *Phys. Chem. Chem. Phys.*, 2018, **20**, 21008

Understanding global infrared opacity and hot bands of greenhouse molecules with low vibrational modes from first-principles calculations: the case of CF_4†

Michaël Rey,* [a] Iana S. Chizhmakova,[bc] Andrei V. Nikitin[b] and Vladimir G. Tyuterev[a]

Fluorine containing molecules have a particularly long atmospheric lifetime and their very big estimated global warming potentials are expected to rapidly increase in the future. This work is focused on the global theoretical prediction of infrared spectra of the tetrafluoromethane molecule that is considered as a potentially powerful greenhouse gas having the largest estimated lifetime of over 50 000 years in the atmosphere. The presence of relatively low vibrational frequencies makes the Boltzmann population of the excited levels important. Consequently, the "hot bands" corresponding to transitions among excited rovibrational states contribute significantly to the CF_4 opacity in the infrared even at room temperature conditions but the existing laboratory data analyses are not sufficiently complete. In this work, we construct the first accurate and complete *ab initio* based line lists for CF_4 in the range 0–4000 cm^{-1}, containing rovibrational bands that are the most active in absorption. An efficient basis set compression method was applied to predict more than 700 new bands and subbands *via* variational nuclear motion calculations. We show that already at room temperature a quasi-continuum of overlapping weak lines appears in the CF_4 infrared spectra due to the increasing density of bands and transitions. In order to converge the infrared opacity at room temperature, it was necessary to include a high rotational quantum number up to J = 80 resulting in 2 billion rovibrational transitions. In order to make the cross-section simulation faster, we have partitioned our data into two parts: (a) strong & medium line lists with lower energy levels for calculation of selective absorption features that can be used at various temperatures and (b) compressed "super-line" libraries of very weak transitions contributing to the quasi-continuum modelling. Comparisons with raw previously unassigned experimental spectra showed a very good accuracy for integrated absorbance in the entire range of the reported spectra predictions. The data obtained in this work will be made available through the TheoReTS information system (http://theorets.univ-reims.fr, http://theorets.tsu.ru) that contains *ab initio* born line lists and provides a user-friendly graphical interface for a fast simulation of the CF_4 absorption cross-sections and radiance under various temperature conditions from 80 K to 400 K.

Received 22nd May 2018,
Accepted 13th July 2018

DOI: 10.1039/c8cp03252a

rsc.li/pccp

1 Introduction

The radiative properties of relatively heavy long-lived greenhouse gases are much less studied compared with those of principal atmospheric absorber lighter species such as water, carbon dioxide or methane. Among these, the fluorine containing molecules (CF_4, C_2F_4, NF_3, SF_6, *etc.*), though being yet minor impurities, have a particularly long atmospheric lifetime and their very big estimated global warming potentials are expected to rapidly increase in the future.[1] Their common feature is a presence of relatively low vibrational frequencies that makes the Boltzmann population of the excited levels important. Consequently, the "hot bands" corresponding to transitions among excited rovibrational states contribute significantly to the opacity in the infrared even at room temperature conditions. This results in very crowded rovibrational spectra that are difficult to resolve line-by-line. Only a few bands of these

[a] *Groupe de Spectrométrie Moléculaire et Atmosphérique, UMR CNRS 7331, BP 1039, F-51687, Reims Cedex 2, France. E-mail: michael.rey@univ-reims.fr*
[b] *Laboratory of Theoretical Spectroscopy, Institute of Atmospheric Optics, SB RAS, 634055 Tomsk, Russia*
[c] *Laboratory of Quantum Mechanics of Molecules and Radiative Processes, Tomsk State University, 36 Lenin Avenue, 634050 Tomsk, Russia*

† Electronic supplementary information (ESI) available: The corresponding full-dimensional potential energy and dipole moment surfaces are provided. See DOI: 10.1039/c8cp03252a

molecules have been analyzed in limited wavenumber ranges and the high-resolution spectral line or band parameters in spectroscopic databases such as HITRAN[2] or GEISA[3] are much sparser than those for lighter greenhouse species. This work is focused on the global theoretical prediction of infrared spectra of the CF_4 molecule. Tetrafluoromethane (CF_4, also denoted as Freon-14, PFC-14, halocarbon 14, carbon tetrafluoride, *etc.*) has the largest estimated lifetime of over 50 000 years in the atmosphere for freons. CF_4 currently present in the atmosphere is predominantly anthropogenic due to fugitive emissions from the aluminium industry and semiconductor manufacturing.[4,5] Together with other perfluorocarbons it is considered as a potentially powerful greenhouse gas that could play an active role in global climate change[6,7] and falls under the directives of the Kyoto Protocol[8] among species recommended for environmental monitoring. To this end the temperature dependence of its contribution to the radiation budget in the troposphere and stratosphere is required, but a significant part of this information is still lacking despite considerable efforts in laboratory experiments and analyses (see Section 2). Purely empirical spectroscopic models are very useful for spectral assignments but limited both in frequency and temperature coverage particularly for hot band contributions. Existing laboratory data are not sufficiently complete for the CF_4 opacity evaluations in the infrared. Recently, progress in *ab initio* calculations and variational predictions for rovibrational spectra from potential energy surfaces (PES) and dipole moment surfaces (DMS) for lighter species such as water,[9,10] ozone,[11–13] ammonia[14–16] methane[17–24] or ethylene[25–28] have permitted a breakthrough in resolving completeness issues and understanding the opacity distributions of these species for various temperature conditions. The new generation of *ab initio* born databases giving access to extensive line lists containing billions of transitions have become the current reference data for various planetary applications (see examples in ref. 29–31 and references therein). For heavier molecules with lower lying vibrational modes such as CF_4, such predictions are even more challenging because they require bigger V and J quantum numbers to be included. At a given temperature, this results in a much larger density of spectral bands and transitions requiring efficient methods for the convergence of variational calculations. In this paper, we report the first large-scale variational predictions for CF_4, including cold, hot, overtone and combination bands, which are the most active in IR absorption up to six vibrational quanta. We show that already at room-T a "quasi-continuum" (QC) of overlapping weak lines appears in CF_4 infrared spectra due to the increasing density of bands and transitions that must be accounted for in the converged opacity. A similar QC has been recently reported for methane spectra, both in theory[32–34] and in observations,[35] but at much higher temperatures of about 1000 K. The paper is structured as follows. The state-of-the art of CF_4 infrared spectroscopy is briefly overviewed in Section 2. Electronic structure calculations and fine tuning of the CF_4 PES using available experimental data are described in Section 3. Section 4 is devoted to the techniques of variational calculations, symmetrization and basis set convergence issues. The full calculated ro-vibrational line list (Section 5) is partitioned into strong & medium intensity transitions and the quasi-continuum of individually indistinguishable weak lines. The latter ones are compressed using "super-lines" (SL) databases for an efficient modelling of absorption cross-sections. Validation *versus* raw experimental spectra is considered in Section 6. Final sets of line parameters and SL libraries are freely available *via* the TheoReTS information system[29] (http://theorets.univ-reims.fr/ or http://theorets.tsu.ru/). Knowledge of excited ro-vibrational states of CF_4 is also of importance for such fundamental phenomena as clustering of high-J level patterns and related symmetry effects.[36,37]

2 State-of-the-art in the spectroscopy of the tetrafluoromethane

$^{12}CF_4$ is a spherical top molecule with tetrahedral (T_d) point group symmetry at the equilibrium geometry similar to $^{12}CH_4$. But in contrast to methane, the relation between the stretching ($\nu_1(A_1)$, $\nu_3(F_2)$) and bending ($\nu_2(E)$, $\nu_4(F_2)$) normal mode frequencies of CF_4 makes the polyad structure much less regular, *e.g.* the resonance scheme for fundamental frequencies $\omega_1:\omega_2:\omega_3:\omega_4$ of methane can be simply approximated as $\approx 2:1:2:1$ while that of CF_4 is given by $\approx 4:2:6:3$. This more complicated polyad scheme and the high molecular symmetry give rise to numerous degeneracies and quasi-degeneracies and to vast and complicated resonance interactions due to inter-mode couplings. Because of the overlapping polyads, many sets of overtone and combination bands are not really isolated from nearby ones. For this reason, empirical effective models are more difficult to apply than for CH_4, and the line-by-line analyses are much less advanced.

Another challenge concerns the modelling of hot bands (HB) that strongly contribute to the absorption, even at room temperature. CF_4 is heavier than methane and has two low-lying bending frequencies at 440 and 640 cm^{-1} leading to a huge number of IR-active transitions belonging to the hot bands. An account of these hot bands using empirical effective spectroscopic models is an issue that has not been yet solved. This is why, except for very few studies, most of the analyses of cold band (CB) transitions has been carried out during the last four decades.

The first experimental study of infrared CF_4 spectra was reported by Bailey *et al.*[38] in 1938. The corresponding measurements covered the range 2–19 μm which was then extended in 1951 by Woltz *et al.*[39] to 2–33 μm. After that, other experimental studies were published[40,41] covering the far-infrared region, complemented later on by a theoretical study.[42] High-resolution spectra of the ν_4 and $\nu_2 + \nu_4$ bands have been recorded by McDowell *et al.*[43] with one of the absorption features identified as belonging to the hot band $\nu_2 + \nu_4 - \nu_2$. McDowell *et al.*[44–46] also carried out the laser spectroscopy of CF_4. Rotational transitions within the (0010) vibrational state were investigated using double-resonance experiments by Takami[47,48] and at nearly the same time both the analysis

of the Q branch of $2\nu_1 + \nu_4$ up to $J = 40$ and of the ν_1 were reported by Pine.[49]

Raman spectra, with underlying $\nu_1 + \nu_2 - \nu_2$ hot band (HB) transitions, have been studied by Esherick *et al.*[50] The ν_3 band was reinvestigated using proton energy-loss spectroscopy by Maring *et al.*[51] followed by line width measurements of the $R(29)$ transitions in the combination band $\nu_2 + \nu_4$ by Hartemink and Godfried.[52] A simultaneous analysis of the ground state (GS) and the bands ν_3 and $2\nu_3$ was performed by Gabard *et al.*[53] using the tetrahedral formalism described by Champion[54] and Zhilinskii *et al.*[55] Boujut *et al.*[56] have studied the energies of ν_3 and ν_4 overtones using previous work[57] and the initial values of the parameters from TDS[58] and STDS[59] (Tetrahedral and Spherical Top Database System). More recently, a study of the $\nu_3/2\nu_4$ was made by Boudon *et al.*[60] also using the tetrahedral formalism of the Dijon group, whereas the subsequent work by Boudon *et al.*[61] was devoted to a simultaneous analysis of the ν_1, $2\nu_1 - \nu_1$, ν_2, $2\nu_2$ and $3\nu_2 - \nu_2$ bands using high-resolution stimulated Raman spectroscopy. The most extensive empirical model to date was constructed very recently by Carlos *et al.*[62] for 17 rovibrational bands, including some HBs, where the reader can find other references to previous spectroscopic works. Note that only line positions have been fitted in the empirical model of ref. 62. For the cross-section simulations old values of two dipole moment derivatives from ref. 63 were used.[60]

As stated in ref. 62 "*no further dipole moment refinement is possible, since no individual line intensities measurements are available, due to the spectroscopic congestion for this molecule, for which almost all observed lines result from the overlap of several transitions*". Lacking information on line-by-line Einstein radiative coefficients for most of the hundreds of bands contributing to the IR absorption is one of the major drawbacks of a purely empirical approach.

3 Potential and dipole moment surfaces

Several empirical and theoretical studies have been devoted to the determination of the equilibrium nuclear configuration[60,62,64,65] and of the harmonic CF_4 frequencies.[64] Cubic and partially quartic force-fields have been fitted to experimental spectral parameters by Jeannotte *et al.*[66] and Brodersen.[67] Previous studies in this domain have been reviewed in detail by Wang *et al.*,[64] who refined *ab initio* harmonic frequencies *via* Van Vleck perturbation theory using experimental vibrational band centers up to 2500 cm^{-1}. They have applied a "mixed approach" combining empirically adjusted harmonic frequencies and *ab initio* cubic and quartic anharmonic constants. The latter ones were computed in a similar way to that described in the *ab initio* work of Lee *et al.*[68] for the methane force field using the Coupled Cluster approach with all the single and double substitutions from the Hartree–Fock reference determinant augmented by a perturbative treatment of triple excitations, CCSD(T). It was also concluded[64] that the T1 diagnostic (which is the measure of the importance of multi-reference effects) was only 0.0119 for CF_4 making the CCSD(T) method an appropriate choice.

Table 1 *Ab initio* and empirical values of the equilibrium C–F bond length for $^{12}CF_4$. An optimized value was obtained in this work (=TW), see Section 3.2

Method/basis	r(C–H) (in Angstrom)	Ref.
CVTZ-DK	1.3171	TW
CVQZ-DK	1.3153	TW
VTZ	1.3192	TW
VQZ	1.3172	TW
CVTZ	1.3171	TW
CVQZ	1.3153	TW
CVTZ-F12	1.3153	TW
CVQZ-F12	1.3147	TW
CVQZ	1.3153	TW
ACVQZ	1.3161	TW
Empirical	1.31588	60
Empirical	1.31486	62
Empirical	1.31526	64
wCVTZ	1.3163	65
wCVQZ	1.3152	65
Exp.	1.3151	65
Optimized value (empirical)	1.315349	TW

3.1 Electronic structure calculations

As in previous electronic structure calculations[64,65,69] on CF_4, we use here the CCSD(T) method,[70] which has been found to provide a reasonably good description of the equilibrium configuration r_e and for the fundamental frequencies. For the atomic basis we employed the standard correlation consistent polarized valence basis sets cc-pVTZ and cc-pVQZ of Dunning and co-workers,[71] where T and Q stand for triple and quadruple cardinal numbers. The abbreviated notations VTZ and QTZ will be used for these sets in what follows. Wang *et al.*[64] have shown that with the VTZ basis set all fundamental frequencies except for the ν_3 band were close to experimental values. They have extended the basis set to "VTZ + 1" for the anharmonic force field calculations, where the suffix " + 1" denoted the addition of a single *d*-function to accommodate polarization effects. Accurate equilibrium structures of fluoro- and chloroderivatives of methane have been found in ref. 65 where the *ab initio* structure was optimized with the CCSD(T) all electrons being correlated and the correlation-consistent polarized weighted core-valence triple- and quadruple-zeta basis sets[72] (cc-pwCVTZ and cc-pwCVQZ) leading for the latter set to $r_e = 1.3152$ Å of CF_4 quoted in Table 1.

Thanks to increasing computational resources, it is now possible to compute a full 9-dimensional PES on a large grid of geometries and not just a cubic or quartic force field near the equilibrium. To this end, we used in this work a similar technique of grid generation as described in our recent studies on methane PES[73] where it was possible to achieve a "spectroscopic accuracy" for *ab initio* calculations over a large range of energies. For CF_4 with 42 electrons an inclusion of all fine correlations considered in the CH_4 case is currently not feasible. As a compromise between accuracy and computational cost, we have chosen the VQZ basis set to compute electronic energies on 19 882 nuclear geometries. The grid of geometries

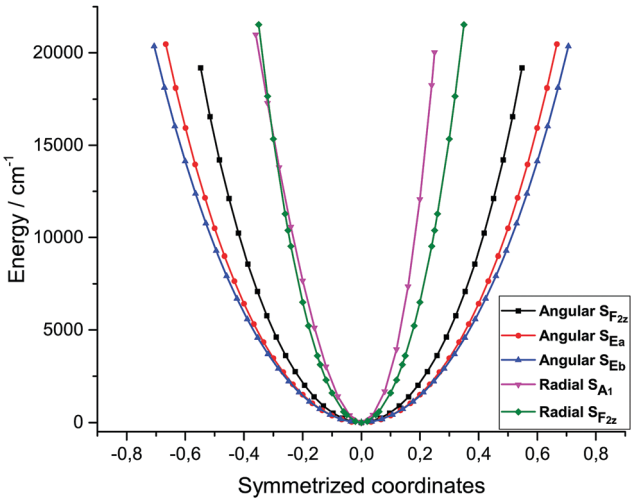

Fig. 1 Characteristic sections of CF_4 *ab initio* PES along dimensionless symmetrized coordinates.

is obtained with the same method as described for the methane PES[73] where symmetry coordinates sample the PES at energy layers of 1000, 2500, 4000, 7000, 10 000, 12 500, and 15 000 cm^{-1}. The VQZ basis reduces significantly the *ab initio* error in the ν_3 band center with respect to VTZ whereas other fundamental frequencies remain consistent with experiment (as shown in the next Section 3.2). This also improves the equilibrium geometry from r_e = 1.319 Å (VTZ) to r_e = 1.317 Å (VQZ) in better agreement with cc-pwCVQZ of ref. 65 that are in the range r_e = 1.315–1.316 Å. For completeness, we have also checked the optimization of the equilibrium geometry with core-valence correlations, including scalar relativistic Douglas–Kroll (DK)[74] contributions, and also with explicitly correlated F12 basis sets. This did not produce significant changes in r_e (see Table 1) whereas the corresponding ansatz would be too expensive for the full surface.

The same analytical PES representation of the 9D PES was used as for other tetrahedral molecules CH_4[18] and GeH_4[75] in terms of an expansion in the symmetrized powers $\mathbf{p} = \{p_1,\ldots,p_{4\sigma}\}$ of the $\left\{S_1^{(A_1)}, S_{2\sigma}^{(E)}, S_{3\sigma'}^{(F_2)}, S_{4\sigma''}^{(F_2)}\right\}$ curvilinear coordinates expressed *via* Morse-type variables for bond stretches and cosine-type variables for angles[18]

$$V(\mathbf{R}) = \sum_{\{\mathbf{p}\}} \mathbf{F}_\mathbf{p} \prod_{i\sigma} \left(S_{i\sigma}^{(\Gamma_i)}\right)^{p_{i\sigma}}. \quad (1)$$

Here A_1, E, and F_2 denote non-degenerate, two-fold and three-fold degenerate irreducible representations (symmetry types) of the T_d point group, the indices σ, σ' and σ'' stand for the components of degenerate vibrations and $\mathbf{F}_\mathbf{p}$ for the set of the PES parameters fitted to *ab initio* electronic energies. We have included in eqn (1) all parameters up to the sixth-order complemented by principal angular parameters up to the eighth-order. Altogether 298 parameters (of 330 adjustable ones for all four modes) were statistically well determined in the least-squares fit to 19 882 *ab initio* points up to $E_{max} \sim 15\,000$ cm^{-1}. The ratio N_param/N_data = 1/65 with the RMS deviation of 0.24 cm^{-1} made the fit quite robust. This PES is given in the ESI.† Characteristic PES sections along several symmetrized coordinates are shown in Fig. 1. Harmonic frequencies and band centers up to second overtones and combination bands are collected in Table 2.

Table 2 Harmonic oscillator frequencies and some band centers (in cm^{-1}) of $^{12}CF_4$ computed from the purely *ab initio* PES and from our empirically refined PES (TW). First dipole moment derivatives (in Debye) are quoted at the lower panel

	VQZ PES (TW)	Refined PES (TW)	Ref. 64
ω_1	921.16	920.85	921.57
ω_2	439.91	439.72	439.91
ω_3	1310.81	1305.36	1303.01
ω_4	638.04	637.18	637.89

	VQZ PES (TW)	Refined PES (TW)	Exp.
$\nu_1(A_1)$	909.35	909.025	909.072
$\nu_2(E)$	435.59	435.410	435.399
$\nu_3(F_2)$	1289.12	1283.770	1283.664
$\nu_4(F_2)$	631.93	631.086	631.059
$2\nu_2(A_1)$	868.40	868.012	867.906
$\nu_2 + \nu_4(F_2)$	1067.23	1066.201	1066.122
$\nu_2 + \nu_4(F_1)$	1067.78	1066.758	1066.698
$2\nu_4(F_2)$	1262.36	1260.593	1260.43
$2\nu_4(A_1)$	1263.55	1261.861	1261.809
$2\nu_4(E)$	1263.87	1262.189	1262.112
$\nu_1 + \nu_4(F_2)$	1540.67	1539.457	1539.3
$2\nu_1 + \nu_4(F_2)$	2447.04	2445.456	2445.596
$2\nu_3(F_2)$	2572.79	2562.175	2561.912
$2\nu_3(E)$	2580.93	2570.223	2570.013

	VQZ DMS (TW)		Exp.[63]
$\lvert\partial\mu/\partial q_3\rvert$	0.491	—	0.473
$\lvert\partial\mu/\partial q_4\rvert$	0.077	—	0.0702

There are very few results available in the literature for a theoretical evaluation of dipole moment parameters of CF_4. To our knowledge, only two first-order derivatives $d\mu/dq_3$, $d\mu/dq_4$ computed using the density functional method have been reported by Papousek *et al.*[63] who also cited previous *ab initio* estimations of ref. 76. Note that our value of 0.077 D for $|d\mu/dq_4|$ is in quite large disagreement with that obtained from the density functional theory ($|d\mu/dq_4|$ = 0.0563 D, see Table 17 of ref. 63).

No full-dimensional DMS has been published for CF_4. Accurate knowledge of this vector quantity is mandatory for the predictions of line and band intensities (see Section 5). We derived the 9D DMS components using the external electric field *ab initio* method. This is more demanding than PES as it requires six calculations for symmetry breaking nuclear displacement for each point of the DMS components. The dipole moments were computed as the derivatives of the energy with respect to the weak external uniform electric field using the finite difference scheme with the field variation of 0.0001 a.u. around the zero field strength in a two step procedure. First VTZ dipole moment calculations were carried out on the full grid of the same 19 882 nuclear geometries as for the PES.

Analytical DMS expansions of the same order as for the PES were fitted to *ab initio* values both in the curvilinear internal

and in rectilinear normal mode coordinates. The final DMS results were parametrized in the molecular fixed Eckart frame (MEF) dipole moment $\mu_\alpha^{\mathrm{MFF}}$ expansion

$$\mu_\alpha^{\mathrm{MFF}} = \sum_i \tilde{K}_i \tilde{R}_{i\alpha}^p,$$

where

$$\tilde{R}_{i\alpha}^p = \left(\left(\left[q_1^{(A_1)} \right]^{p_1} \times \left[q_2^{(E)} \right]^{p_2} \right)^{(C_1)} \times \left(\left[q_3^{(F_2)} \right]^{p_3} \times \left[q_4^{(F_2)} \right]^{p_4} \right)^{(C_2)} \right)_\alpha^{(F_2)} \quad (2)$$

using couplings ($\times$) of successive powers $p = \{p_1,p_2,p_3,p_4\}$ of irreducible T_d tensors corresponding to one $\left\{q_1^{(A_1)}\right\}$, two-fold $\{q_2^{(E)}\}$ and three-fold $\left\{q_3^{(F_2)}, q_4^{(F_2)}\right\}$ degenerate normal mode vibrations. Here C_1 and C_2 denote tetrahedral symmetry species of intermediate tensor couplings belonging to $\{A_1,A_2,E,F_1,F_2\}$ types, $\alpha = x, y, z$ are the components of the three-fold degenerate F_2 species and $\tilde{K}_i$ are DMS parameters. We use the form (2) of the DMS because our TENSOR code, which is employed for intensity calculations, was programmed in this representation. The reader can find technical details of the formalism in ref. 77 and 78 devoted to the molecules of the same T_d symmetry. The normal-mode tensor representation is also compatible with the MIRS code[79] that was used for many recent analyses of methane and phosphine experimental spectra. 604 parameters (of the total 680 sixth-order ones) were statistically well determined in the fit using eqn (2) to VTZ dipole moment values on the full grid of 19 882 geometries with the RMS deviation of 0.00001 Debye.

As a next step, we computed the dipole moments with a larger atomic basis VQZ using the same scheme but on a reduced grid of 1020 geometries below $E_{\max}$ = 5000 cm^{-1}. The dipole differences (VQZ-VTZ) were fitted by a fourth order expansion (2) using 103 adjusted parameters. This was used as a correction to the sixth-order VTZ DMS surface. The final DMS surface is provided in the ESI.†

3.2 Refining quadratic forces constants and geometry

The force constant matrix F, together with the geometry-based Wilson[80,81] matrix G, are used to determine the vibrational frequencies and the associated normal modes. The force constant matrix F directly follows from *ab initio* force field calculations but the eigenvalues of the GF matrix usually differ from the experimental measurements by some wavenumbers, typically 1–10 cm^{-1} for multi-electron molecules depending on the electronic structure calculation method. Here we start with the *ab initio* VQZ equilibrium geometry and held fixed the G matrix elements in what follows. The force constants computed at the *ab initio* CCSD(T)/VQZ level will be denoted by F_0 and the corresponding vibrational frequencies by Λ_0. Assuming that symmetry coordinates are used, the number of independent force constants for each symmetry block is $n_\mathrm{s}(n_\mathrm{s}+1)/2$, where n_s is the number of vibrational modes of symmetry type s such that $\sum_\mathrm{s} n_\mathrm{s} = 3N - 6$. In this section, we briefly describe a simple method for an empirical optimization of an *ab initio* force field. This method is quite general and could be easily applied for other molecules for a fast "fine tuning" of the equilibrium geometries and quadratic force constants.

Let Λ be of a set a "refined" harmonic frequencies. We intend to solve the inverse harmonic eigenvalue problem written as

$$GFL = L\Lambda \quad (3)$$

to extract an optimized F matrix. At this stage, the difficulty when solving eqn (3) is twofold. First, this equation is valid only in the harmonic approximation whereas the true vibrational frequencies are always anharmonic; that is the harmonic frequencies Λ are not observed quantities. Second, this is a typical ill-defined problem since we have to find $n_\mathrm{s}(n_\mathrm{s}+1)/2$ unknown values from n_s data. One way to circumvent the first problem is to assume that the major part of the deviation Δ between the anharmonic variationally computed band centers and the experimental values originates from the error in the harmonic frequencies, that is $\Lambda \approx \Lambda_0 + \Delta$. To regularize the ill-defined problem (second issue), we apply supplementary constraints. A simple transformation of eqn (3) permits obtaining an explicit expression for the F matrix following ref. 82

$$F = G^{-1/2} C \Lambda C^{-1} G^{-1/2} \quad (4)$$

where $C = G^{-1/2}L$ is an arbitrary orthogonal matrix chosen to be eigenvectors of the $(G^{-1/2}FG^{-1/2})$ matrix. For each symmetry block, C is related to the representations of the rotation group $SO(n_\mathrm{s})$ that can be parametrized by means of $n_\mathrm{s}(n_\mathrm{s}-1)/2$ parameters (generators) $\{\varphi_{ij}\}$ describing successive rotations in space. To avoid obtaining non-physical solutions of eqn (4), we consider F_0 as a first guess and constrain the force constants in the F matrix to have a minimal deviation from F_0. Mathematically speaking, the physical solutions are obtained as the minimum of the functional $\|F - F_0\|$, where $\|\cdot\|$ is the Euclidean norm.

For the optimization of the geometry (r_e), we have proceeded as follows. We first compute the ground vibrational state $J = 1$ rotational levels using the *ab initio* geometry r_e^{ab} and the force constants F_0. The variational method is fully converged and numerically exact in this case. Then we compare this to the "observed" value ($E_{J=1}$ = 0.382386 cm^{-1}) computed from the STDS empirical parameters.[83] Assuming that the obs.–calc. error mainly originates from the rotational constant $B_\mathrm{e} = 6.321611/m_Y r_\mathrm{e}^2$, we can deduce an improved r_e as an initial guess. By proceeding iteratively, we obtain simultaneously an optimal set of $\{r_\mathrm{e}^{\mathrm{opt}}, F_{ij}\}$ values.

As a simple illustration, let us consider the case of the two F_2-type normal modes of CF_4. We can parametrize the 2×2 rotation matrix $C \in SO(2)$ by means of one angle φ. After optimizing r_e and solving the equation $\partial\|F - F_0\|/\partial\varphi = 0$, we finally obtained

$$F_0^{(F_2)} = \begin{pmatrix} 0.3168 & 0.1675 \\ & 0.2374 \end{pmatrix} \rightarrow F^{(F_2)} = \begin{pmatrix} 0.3157 & 0.1684 \\ & 0.2355 \end{pmatrix}$$

$$\Lambda_0^{(F_2)} = (638.75, 1311.22) \rightarrow \Lambda^{(F_2)} = (637.18, 1305.36)$$

$$r_\mathrm{e}^{ab} = 1.317228 \rightarrow r_\mathrm{e}^{\mathrm{opt}} = 1.315349$$

where all force constants are given in a.u., the Λ's in cm^{-1} and r_e in Angstroms. We give in Tables 1 and 2 the optimized geometry r_e and the harmonic oscillator frequencies $\{\omega_i\} \equiv \Lambda$ for each irreducible representation Γ.

Our optimized r_e^{opt} value can be compared to those obtained from different studies (see Table 1). In comparison with the STDS database, we have estimated errors in the rotation energies of the vibration ground state errors as $\sim 10^{-5}$ cm^{-1} at J = 1, $\sim 10^{-4}$ cm^{-1} at J = 20 and $\sim 10^{-2}$ cm^{-1} at J = 50. From the different r_e values, we have computed the corresponding B_e values and estimated rotational errors with respect to this work (TW), taken as reference values. We obtained Δ(TW–ref. 64) = 0.01 cm^{-1}, Δ(TW–ref. 60) = −0.07 cm^{-1}, Δ(TW–ref. 62) = 0.06 cm^{-1} for J = 20, 0.06, −0.4 and 0.36 cm^{-1} for J = 50 and 0.13, −0.8 and finally 0.7 cm^{-1} for J = 70. We clearly see, according to Table 1, that our levels would be much closer to those obtained from the pure or refined *ab initio* studies[64] while the two r_e's deduced from high resolution analyses are respectively over- and underestimated and give larger discrepancies.

4 Theoretical background of quantum nuclear motion calculations

4.1 Hamiltonian model

If all vibrations are of a small amplitude and confined around a single well-defined minimum, the normal mode representation of the Hamiltonian turns out to be efficient. It generally provides an adequate description of the nuclear motions for all semirigid molecules, at least up to half way to the dissociation. The commonly used vibration–rotation Hamiltonian for a nonlinear polyatomic molecule in normal coordinates was formulated in the Eckart molecular frame in its most compact form given by Watson,[84] following previous studies of Wilson and Howard and Darling and Dennison. It will be simply referred to as the Eckart–Watson Hamiltonian (EWH). For a molecule with N atoms, the EWH is written in terms of dimensionless symmetry-adapted normal coordinates as

$$H^{EWH} = \frac{1}{2}\sum_{k\sigma}\omega_k p_{k\sigma}^{2(\Gamma)} + \frac{1}{2}\sum_{\alpha\beta}(J_\alpha - \pi_\alpha)\mu_{\alpha\beta}(J_\beta - \pi_\beta) + U(q) + U_W, \quad (5)$$

where $\alpha = x, y, z$ are the Cartesian components in the Eckart frame. For a XY_4 type molecule, k = 1,...,4 labels the four normal modes and σ is the component of a degenerate vibration of symmetry Γ (A_1, E, F_2) in the T_d point group so that $\dim(p_{k\sigma}) = \dim(q_{k\sigma}) = 3N - 6 = 9$. Here J_α and π_α are dimensionless molecular frame components of the total and vibrational angular momentum, respectively. $V(\mathbf{q})$ is the potential function converted to normal coordinates $\mathbf{q}$ from the internal PES (1) of Section 3.1 and $U_W(\mathbf{q}) = -\left(\sum_\alpha \mu_{\alpha\alpha}(\mathbf{q})\right)\Big/ 8$ is the Watson correction term.[84] The reciprocal inertia tensor $\mu \equiv \mu(\mathbf{q})$ is a 3 × 3 matrix related to the $\Omega^i_{\alpha\beta}$ coefficients (see eqn (23) of ref. 85 for the definition) as[86] $\mu(\mathbf{q}) = \sum_i \tilde{\Omega}^i \mathbf{m}_i^{-1} \Omega^i$. For a spherical top molecule like $^{12}CF_4$ that possesses three equal principal equilibrium moments of inertia, it reads

$$\mu = I_0^{-1}\left(I_3 + I_0^{-1}\sum_{i\sigma} A_{i\sigma} q_{i\sigma}\right)^{-2}$$
$$I_0 = 2\sum_i m_i a_\alpha^i a_\alpha^i, \quad \alpha = x, y, z, i = 1, \ldots, N = 5. \quad (6)$$

where the a_α^i's are the Cartesian coordinates at the equilibrium configuration and $A_{i\sigma}$ is given in ref. 86. The equilibrium rotational constant B_e for $^{12}CF_4$ is given by B_e ($\equiv \mu^e_{\alpha\alpha}/2$) = 6.321611/$m_Y r_e^2$ = 0.1923219 cm^{-1}.

We now define a so-called reduced Hamiltonian expressed in terms of creation ($a^{+(\Gamma)}_{k\sigma}$) and annihilation ($a^{(\Gamma)}_{k\sigma}$) operators which are more convenient to handle the algebraic expressions involved following the method described in ref. 77 and 78. As has been shown in previous studies, this permits a drastic reduction of the number of terms in the Hamiltonian by two or three orders of magnitude, with a minimal loss of accuracy and to get rid of some artefacts inherent to high-order Taylor expansions. Following the procedure described elsewhere (see ref. 77, 85, 87 and 88 for more details), the p-order polynomial expansion of EWH in normal coordinates was reduced to a polynomial expansion of a lower order p', such that $p' < p$ (see Appendix B for a discussion). The reduced ($p \rightarrow p'$) EWH can be written in a normal ordering form as follows:[77]

$$H^{EWH}_{red} = \sum_{\text{all indices}} h^{n_\alpha, n_\beta}_{\mathbf{m},\mathbf{n}} \left(\prod_{k\sigma}\left(a^{+(\Gamma)}_{k\sigma}\right)^{m_{k\sigma}}\left(a^{(\Gamma)}_{k\sigma}\right)^{n_{k\sigma}}\right)(J_\alpha)^{n_\alpha}(J_\beta)^{n_\beta}, \quad (7)$$

where $n_\alpha + n_\beta \leq 2$ and $\{\mathbf{m},\mathbf{n}\} = \{m_1, n_1; m_{2a}, n_{2a}, \ldots\}$ is a set of 9 × 2 vibrational indices. This sum-of-product Hamiltonian is thus a non-linear function of rotation–vibration operators. By defining $\{T_i\}$ the space of operators spanned by the T_i's where each operator T_i is associated with a specific non-linear function $(\prod a^{+m} a^n) J_\alpha J_\beta$ *e.g.* $a_1^+ \equiv T_1$, $a_2 \equiv T_2, \ldots$, $a^+_{3a} a_{4x}{}^3 J_x \equiv T_j$ and so on, and $\{h_i\}$ the set of parameters, the reduced Hamiltonian (7) can be cast into the compact vector–vector product

$$H^{EWH}_{red} = (h_1 h_2 \cdots)\begin{pmatrix} T_1 \\ T_2 \\ \vdots \end{pmatrix} = \tilde{\mathbf{h}}\mathbf{T}, \quad (8)$$

where $\tilde{X}$ is the transpose of X. As is well-known, it is highly advantageous to exploit molecular symmetry to reduce the cost of computation of the nuclear motion problem because linear combinations among some h_i parameters associated with the different components of a two or three dimensional vibrational mode are automatically accounted for in a more compact form. To obtain a "factorized" form of the Hamiltonian with linearly independent parameters, the tensor formalism proposed by Nikitin *et al.*[89] turns out to be very appropriate. It was initially designed for spherical top effective models and was recently extended to nuclear *ab initio* Hamiltonians

in ref. 77 and 79. In this representation, the reduced ($p \rightarrow p'$) EWH can be written as

$$H_{\text{tens}}^{\text{EWH}}(p \rightarrow p') = \sum_{\text{all indices}} t_{(\mathbf{lmn})}^{\Omega(K,\Gamma)} \left({}^{\varepsilon}V^{(\Gamma)} \otimes R^{\Omega(K,\Gamma)} \right)^{(A_1)}, \quad (9)$$

where V and R stand for the vibrational (defined in terms of the creation/annihilation operators) and rotational (defined in terms of J_x, J_y and J_z) tensors, respectively. At this stage the main point is to relate the non-empirical tensor parameters t to the *ab initio* parameters h in (7). This can be done in a straightforward manner by re-writing (9) as

$$H_{\text{tens}}^{\text{EWH}} = \tilde{\mathbf{t}}\mathbf{U}\mathbf{T}, \quad (10)$$

where $\mathbf{U}$ is a $\dim(t) \times \dim(h)$ group symmetry transformation matrix built by expanding (9) from T_d coupling (Clebsch–Gordan) coefficients. By sorting the $\mathbf{T}$ vector in (10) in the same way as in eqn (8) and by equating to the Hamiltonians (7) and (9) expanded at the same order, the set $\mathbf{t}$ is obtained by solving the over-determined system of equations

$$\tilde{\mathbf{U}}\mathbf{t} = \mathbf{h}, \quad (11)$$

using *e.g.* parallelized MKL libraries. Note that some values of $\dim(h)$ and $\dim(t)$ up to order 10 are given respectively in the second and third column of Table 3 of ref. 77.

Note that though the EWH – based on a locally-defined Taylor expansion – was initially designed for studying vibrational states "not far from" the bottom of the potential well, the combination of the Eckart frame/normal mode formalism with the reduced PES minimizing artefacts of the Taylor series proved to be very efficient to accurately characterize cold/hot methane[28,32,34,90] and ethylene[28] spectra, even for high wavenumber ranges.

4.2 Symmetry-adapted primitive basis functions

For an N atomic nonlinear molecule, the simplest way to build a multi-dimensional vibrational basis consists in forming a direct product of $3N - 6$ primitive 1D functions as

$$|v_1 v_2 \ldots v_{3N-6}\rangle \equiv \phi_{v_1}(q_1)\phi_{v_2}(q_2)\ldots\phi_{v_{3N-6}}(q_{3N-6}). \quad (12)$$

Without symmetry considerations, if we assume for example that 10 functions (even more are often necessary) are taken for each degree of freedom to converge properly the energy levels, then the matrix to be diagonalized will be of the size $D_0 \times D_0 = 10^{3N-6} \times 10^{3N-6}$. When adding the rotational part, the size of Hamiltonian matrix will be scaled by an additional factor $2J + 1$. It is thus clearly seen that computing and/or storing eigensolutions from direct or even iterative eigensolvers becomes an extremely computationally demanding problem for molecules with more than four atoms.

If now we exploit the T_d symmetry where two and three dimensional degenerate irreducible representations (irreps) are involved, our primitive vibrational basis will be built as a tensor product of non-degenerate, two- and three-fold degenerate harmonic oscillator functions

$$\phi_{v,\sigma_v}^{(C_v)} = \left(\phi_{v_1}^{(l_1,A_1)} \otimes \phi_{v_2}^{(l_2 m_2,C_2)} \otimes \phi_{v_3}^{(l_3 m_3 n_3,C_3)} \otimes \phi_{v_4}^{(l_4 m_4 n_4,C_4)} \right)_{\sigma_v}^{(C_v)}, \quad (13)$$

where the indices l_i, m_i, n_i and their permutations completely characterize the symmetrized powers of the creation operators with $v_i = l_i + m_i + n_i$ for each mode. Using the symmetry-adapted basis functions (13) (SABF) allows (i) to block-diagonalize the Hamiltonian matrix and (ii) to classify and label the eigenstates of the Hamiltonian according to the different irreps of the symmetry group.

For $J > 0$ calculations, the direct way is to construct the Hamiltonian matrix in a primitive basis obtained as the coupling between vibrational and rotational functions

$$\Phi_{v,M,\sigma}^{(J,C)} \equiv |(v_1 v_2 v_3 v_4) C_v, JnC_r; C\sigma, M\rangle = \left(\Phi_v^{(C_v)} \otimes \Phi_M^{(J,nC_r)} \right)_{\sigma}^{(C)} \quad (14)$$

SABF are generally built as a linear combination of the primitive functions (12). Different methods can be used to construct explicitly such basis functions. For instance, Yurchenko *et al.*[91] proposed a numerical method implemented in TROVE for the construction of SABF by solving eigenfunctions problems for a set of reduced (not in the sense defined in Section 4.1) Hamiltonian operators. For this work, the symmetrization coefficients are computed algebraically from irreducible tensor operators. Toward this end, each vibrational SABF is obtained by applying successive creation tensor operators on the vacuum state while the rotational SABF (also called non standard basis) defined in $O(3) \supset T_d$ are obtained by applying a similarity transformation[92] G on the standard basis $|J,K,M\rangle$; K and M being respectively the projection onto the molecular- and lab-fixed axis. The symmetry-adapted basis set is built as follows:

$$\begin{aligned} \Phi_{v\sigma_v}^{(C_v)} &\equiv |(v_1 v_2 v_3 v_4) C_v \sigma_v\rangle = \left(\mathscr{A}^{+(l_1,A_1)} \otimes \cdots \otimes \mathscr{A}^{+(l_4 m_4 n_4,C_4)} \right)_{\sigma_v}^{(C_v)} |0\rangle, \\ \Phi_{M\sigma_r}^{(J,nC_r)} &\equiv |J,nC_r\sigma_r,M\rangle = \sum_K {}^{(J)}G_{nC\alpha}^K |J,K,M\rangle. \end{aligned} \quad (15)$$

If the molecule is in a field-free environment, then the M quantum number can be omitted in the following. As an illustration, we give below some normalized SABF expressed as a linear combination of non-symmetrized functions

$$|(0012)F_2 x\rangle = \frac{1}{\sqrt{3}}[|000100200\rangle + |000100020\rangle + |000100002\rangle],$$

$$\begin{aligned} |(2100)E,5E;A_1\rangle &= \frac{i}{2}[|210000000\rangle(|5,4\rangle - |5,-4\rangle)] \\ &\quad + \frac{i}{2}[|201000000\rangle(|5,-2\rangle - |5,2\rangle)] \end{aligned}$$

$$\begin{aligned} |(0110)F_1,4A_1;F_1 x\rangle\rangle &= |010100000\rangle \left(\frac{\sqrt{5}}{4\sqrt{2}}|4,-4\rangle \right. \\ &\quad \left. + \frac{\sqrt{7}}{4}|4,0\rangle + \frac{\sqrt{5}}{4\sqrt{2}}|4,4\rangle \right) \\ &\quad + |001100000\rangle \left(\frac{\sqrt{5}}{4\sqrt{6}}|4,-4\rangle \right. \\ &\quad \left. + \frac{\sqrt{7}}{4\sqrt{3}}|4,0\rangle + \frac{\sqrt{5}}{4\sqrt{6}}|4,4\rangle \right) \end{aligned}$$

Table 3 Vibrational band centers (in cm^{-1}) for $^{12}CF_4$ up to 3000 cm^{-1}. Vibrational sublevels are specified and "Eig" corresponds to max($\mathbf{c}^{\Gamma}$) in eqn (A2) that is the maximum contribution in the wavenumber decomposition

Band, sym., eig.	Band center	Band, sym., eig.	Band center	Band, sym., eig.	Band center
ν_2,E(0.99)	435.41	$\nu_2 + \nu_3 + \nu_4$,F_2(0.78)	2345.64	$2\nu_2 + \nu_3 + \nu_4$,F_1(0.87)	2779.48
ν_4,F_2(0.98)	631.09	$\nu_2 + \nu_3 + \nu_4$,F_2(−0.77)	2346.00	$2\nu_2 + \nu_3 + \nu_4$,F_2(0.83)	2779.48
$2\nu_2$,A_1(0.97)	868.01	$\nu_2 + \nu_3 + \nu_4$,F_1(0.89)	2346.12	$2\nu_2 + \nu_3 + \nu_4$,F_1(−0.88)	2779.71
$2\nu_2$,E(0.98)	871.21	$\nu_2 + \nu_3 + \nu_4$,E(−0.89)	2349.41	$2\nu_2 + \nu_3 + \nu_4$,F_2(−0.84)	2779.73
ν_1,A_1(−0.94)	909.03	$4\nu_2 + \nu_4$,F_2(0.89)	2362.15	$2\nu_2 + \nu_3 + \nu_4$,A_1(−0.85)	2780.06
$\nu_2 + \nu_4$,F_2(−0.98)	1066.20	$4\nu_2 + \nu_4$,F_1(0.94)	2365.52	$2\nu_2 + \nu_3 + \nu_4$,E(0.87)	2783.21
$\nu_2 + \nu_4$,F_1(−0.98)	1066.76	$4\nu_2 + \nu_4$,F_2(−0.90)	2365.77	$5\nu_2 + \nu_4$,F_2(0.90)	2792.38
$2\nu_4$,F_2(−0.96)	1260.59	$4\nu_2 + \nu_4$,F_1(−0.97)	2374.93	$5\nu_2 + \nu_4$,F_1(0.92)	2794.00
$2\nu_4$,A_1(−0.98)	1261.86	$4\nu_2 + \nu_4$,F_2(−0.97)	2374.94	$\nu_1 + 3\nu_4$,A_1(0.84)	2795.69
$2\nu_4$,E(−0.98)	1262.19	$\nu_1 + 2\nu_2 + \nu_4$,F_2(−0.87)	2407.29	$\nu_1 + 3\nu_4$,F_2(0.83)	2796.41
ν_3,F_2(−0.94)	1283.77	$\nu_1 + 2\nu_2 + \nu_4$,F_1(−0.91)	2410.78	$\nu_1 + 3\nu_4$,F_1(0.84)	2796.65
$3\nu_2$,E(−0.96)	1301.09	$\nu_1 + 2\nu_2 + \nu_4$,F_2(0.90)	2410.87	$5\nu_2 + \nu_4$,F_2(0.92)	2799.46
$3\nu_2$,A_1(0.98)	1307.37	$2\nu_1 + \nu_4$,F_2(0.86)	2445.46	$5\nu_2 + \nu_4$,F_1(0.95)	2799.58
$3\nu_2$,A_2(0.98)	1307.40	$4\nu_4$,A_1(−0.83)	2516.33	$\nu_1 + 3\nu_4$,F_2(0.90)	2799.88
$\nu_1 + \nu_2$,E(0.93)	1344.56	$4\nu_4$,F_2(−0.86)	2516.40	$5\nu_2 + \nu_4$,F_2(−0.99)	2811.81
$2\nu_2 + \nu_4$,F_2(0.95)	1498.94	$4\nu_4$,E(0.85)	2517.09	$5\nu_2 + \nu_4$,F_1(−0.99)	2811.81
$2\nu_2 + \nu_4$,F_1(−0.98)	1502.25	$4\nu_4$,F_2(−0.87)	2518.34	$\nu_1 + \nu_3 + \nu_4$,E(−0.87)	2812.24
$2\nu_2 + \nu_4$,F_2(−0.96)	1502.34	$4\nu_4$,F_1(−0.88)	2518.85	$\nu_1 + \nu_3 + \nu_4$,F_2(−0.81)	2814.92
$\nu_1 + \nu_4$,F_2(0.93)	1539.46	$4\nu_4$,E(−0.96)	2523.73	$\nu_1 + \nu_3 + \nu_4$,F_1(−0.83)	2815.26
$\nu_2 + 2\nu_4$,F_1(0.95)	1695.62	$4\nu_4$,A_1(−0.96)	2523.75	$\nu_1 + \nu_3 + \nu_4$,A_1(0.81)	2818.68
$\nu_2 + 2\nu_4$,F_2(−0.95)	1696.05	$2\nu_3$,A_1(0.68)	2534.60	$\nu_1 + 3\nu_2 + \nu_4$,F_2(0.84)	2839.64
$\nu_2 + 2\nu_4$,E(−0.78)	1696.81	$\nu_3 + 2\nu_4$,F_2(0.60)	2536.17	$\nu_1 + 3\nu_2 + \nu_4$,F_1(0.85)	2840.80
$\nu_2 + 2\nu_4$,A_1(−0.97)	1696.98	$\nu_3 + 2\nu_4$,F_1(−0.96)	2536.51	$\nu_1 + 3\nu_2 + \nu_4$,F_2(0.89)	2846.89
$\nu_2 + 2\nu_4$,E(0.78)	1697.97	$\nu_3 + 2\nu_4$,E(0.82)	2540.86	$\nu_1 + 3\nu_2 + \nu_4$,F_1(0.90)	2846.93
$\nu_2 + 2\nu_4$,A_2(0.98)	1698.12	$\nu_3 + 2\nu_4$,F_2(0.74)	2541.09	$2\nu_1 + \nu_2 + \nu_4$,F_2(0.84)	2880.83
$\nu_2 + \nu_3$,F_2(−0.93)	1716.78	$\nu_3 + 2\nu_4$,F_1(0.86)	2541.43	$2\nu_1 + \nu_2 + \nu_4$,F_1(−0.84)	2881.47
$\nu_2 + \nu_3$,F_1(0.94)	1717.19	$\nu_3 + 2\nu_4$,F_2(0.57)	2544.07	$\nu_2 + 4\nu_4$,E(−0.77)	2950.82
$4\nu_2$,A_1(0.93)	1731.52	$\nu_3 + 2\nu_4$,A_1(0.66)	2547.91	$\nu_2 + 4\nu_4$,F_2(0.84)	2950.98
$4\nu_2$,E(0.95)	1734.62	$3\nu_2 + 2\nu_4$,F_1(0.91)	2560.58	$\nu_2 + 4\nu_4$,F_1(0.83)	2951.37
$4\nu_2$,E(−0.98)	1743.93	$3\nu_2 + 2\nu_4$,F_2(0.90)	2561.34	$\nu_2 + 4\nu_4$,A_2(0.84)	2951.52
$\nu_1 + 2\nu_2$,A_1(0.89)	1777.04	$3\nu_2 + 2\nu_4$,E(−0.69)	2561.61	$\nu_2 + 4\nu_4$,E(0.80)	2951.86
$\nu_1 + 2\nu_2$,E(−0.92)	1780.40	$3\nu_2 + 2\nu_4$,A_1(0.92)	2561.73	$\nu_2 + 4\nu_4$,A_1(−0.82)	2952.13
$2\nu_1$,A_1(0.88)	1815.74	$2\nu_3$,F_2(0.87)	2562.17	$\nu_2 + 4\nu_4$,F_1(0.79)	2952.67
$3\nu_4$,A_1(−0.92)	1888.80	$3\nu_2 + 2\nu_4$,E(0.71)	2563.79	$\nu_2 + 4\nu_4$,F_2(0.66)	2952.90
$3\nu_4$,F_2(0.92)	1889.63	$3\nu_2 + 2\nu_4$,A_2(0.94)	2563.96	$\nu_2 + 4\nu_4$,F_2(−0.66)	2953.91
$3\nu_4$,F_1(−0.92)	1889.89	$3\nu_2 + 2\nu_4$,F_2(0.92)	2567.32	$\nu_2 + 4\nu_4$,F_1(0.80)	2954.21
$3\nu_4$,F_2(0.97)	1892.98	$3\nu_2 + 2\nu_4$,F_1(0.93)	2567.35	$\nu_2 + 4\nu_4$,A_1(0.94)	2957.84
$\nu_3 + \nu_4$,E(−0.96)	1909.63	$3\nu_2 + 2\nu_4$,A_1(0.96)	2569.17	$\nu_2 + 4\nu_4$,E(0.66)	2957.85
$\nu_3 + \nu_4$,F_2(−0.90)	1912.32	$3\nu_2 + 2\nu_4$,A_2(0.95)	2569.25	$\nu_2 + 4\nu_4$,A_2(−0.97)	2960.14
$\nu_3 + \nu_4$,F_1(0.91)	1912.59	$3\nu_2 + 2\nu_4$,E(0.95)	2569.48	$\nu_2 + 4\nu_4$,E(0.68)	2960.15
$\nu_3 + \nu_4$,A_1(−0.90)	1916.00	$3\nu_2 + 2\nu_4$,E(−0.95)	2569.55	$\nu_2 + 2\nu_3$,E(0.72)	2966.82
$3\nu_2 + \nu_4$,F_2(0.94)	1931.48	$2\nu_3$,E(−0.93)	2570.22	$\nu_2 + \nu_3 + 2\nu_4$,F_2(0.60)	2968.64
$3\nu_2 + \nu_4$,F_1(−0.96)	1932.58	$3\nu_2 + \nu_3$,F_2(−0.88)	2577.97	$\nu_2 + \nu_3 + 2\nu_4$,F_1(0.75)	2969.32
$3\nu_2 + \nu_4$,F_2(0.97)	1938.41	$3\nu_2 + \nu_3$,F_1(−0.90)	2578.61	$\nu_2 + \nu_3 + 2\nu_4$,F_2(−0.93)	2969.61
$3\nu_2 + \nu_4$,F_1(0.98)	1938.45	$3\nu_2 + \nu_3$,F_2(0.91)	2584.64	$\nu_2 + \nu_3 + 2\nu_4$,F_1(0.59)	2969.95
$\nu_1 + \nu_2 + \nu_4$,F_2(−0.92)	1974.67	$3\nu_2 + \nu_3$,F_1(0.92)	2584.67	$\nu_2 + \nu_3 + 2\nu_4$,A_2(0.81)	2974.09
$\nu_1 + \nu_2 + \nu_4$,F_1(0.92)	1975.27	$6\nu_2$,A_1(0.89)	2590.86	$\nu_2 + \nu_3 + 2\nu_4$,F_1(−0.65)	2974.10
$2\nu_2 + 2\nu_4$,F_2(−0.92)	2128.14	$6\nu_2$,E(0.90)	2593.90	$\nu_2 + \nu_3 + 2\nu_4$,F_2(−0.63)	2974.20
$2\nu_2 + 2\nu_4$,A_1(0.92)	2129.41	$6\nu_2$,E(−0.93)	2603.00	$\nu_2 + \nu_3 + 2\nu_4$,E(−0.80)	2974.29
$2\nu_2 + 2\nu_4$,E(0.91)	2129.67	$\nu_1 + \nu_2 + 2\nu_4$,F_1(−0.87)	2603.31	$\nu_2 + \nu_3 + 2\nu_4$,A_1(0.79)	2974.58
$2\nu_2 + 2\nu_4$,F_1(−0.94)	2131.42	$\nu_1 + \nu_2 + 2\nu_4$,F_2(−0.87)	2603.74	$\nu_2 + \nu_3 + 2\nu_4$,F_2(−0.56)	2975.21
$2\nu_2 + 2\nu_4$,F_2(−0.93)	2131.46	$\nu_1 + \nu_2 + 2\nu_4$,E(−0.70)	2604.56	$\nu_2 + \nu_3 + 2\nu_4$,F_1(0.76)	2975.39
$2\nu_2 + 2\nu_4$,E(0.87)	2133.07	$\nu_1 + \nu_2 + 2\nu_4$,A_1(0.90)	2604.70	$\nu_2 + \nu_3 + 2\nu_4$,F_2(−0.56)	2977.03
$2\nu_2 + 2\nu_4$,A_2(−0.97)	2133.29	$\nu_1 + \nu_2 + 2\nu_4$,E(−0.71)	2605.79	$\nu_2 + \nu_3 + 2\nu_4$,F_1(−0.54)	2977.61
$2\nu_2 + 2\nu_4$,E(−0.85)	2133.54	$\nu_1 + \nu_2 + 2\nu_4$,A_2(0.91)	2605.93	$\nu_2 + \nu_3 + 2\nu_4$,E(0.70)	2980.25
$2\nu_2 + 2\nu_4$,A_1(−0.93)	2133.59	$6\nu_2$,A_2(0.99)	2618.15	$4\nu_2 + 2\nu_4$,F_2(0.87)	2990.92
$2\nu_2 + \nu_3$,F_2(0.91)	2147.34	$6\nu_2$,A_1(−0.99)	2618.15	$4\nu_2 + 2\nu_4$,A_1(0.84)	2992.09
$2\nu_2 + \nu_3$,F_1(−0.93)	2150.60	$\nu_1 + \nu_2 + \nu_3$,F_2(0.85)	2620.18	$4\nu_2 + 2\nu_4$,E(−0.82)	2992.29
$2\nu_2 + \nu_3$,F_2(−0.92)	2150.65	$\nu_1 + \nu_2 + \nu_3$,F_1(−0.85)	2620.59	$\nu_2 + 2\nu_3$,F_1(−0.85)	2993.11
$5\nu_2$,E(0.91)	2162.46	$\nu_1 + 4\nu_2$,A_1(0.81)	2640.10	$\nu_2 + 2\nu_3$,F_2(−0.86)	2993.38
$\nu_1 + 2\nu_4$,F_2(0.89)	2168.21	$\nu_1 + 4\nu_2$,E(0.83)	2643.33	$4\nu_2 + 2\nu_4$,F_1(−0.89)	2994.16
$5\nu_2$,A_1(−0.92)	2168.54	$\nu_1 + 4\nu_2$,E(0.91)	2653.00	$4\nu_2 + 2\nu_4$,F_2(−0.88)	2994.24
$5\nu_2$,A_2(0.95)	2168.65	$2\nu_1 + 2\nu_2$,A_1(0.80)	2683.82	$4\nu_2 + 2\nu_4$,E(−0.75)	2996.13
$\nu_1 + 2\nu_4$,A_1(−0.91)	2169.55	$2\nu_1 + 2\nu_2$,E(0.85)	2687.37	$4\nu_2 + 2\nu_4$,A_2(0.95)	2996.30
$\nu_1 + 2\nu_4$,E(0.92)	2169.84	$3\nu_1$,A_1(−0.80)	2720.18	$4\nu_2 + 2\nu_4$,E(−0.69)	2997.09
$5\nu_2$,E(−0.97)	2180.86	$2\nu_2 + 3\nu_4$,A_1(−0.88)	2755.97	$4\nu_2 + 2\nu_4$,A_1(0.85)	2997.10
$\nu_1 + \nu_3$,F_2(0.87)	2186.97	$2\nu_2 + 3\nu_4$,F_2(−0.86)	2756.65	$\nu_2 + 2\nu_3$,A_1(0.92)	3000.49
$\nu_1 + 3\nu_2$,E(0.86)	2209.97	$2\nu_2 + 3\nu_4$,F_1(0.85)	2756.88	$\nu_2 + 2\nu_3$,E(0.92)	3001.16
$\nu_1 + 3\nu_2$,A_1(0.91)	2216.52	$2\nu_2 + 3\nu_4$,E(0.89)	2759.20	$\nu_2 + 2\nu_3$,A_2(−0.93)	3001.69

Table 3 (*continued*)

Band, sym., eig.	Band center	Band, sym., eig.	Band center	Band, sym., eig.	Band center
$\nu_1 + 3\nu_2,A_2(0.92)$	2216.56	$2\nu_2 + 3\nu_4,F_2(-0.69)$	2759.91	$4\nu_2 + 2\nu_4,F_2(0.92)$	3003.53
$2\nu_1 + \nu_2,E(-0.86)$	2251.46	$2\nu_2 + 3\nu_4,F_2(0.71)$	2760.10	$4\nu_2 + 2\nu_4,F_1(-0.92)$	3003.54
$\nu_2 + 3\nu_4,E(0.91)$	2323.84	$2\nu_2 + 3\nu_4,F_1(0.85)$	2760.18	$4\nu_2 + 2\nu_4,E(0.97)$	3005.65
$\nu_2 + 3\nu_4,F_1(-0.77)$	2324.39	$2\nu_2 + 3\nu_4,F_1(-0.87)$	2760.30	$4\nu_2 + 2\nu_4,A_2(0.97)$	3005.95
$\nu_2 + 3\nu_4,F_2(-0.69)$	2324.43	$2\nu_2 + 3\nu_4,F_2(0.84)$	2760.43	$4\nu_2 + 2\nu_4,E(0.97)$	3005.96
$\nu_2 + 3\nu_4,F_2(0.69)$	2325.18	$2\nu_2 + 3\nu_4,F_1(-0.96)$	2763.99	$4\nu_2 + 2\nu_4,A_1(0.98)$	3005.97
$\nu_2 + 3\nu_4,F_1(0.78)$	2325.22	$2\nu_2 + 3\nu_4,F_2(-0.88)$	2764.68	$4\nu_2 + \nu_3,F_2(0.85)$	3006.53
$\nu_2 + 3\nu_4,F_2(-0.95)$	2327.45	$2\nu_2 + \nu_3 + \nu_4,E(0.92)$	2772.75	$4\nu_2 + \nu_3,F_1(0.87)$	3009.72
$\nu_2 + 3\nu_4,F_1(-0.97)$	2329.15	$2\nu_2 + \nu_3 + \nu_4,A_1(0.93)$	2775.93	$4\nu_2 + \nu_3,F_2(-0.86)$	3009.80
$\nu_2 + \nu_3 + \nu_4,A_1(-0.96)$	2342.20	$2\nu_2 + \nu_3 + \nu_4,A_2(0.96)$	2776.09	$4\nu_2 + \nu_3,F_1(-0.90)$	3019.11
$\nu_2 + \nu_3 + \nu_4,E(-0.96)$	2342.65	$2\nu_2 + \nu_3 + \nu_4,F_2(0.85)$	2776.09	$4\nu_2 + \nu_3,F_2(0.90)$	3019.11
$\nu_2 + \nu_3 + \nu_4,A_2(-0.96)$	2343.31	$2\nu_2 + \nu_3 + \nu_4,F_1(0.86)$	2776.35		
$\nu_2 + \nu_3 + \nu_4,F_1(0.88)$	2345.41	$2\nu_2 + \nu_3 + \nu_4,E(0.94)$	2776.43		

A comparison of the symmetrized Cartesian and angular momentum basis sets in spherical tops is given in ref. 93.

4.3 Basis set compression

A full account of all symmetry properties is a necessary but unfortunately not a sufficient condition to drastically reduce the size of the basis and to make the rovibrational calculations more tractable as V, J and/or N increase. Typically, block-diagonalization of the Hamiltonian matrix for XY_4 reduces the size of the problem by one order of magnitude while it should be reduced ideally by five orders of magnitude to facilitate calculations. Many methods have been developed these past few years for reducing the size of the basis set and computing eigensolutions of a (ro)-vibrational problem.[91,94–100] Very recently, in a rather pedagogical paper[101] Carrington reviewed the main methods for computing spectra of molecules with more than four atoms using pruned-and-contracted-basis sets and direct/iterative eigensolvers.

In this work, we applied the strategy combining the basis set "pruning" and reduction–compression scheme ref. 77, 78 and 88. This approach, which permits the use of a realistic reduced anharmonic basis set for ro-vibrational calculations, has proven its efficiency for methane calculations for a large ranges of wavenumbers and temperatures. Technical details are given in Appendix A.

To summarize, the number of vibrational functions in a XY_4 molecule can be drastically reduced using the following scheme

$$\begin{array}{ccccccc} \text{Eqn (12)} & \rightarrow & \text{Eqn (13), (A1)} & \rightarrow & \text{Eqn (A3)} \\ D_0 \sim 10^9 & \xrightarrow[\text{Pruning}]{\text{Symmetry}} & D_1 \sim 10^5 & \xrightarrow{\text{Reduction}} & D_2 \sim 10^3, \end{array}$$

where D_i is the size of the Hamiltonian matrix: D_0 is defined below eqn (12), D_1 is defined below eqn (A1) for each symmetry block and D_2 is defined above eqn (A3). Without such a compression of the basis set, full quantum calculation of five atomic systems with high J would not be feasible, even using the latest generation of computers.

170 band centers predicted from the refined PES together with their vibrational assignments, symmetry types and major basis set contributions are given in Table 3.

5 Line list calculation: completeness issues

Full quantum-mechanical calculations of CF_4 spectra are an extremely challenging problem because highly excited basis

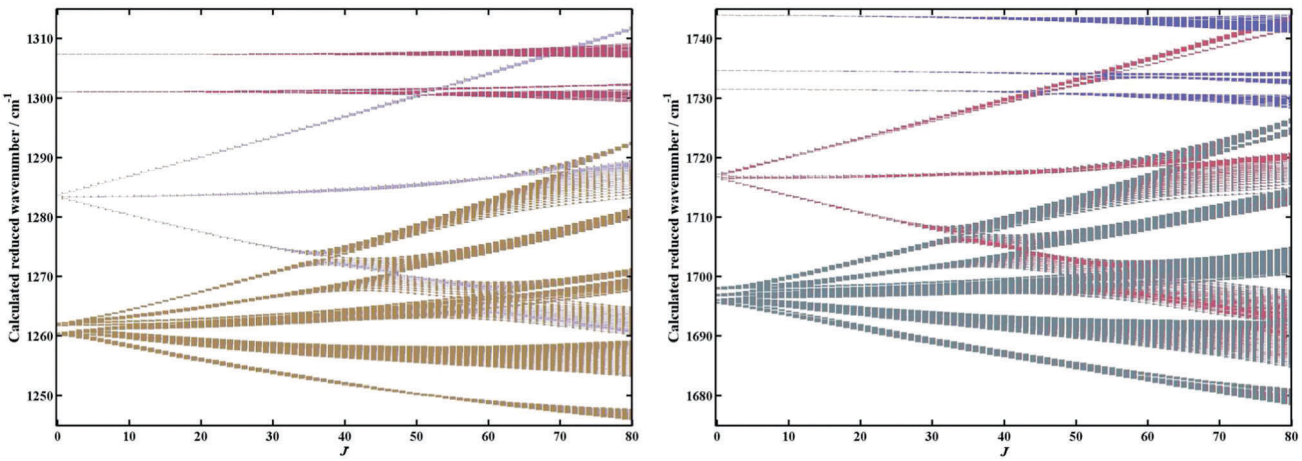

Fig. 2 Reduced energy level $E_{vJ} - E_r^{(0)}$ for CF_4 for the $2\nu_4(F_2,A_1,E)$, $\nu_3(F_2)$, $3\nu_2(E,A_1,A_2)$ (left panel) and $\nu_2 + 2\nu_4(F_1,F_2,E,A_1,E)$, $\nu_2 + \nu_3(F_2)$, $4\nu_2(A_1,2E)$ (right panel). $E_r^{(0)}$ stands for the semirigid rotor energies (see text). For each panel, the subbands are listed by increasing energy order.

states in a wide spectral range have to be involved. This requires efficient computational methods for (1) computing converged line positions – diagonalization of very large matrices being the most demanding part – as well as an efficient procedure for (2) taking into account all necessary line transitions with appropriate intensity cut-offs for converged opacities. All calculations were performed using our home-made computer code 'TENSOR'.

5.1 Vibration–rotation energy levels and partition function

All details for the basis compression are given in Appendix B. To illustrate how dense the CF_4 energy patterns are with complex level inter-mode coupling, we plot in Fig. 2 and 3 some reduced variationally-predicted energy levels as a function of the J rotational quantum number. The term reduced means that we subtract the semirigid rotor energies $E_r^{(0)} = 0.1902J(J+1) - 6.13 \times 10^{-8}J^2(J+1)^2$ from the total energy E_{vJ}. In Fig. 2 the sublevels $2\nu_4(A_1,E,F_2)$, $\nu_3(F_2)$, $3\nu_2(A_1,A_2,E)$ are displayed on the left panel and $\nu_2 + 2\nu_4(A_1,2E,F_1F_2)$, $\nu_2 + \nu_3(F_2)$, $4\nu_2(A_1,A_2,E)$ on the right panel that is "right" = "left" + ν_2. The $\nu_4 = 2$ levels are split to $l_4 = 0$ and $l_4 = 2$ in the $O(3)$ rotation group and the $l_4 = 2$ sublevel further splits into E and F_2 according to the T_d symmetry types. The tetrahedral splitting is thus clearly seen as J increases.

Different colours are also displayed on these 3 figures, they give information on how the energy states are mixed altogether. Each eigenvector is decomposed as $\Psi_j = c_1^j\Phi_1 + c_2^j\Phi_2 + \ldots$ in the primitive basis (14), then different colours will represent a mixing coefficient $(c_i^j)^2$. Information in these figures is twofold. First one clearly sees the numerous overlapping vibration–rotation patterns as E and J increase making an appropriate choice of effective empirical model hazardous for the corresponding complicated band system. This point will be discussed in more detail in Section 7.1. Second, the density of state rapidly increases with J resulting in strongly congested CF_4 spectra even for the region below 3000 cm^{-1}.

Another quantity that can computed from energy levels is the total internal partition function expressed as a direct sum of Boltzmann factors at a given temperature

$$Q_{dir}(T) = \sum(2J+1)g_C \exp(-hcE_{vJ}/kT). \quad (16)$$

where g_C are the nuclear spin statistical weights. For CF_4 they are given by $g_A = 5$, $g_E = 2$ and $g_F = 3$. At $T = 296$ K, we obtain

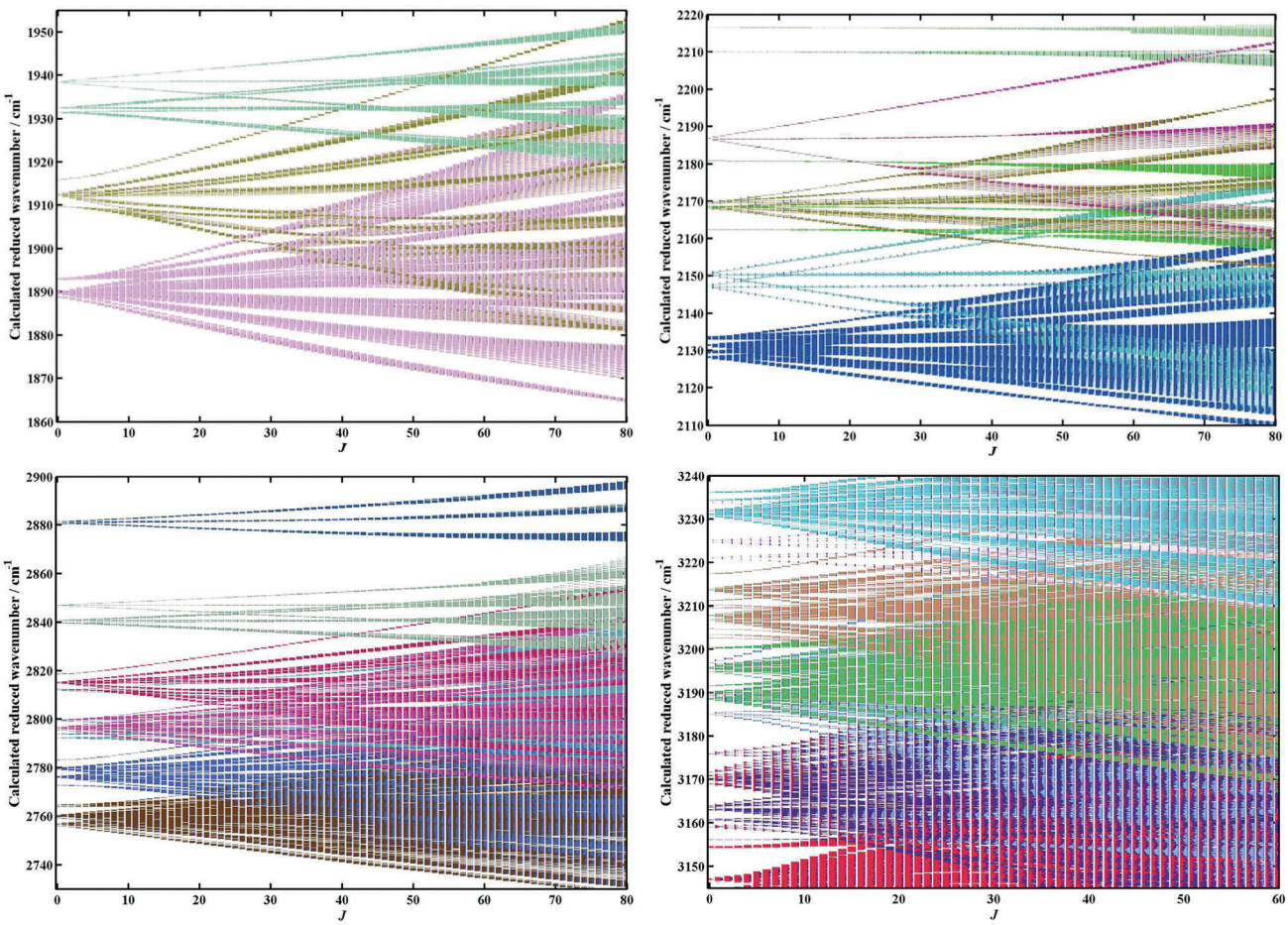

Fig. 3 Reduced energy level $E_{vJ} - E_r^{(0)}$ for CF_4 in the region of the $3\nu_4$, $\nu_3 + \nu_4$, $3\nu_2 + \nu_4$ (top, left-hand side), $2\nu_2 + 2\nu_4$, $2\nu_2 + \nu_3$, $5\nu_2$, $\nu_1 + 2\nu_4$, $\nu_1 + \nu_3$, $\nu_1 + 3\nu_2$ (top, right-hand side), $2\nu_2 + 3\nu_4$, $2\nu_2 + \nu_3 + \nu_4$, $5\nu_2 + \nu_4$, $\nu_1 + 3\nu_4$, $\nu_1 + \nu_3 + \nu_4$, $\nu_1 + 3\nu_2 + \nu_4$, $2\nu_1 + \nu_2 + \nu_4$ (bottom, left-hand side) and $5\nu_4$, $3\nu_4 + \nu_2$, $2\nu_3 + \nu_4$, $\nu_3 + 3\nu_4$, $3\nu_2 + 3\nu_4$, *etc.* (bottom, right-hand side). For each panel, the bands are listed by increasing energy order (see Table 3 for details about the vibrational sublevels).

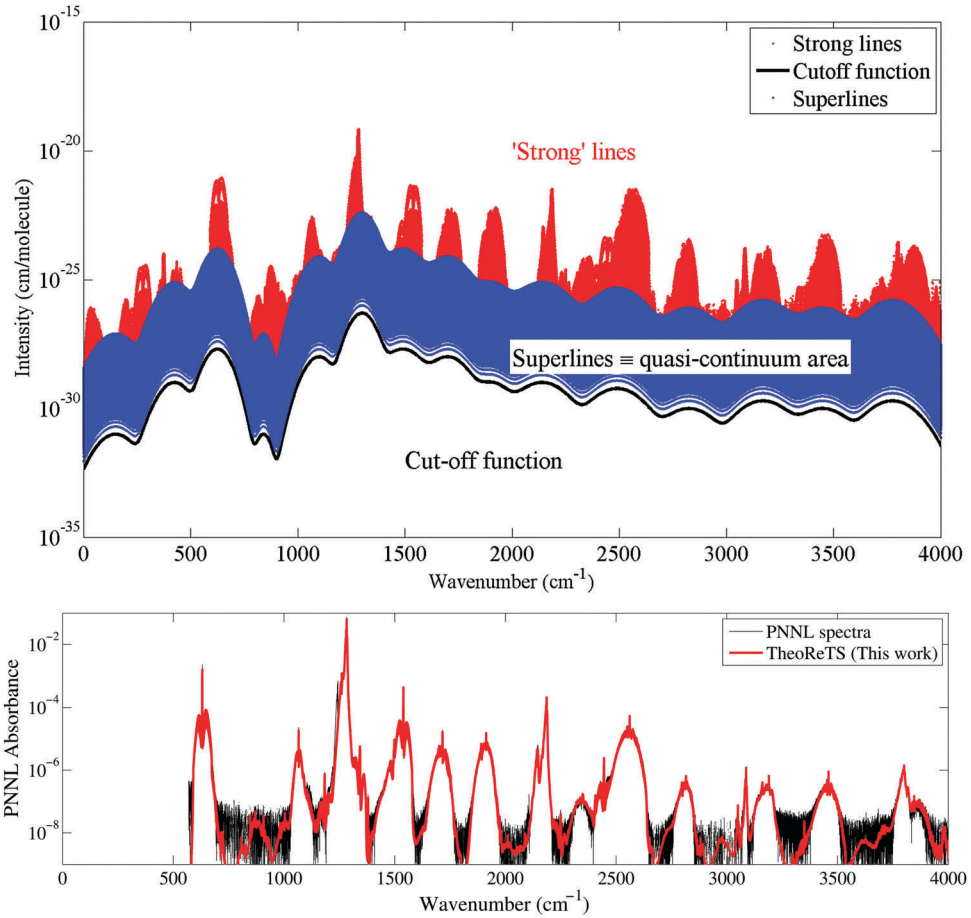

Fig. 4 Top panel: Strong line intensities (in red) and schematic representation of the quasi-continuum area (QC, in blue, treated using super-lines) of tetrafluoromethane at 296 K. A plot of the cut-off function (see Section 5.2) is also given (black line). Bottom panel: Plot of the PNNL absorbance and comparison with TheoReTS (this work).

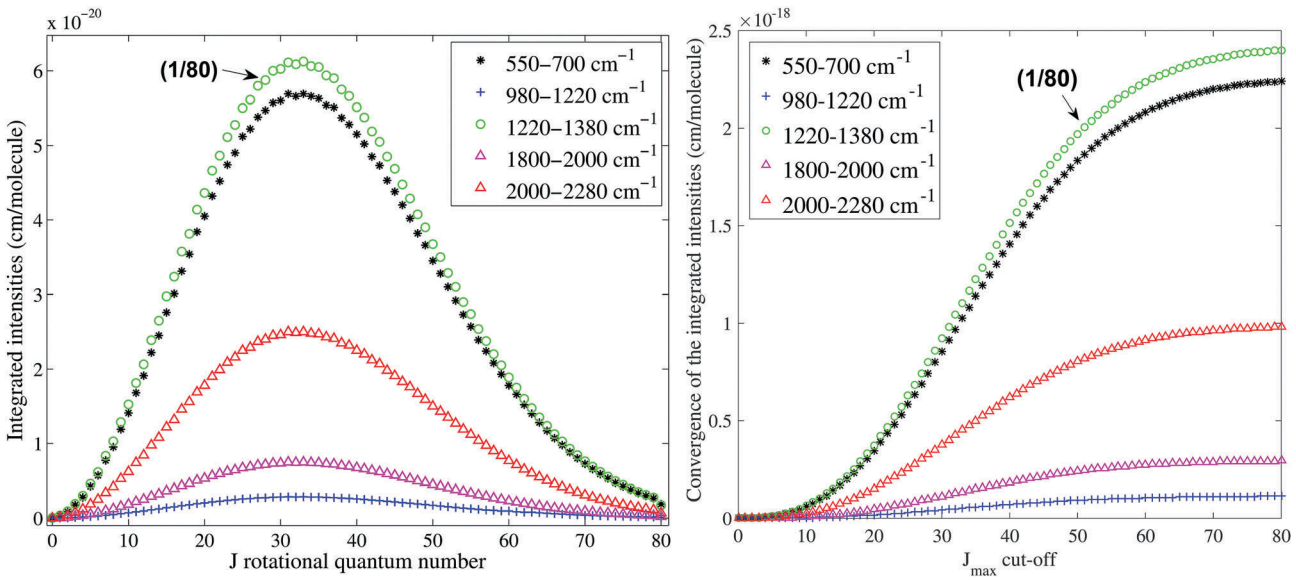

Fig. 5 Integrated intensities (in cm per molecules) for different spectral ranges (see Fig. 4) at different values of the rotational angular momentum J (left panel). Convergence of the integrated intensities (in cm per molecules) with respect to a given J_{max} value is also shown (right panel, see Discussion in Appendix B).

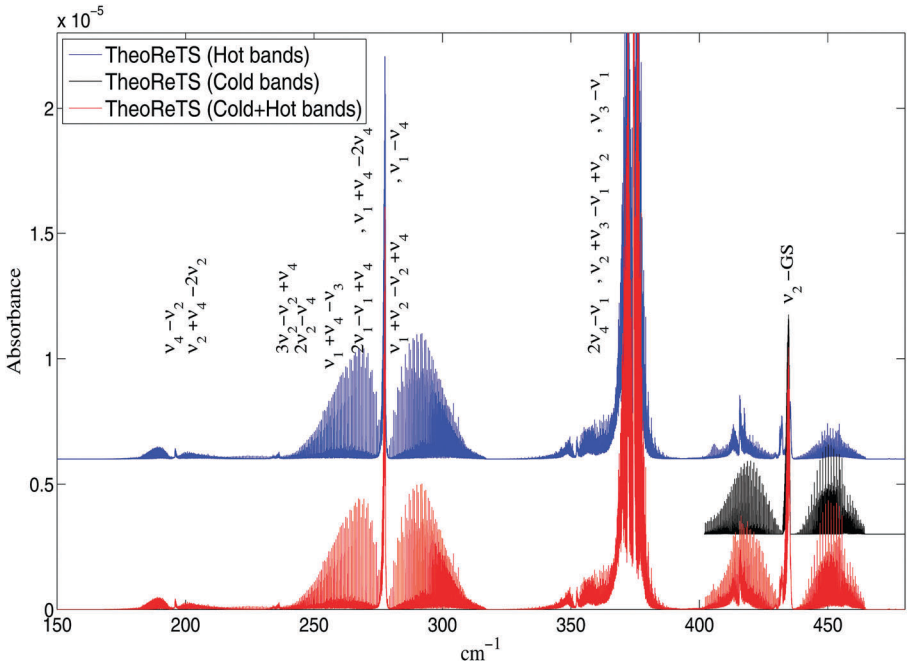

Fig. 6 Theoretical absorbance computed at 296 K with contributions of the cold and hot band transitions. The main CBs and HBs are indicated in vertical text.

Q_{dir} = 126 600. Note that at 180 K, the convergence of the partition function is better than 1% at J_{max} = 60 and better than 0.1% at J_{max} = 71. At 250 K the convergence is better than 1% at J_{max} = 70 and better than 0.1% at J_{max} = 78 while at 296 K the convergence is better than 1% at J_{max} = 74 and better than 0.1% at J_{max} = 80. For higher temperatures, the partition function is not totally converged at J_{max} = 80. Note that in the direct-product approximation $Q_{prod}(T) \approx Q_{vib}Q_{rot}$ as usually used in effective models, the value given in HITRAN[2] is $Q_{prod}(296)$ = 121 270. The discrepancy between Q_{prod} and Q_{dir} is 4.2% at room temperature which is not negligible but this difference may be absorbed by the empirically-determined dipole moment parameters during the fit. Concerning the energy cut-off, the maximum E_{max} value used to compute the partition function is 6700 cm^{-1}. The partition function is totally converged using this cut-off. Even if E_{max} = 5500 cm^{-1}, the convergence error of the partition function is less than 0.001%. Values of the partition function are provided in TheoReTS from 100 to 300 K.

5.2 Completeness criteria for intensities and quasi-continuum absorption

With the cut-offs E_{low}^{max} and $I^{cut}(W)$ defined in Appendix B, the final room-temperature list is composed of more than 2 billion transitions. Such a huge number of lines is hardly manageable for practical applications using standard radiative transfer codes. We employed here the same strategy as for exhaustive high-temperature line lists, namely a separate treatment of a much smaller set of strong (sharp) absorption features and the remaining bulk of blended weak lines, resulting in quasi-continuum (QC) cross-sections.[33–35] The QC is not a true continuum *stricto sensu* but rather an accumulation of very weak overlapping lines. Their individual contribution is quite negligible but the sum over a hundred million weak lines turns out to be absolutely essential for an accurate modelling of the observed opacity and of its temperature dependence.

The strong lines are selected by the condition $I \geq \alpha I^{cut}(W)$ where α is a scaling factor used for an optimal separation of the QC lines and defined to get the best ratio (number of lines)/(integrated intensity) in the file of strong lines. At 296 K we fixed α = 8000 for which 0.0237% of strong lines gives $\sim$91.5% of opacity in the full W range. The "strong lines" file contains 512 000 lines while the QC includes $\sim$2.162 billion lines. This huge amount of data was compressed using the super-line (SL) approach, as described in ref. 29 and 34. This is a quite simple tool to drastically reduce the number of lines by several orders of magnitude with almost no impact on the accuracy of the calculated absorbance. This becomes much more flexible for the user. For this work, all intensities were summed up by steps of 0.001 cm^{-1} to form only one compressed SL. This final SL library now contains 3.89 million entries, the corresponding compression is thus scaled by three orders of magnitude.

6 Comparison with PNNL experimental spectra

Validation of our variationally computed CF_4 line lists with experimental data is an important step in order to evaluate the accuracy of *ab initio* PES and DMS with respect to predicted CB and HB transitions. A possible source of validation is the comparison of theoretical absorbance with medium-resolution

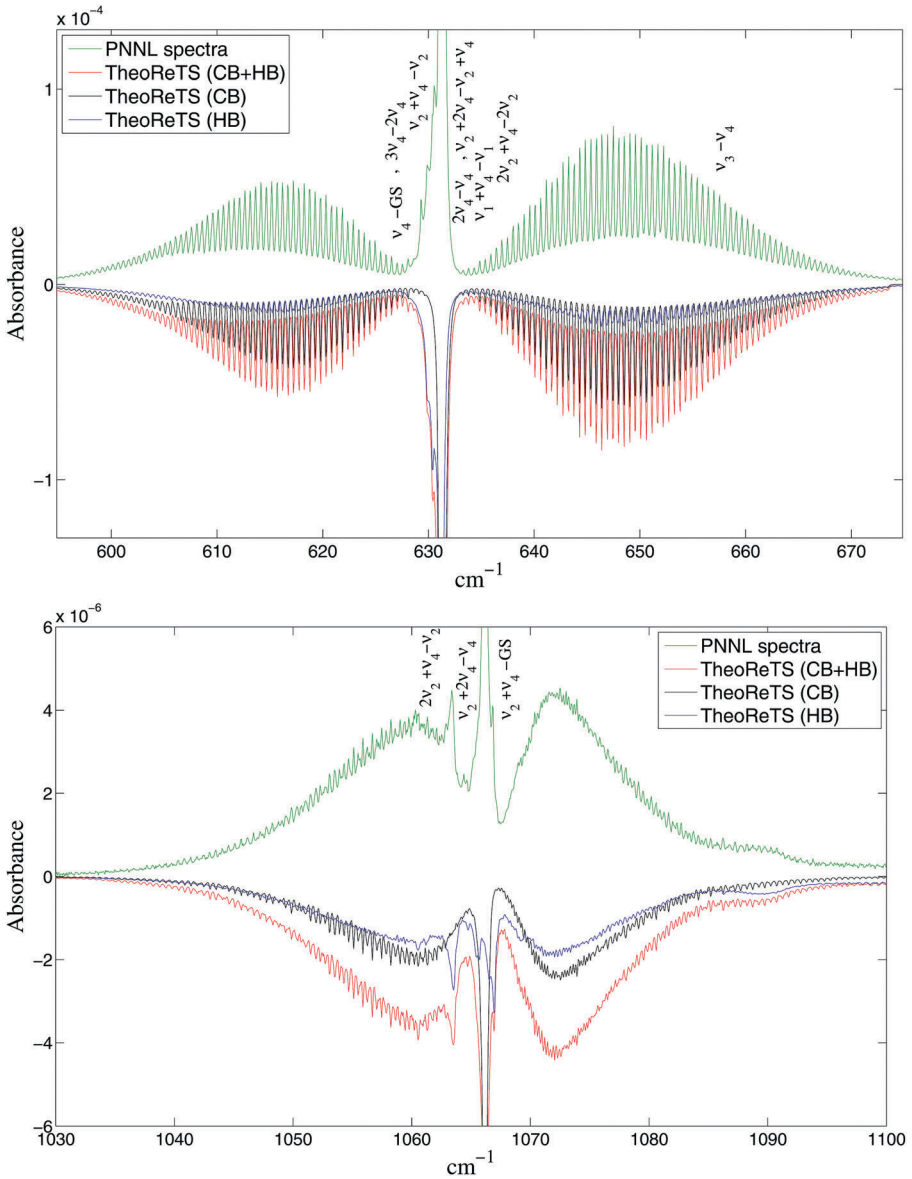

Fig. 7 Example comparison of theoretical (CB, HB and CB + HB transitions) absorption spectra of CF_4 with experimental PNNL records at room temperature in the ν_4 region (top panel) and $\nu_2 + \nu_4$ region (bottom panel) around 600–1100 cm^{-1}. The main CBs and HBs are also indicated in vertical text (see also Sections 6.2 and 6.3).

experimental Fourier-transform laboratory PNNL[103] spectra.‡ They are recorded at temperatures of 5, 25, and 50 °C with a pressure of 1 atm over in a large spectral range of 570–6500 cm^{-1}. Note that the PNNL spectra have not been assigned. Consequently, their line or band parameters have not been extracted, but these raw data provide a wealth of experimental information for validation of theoretical predictions. All comparisons of this section correspond to 296 K. The main absorption regions are considered below and in order to avoid overloading the figures, only the strongest absorption bands are specified on each one; there are many more in reality (see Section 7.1 for more details).

‡ If necessary, the PNNL absorbance spectra could be converted into cross sections (in cm^2 per molecule) using the factor 9.28697×10^{-16}.

6.1 Region 150–500 cm^{-1}

Since PNNL spectra are not available in this region, we only give theoretical predictions of CBs and HBs, which are displayed in Fig. 6. In this region, our list contains 36 million lines essentially composed of HB transitions, except for the interval around 435 cm^{-1} of the ν_2 fundamental band. The four strongest absorption intervals, in decreasing order, correspond to the HB and CB transitions belonging to $\nu_3 - \nu_1$, $\nu_1 - \nu_4$, ν_2 and $\nu_2 + \nu_3 - \nu_1 - \nu_2$ with integrated intensities of 1.48×10^{-21}, 5.96×10^{-22}, 2.28×10^{-22} and 1.44×10^{-22} cm per molecule, respectively, which is clearly dominated by HBs. Here and below we quote the integrated intensities of individual bands or of selective absorption features using the "strong lines" sample only. For QCs the contributions of individual band are not separable.

Table 4 Comparison of the integrated PNNL absorbance of CF_4 with TheoReTS (this work) and TFMeCaSDa[102] (http://vamdc.icb.cnrs.fr/PHP/tfmecasda.php)

Region (cm^{-1})	TheoReTS (TW)	PNNL	Error (%)
570–700	3.96×10^{-2}	3.84×10^{-2}	−3.0
980–1220	2.00×10^{-3}	2.25×10^{-3}	12.0
1220–1380	3.39	3.42	0.9
1380–1600	2.30×10^{-2}	2.39×10^{-2}	3.8
1600–1800	3.64×10^{-3}	3.73×10^{-3}	2.5
1800–2000	5.18×10^{-3}	5.20×10^{-3}	0.4
2000–2280	1.73×10^{-2}	1.75×10^{-3}	1.2
2280–2700	2.05×10^{-2}	1.94×10^{-2}	−5.5
2700–2950	3.00×10^{-4}	2.99×10^{-4}	−0.3
2950–3300	3.77×10^{-4}	4.04×10^{-4}	6.7
3300–3950	8.68×10^{-4}	9.07×10^{-4}	4.5
Region (cm^{-1})	TFMeCaSDa[102]	PNNL	Error (%)
980–1220	1.42×10^{-3}	2.25×10^{-3}	74.0
1220–1380	3.12	3.42	9.0
1380–1600	1.74×10^{-4}	2.39×10^{-2}	—

6.2 Region 570–700 cm^{-1}

In this region, mainly dominated by the ν_4 fundamental band, the list contains a total of ~20.4 million lines with the integrated intensity of 1.40×10^{-18} cm per molecule. The three main HBs which fall in this region are $\nu_2 + \nu_4 - \nu_2$, $2\nu_4 - \nu_4$ and $2\nu_2 + \nu_4 - 2\nu_2$ with integrated intensities of 3.19×10^{-19}, 1.96×10^{-19} and 3.97×10^{-20} cm per molecule. There also exist other bands such as $\nu_3 - \nu_4$, $\nu_2 + 2\nu_4 - \nu_2 - \nu_4$, *etc.* whose contributions are respectively about 65%, 59%, *etc.* of $2\nu_2 + \nu_4 - 2\nu_2$. At 296 K, the HB contribution represents ~44% of the total opacity in this region making analyses with "traditional" spectroscopic models very challenging. Fig. 7 (top) shows comparisons between theory and the observed PNNL spectra and confirms a very good agreement in the integrated absorbance of about 3% (see Table 4).

6.3 Region 980–1220 cm^{-1}

In this spectral range, the list contains about 21 million lines and is dominated by the $\nu_2 + \nu_4$, $2\nu_2 + \nu_4 - \nu_2$ and $\nu_2 + 2\nu_4 - \nu_4$ bands around 1062 cm^{-1}. Their integrated intensities are respectively 4.72×10^{-20}, 9.10×10^{-21} and 1.40×10^{-21} cm per molecule. The hot band $2\nu_1 - \nu_4$ around 1177 cm^{-1} has the integrated intensities of 8.92×10^{-22} cm per molecule. The HBs contribute at ~25% of the total opacity in this region. Again, comparison with PNNL spectra in Fig. 7 (bottom panel) shows a very good agreement.

6.4 Region 1220–1380 cm^{-1}

The bands of this region containing about 61 million lines in our list clearly dominate the absorption CF_4 spectrum in the infrared. The main absorption corresponds to the fundamental stretching band ν_3 but also, to a lesser extent, to the overtones $2\nu_4$ and $3\nu_2$ (resp. about 14.5% and 2.3% of the ν_3 opacity). The most active HBs falling in this region are $\nu_2 + \nu_3 - \nu_2$, $\nu_3 + \nu_4 - \nu_4$, $\nu_2 + 2\nu_4 - \nu_2$, $4\nu_2 - \nu_2$, $2\nu_2 + \nu_3 - 2\nu_2$, $3\nu_4 - \nu_4$, *etc.* that contribute to 22.0, 11.5, 3.6, 3.2 and 2.3% of the ν_3 opacity, respectively. This means that even bands with three vibrational quanta give non negligible opacity contributions, making an analysis with effective empirical Hamiltonian and effective fitted transition moments very complicated (see Section 7.1 for more discussion). The total integrated intensity at this range is 1.91×10^{-16} cm per molecule with ~60% originating from CBs. Fig. 8 (top) displays a very dense absorption pattern of the CF_4 spectrum in the ν_3 region. The bottom panel shows very good agreement between the integrated absorbance and the PNNL measurements, within 0.9%, where the low-resolution theoretical spectrum simulations match nearly perfectly the observed cross-sections.

6.5 Region 1380–1600 cm^{-1}

This is the region of the $\nu_1 + \nu_4$ combination band centered around 1540 cm^{-1} that has an integrated intensity of 7.69×10^{-19} cm per molecule. This band dominates $\nu_1 + \nu_2 + \nu_4 - \nu_2$ and $\nu_1 + 2\nu_4 - \nu_4$ by factors of 4.5 and of 6.7, respectively. The fourth strongest absorption is due to $2\nu_2 + \nu_4$ around 1500 cm^{-1}. The absorbance in the region is by two orders of magnitude weaker than in the ν_3 region. The HB transition represents here about 42% of the total opacity. The total number of lines in our lists is about 23.5 million. A detailed comparison with PNNL spectra is given in Fig. 9, where again we find an overall agreement with the observed cross-section, the error on the integrated absorbance being 3.8%.

6.6 Region 1600–1800 cm^{-1}

In this region, the line list contains about 24 million transitions corresponding mainly to three CBs and two HBs that are assigned as $\nu_2 + \nu_3$, $\nu_2 + 2\nu_4$, $4\nu_2$ and $2\nu_2 + \nu_3 - \nu_2$, $\nu_2 + \nu_3 + \nu_4 - \nu_4$. CBs represent about 85% of the opacity in this region. Fig. 10 gives the respective contributions of the cold and hot band (top panel) as well as a detailed comparison with PNNL spectra (bottom panel) which proves again the consistency of our calculations and the validity of the *ab initio* DMS (the obs.–calc. error of ~2.5% in the integrated absorbance).

6.7 Region 1800–2000 cm^{-1}

This dense region (about 125 million lines in the theoretical list) is dominated by the $\nu_3 + \nu_4$ combination band around 1913 cm^{-1} that has an integrated intensity of 1.40×10^{-19} cm per molecule. The second strongest absorption is due to $3\nu_4$ around 1890 cm^{-1}, which is four times less important than $\nu_3 + \nu_4$ in terms of opacity. The next five strongest absorptions (in decreasing order) are due to the $\nu_2 + \nu_3 + \nu_4 - \nu_2$, $\nu_3 + 2\nu_4 - \nu_4$, $\nu_2 + 3\nu_4 - \nu_2$, $4\nu_4 - \nu_4$ and $2\nu_3 - \nu_4$ bands with integrated intensities of 2.70×10^{-20}, 1.37×10^{-20}, 5.1×10^{-21}, 3.69×10^{-21} and 2.64×10^{-21} cm per molecule. The cold band $3\nu_2 + \nu_4$ around 1937 cm^{-1} is completely diluted among all the other ones. The comparison with PNNL is given in Fig. 11, the error in integrated absorbance being very small (~0.4%).

6.8 Region 2000–2280 cm^{-1}

This strongest absorption in this dense region, composed of about 168 million lines in the list, is due to $\nu_1 + \nu_3$ with the integrated intensity of 5.00×10^{-19} cm per molecule. The $\nu_1 + \nu_2 + \nu_3 - \nu_2$ and $\nu_1 + 2\nu_4$ bands are five times weaker than this band while

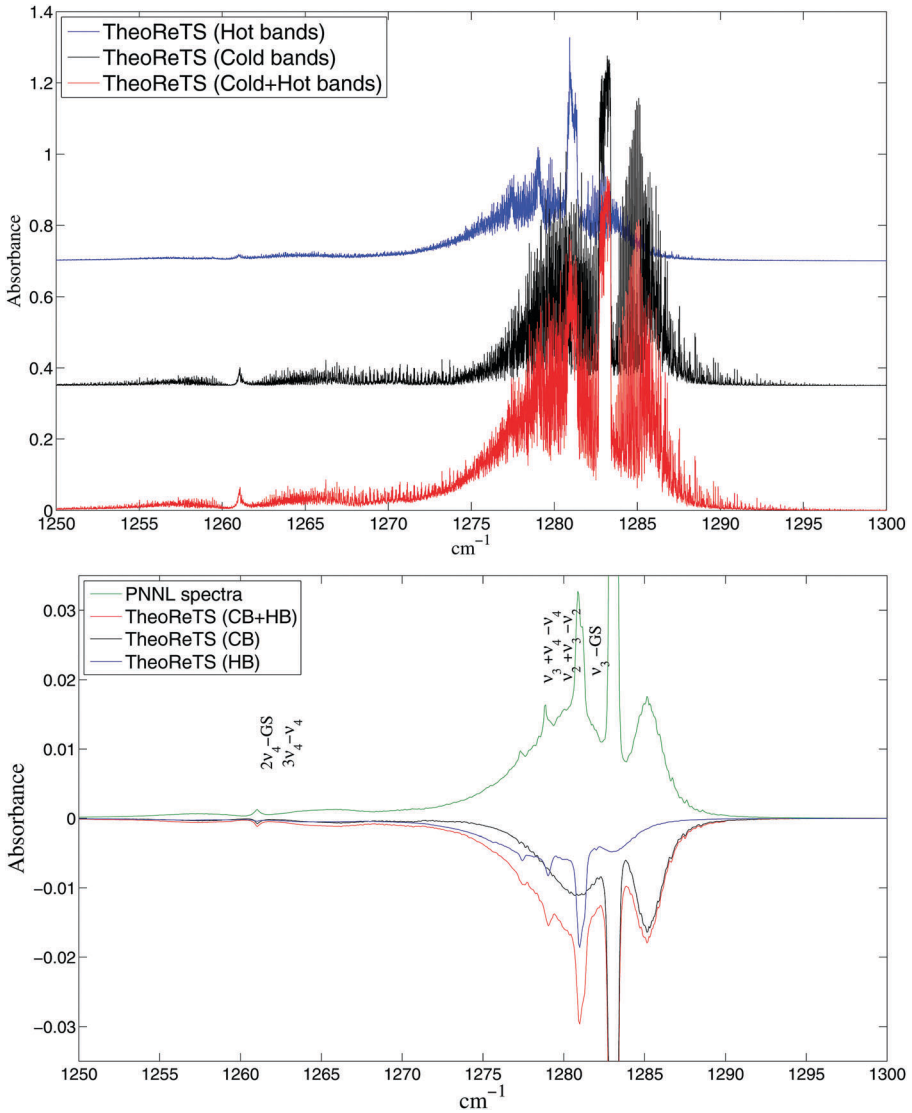

Fig. 8 Theoretical absorbance computed at 296 K with the contribution of cold and hot band transitions (top panel). Example comparison of theoretical (CB, HB and CB + HB transitions) absorption spectra of CF_4 with experimental PNNL records at room temperature in the ν_3 region around 1250–1300 cm^{-1} (bottom panel). The main CBs and HBs are also indicated in vertical text (see also Section 6.4).

$\nu_1 + \nu_3 + \nu_4 - \nu_4$, $\nu_1 + \nu_2 + 2\nu_4 - \nu_2$, $\nu_1 + 3\nu_4 - \nu_4$, $\nu_1 + 2\nu_2 + \nu_3 - 2\nu_2$ and $2\nu_2 + \nu_3$ are one order of magnitude weaker. The impressive complexity of the CF_4 spectra is due to the more than 40 CBs and HBs that fall in this region, including three, four, five and even six quanta bands such as $6\nu_2 - \nu_2$ which is by three orders of magnitude weaker than $\nu_1 + \nu_3$. Despite such complexity, the comparison with PNNL is very good (see Fig. 11, middle and bottom panels) and the error in integrated absorbance is only 1.2%. The HB transition represents about 44% of the total opacity in this region.

6.9 Region 2280–2700 cm^{-1}

This is again a very dense and rich region composed by more than 760 million lines at 296 K. Among the strongest bands, we have the CBs $2\nu_3$ (the strongest one, with an integrated intensity of 4.98×10^{-19} cm per molecule), $\nu_3 + 2\nu_4$, $4\nu_4$ and $3\nu_2 + 2\nu_4$ around 2560 cm^{-1} and $2\nu_1 + \nu_4$ around 2445 cm^{-1}. Concerning the HBs, we find $\nu_2 + 2\nu_3 - \nu_2$, $2\nu_3 + \nu_4 - \nu_4$, $\nu_2 + \nu_3 + 2\nu_4 - \nu_2$, $\nu_3 + 3\nu_4 - \nu_4$, $2\nu_2 + 2\nu_3 - 2\nu_2$, $\nu_2 + 4\nu_4 - \nu_2$, *etc.* contributing to 20, 10, 7, 3.6, 2.5 and 1.9% of the $2\nu_3$ intensity. Fig. 12 (top and middle panels) shows very good agreement with the observed PNNL cross-sections.

6.10 Region 2700–2950 cm^{-1}

This region contains about 165 million lines and is dominated by the two CB $\nu_1 + \nu_3 + \nu_4$ and $\nu_1 + 3\nu_4$ that are 70% stronger than the four HBs $\nu_1 + \nu_2 + \nu_3 - \nu_2$, $\nu_1 + \nu_3 + 2\nu_4 - \nu_4$, $\nu_1 + \nu_2 + 3\nu_4 - \nu_2$ and $\nu_1 + 4\nu_4 - \nu_4$. Once again, Fig. 12 (bottom panel) shows a very good agreement with PNNL (error $\sim$0.3% for integrated absorbance).

6.11 Region 2950–3300 cm^{-1}

This weak, but dense, region contains more than 250 million lines and is clearly dominated by three CBs, namely $2\nu_3 + \nu_4$,

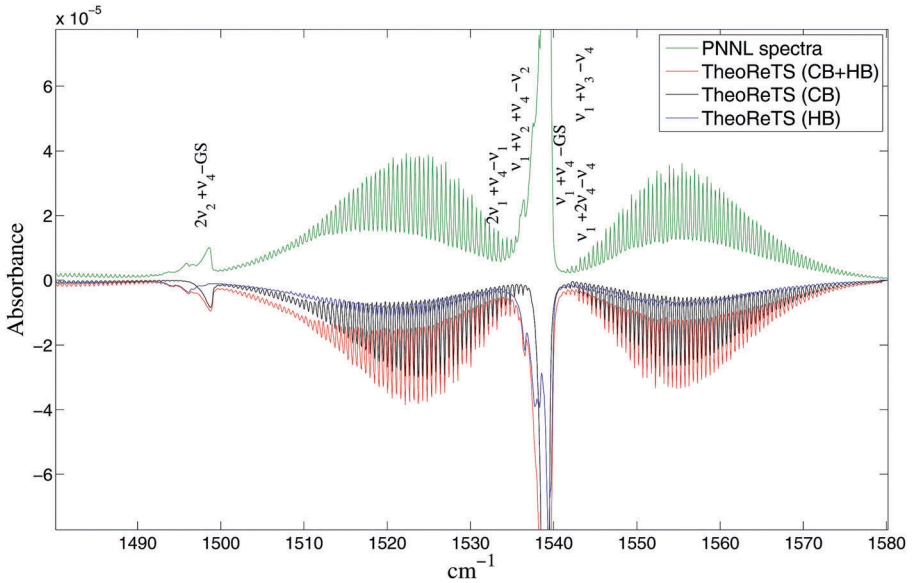

Fig. 9 Example comparison of theoretical (CB, HB and CB + HB transitions) absorption spectra of CF_4 with experimental PNNL records at room temperature in the $\nu_1 + \nu_4$ region around 1480–1580 cm^{-1}. The main cold and hot bands are also indicated in vertical text (see also Section 6.5).

$2\nu_1 + \nu_3$ and $\nu_3 + 3\nu_4$ whose total opacity represents almost 70% of the other cold and hot bands. For example the two first HB are $\nu_2 + 2\nu_3 + \nu_4 - \nu_2$ and $2\nu_1 + \nu_2 + \nu_3 - \nu_2$ and are respectively 10 and 15 times weaker than $2\nu_3 + \nu_4$. Fig. 13 (top panel) gives an overview of the calculated spectrum compared with PNNL. One can see that the agreement is quite good, even for such a weak region.

6.12 Region 3300–3950 cm^{-1}

In this region, composed by 290 million lines, the $\nu_1 + 2\nu_3$ band around 3450 cm^{-1} and the $3\nu_3$, $2\nu_3 + 2\nu_4$, $\nu_3 + 4\nu_4$ bands around 3800 cm^{-1} give the strongest contributions. The first HBs are $\nu_1 + \nu_2 + 2\nu_3 - \nu_2$, $\nu_1 + \nu_2 + \nu_3 - \nu_2$ and $\nu_2 + 3\nu_3 - \nu_2$ and are one order of magnitude weaker than the cold bands. Fig. 13 (bottom panel) confirms the relatively small error on the integrated intensities ($\sim$4.5%) compared to PNNL. Line-by-line analyses of experimental spectra in such a complex region involving 6 quanta bands using traditional polyad models would be hardly feasible, at least at T = 296 K; only low-T spectra could help the assignments.

7 Discussion

7.1 Global *ab initio versus* phenomenological spectroscopic models

As was mentioned in Section 2, much effort has been devoted to attempt to understand the complex polyad structure of CF_4. Analysis of ro-vibrational lines has been previously conducted using phenomenological effective spectroscopic models (ESMs) that involve empirically determined parameters fitted to experimental line positions and line intensities. This is the first of the two possible approaches. For molecules exhibiting quite regular patterns, such empirical models have proved their efficiency these past few decades in spectroscopic data reduction and in the construction of well-known databases such as HITRAN[2] or GEISA.[3] They are particularly well adapted to provide very precise line positions, approaching experimental accuracy. However, in the case of molecules with low-frequency vibrational modes and relatively heavy "edge atoms" as for CF_4, the vibrational polyad structure is not well defined and high-J transitions make the spectra very crowded. This makes the empirical line-by-line analyses much more complicated. Due to the huge number of overlapping lines forming dense and complex patterns composed of both CBs and HBs, the effective models could face their intrinsic limit, even though several bands were fitted simultaneously.

Very recently, a partial high-resolution analysis of CF_4 spectra in the infrared has been performed[62] to better understanding complex absorption features. This led to the first determination of the effective parameters for 17 rovibrational bands included in a fitted effective Hamiltonian model. Their analysis was essentially focused on line positions while effective dipole parameters were fixed by manual adjustment. A part of the result of Carlos *et al.*[62] was used to update the Dijon University TFMeCaSDa database,[102] up to 1700 cm^{-1}, with an intensity cut-off of 10^{-24} cm per molecule that provided the most extended line list for the CF_4 in the infrared range currently computed in the framework of an ESM.

A comparison of the experimental PNNL spectra with *ab initio* born variational calculations (this work) and with the TFMeCaSDa database clearly shows limitations of the effective models in terms of extrapolation (see Fig. 14). The medium-resolution absorbance simulations are quite similar in the narrow range around 1280 cm^{-1} included in the EMS empirical line-by-line fits but are very different beyond this region (see Fig. 14, upper panels). Fig. 7–13 show a good agreement between our *ab initio* intensities and experiments in the whole wavenumber

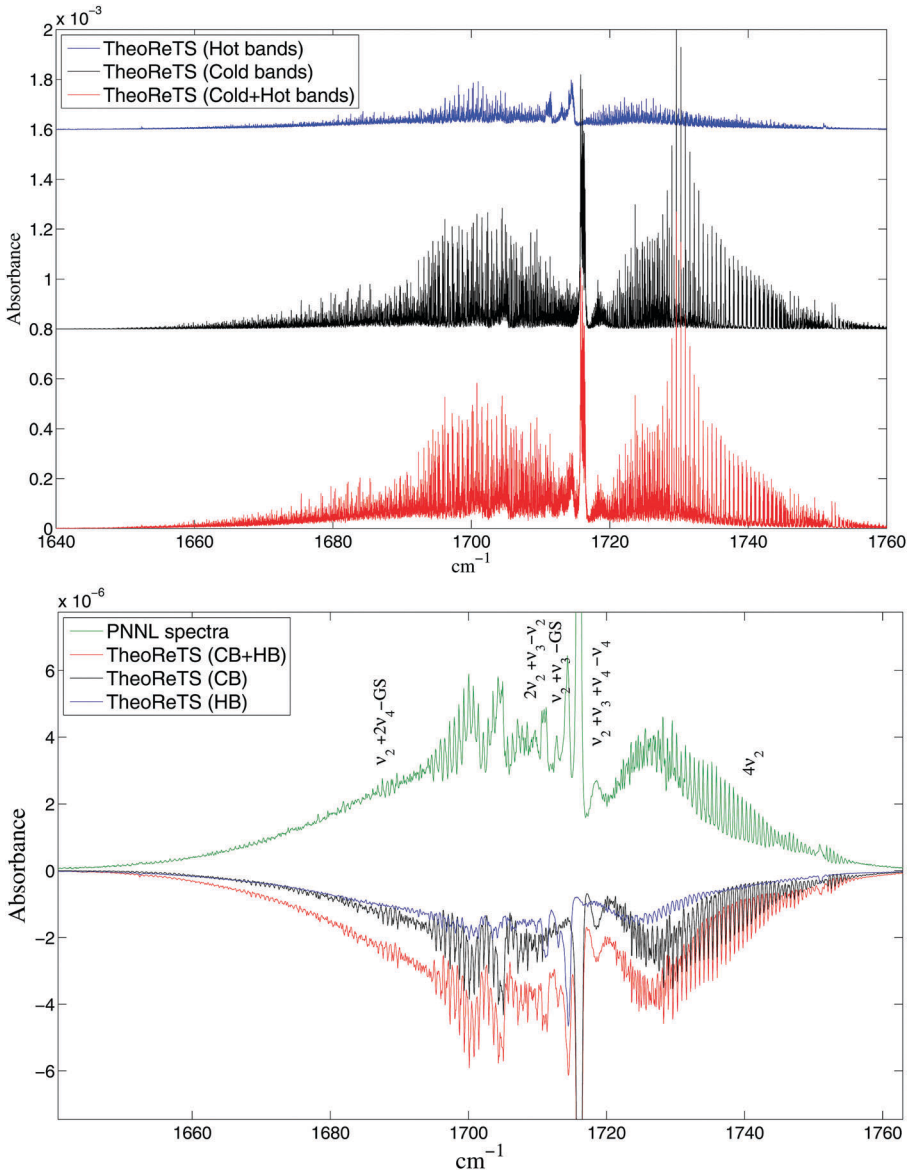

Fig. 10 Theoretical absorbance computed at 296 K with the contribution of cold and hot band transitions (top panel). Example comparison of theoretical (CB, HB and CB + HB transitions) absorption spectra of CF_4 with experimental PNNL records at room temperature in the $\nu_2 + 2\nu_4/\nu_2 + \nu_3$ region around 1640–1760 cm^{-1} (bottom panel). The main CBs and HBs are also indicated in vertical text (see also Section 6.6).

range of available PNNL cross-sections. In contrast, the EMS line list shows erratic absorbance behaviour below 1250 cm^{-1} and above 1300 cm^{-1} in a qualitative disagreement with the PNNL experiment (Fig. 14, right-hand panels). The deviations in hot bands are particularly large (Fig. 14, left-hand upper panel) leading to quite different temperature dependence of the opacity. The reasons for these disagreements could be the following.

• First, very few experimental assignments are available in the literature for the HB transitions and for the corresponding excited vibrational states. CB and HB transitions are often blended together, consequently it was not possible to measure their individual line intensities.[62] If the line strength information on HBs was not included in the EMS, their contributions to the observed cross-sections could be "absorbed" by effective dipole moments of CBs. For example, in the 1220–1380 cm^{-1} region the integrated PNNL absorbance using the TFMeCaSDa database[102] is higher than ours (2.49 *vs.* 2.24) while it is inverted for HBs (0.62 *vs.* 1.16).

• As only partial information on energy levels was obtainable from empirically assigned lines, the ESM calculations are not complete and include extrapolations beyond the range of observed data that are not always reliable. This was the case of energy patterns in the region 2080–2160 cm^{-1} given in Fig. 12 of ref. 62. In this range where no experimental assignments were included, the extrapolated level exhibited drastically different behaviour from the *ab initio* levels (Fig. 2) at large *J*-values that may explain the disagreement of ESM with observations in Fig. 14. This is also corroborated by comparing Fig. 2 of ref. 60

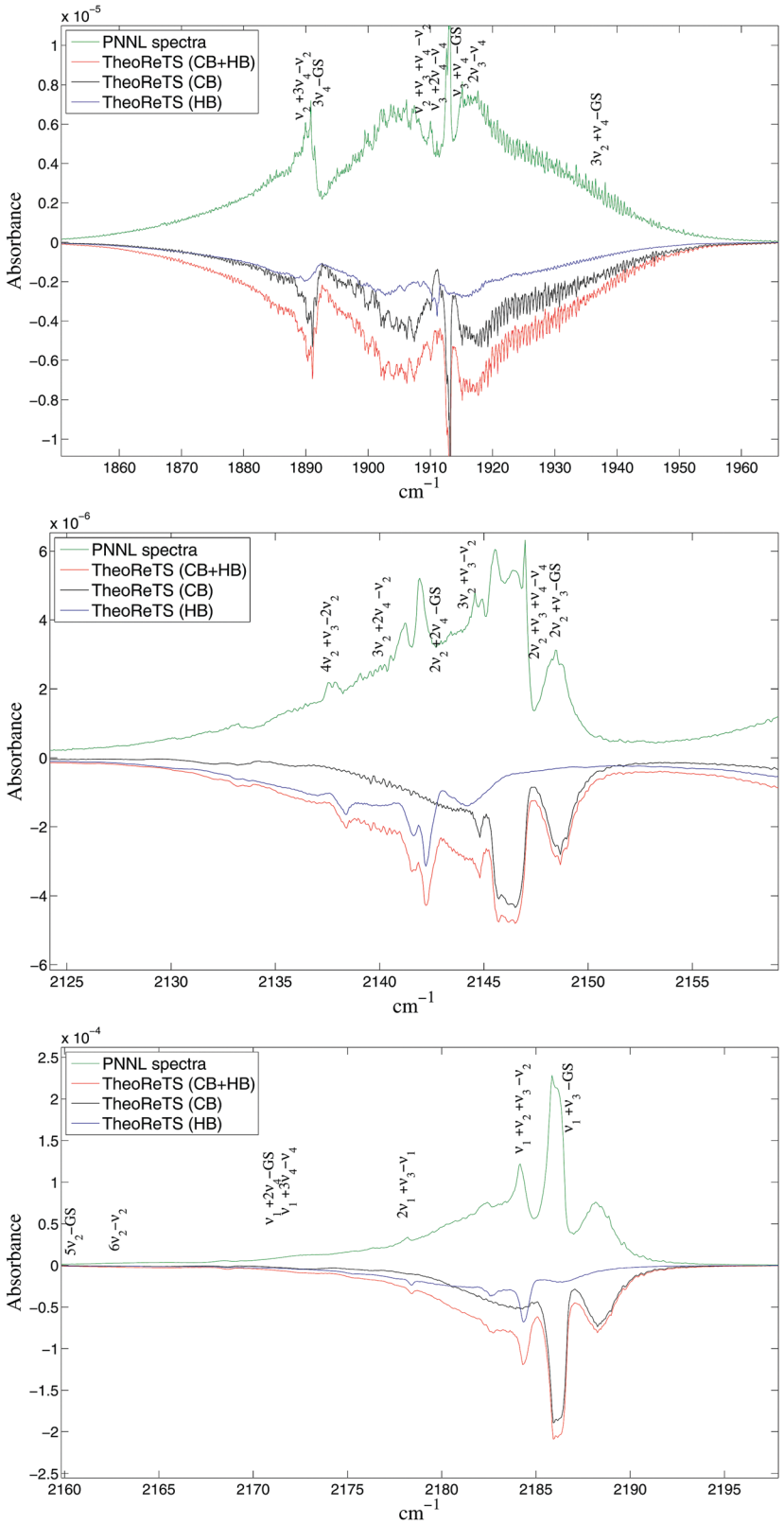

Fig. 11 Example comparison of theoretical (CB, HB and CB + HB transitions) absorption spectra of CF_4 with experimental PNNL records at room temperature in the region 1850–2200 cm^{-1}. The main CBs and HBs are also indicated in vertical text (see also Sections 6.7 and 6.8).

with our Fig. 2 (top panel) or Fig. 8 of ref. 62 with our Fig. 2 (bottom panel). In one case, the three vibrational sublevels $3\nu_2(A_1,A_2,E)$ were missing in ref. 60 and in the other case the three vibrational sublevels $4\nu_2(A_1,A_2,E)$ were missing in ref. 62.

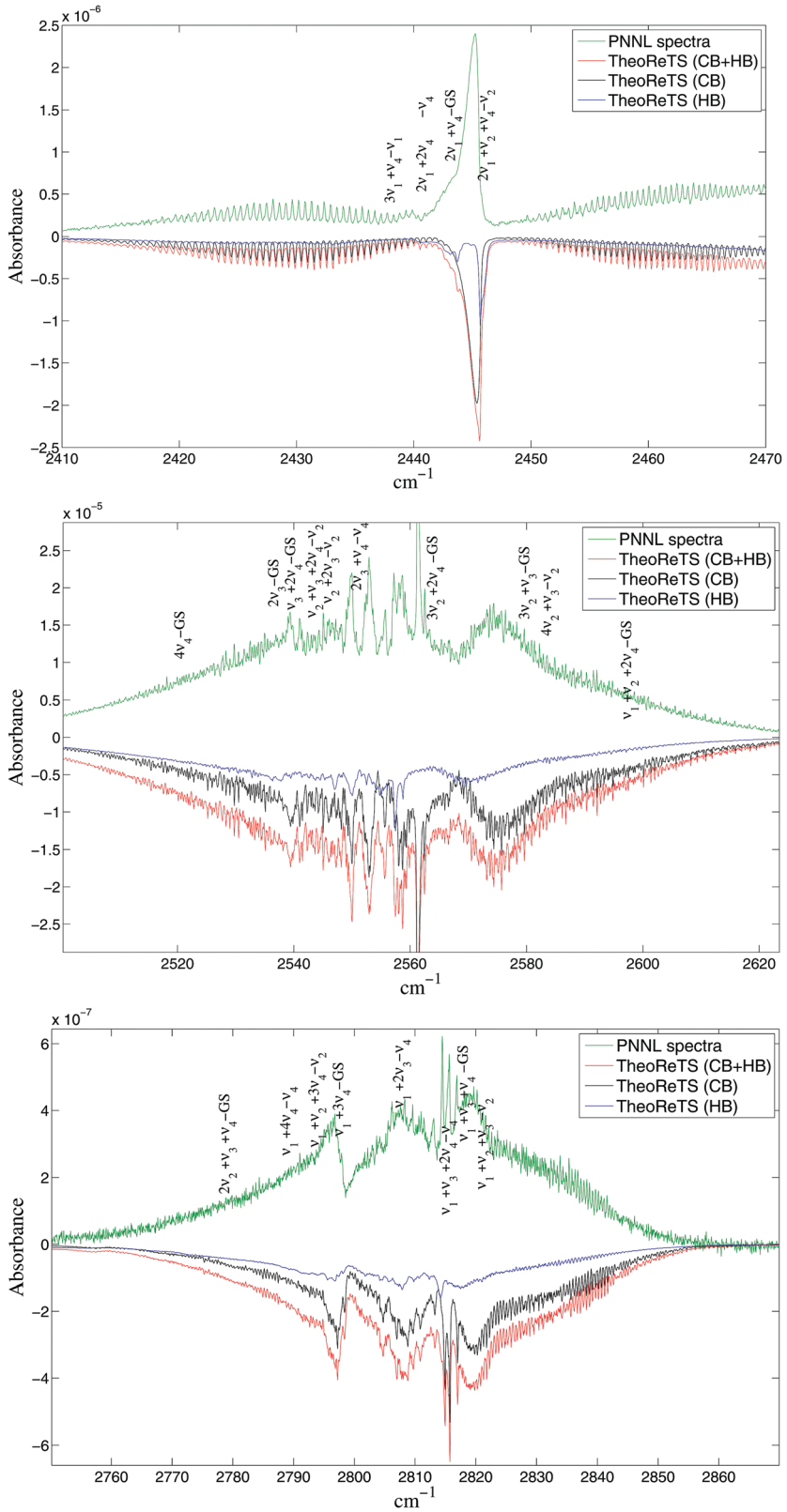

Fig. 12 Example comparison of theoretical (CB, HB and CB + HB transitions) absorption spectra of CF_4 with experimental PNNL records at room temperature in the region 2500–2870 cm^{-1}. The main CBs and HBs are also indicated in vertical text (see also Sections 6.9 and 6.10).

Note that one of the two sublevels $\nu_2 + 2\nu_4(A_1)$ should read $\nu_2 + 2\nu_4(A_2)$ in Fig. 8 of ref. 62.

• The term "global" in some previous ESM analyses has to be taken with caution because many CBs and HBs falling in the

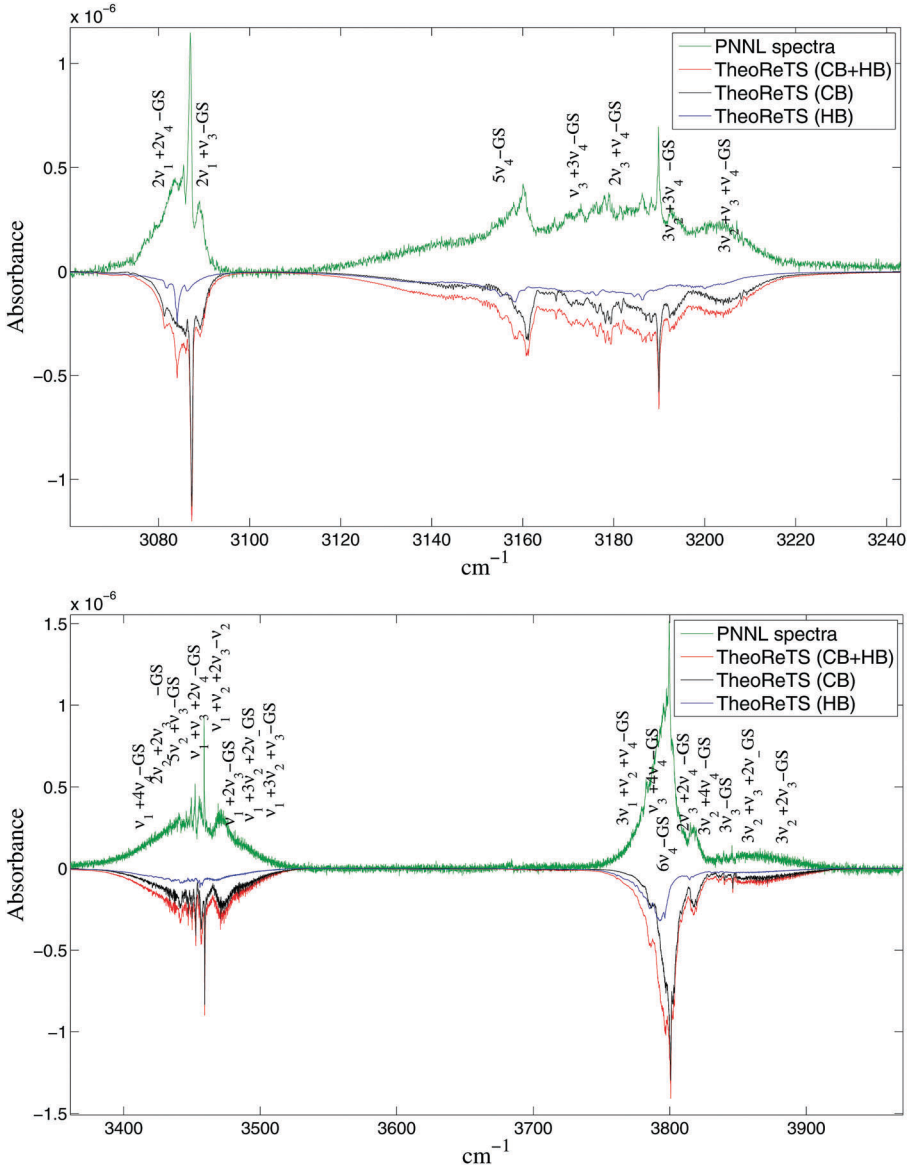

Fig. 13 Sample comparison of theoretical (CB, HB and CB + HB transitions) absorption spectra of CF_4 with experimental PNNL records at room temperature in the region 3400–3950 cm^{-1}. The main CBs and HBs are also indicated in vertical text (see also Section 6.12).

same spectral range have been omitted and many resonance coupling parameters had to be neglected. Modelling of "dark states" (which are not directly observable, but perturb active bands) is one of the major obstacles for a purely empirical approach. Variational *ab initio* based calculations include an entire set of bands contributing to the opacity and account for all interactions among them. For example, 17 rovibrational bands have been included in the last ESM analysis[62] up to 2200 cm^{-1}; in our variational calculations, we predict at least 160 rovibrational bands of the type $\sum_i \alpha_i \nu_i - \sum_j \beta_i \nu_j$ in the same region. Up to 4000 cm^{-1}, almost 800 vibrational states need to be included, leading to ~300 "strong" transitions of the type $\sum_i \alpha_i \nu_i - \sum_j \beta_i \nu_j$ and many more in the QC absorption.

Though *ab initio* methods do not achieve high-resolution accuracy for individual line positions, the comparison with experimental PNNL spectra (Fig. 7–13) clearly show that our calculations provide more complete and reliable intensities both for CBs and HBs than the available ESM line lists in a large wavenumber range.

7.2 Hints for further improving line-by-line analyses

CF_4 belongs to the category of molecules where a complete line-by-line analysis of the overall rotation–vibration spectrum in the infrared will take many years or even decades, similar to the long history of methane studies (see for example the review by Brown *et al.*[104]) but with a much larger number of lines. One of the well known issues is that empirical ESM fits behave as mathematically ill-defined problems (see ref. 105 and 106) because the effective Hamiltonian matrices and coupling parameters are not unambiguously determined from experimental levels.

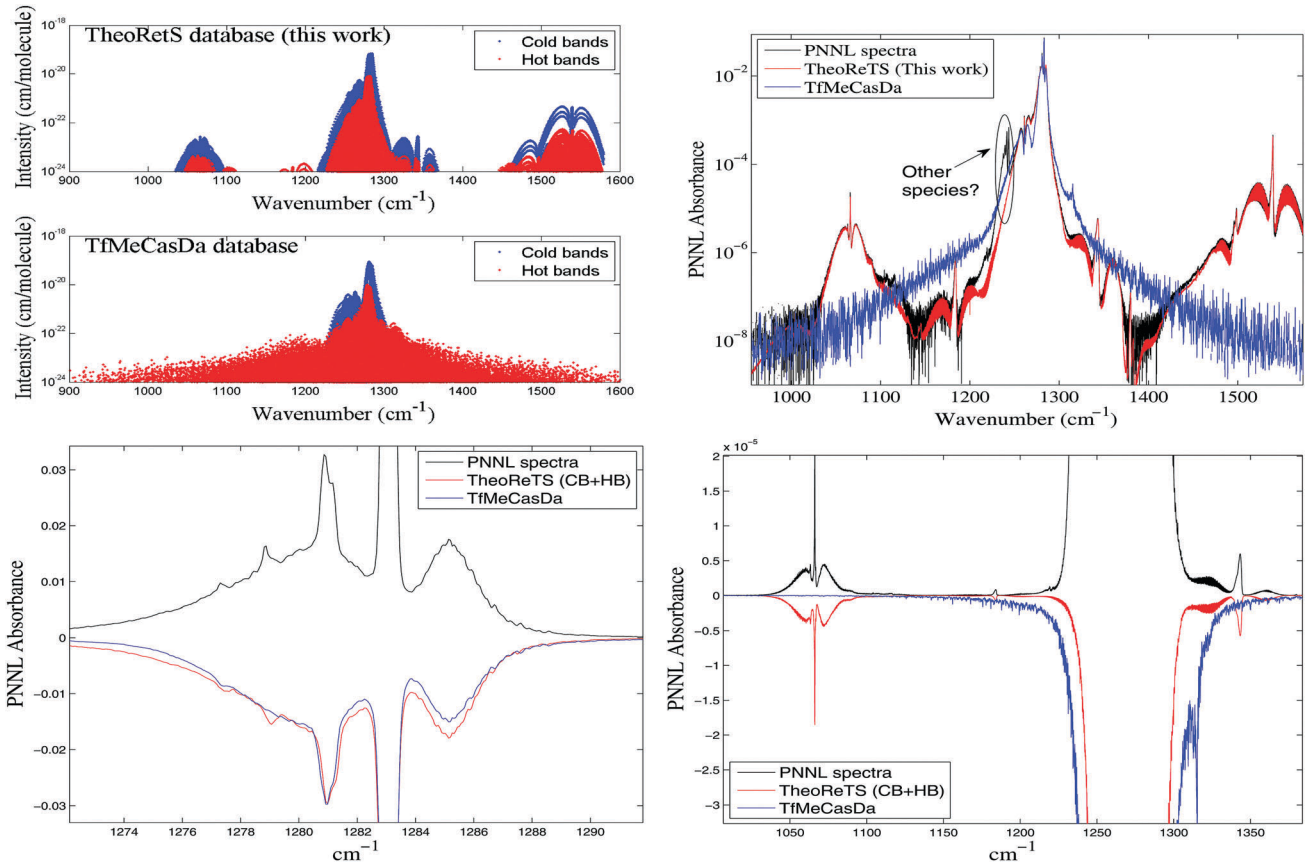

Fig. 14 Comparison of the TheoReTS and TFMeCasDa[102] (http://vamdc.icb.cnrs.fr/PHP/tfmecasda.php, downloaded on 20/05/2018) line intensities (top panel, left-hand side) in the range 900–1600 cm^{-1} and detailed comparison of the simulated absorption spectra of CF_4 with experimental PNNL records at room temperature.

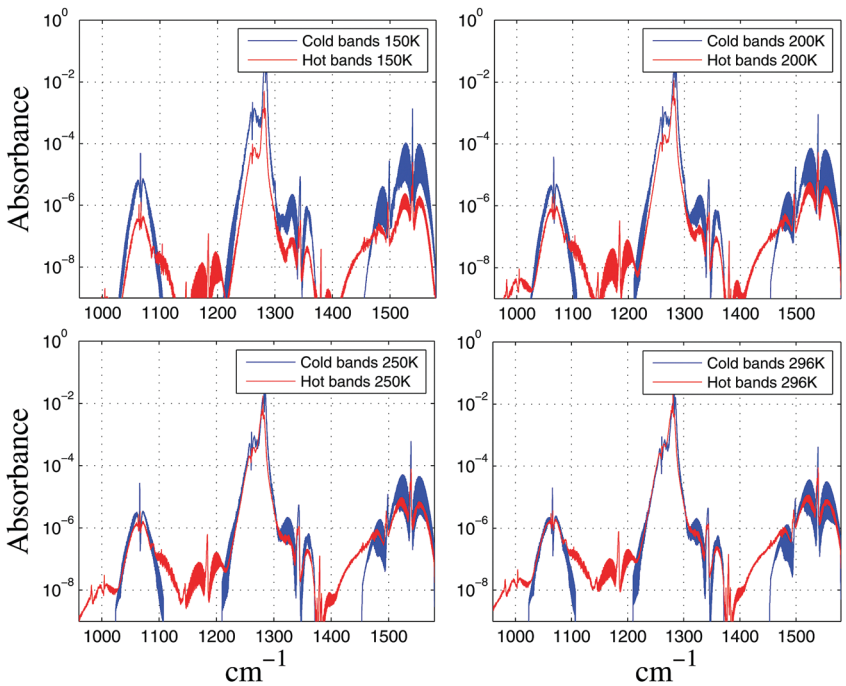

Fig. 15 Temperature effect on the absorption spectra of CF_4 in the range 1000–1500 cm^{-1} and impact on the HB contributions from 150 to 296 K.

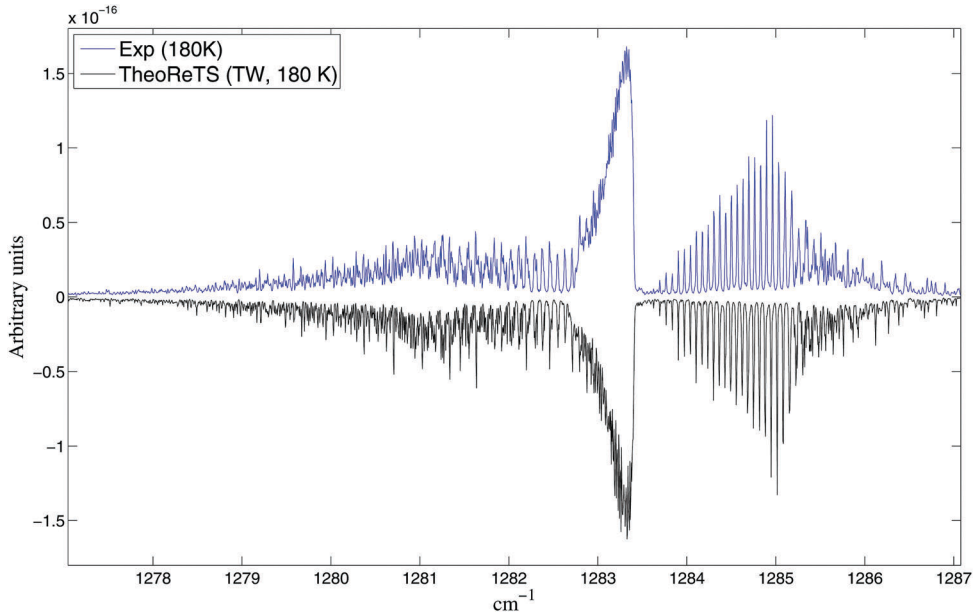

Fig. 16 Comparison of the simulated spectra (this work) of CF_4 with experiment at 180 K, in the ν_3 region.

This can lead to false resonance mixing of wavefunctions and consequently erratic intensity borrowing effects among coupled strong and weak bands.

In order to make the analyses of high-resolution spectra more robust, the *ab initio* effective spectroscopic models adapted to successive spectral ranges can be accurately constructed from the potential energy surface by the high-order contact transformation method.[64,107] For the sets of states contributing to a considered range (including ''dark'' states) this will provide initial physically meaningful coupling parameters and wavefunctions, which were poorly determined in a purely empirical approach. Diagonal parameters, including band centers and rotational constants can be optimized by fine tuning to experimental spectra, while band intensities can be evaluated using *ab initio* DMS. Such a strategy has been recently proven efficient for CH_4[107] and an analysis of room-temperature CF_4 Fourier transform spectra in the region 1600–1800 cm^{-1} is currently in progress using this method.

It will be also useful to record cooled CF_4 spectra down to T = 100 or 150 K, in order to simplify CB analyses by removing completely or partially HB transitions. Fig. 15 shows the temperature effect when cooling spectra at 150, 200, 250 K. We can see that HB contributions are reduced by one order of magnitude from T = 296 to T = 150 K. Thus recording low-T spectra in a large range in the future would be of great help for progress in the line-by-line assignment procedure. Fig. 16 gives a comparison of the experimental and calculated spectra at 180 K in the ν_3 interval.

8 Conclusion

In this work, we have shown that an efficient variational method for nuclear motion calculations permitted reliable predictions of rotationally resolved spectra and a full understanding of the hot band patterns in the wide IR spectral range for a five-atomic molecule with relatively heavy edge F atoms. In previous studies[23,34,75,90,108] such quality of theoretical IR spectra has been achieved for lighter molecules only with hydrogen edge atoms like CH_4, SiH_4, or GeH_4. A big difference is that CF_4 has much lower vibrational modes and much higher J-levels are populated making the HB spectral patterns significantly more complicated. We show that the strong absorption features are superimposed with a kind of quasi-continuum already at room temperature conditions, similarly to that observed[35] and calculated[32–34] in hot methane spectra at about 1000 K.

Minor empirical refinement of the equilibrium geometry and of force constants of the PES combined with purely *ab initio* DMS (provided as ESI†) yielded a correct global description of the positions and shapes of the overtone and combination bands up to five or six vibrational quanta validated by detailed comparisons with experimental PNNL spectra.

This was used to construct the first accurate and complete *ab initio* based line lists for CF_4 in the range 0–4000 cm^{-1}, containing absorption bands that are the most active in IR. In order to converge the IR opacity at room temperature, it was necessary to include a high rotational quantum number up to J = 80 resulting in 2 billion rovibrational transitions. In practical terms, these data can be used for a reliable modelling of the full IR opacity of this long-lived greenhouse molecule under various temperature conditions.

The data obtained in this work will be made available through the TheoReTS[29] information system (http://theorets.univ-reims.fr, http://theorets.tsu.ru) that contains *ab initio* born line lists and provides a user-friendly graphical interface for a fast simulation of the absorption cross-sections and radiance.

In order to make the cross-section simulation faster, we have partitioned our data in two parts: (a) strong + medium line lists

with lower energy levels for calculation of selective absorption features that can be used at various temperatures and (b) compressed "super-line" libraries of very weak transitions contributing to the quasi-continuum modelling. The latter ones will be available in TheoReTS, from T = 100 K to 300 K by steps of 20 K and also for 400 K. Extrapolations for higher temperatures can be produced by request if necessary for some particular applications.

We also propose solutions (see Section 7.2) to combine completeness and line position accuracy for future *ab initio* guided high-resolution spectra analyses. Further progress in the description absorption/emission for fluoro-containing greenhouse molecule in a wider range and for applications under various conditions could benefit from a collaboration of spectroscopists, theoretical chemists, and specialists in atmospheric modelling.

Conflicts of interest

There are no conflicts to declare.

Appendix A: construction of a "pruned" vibrational basis set

• First, a "pruned basis" is defined by selecting only a limited set of relevant primitive vibrational functions as

$$F_{\kappa}^{\Gamma}(n) \Leftrightarrow \sum_{i=1}^{4} \kappa_i v_i \leq n, \tag{A1}$$

with v_i = 0,...,n, for a symmetry block $\Gamma(\equiv C_v)$. Here κ_i are certain weight coefficients chosen to select and optimize an appropriate number of stretching and bending basis functions for each mode. The associated vibrational subspace will be denoted as $\mathscr{F}_p^{\Gamma}(n)$ such that $\dim(\mathscr{F}_p^{\Gamma}) = D_1^{\Gamma}$ that is the basis in the block Γ will contain D_1^{Γ} vibrational functions. Here the "p" index stands for a pruned subspace. This pruning scheme amounts to discarding "unnecessary" functions having a very small impact on calculations or probing non-physical regions of the PES. For example, the matrix element $\langle 9,0,10,0|a_1^{+3}a_4|6,0,11,0\rangle$ computed in the unconstrained basis (12) couples vibrational states located at 20 900 and 19 500 cm^{-1} for $^{12}CF_4$, which is quite useless for practical calculations. Setting n = 11, such matrix elements would be not considered from the pruning scheme (A1) with all κ_i = 1. In the case of T_d symmetry, the number of pruned basis functions in the F (F_1 or F_2) symmetry blocks is $D_1^F \sim 10^5$ ($\approx$100 GB of computer memory against hundreds of TBytes from eqn (12)).

• Pruning decreases the number of basis functions but is still not sufficient to make rovibrational calculations feasible, especially for the very large values of the rotational angular momentum involved in hot calculations and/or heavy molecules. Typically, energy levels have to be computed up to $J \approx 80$ to predict CF_4 room temperature spectra.

In the next step, we apply our two-step procedure to reduce the length D_1^{Γ}. First, the Hamiltonian (9) is partitioned as $H = H_v + H_{vr}$ and the eigenvalue equation $H_v\Psi_v^{\Gamma} = E_v^{\Gamma}\Psi_v^{\Gamma}$ is variationally solved with a primitive $F_{\kappa}^{\Gamma}(n)$ and the vibrational eigensolutions $\{E_v^{\Gamma(n)}, \Psi_v^{\Gamma(n)}\}$ are stored. Here n is chosen to properly converge all necessary energy levels. The resulting anharmonic vibrational eigenfunctions Ψ_v for a given block Γ read

$$\Psi_v^{\Gamma(n)} = \sum_{\mathscr{F}(n)} c_i^{\Gamma} \Phi_{iv}^{\Gamma}. \tag{A2}$$

Let us assume now that there exist a basis set $F_{\kappa_2}(m) \in \mathscr{F}_r^{\Gamma}$ ($m < n$) of size $\dim(\mathscr{F}_r^{\Gamma}) = D_2^{\Gamma}$ with $D_2^{\Gamma} \ll D_1^{\Gamma}$ such that the $J > 0$ vibration–rotation calculations are feasible. This amounts to project the anharmonic solutions (A2) onto the reduced subspace $\mathscr{F}_r^{\Gamma}$ where the "r" index stands for the reduced subspace. The resulting set of anharmonic vibrational reduced functions $\{\Psi_v^{(n\to m)}\}$ are given by

$$\mathscr{G}\mathscr{P}^{(m)}\Psi_v^{\Gamma(n)} = \Psi_v^{\Gamma(n\to m)} = \sum_{\mathscr{F}_r(m)} c_i'^{\Gamma} \Phi_{iv}^{\Gamma} \tag{A3}$$

and will be used for further $J > 0$ calculations. Here $\mathscr{P}^{(m)}$ is a projector onto the $\mathscr{F}_r(m)$ subspace and $\mathscr{G}$ is the Gram–Schmidt transformation.

Note that in the range of the observed energy levels the new expansion coefficients $c_i'^{\Gamma}$ are quite close to the initial c_i^{Γ} coefficients so that we can write $H_v\Psi_v^{\Gamma(n\to m)} \approx E_v^{\Gamma(n)}\Psi_v^{\Gamma(n\to m)}$. Finally the size D_2^{Γ} of the reduced basis is of the order $\sim 10^2$–10^3 (only few Mb of memory for the J = 0 problem) and the largest matrices to be diagonalized will be of size $\sim 10^5$ for high J values. Thus the full problem has been scaled by several orders of magnitude.

Appendix B: cut-off criteria in variational spectra calculations

Hamiltonian expansion and vibrational basis set

Initially, the Eckart–Watson nuclear Hamiltonian was expanded up to the total powers $p = (m_{k\sigma} + n_{k\sigma})$ in the tensor representation of eqn (7) and (8) with a subsequent reduction to p' = 7 as described in ref. 77. In the case of methane, it has been shown that such (p = 14 → p' = 7) Hamiltonian reduction provides good convergence in energies up to five-quanta vibrational overtones and combination states.[88] Also, agreement within $\sim$0.1 cm^{-1} was obtained with respect to independent variational calculations using the exact kinetic energy operator and curvilinear internal coordinates.[109] The corresponding tensor expansion (9) contains 23 548 rovibrational terms.

The vibrational basis $F_{\mathbf{k}}(n = 14)$ in eqn (A1) was used with the weighting coefficient vector κ = (1.05;1;1.18;1) to select an appropriate number of bending/stretching functions. The larger matrix to be considered in this step is of size $D_1^{F_2} \sim 55\,000$. For $J > 0$ calculations, these functions have been further reduced to eqn (A3) using m = 7 and the κ_1's chosen below.

To ensure the completeness of our line lists at least up to T = 296 K, a global set of variational vibration–rotation energy levels was computed up to J = 80. Let us recall that our recent hot methane calculations were practically converged at J = 67

for $T > 2000$ K. Much higher J-values required for CF_4 made calculations very demanding though the wavenumber range considered in this work will not be as extended as that of methane. Thus a heavy molecule such as CF_4 requires the same amount of computational effort at room temperature as lighter systems such as methane for very hot temperatures.

Since the sizes of the matrices become larger as J increases, we have adopted a strategy similar to that of ref. 32, 34, 78 and 87 which consists of partitioning the rovibrational problem as follows: calculations were performed using the weighting coefficient vector κ_1 = (1.38;1;1.38;1) up to J = 60 and κ_1 = (1.3;1;1.5;1.1) from J = 61 to up to 80. For the first case, the larger vibrational basis is of size $D_2^{F_2} \sim 500$ while for the second case, we have $D_2^{F_2} \sim 390$. Combining also with the parameter %VSS defined in ref. 88, the size of the rovibrational blocks (J,$C = F$), $F = F_1$ or F_2, to be diagonalized does not exceed 100 000 such that it can be easily managed with a standard modern PC.

Cut-off for intensities

For the present study, because of the increasing number of vibrational excitations involved in overtones and combination bands, we concluded that it was reasonable to limit the line list to the spectral range [0–4000] cm^{-1}. Beyond 4000 cm^{-1}, the line intensities are very weak and not clearly observable in existing experimental spectra (such as PNNL cross-section libraries[103]) due to the decreasing signal/noise ratio. Because the CF_4 room-T calculations are almost as demanding as the CH_4 high-T calculations, we have adopted a strategy as that of ref. 34 producing full theoretical spectra. Completeness of line lists is essential for appropriate atmospheric retrievals. At least three criteria are required to properly converge opacity calculations (or integrated intensities in other words). The first one is to choose a J_{max} that can be evaluated from the temperature dependence of the partition function. Here the value J_{max} = 80 turns out quite reasonable to converge $Q(296)$ and also the integrated intensities for various spectral ranges (see Fig. 5). For example, in the range 550–700 cm^{-1}, the integrated intensity up to J = 80 is 4.010 cm per molecule. At J_{max} = 75, this value is 3.970 cm per molecule and at J_{max} = 79, we have 4.005 cm per molecule. So we have convergence errors of 1.03% and 0.13% at J_{max} = 75 and J_{max} = 79, respectively. Similarly, in the 980–1220 cm^{-1} region, we have errors of 0.43% and 0.07% if J_{max} = 75 and 79, respectively. Higher J values will not bring additional opacity at 296 K. The second one is to choose the maximum lower state energy cut-off that will govern the total number of HB transitions. After some trial tests, we have chosen $E_{low}^{max} = [2700 + 0.19J(J+1)]$ cm^{-1}. This value permitted to account for all HBs that produce a significant contribution to the integrated intensities in the range from T = 80 K to T = 400 K. Finally last but not least is to choose the intensity cut-off I_{cut}^{max}. This value is crucial and will control the total number of lines in the construction of the final line lists. Following ref. 34, we introduce wavenumber-dependent intensity cut-off functions $I^{cut}(W)$ by splitting the whole wavenumber range W = 0–4000 cm^{-1} in fifteen intervals R_k (k = 1,...,15), each one roughly corresponding to the most abundant band systems (see Fig. 4). To define $I^{cut}(W)$ for each interval, the function should mimic the shape of the absorption spectrum so that we can write $I^{cut}(W) = \sum_k I_k^{cut}(W)$ (see Fig. 4, black curve). Appropriate analytical forms are given by Gaussian functions as $I_k^{cut}(W) = I_k^{(m)} \exp(-2(W - W_k^{(m)})/{A_k}^2)$ where $W_k^{(m)}$ is a wavenumber corresponding to the maximum absorption in every R_k, and $I_k^{(m)}$, A_k are adjustable parameters so that the integrated intensity in each R_k converge. The $I_k^{(m)}$'s vary from 10^{-31} to 5×10^{-27} cm per molecule.

Acknowledgements

We acknowledge the support from the e-PYTHEAS project (ANR-16-CE31-0005-04), from LIA SAMIA between CNRS (France) and RFBR (Russia), from the IDRIS/CINES computer centers of France and from the computer centers Reims-Champagne-Ardenne and SKIF Siberia (Tomsk). I. C. acknowledges the support from Tomsk State University D. Mendeleev funding program. The research at the Institute of Atmospheric Optics was performed under contract Number 17-17-01170 with the Russian Scientific Foundation.

References

1 C. Scheutz, P. Kjeldsen and E. Gentil, *Waste Manage. Res.*, 2009, **27**, 716–723.
2 I. E. Gordon, L. S. Rothman, C. Hill, R. V. Kochanov, Y. Tan and P. F. Bernath, *et al.*, *J. Quant. Spectrosc. Radiat. Transfer*, 2017, **203**, 3–69.
3 N. Jacquinet-Husson, R. Armante, N. Scott, A. Chédin, L. Crépeau, C. Boutammine and A. Bouhdaoui, *et al.*, *J. Mol. Spectrosc.*, 2016, **327**, 31–72.
4 J. Marks, R. Kantamaneni, D. Pape and S. Rand, *TMS Light Met.*, 2003, 221–225.
5 J. Muhle, A. L. Ganesan, B. R. Miller, P. K. Salameh, C. M. Harth, B. R. Greally, M. Rigby, L. W. Porter, L. P. Steele, C. M. Trudinger, P. B. Krummel, S. O'Doherty, P. J. Fraser, P. G. Simmonds, R. G. Prinn and R. F. Weiss, *Atmos. Chem. Phys.*, 2010, **10**, 5145–5164.
6 M. J. Elrod, *J. Chem. Educ.*, 1999, **76**, 1702–1705.
7 A. K. Jain, B. P. Briegleb, K. Minschwaner and D. J. Wuebbles, *J. Geophys. Res.: Atmos.*, 2000, **105**, 20773–20790.
8 A. M. Jubb, M. R. McGillen, R. W. Portmann, J. S. Daniel and J. B. Burkholder, *Geophys. Res. Lett.*, 2015, **42**, 9505–9511.
9 H. Partridge and D. W. Schwenke, *J. Chem. Phys.*, 1997, **106**, 4618–4639.
10 O. Polyansky, R. Ovsyannikov, A. Kyuberis, L. Lodi, J. Tennyson and N. Zobov, *J. Phys. Chem. A*, 2013, **117**, 9633–9643.
11 V. G. Tyuterev, R. V. Kochanov, S. A. Tashkun, F. Holka and P. G. Szalay, *J. Chem. Phys.*, 2013, **139**, 134307.
12 V. Tyuterev, R. Kochanov, A. Campargue, S. Kassi, D. Mondelain, A. Barbe, E. Starikova, M. R. De Backer, P. G. Szalay and S. Tashkun, *Phys. Rev. Lett.*, 2014, **113**, 143002.

13 V. G. Tyuterev, R. V. Kochanov and S. A. Tashkun, *J. Chem. Phys.*, 2017, **146**, 064304.
14 R. Marquardt, K. Sagui, W. Klopper and M. Quack, *J. Phys. Chem. B*, 2005, **109**, 8439–8451.
15 X. Huang, D. W. Schwenke and T. J. Lee, *J. Chem. Phys.*, 2011, **134**, 044320.
16 S. N. Yurchenko, R. J. Barber and J. Tennyson, *Mon. Not. R. Astron. Soc.*, 2011, **413**, 1828–1834.
17 R. Marquardt and M. Quack, *J. Chem. Phys.*, 1998, **109**, 10628–10643.
18 A. V. Nikitin, M. Rey and V. G. Tyuterev, *Chem. Phys. Lett.*, 2011, **501**, 179–186.
19 A. V. Nikitin, M. Rey and V. G. Tyuterev, *Chem. Phys. Lett.*, 2013, **565**, 5–11.
20 P. Cassam-Chena and J. Liévin, *J. Mol. Spectrosc.*, 2013, **291**, 77–84.
21 X. G. Wang and T. Carrington, *J. Chem. Phys.*, 2014, **141**, 154106.
22 M. Majumder, S. Hegger, R. Dawes, S. Manzhos, X. G. Wang, C. Tucker, J. Li and H. Guo, *Mol. Phys.*, 2015, **113**, 1823–1833.
23 A. Owens, S. N. Yurchenko, A. Yachmenev, J. Tennyson and W. Thiel, *J. Chem. Phys.*, 2016, **145**, 104305.
24 A. V. Nikitin, M. Rey and V. G. Tyuterev, *J. Quant. Spectrosc. Radiat. Transfer*, 2017, **200**, 90–99.
25 J. Martin, T. Lee, P. Taylor and J.-P. Francois, *J. Chem. Phys.*, 1995, **103**, 2589–2602.
26 T. Delahaye, A. V. Nikitin, M. Rey, P. G. Szalay and V. G. Tyuterev, *J. Chem. Phys.*, 2014, **141**, 104301.
27 T. Delahaye, A. V. Nikitin, M. Rey, P. Szalay and V. G. Tyuterev, *Chem. Phys. Lett.*, 2015, **639**, 275–282.
28 M. Rey, T. Delahaye, A. V. Nikitin and V. G. Tyuterev, *Astron. Astrophys.*, 2016, **594**, A47.
29 M. Rey, A. V. Nikitin, Y. L. Babikov and V. G. Tyuterev, *J. Mol. Spectrosc.*, 2016, **327**, 138–158.
30 S. N. Yurchenko and J. Tennyson, *Mon. Not. R. Astron. Soc.*, 2014, **440**, 1649–1661.
31 X. Huang, D. W. Schwenke, S. A. Tashkun and T. J. Lee, *J. Chem. Phys.*, 2012, **136**, 124311.
32 M. Rey, A. V. Nikitin and V. G. Tyuterev, *Astrophys. J.*, 2014, **789**, 2.
33 S. N. Yurchenko, D. S. Amundsen, J. Tennyson and I. P. Waldmann, *Astron. Astrophys.*, 2017, **605**, A95.
34 M. Rey, A. V. Nikitin and V. G. Tyuterev, *Astrophys. J.*, 2017, **847**, 1.
35 R. Hargreaves, P. Bernath, J. Bailey and M. Dulick, *Astrophys. J.*, 2015, **813**, 1–8.
36 S. Brodersen and B. I. Zhilinskii, *J. Mol. Spectrosc.*, 1995, **169**, 1–17.
37 S. Brodersen and B. I. Zhilinskii, *J. Mol. Spectrosc.*, 1995, **172**, 303–318.
38 C. R. Bailey, J. B. Hale and J. W. Thompson, *Proc. R. Soc. A*, 1938, **167**, 555.
39 P. J. H. Woltz and A. H. Nielsen, *J. Chem. Phys.*, 1952, **20**, 307–312.
40 A. Rosenberg and G. Birnbaum, *J. Chem. Phys.*, 1968, **48**, 1396–1397.
41 I. W. Levin and T. P. Lewis, *J. Chem. Phys.*, 1970, **52**, 1608–1609.
42 C. G. Joslin, C. G. Gray and S. Singhj, *Mol. Phys.*, 1985, **54**, 1469–1489.
43 R. S. McDowell, M. J. Reisfeld, H. W. Galbraith, B. J. Krohn, H. Flicker, R. Kennedy, J. Aldridge and N. Nereson, *J. Mol. Spectrosc.*, 1980, **83**, 440–450.
44 R. S. McDowell, C. W. Patterson, C. R. Jones, M. I. Buchwald and J. M. Telle, *Opt. Lett.*, 1979, **4**, 274–276.
45 C. W. Patterson, R. S. Mcdowell and N. G. Nereson, *IEEE J. Quantum Electron.*, 1980, **16**, 1164–1169.
46 R. S. McDowell, C. W. Patterson, C. R. Jones, M. I. Buchwald and J. M. Telle, *Proc. SPIE*, 1980, **190**, 262–269.
47 M. Takami, *J. Chem. Phys.*, 1976, **71**, 4164–4165.
48 M. Takami, *J. Chem. Phys.*, 1980, **73**, 2665–2672.
49 A. S. Pine, *J. Mol. Spectrosc.*, 1982, **96**, 395–403.
50 P. Esherick, A. Owyoung and C. W. Patterson, *J. Mol. Spectrosc.*, 1981, **86**, 250–257.
51 W. Maring, J. P. Toennies, R. G. Wang and H. B. Levene, *Chem. Phys. Lett.*, 1991, **184**, 262–266.
52 M. Hartemink and H. P. Godfried, *J. Mol. Spectrosc.*, 1991, **148**, 1–12.
53 T. Gabard, A. Nikitin, J. P. Champion, G. Pierre and A. S. Pine, *J. Mol. Spectrosc.*, 1995, **170**, 431–448.
54 J. P. Champion, M. Loëte and G. Pierre, in *Spherical Top Spectra*, ed. K. N. Rao and A. Weber, Academic Press, San Diago, 1992.
55 B. I. Zhilinskii, V. I. Perevalov and V. G. Tyuterev, *Method of Irreducible Tensorial Operators in the Theory of Molecular Spectra*, Nauka, Novosibirsk, Nauka (in Russian), 1984.
56 V. Boujut, F. Michelot and C. Leroy, *Mol. Phys.*, 1998, **93**, 879–885.
57 T. Gabard, G. Pierre and M. Takami, *J. Mol. Spectrosc.*, 1995, **85**, 735–744.
58 V. G. Tyuterev, Y. L. Babikov, S. A. Tashkun, V. I. Perevalov, A. V. Nikitin, J. P. Champion, J. C. Hilico, M. Loete, C. Pierre, G. Pierre and C. Wenger, *J. Quant. Spectrosc. Radiat. Transfer*, 1994, **52**, 459–480.
59 C. Wenger and J. P. Champion, *J. Quant. Spectrosc. Radiat. Transfer*, 1998, **59**, 471–480.
60 V. Boudon, J. Mitchell, A. Domanskaya, C. Maul, R. Georges, A. Benidar and W. G. Harter, *Mol. Phys.*, 2011, **109**, 2273–2290.
61 V. Boudon, D. Bermejo and R. Z. Martínez, *J. Raman Spectrosc.*, 2013, **44**, 731–738.
62 M. Carlos, O. Gruson, C. Richard, V. Boudon, M. Rotger, X. Thomas, C. Maul, C. Sydow, A. Domanskaya, R. Georges, P. Soulard, O. Pirali, M. Goubet, P. Asselin and T. R. Huet, *J. Quant. Spectrosc. Radiat. Transfer*, 2017, **201**, 75–93.
63 D. Papousek, Z. Papouskova and D. P. Chong, *J. Phys. Chem.*, 1995, **99**, 15387–15395.
64 X. G. Wang, E. L. Sibert III and J. M. L. Martin, *J. Chem. Phys.*, 2000, **112**, 1353–1366.
65 N. Vogt, J. Demaison and H. D. Rudolph, *Mol. Phys.*, 2014, **112**, 2873–2883.
66 A. C. Jeannotte II, C. Marcott and J. Overend, *J. Chem. Phys.*, 1978, **68**, 2076–2080.

67 S. Brodersen, *J. Mol. Spectrosc.*, 1995, **145**, 331–351.
68 T. J. Lee, J. M. L. Martin and P. R. Taylor, *J. Chem. Phys.*, 1995, **102**, 254–261.
69 H. Tachikawa, *J. Phys. B: At., Mol. Opt. Phys.*, 2000, **33**, 2367–2376.
70 G. D. Purvis III and R. J. Bartlett, *J. Chem. Phys.*, 1982, **76**, 1910–1918.
71 T. H. Dunning Jr., *J. Chem. Phys.*, 1989, **90**, 1007–1023.
72 K. A. Peterson and T. H. Dunning Jr., *J. Chem. Phys.*, 2002, **117**, 10548–10560.
73 A. V. Nikitin, M. Rey and V. G. Tyuterev, *J. Chem. Phys.*, 2016, **145**, 114309.
74 M. Reiher and A. Wolf, *J. Chem. Phys.*, 2004, **121**, 10945–10956.
75 A. V. Nikitin, M. Rey, A. Rodina, B. M. Krishna and V. G. Tyuterev, *J. Phys. Chem. A*, 2016, **17**, 8983–8997.
76 K. Kim and C. Woo Park, *J. Mol. Struct.*, 1987, **161**, 297–309.
77 M. Rey, A. V. Nikitin and V. G. Tyuterev, *J. Chem. Phys.*, 2012, **136**, 244106.
78 M. Rey, A. V. Nikitin and V. G. Tyuterev, *Phys. Chem. Chem. Phys.*, 2013, **15**, 10049–10061.
79 A. V. Nikitin, M. Rey, J. P. Champion and V. Tyuterev, *J. Quant. Spectrosc. Radiat. Transfer*, 2012, **113**, 1034–1042.
80 E. B. Wilson, J. C. Decius and P. C. Cross, *Molecular Vibrations*, 1955.
81 D. Papousek and M. R. Aliev, *Molecular vibrational-rotational spectra*, 1982.
82 A. G. Yagola, I. V. Kochikov, G. M. Kuramshina and Y. A. Pentin, *Inverse problems of vibrational spectroscopy*, VSP, The Netherlands, 1999.
83 C. Wenger and J. Champion, *J. Quant. Spectrosc. Radiat. Transfer*, 1998, **53**, 471–480.
84 J. K. G. Watson, *Mol. Phys.*, 1968, **15**, 479–490.
85 M. Rey, A. V. Nikitin and V. G. Tyuterev, *J. Chem. Phys.*, 2014, **141**, 044316.
86 L. C. Biederharn and J. D. Louck, *Angular momentum in quantum physics*, Cambridge University press, New York, 1985.
87 M. Rey, A. V. Nikitin and V. G. Tyuterev, *J. Phys. Chem. A*, 2015, **119**, 4763–4779.
88 M. Rey, A. V. Nikitin and V. G. Tyuterev, *J. Quant. Spectrosc. Radiat. Transfer*, 2015, **164**, 207–220.
89 A. Nikitin, J. P. Champion and V. G. Tyuterev, *J. Mol. Spectrosc.*, 1997, **182**, 72–84.
90 M. Rey, A. V. Nikitin, B. Bézard, P. Rannou, A. Coustenis and V. G. Tyuterev, *Icarus*, 2018, **303**, 114–130.
91 S. N. Yurchenko, A. Yachmenev and R. I. Ovsyannikov, *J. Chem. Theory Comput.*, 2017, **13**, 4368–4381.
92 M. Rey, V. Boudon, C. Wenger, G. Pierre and B. Sartakov, *J. Mol. Spectrosc.*, 2003, **219**, 313–325.
93 H. Levene and D. Perry, *J. Chem. Phys.*, 1983, **79**, 4397–4406.
94 T. Carrington, in *Methods for computing ro-vibrational energy levels*, ed. J. Leszczynski and M. K. Shukla, Springer Science, 2016, pp. 135–149.
95 A. Leclerc and T. Carrington, *Chem. Phys. Lett.*, 2016, **644**, 183–188.
96 X. G. Wang and T. Carrington, *J. Chem. Phys.*, 2016, **144**, 204304.
97 G. Avila and T. Carrington, *J. Chem. Phys.*, 2017, **482**, 3–8.
98 G. Avila and T. Carrington, *J. Chem. Phys.*, 2017, **147**, 064103.
99 E. Castro, G. Avila, S. Manzhos, J. Agarwal, H. F. Schaefer and T. Carrington, *Mol. Phys.*, 2017, **115**, 1775–1785.
100 A. Leclerc, P. S. Thomas and T. Carrington, *Mol. Phys.*, 2017, **115**, 1740–1749.
101 T. Carrington, *J. Chem. Phys.*, 2017, **146**, 120902.
102 M. Dubernet-Tuckey, B. Antony, Y. Ba, Y. Babikov, K. Bartschat and V. Boudon, *et al.*, *J. Phys. B: At., Mol. Opt. Phys.*, 2016, **49**, 074003.
103 T. J. Johnson, R. L. Sams and S. W. Sharpe, *Proc. SPIE*, 2004, **5269**, 159–167.
104 L. R. Brown, K. Sung, D. C. Benner, V. M. Devi, V. Boudon, T. Gabard, C. Wenger, A. Campargue, O. Leshchishina, S. Kassi, D. Mondelain, L. Wang, L. Daumont, L. Régalia, M. Rey, X. Thomas, V. G. Tyuterev, O. M. Lyulin, A. V. Nikitin, H. M. Niederer, S. Albert, S. Bauerecker, M. Quack, J. J. O'Brien, I. E. Gordon, L. S. Rothman, H. Sasada, A. Coustenis, M. A. H. Smith, T. Carrington, X.-G. Wang, A. W. Mantz and P. T. Spickler, *J. Quant. Spectrosc. Radiat. Transfer*, 2013, **130**, 201–219.
105 V. I. Perevalov, V. Tyuterev and B. I. Zhilinskii, *Chem. Phys. Lett.*, 1984, **104**, 455–461.
106 V. Tyuterev, J. P. Champion, G. Pierre and V. I. Perevalov, *J. Mol. Spectrosc.*, 1986, **120**, 49–78.
107 V. Tyuterev, S. Tashkun, M. Rey, R. Kochanov, A. Nikitin and T. Delahaye, *J. Phys. Chem. A*, 2013, **117**, 13779–13805.
108 A. Owens, S. N. Yurchenko, A. Yachmenev and W. Thiel, *J. Chem. Phys.*, 2015, **143**, 244317.
109 A. V. Nikitin, M. Rey and V. G. Tyuterev, *J. Chem. Phys.*, 2015, **142**, 094118.

Preliminary analysis of the interacting pentad bands ($\nu_2 + 2\nu_4, \nu_2 + \nu_3, 4\nu_2, \nu_1 + 2\nu_2, 2\nu_1$) of CF_4 in the 1600 – 1800 cm^{-1} region

M. Mattoussi, M. Rey, M. Rotger, A.V. Nikitin, I. Chizhmakova, X. Thomas, H. Aroui, S. Tashkun, V.G. Tyuterev

J. Quant. Spectrosc. Radiat. Transfer., 226, (2019)

Journal of Quantitative Spectroscopy & Radiative Transfer 226 (2019) 92–99

Contents lists available at ScienceDirect

Journal of Quantitative Spectroscopy & Radiative Transfer

journal homepage: www.elsevier.com/locate/jqsrt

Preliminary analysis of the interacting pentad bands ($\nu_2+2\nu_4$, $\nu_2+\nu_3$, $4\nu_2$, $\nu_1+2\nu_2$, $2\nu_1$) of CF_4 in the 1600 – 1800 cm^{-1} region

M. Mattoussi[a], M. Rey[a,*], M. Rotger[a], A.V. Nikitin[b], I. Chizhmakova[c], X. Thomas[a], H. Aroui[d], S. Tashkun[b], Vl.G. Tyuterev[a,c]

[a] GSMA, UMR CNRS 7331, University of Reims Champagne Ardenne, Moulin de la Housse B.P. 1039, Cedex Reims F-51687, France
[b] V.E. Zuev Institute of Atmospheric Optics, Russian Academy of Sciences, 1, Akademichesky Avenue, 634055 Tomsk, Russian Federation
[c] Laboratory of Quantum Mechanics of Molecules and Radiative Processes, Tomsk State University, 36 Lenin Avenue, Tomsk 634050, Russia
[d] LDMMP, ENSIT, University of Tunis, 5 Av Taha Hussein, Tunis 1008, Tunisia

ARTICLE INFO

Article history:
Received 28 November 2018
Revised 16 January 2019
Accepted 16 January 2019
Available online 17 January 2019

Keywords:
CF_4
Tensorial formalism
ab initio
Infrared spectrum
Line positions and intensities

ABSTRACT

The Fourier transform spectrum of CF_4 in the 1600–1800 cm^{-1} was recorded in Reims by using a White-type multi-pass cell to provide a path length of 8.262 m. In the present work, all spectrum analyses and fits were realized using the MIRS software based on tetrahedral tensorial formalism. By combining non-empirical contact transformation Hamiltonians for line positions and *ab initio* ro-vibrational normal-mode predictions for line intensities, we are able to achieve a simultaneous fit of effective Hamiltonian and dipole moment parameters of several cold and hot bands of CF_4. Hamiltonian operator was expanded up to the sixth order for the ground state and for the $\{\nu_2+2\nu_4, \nu_2+\nu_3, 4\nu_2, \nu_1+2\nu_2, 2\nu_1\}$ pentad. 1831 line positions were fitted to RMS of 1.5X10^{-3} cm^{-1}. The standard deviation for line intensities for the cold bands $\{\nu_2+2\nu_4, \nu_2+\nu_3, 4\nu_2, \nu_1+2\nu_2, 2\nu_1\}$ is of 1.1% and of 8% and 5% for the hot band transitions $\{2\nu_2+2\nu_4-\nu_2, 2\nu_2+\nu_3-\nu_2\}$ and $\{\nu_2+3\nu_4-\nu_4, \nu_2+\nu_3+\nu_4-\nu_4\}$, respectively.

1. Introduction

Tetrafluoromethane CF_4 appears to be of vast industrial, environmental and economical interest. For these reasons, the ro-vibrational spectroscopy of this molecule was a subject of several theoretical and experimental studies. CF_4 belongs to the group of perfluorocarbons (PFCs) which designates the chemicals composed of carbon and fluorine only. These species predominantly CF_4 are extremely stable, inoffensive for the stratospheric ozone layer but powerful greenhouse gases (GHGs). This molecule is found among the longest-lived atmospheric trace gases because of its great chemical stability with an estimated lifetime of more than 50,000 years [1,2]. In addition, it seems to be the most abundant PFC in the stratosphere. Infrared high spectral resolution solar occultation spectrometer lead to an abundance of 70.45 ±3.40 ppt [3]. Because of this atmospheric persistence, CF_4 is regulated by the Kyoto Protocol of the United Nations Framework Convention on Climate Change (UNFCCC) [4–6] as a substance whose atmospheric concentration should be supervised and reduced. Besides its natural origin [7–9], the second source of CF_4 is linked to aluminium production and to the manufacturing of semiconductor [10]. The spectroscopic databases like HITRAN [11,12] or GEISA [13,14] only contain a limited range of data for CF_4, without intensity analysis. The spectroscopy of CF_4 which is essential for quantitative measurement in the atmosphere still remains relatively poorly studied because of the complexity of analyses. Some detailed high-resolution studies exist, however they mostly concern line positions. This was the case of the analysis of the ν_3 fundamental with the $2\nu_3$ overtone [15] and the interaction of this stretching state with the $2\nu_4$ overtone [16]. Recent work was already dedicated to the analysis of some rovibrational bands of this molecule including some hot bands around 1283 cm^{-1} [17], the data being included in the Dijon database [18]. First accurate and complete *ab initio* based line lists for CF_4 up to 400 K in the range 0–4000 cm^{-1} have been recently published by the Reims–Tomsk groups [19], resulting in 2 billion rovibrational transitions. In Ref. [19], although the variationally-predicted were not computed at the spectroscopic accuracy, the error on line intensities was only of few % allowing a correct global description of the overtones and combination bands up to 6 vibrational quanta validated by direct comparisons with experimental PNNL spectra.

* Corresponding author.
E-mail address: michael.rey@univ-reims.fr (M. Rey).

https://doi.org/10.1016/j.jqsrt.2019.01.018
0022-4073/

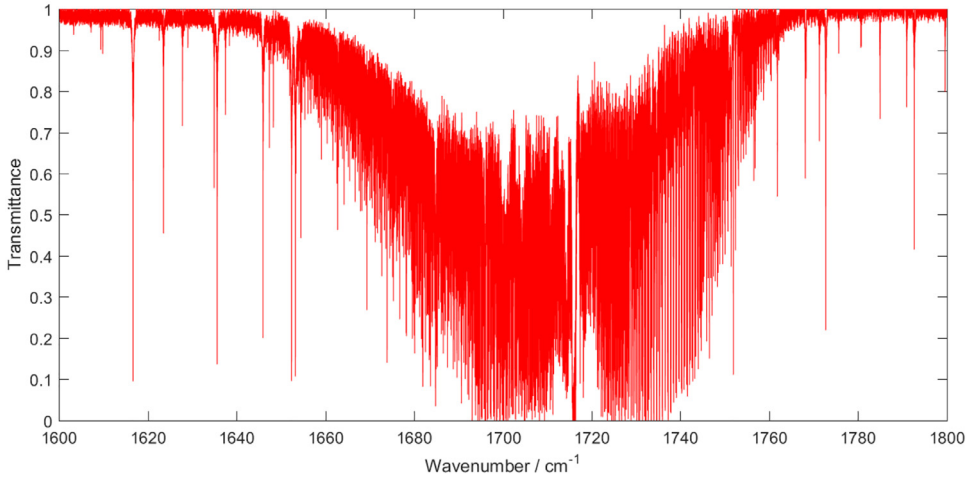

Fig. 1. Transmittance spectrum of CF_4, recorded at 294 K at a pressure of 9.93 Torr in the spectral range between 1600 and 1800 cm^{-1}.

In this work, we report the analysis of rovibrational interacting pentad bands $(\nu_2+2\nu_4, \nu_2+\nu_3, 4\nu_2, \nu_1+2\nu_2, 2\nu_1)$ of this molecule, in order to obtain a reliable simulation of CF_4' atmospheric absorption in the region between 1600–1800 cm^{-1}, including the most significant hot bands. The study of this system of bands requires the investigation of various vibrational fundamentals, combinations and harmonics bands. For the first time, high resolution analysis was made by combining spectroscopic effective models and information provided by accurate *ab initio* potential energy (PES) and dipole moment (DMS) surfaces both for line positions and line intensities.A non-empirical effective Hamiltonian was built from a PES by applying high-order contact-transformations (CT) [20,21]. For the line intensities, some effective dipole moment parameters have been adjusted directly on the *ab initio* intensities [19]. Section 2 describes the experimental data used, while Section 3 reviews some basic principles concerning the theoretical model for tetrahedral molecules used for our analysis and presents the obtained results.

2. Experimental details

Spectra measurements were carried out with the Fourier Transform Spectrometer (FTS) of GSMA laboratory [22]. The CF_4 spectrum was recorded at room temperature over the range 1600–1800 cm^{-1}, with a spectral resolution of 0.003 cm^{-1} (maximum optical path length of 2.99 m). This experimental setup was equipped with a globar source, a CaF_2 beam splitter and a HgCdTe detector. A White-type multi-pass cell with a basis length of 2 m was used to provide a path length of 8.262 m. The pressure in the cell was maintained at 9.93 Torr. The spectrum was obtained by co-adding and averaging 289 one-sided interferometer scans in order to achieve a sufficient signal-to-noise ratio. The diaphragm diameter was set to 4.5 mm. Wavenumber calibration was carried out using residual of ten water lines with intensities in the range 2×10^{-19} - 2×10^{-20} cm/molecule.

The detailed experimental conditions are listed in Table 1, and an overview of transmittance spectrum of the $(\nu_2+2\nu_4, \nu_2+\nu_3, 4\nu_2, \nu_1+2\nu_2, 2\nu_1)$ pentad is plotted in Fig. 1.

Table 1
Experimental details.

Spectral range (cm^{-1})	1600–1800
Resolution (cm^{-1})	0.003
Source	Globar
Separator	CaF_2
Detector	HgCdTe
Cell	White multi-pass
Optical Path (m)	8.262
Temperature (K)	294
Pressure (Torr)	9.93
Aperture diameter (mm)	4.5

3. Spectra analysis and modeling

3.1. Theoretical methods

The aim of the present work is the detailed analysis of the pentad system composed of five bands, namely $\nu_2+2\nu_4$, $\nu_2+\nu_3$, $4\nu_2$, $\nu_1+2\nu_2$ and $2\nu_1$ in the spectral range 1600–1800 cm^{-1} using a specific spectroscopic model (see also section 4.2). The absorption in this range is dominated by $\nu_2+\nu_3$ with the band center near 1717 cm^{-1}. The complexity of CF_4 vibrational states is outlined in Fig. 2 where the scale on the right panel represents sublevel with their symmetry type of the pentad split into 14 different components. The ν_2+2ν_4 vibrational band has 6 vibrational sublevels ofA_1, A_2, 2E, F_1 and F_2 symmetry types, the $\nu_2+\nu_3$ band has 2 sublevels (F_1, F_2), $4\nu_2$ has 3 sublevels of symmetryA_1 and 2E, $\nu_1+2\nu_2$ has 2 sublevels (A_1,E) and $2\nu_1$ has one upper state vibrational level of A_1 symmetry.

The infrared tetrafluoromethane spectra are known to be very complex due to the high tetrahedral symmetry of CF_4 which causes degeneracies and quasi-degeneracies of the vibration modes and large and complicated resonance interactions because of the inter-modes coupling. Note that such a line-by-line analysis from a judicious combination of effective and *ab initio* models - both for line positions and line intensities - was not yet available in this spectral interval. In order to extend rovibrational analyses of experimental spectra, we used a tensorial formalism with vibrational extrapolation [23,24] including supplementary information derived from *ab initio* PES/DMS and first-principles calculations. These *ab initio* variational line lists are available in the TheoReTS information system [25]. Significant recent advance in *ab initio* PES, DMS and in rotationally resolved variational spectra calculations reported by Rey et al. [19] permitted identification of the most important bands in this range. But, many weak transitions remained not yet assigned.

The rovibrational model for line-by-line analysis is built by admitting that the vibrational energy levels of CF_4 can be gathered in a series of polyads. In the framework of this theory, an effective Hamiltonian (EH) for all the considered polyads was constructed from high-order contact transformations (CT) to eliminate inter-

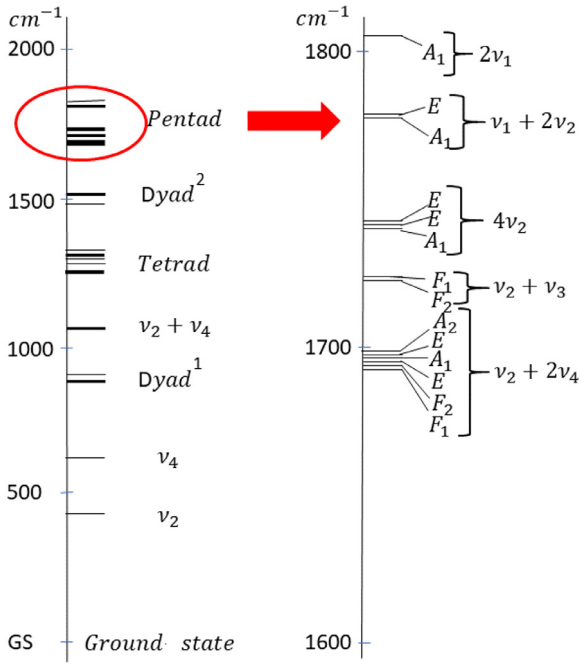

Fig. 2. Scheme of vibrational level patterns of the CF_4 polyads (left side) and vibrational sublevels of the part of the pentad system corresponding to ro-vibrational bands analyzed in this work. At the right hand side panel, symmetry type (T_d irreducible representations) of vibration sublevels, vibrational ranking numbers within the pentad and the corresponding vibrational bands are given. The first dyad is composed of [$2\nu_2$, ν_1], the tetrad is composed of [$2\nu_4$, ν_3, $3\nu_2$, $\nu_1 + \nu_4$] and the second dyad is composed of [$\nu_1 + \nu_2$, $2\nu_2 + \nu_4$].

polyad interaction terms in the rovibrational Hamiltonian (transform completely the Hamiltonian to a block-diagonal form) [20,21]. This approach allows a fairly precise characterization of resonance coupling terms to avoid the ambiguity of purely empirical EH models [26,27]. The effective Hamiltonian operator $\widetilde{H}$ adapted to the polyad structure of the CF_4 is constructed as the sum of contributions appropriate to the various polyads designed by P_k (k=0, 1,..., k,...), P_0 being the ground state (GS). This effective Hamiltonian is expressed as (see Fig. 2)

$$\begin{aligned}\widetilde{H} &= \sum \widetilde{H}_{\{P_k\}} = \widetilde{H}_{\{P_0\}} + \widetilde{H}_{\{P_1\}} + \ldots + \widetilde{H}_{\{P_k\}} + \ldots \\ &= \widetilde{H}_{\{P_0\}} + \widetilde{H}_{\{\nu_2\}} + \widetilde{H}_{\{\nu_4\}} + \widetilde{H}_{\{Dyad1\}} + \widetilde{H}_{\{\nu_2+\nu_4\}} + \widetilde{H}_{\{Tetrad\}} \\ &\quad + \widetilde{H}_{\{Dyad2\}} + \widetilde{H}_{\{Pentad\}} \end{aligned} \quad (1)$$

The terms of this expansion gather operators specific to the successive polyads in the representation of the irreducible tensor operators (ITO) [24,28,29]. They are written as a linear combination of rovibrational operators $T^{\Omega(K,n\Gamma_r)\Gamma_1\Gamma_2\Gamma_v}_{\{n_s\}\{m_s\}}$ as

$$\widetilde{H}_{\{P_k\}} = \sum_{\text{all indices}} t^{\Omega(K,n\Gamma_r)\Gamma_1\Gamma_2\Gamma_v}_{\{n_s\}\{m_s\}} T^{\Omega(K,n\Gamma_r)\Gamma_1\Gamma_2\Gamma_v}_{\{n_s\}\{m_s\}}. \quad (2)$$

In this equation, the t's are the corresponding adjustable parameters to be determined. All the indices represent the intermediate quantum numbers and symmetries. Here T refers to a rovibrational operator expressed as a tensor product between rotational and vibrational operators as

$$T^{\Omega(K,n\Gamma_r)\Gamma_1\Gamma_2\Gamma_v}_{\{n_s\}\{m_s\}} = \beta\left(R^{\Omega(K,n\Gamma_r)} \otimes {}^{\varepsilon}V^{\Gamma_1\Gamma_2\Gamma_v}_{\{n_s\}\{m_s\}}\right)^{(A_1)}. \quad (3)$$

Rotational operators $R^{\Omega(K,n\Gamma_r)}$ are the usual symmetry-adapted irreducible tensor operators (ITO) for spherical top molecules [23,24,30–34]. The upper index Ω is the rotational degree in the molecular frame components J_x, J_y and J_z; K is the tensor rank relative to the full rotation group $O(3)$, n is a multiplicity index and Γ_r (=A_1, A_2, E, F_1 or F_2) is the rotational symmetry in the T_d point group. The vibrational ITOs are constructed by recursive coupling of elementary creation a^+ and annihilation a operators for each of the four normal modes. ε is the parity in conjugate momenta with the condition $\varepsilon = (-1)^{\Omega}$ and Γ_1 and Γ_2 are the symmetries of vibrational operators; n_s and m_s are the degrees in the a^+ and a operators. Here, β is a numerical factor, equal to $[\Gamma_1]^{1/2}(-\sqrt{3}/4)^{\Omega/2}$ if $(K, n\Gamma_r) = (0, 0A_1)$, and 1 otherwise. Since the Hamiltonian is totally symmetric, we have necessary $\Gamma_r = \Gamma_v$. The order of the individual terms in T is defined as $\sum_s(n_s + m_s) + \Omega - 2$. Orientation of the ITOs in the chain $O(3) \supset T_d$ has been described in details in Ref. [35].

In order to perform intensity calculation, the dipole moment operator is built in the same way as the effective Hamiltonian operator. Its components μ_Θ ($\Theta = X, Y$ or Z) in the laboratory fixed frame (LFF) are linked to the components μ_θ ($\theta = x, y$ or z) in the molecule fixed frame (MFF) as

$$\mu_\Theta = \sum_\theta \lambda_{\Theta\theta}\mu_\theta, \quad (4)$$

where $\lambda_{\Theta\theta}$ are the direction cosines. The transformed LFF components can be expressed in terms of the MFF transformed components as

$$\widetilde{\mu}_\Theta = \frac{1}{2}\sum_\theta(\lambda_{\Theta\theta}\widetilde{\mu}_\theta + \widetilde{\mu}_\theta\lambda_{\Theta\theta}), \quad (5)$$

where the MFF effective dipole moment is of symmetry F_2 with its three components $\widetilde{\mu}_\theta$ expanded as a series of rovibrational operators [23,36]

$$\widetilde{\mu}_\theta^{(F_2)} = \sum_{\{i\}} \widetilde{\mu}^{\{i\},\Gamma}\left(R^{\Omega(K,n\Gamma_r)} \otimes {}^{\varepsilon}V^{\Gamma_1\Gamma_2\Gamma_v}_{\{n_s\}\{m_s\}}\right)^{(F_2)}_\theta. \quad (6)$$

Here $\widetilde{\mu}^{\{i\},\Gamma}$ are the effective dipole moment parameters to be determined. A way to determine these parameters will be described in the Section 3.2.2. Note that the order of the individual terms of the dipole moment is $\sum_s(n_s + m_s) + \Omega - 1$.

3.2. Analysis and discussion

3.2.1. Line positions

Line-by-line analysis and assignments of experimental spectra are known to be tedious and difficult tasks. They are usually based on empirical models for the polyads of close states where line positions are generated from empirically-fitted effective Hamiltonians (EH). Using a vibrational extrapolation scheme, we simulate the spectrum by considering the polyad P_0, which contains the GS level and the polyad P_7 containing the ν_2+$2\nu_4$, $\nu_2 + \nu_3$, $4\nu_2$, ν_1+$2\nu_2$ and $2\nu_1$ levels as the upper polyad. To obtain a result with a precision comparable with the experimental accuracy, the effective Hamiltonian was expanded up to the sixth order. As a starting point, we needed a first estimation of the tensorial parameters. That permitted a correct description of the experimental spectrum at a given temperature. Starting with the best possible set of parameters permits to identify a large number of observed line positions. Here as a first guess, the *ab initio* based EH parameters obtained via the CT method were used and further refined after various iterations by increasing the number of assigned lines. This supplied realistic estimations for the rovibrational coupling parameters between various bands of a given polyad that are responsible for the intensity perturbations due to accidental resonances. This first set of parameters allowed a preliminary simulation. In what follows, parameters for ν_2, ν_4, ($2\nu_2$, ν_1) dyad, $\nu_2 + \nu_4$, ($2\nu_4$, ν_3, $3\nu_2$, ν_1) tetrad and ($2\nu_2 + \nu_4$, $\nu_1 + \nu_4$) dyad states will be fixed to the "*ab initio*" values derived from CTs. That means that only

the parameters for the ground state and ($\nu_2 + \nu_4$, $\nu_2 + \nu_3$, $4\nu_2$, ν_1+$2\nu_2$, $2\nu_1$) are adjusted. Spectrum simulations, line assignments and the fitting process were carried out using the MIRS [37,38] and SpectrAssign softwares based on an iterative semi-automatized comparison of synthetic and experimental spectra. The T_d formalism is implemented in MIRS that thus provides all vibrational and rotational quantum numbers. The SpectrAssign program was used for assignments and visualization. It allows a simultaneous display of predicted lines from MIRS output and of an experimental spectrum. A limited number of observed lines were assigned by comparing the positions and intensities of the observed and simulated lines calculated from the initial values of the spectroscopic parameters. Afterwards, new assignments were made leading to a new set of fitted tensorial parameters. This process was performed iteratively until no more lines could be assigned.

Finally, among the 618 parameters included in the sixth order effective Hamiltonian, only 48 have been fitted. The root mean square (RMS) deviation of the IR data is very satisfactory. In Fig. 3, we present an overview of the pentad region. It compares the observed spectrum with the calculated one at the same experimental conditions by using our final set of parameters in the region 1600–1800 cm^{-1} dominated by the $\nu_2 + \nu_3$ combination band. As shown in this figure, calculated and observed spectra are in very good agreement. As can be seen in Fig. 4, different zooms reveal the precision obtained of calculated positions in the*R* and *P*-branches though weaker lines belonging to hot bands need to be still improved. Note that the *Q*-branch has an unresolved structure due to a tremendous number of overlapping lines making assignments very complicated. In order to keep the total number of adjusted parameters reasonable and to make the model "stable" when slightly changing parameters, an important part of the non-diagonal resonance parameters have been kept fixed to their theoretical values generated from the PES [19] in a manner similat to that described for the methane molecule [23]. Although the *ab initio* values for non-diagonal parameters are approximations, they describe the resonance couplings in a quite qualitatively correct way. On the other hand, an empirical "blind' ' fitting of a big set of effective polyad Hamiltonian parameters to rovibrational energies is known as a mathematically poorly defined inverse problem [26,27]. Purely empirical approach could improve a root-mean-square deviation on line positions, but it often results in wrong values of interaction parameters and thus wrong intensity extrapolations. The accurate theoretical calculations of resonance coupling parameters from *ab initio* PES and of the corresponding intensities are difficult tasks.

According to this preliminary study, we were able to assign 1831 line positions, belonging mainly to the $\nu_2 + \nu_3$ combination band, with a root mean square deviation of 1.590×10^{-3} cm^{-1}. Nevertheless, a large part of the transitions remained unassigned. A complete modelling of all bands in this region will require more assignments of both hot and cold transitions. Number of assigned transitions per band depends on the inherent intensity of the band and on the degree of interaction with other states. Fig. 5 shows the residual defined by the difference between the observed and calculated wavenumbers versus *J*. It gives a global idea of the quality of the fit. We note that the data are well distributed on the scale of the *J* values. It allowed to make sure that the rovibrational energy levels are well sampled and that the results of the fit are reliable. Fig. 6 presents the resulting calculated reduced upper state energies vs *J* showing the mixtures between the vibrational sub-levels.

3.2.2. Line intensities

Tetrafluoromethane has the same tetrahedral geometry as methane but the main difference is that the CF_4 molecule is heavier and consequently has much lower vibrational modes and much higher *J*-levels are populated. This leads to a considerable number of IR-active transitions belonging to hot bands that make the experimental spectra more complicated to analyse. Rey et al. [19] showed that the CF_4 spectra could be described from (i) a set of strong lines responsible for the strongest absorption features and (ii) of a kind of quasi-continuum formed by an accumulation of very week overlapping lines (see figure of [19]). This situation is quite similar to that observed in hot methane spectra at $\approx$ 1000–1200 K [39]. Because the infrared spectra of CF_4 are very congested, no single line intensity measurements were made. Almost all the observed lines result from overlapping of several transitions. To overcome such a difficulty, we have adopted a strategy quite different from "usual" spectroscopic studies. It consists in fitting the effective dipole moment parameters directly on the variationally-determined *ab initio* intensities. In other words, the variational line list built in Ref. [19] was taken as an "observed" line list for the present work. To our knowledge, this procedure has never been applied before for such a complex

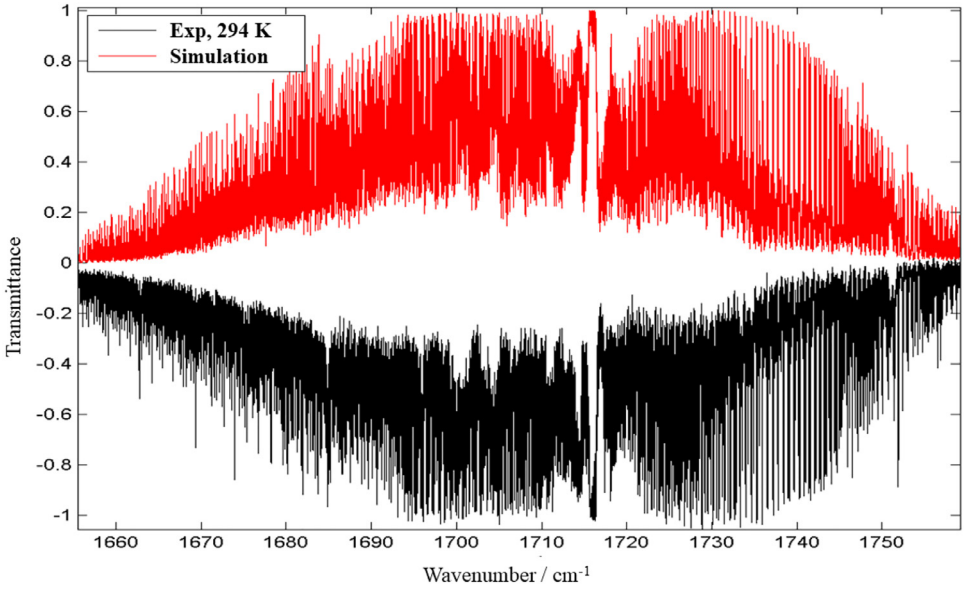

Fig. 3. Comparaison between experimental and simulated spectra of CF_4 at 294 K.

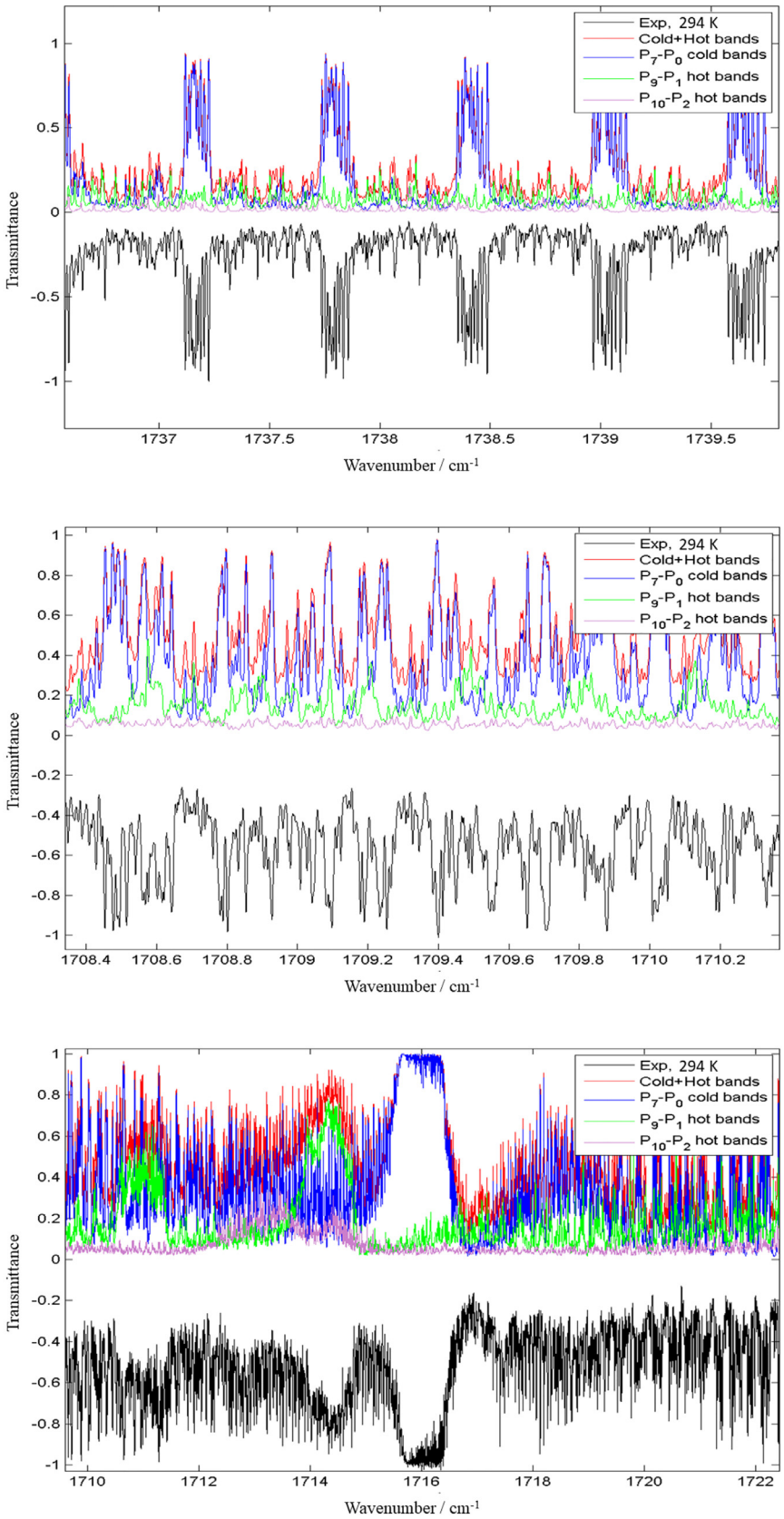

Fig. 4. Detailed comparison of the *R*, *P* and *Q*-branches between the observed spectrum and the simulation.

Table 2
Summary of the intensity fit statistics of hot and cold bands.

Bands		J_{max}	Parameters	Assignments	St. Deviation (%)
Hot Bands	$\{2\nu_2+2\nu_4-\nu_2,\ 2\nu_2+\nu_3-\nu_2\}$	35	28	1871	8
	$\{\nu_2+3\nu_4-\nu_4,\ \nu_2+\nu_3+\nu_4-\nu_4\}$	30	34	21,779	5
Cold Bands	$\{\nu_2+2\nu_4,\ \nu_2+\nu_3,\ 4\nu_2,\ \nu_1+2\nu_2,\ 2\nu_1\}$	70	16	36,896	1.1

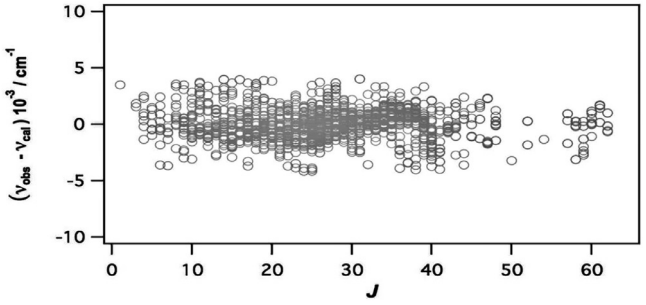

Fig. 5. Observed minus calculated wavenumbers versus J for the pentad obtained using the tensorial model. We have a lack of assignments between $J = 50$ and $J = 60$ because of the complexity of the CF_4 spectrum in this region.

Table 3
Effective dipole moment parameters for the pentad $\{\nu_2+2\nu_4,\ \nu_2+\nu_3,\ 4\nu_2,\ \nu_1+2\nu_2,\ 2\nu_1\}$.

	Tensorial nomenclature		Parameter value
	Rotational	Vibrational	
1	$R\ 0(0,\ 0A_1)$	0000 0102	−3.1864538041E−04
2	$R\ 0(0,\ 0A_1)$	0000 0110	9.2315030571E−03
3	$R\ 1(1,\ 0F_1)$	0000 0102	1.2645029053E−06
4	$R\ 1(1,\ 0F_1)$	0000 0102	−1.5390407345E−06
5	$R\ 1(1,\ 0F_1)$	0000 0102	−1.0548647219E−06
6	$R\ 1(1,\ 0F_1)$	0000 0102	1.2126152550E−06
7	$R\ 1(1,\ 0F_1)$	0000 0102	1.5140232527E−06
8	$R\ 1(1,\ 0F_1)$	0000 0110	−1.2529078490E−05
9	$R\ 1(1,\ 0F_1)$	0000 0110	2.2076230400E−05
10	$R\ 1(1,\ 0F_1)$	0000 1200	2.2577731112E−05
11	$R\ 2(2,\ 0E)$	0000 0110	1.5222082012E−08
12	$R\ 2(2,\ 0F_2)$	0000 0110	−1.6089425075E−08
13	$R\ 2(0,\ 0A_1)$	0000 0110	−1.5434076560E−08
14	$R\ 2(2,\ 0E)$	0000 0110	−2.6796194562E−09
15	$R\ 2(2,\ 0F_2)$	0000 0110	−4.8524933639E−09
16	$R\ 2(2,\ 0F_2)$	0000 2000	−2.7018916009E−06

five-atomic molecular system. The improvement of hot bands intensity modelling will be necessary to achieve a more detailed assignment in the region between 1600 and 1800 cm^{-1} because many other bands belonging to upper polyads e.g. $\{2\nu_2+2\nu_4-\nu_2,\ 2\nu_2+\nu_3-\nu_2,\ \nu_2+3\nu_4-\nu_4,\ \nu_2+\nu_3+\nu_4-\nu_4\}$ contribute to the absorption. Detailed statistics on this fit are listed in Table 2. The obtained effective dipole moment parameters for each band summarized in Tables 3–5 rely on tensorial formalism notations. Fig. 7 presents the resulting comparison between experiment and simulation, with a nice agreement.

4. Conclusion

In this work, we have built a tensorial model that permitted for the first time a detailed analysis of the $(\nu_2+2\nu_4,\ \nu_2+\nu_3,\ 4\nu_2,\ \nu_1+2\nu_2,\ 2\nu_1)$ band system of CF_4 by combining non-empirical CT Hamiltonian, *ab initio* based variational predictions and experimental information. The present analysis supplies a first accurate and

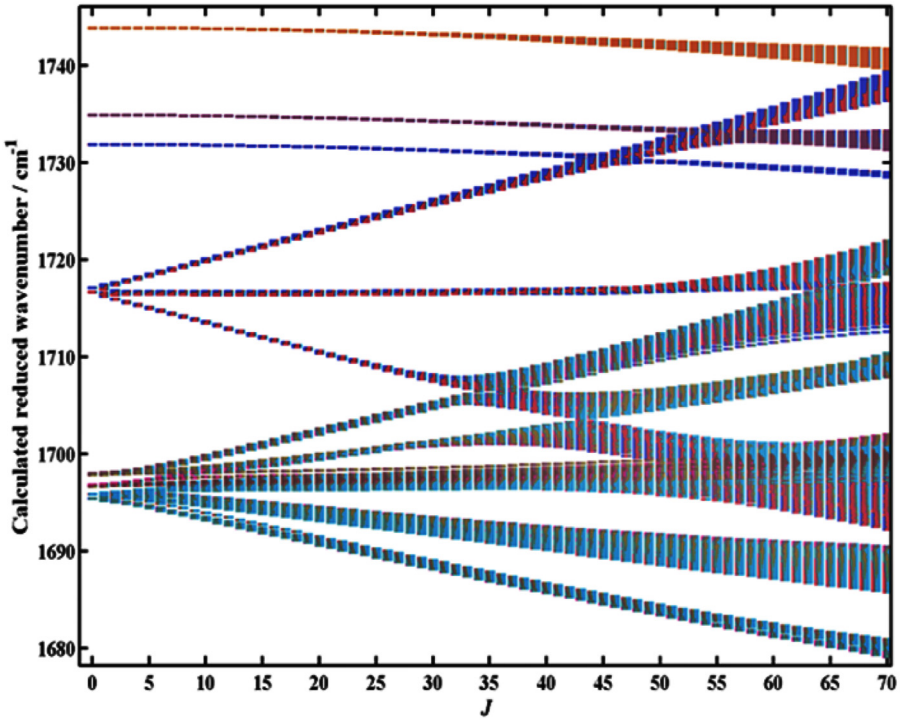

Fig. 6. Calculated reduced rovibrational energy levels of CF_4 transitions from 1600 to 1800 cm^{-1} up to $J = 70$. Various colors correspond to mixing coefficients of normal mode wavefunctions due to resonance interactions.

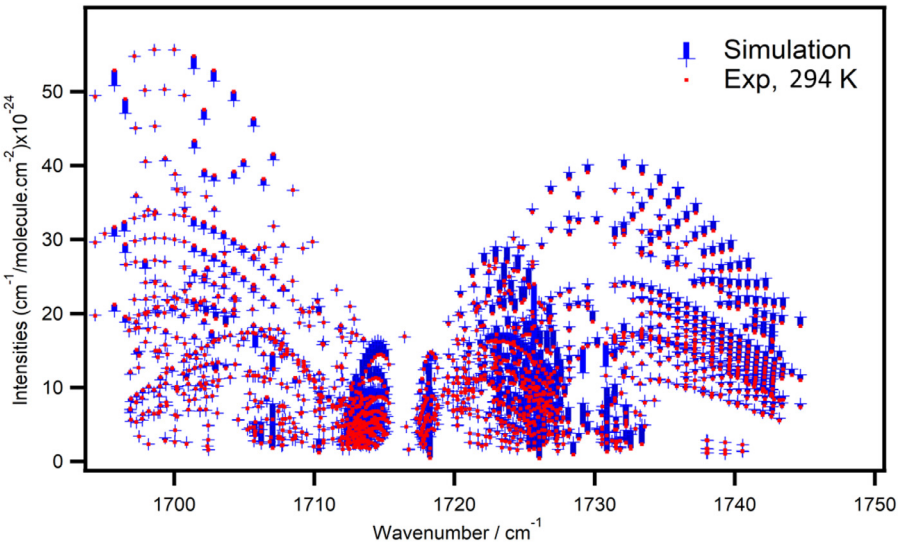

Fig. 7. Observed and calculated intensities in (cm^{-1}/molecule.cm^{-2}) vs line positions in (cm^{-1}) for the pentad transitions.

Table 4
Effective dipole moment parameters for the $\{2\nu_2+2\nu_4-\nu_2, 2\nu_2+\nu_3-\nu_2\}$ bands.

	Tensorial nomenclature		Parameter value
	Rotational	Vibrational	
1	R 0(0, $0A_1$)	0100 0202	3.9825129095E−04
2	R 0(0, $0A_1$)	0100 0210	8.5008049280E−03
3	R 0(0, $0A_1$)	0100 0202	6.5544003405E−06
4	R 0(0, $0A_1$)	0100 0210	7.9030718238E−05
5	R 0(0, $0A_1$)	0100 0202	−4.4623481744E−04
6	R 0(0, $0A_1$)	0100 0210	1.2930872868E−02
7	R 0(0, $0A_1$)	0100 1002	−4.6917331225E−03
8	R 0(0, $0A_1$)	0100 1010	2.4241217720E−03
9	R 1(1, $0F_1$)	0100 0210	−1.4446087275E−05
10	R 1(1, $0F_1$)	0100 0210	2.0583793143E−05
11	R 1(1, $0F_1$)	0100 0210	−2.4295434890E−08
12	R 1(1, $0F_1$)	0100 0210	6.1335719221E−07
13	R 1(1, $0F_1$)	0100 0210	−1.8777757468E−05
14	R 1(1, $0F_1$)	0100 0210	3.0644918638E−05
15	R 1(1, $0F_1$)	0100 1002	3.2123332254E−05
16	R 1(1, $0F_1$)	0100 1002	3.4243832575E−05
17	R 1(1, $0F_1$)	0100 1002	−5.2783161222E−05
18	R 1(1, $0F_1$)	0100 1002	−2.0547145593E−05
19	R 1(1, $0F_1$)	0100 1002	3.2786033893E−06
20	R 1(1, $0F_1$)	0100 1010	4.8417050701E−04
21	R 1(1, $0F_1$)	0100 1010	2.4135565610E−04
22	R 1(1, $0F_1$)	0100 2100	6.9831133618E−05
23	R 1(1, $0F_1$)	0100 2100	2.7944989174E−04
24	R 2(2, $0E$)	0100 1010	1.1388797951E−07
25	R 2(2, $0F_2$)	0100 1010	1.6758890863E−07
26	R 2(0, $0A_1$)	0100 1010	−3.1635728036E−07
27	R 2(2, $0E$)	0100 1010	3.0201035785E−07
28	R 2(2, $0F_2$)	0100 1010	−6.7979486512E−09

Table 5
Effective dipole moment parameters for the $\{\nu_2+3\nu_4-\nu_4, \nu_2+\nu_3+\nu_4-\nu_4\}$ bands.

	Tensorial nomenclature		Parameter value
	Rotational	Vibrational	
1	R 0(0, $0A_1$)	0001 0103	4.2413135847E−04
2	R 0(0, $0A_1$)	0001 0103	2.7477468633E−05
3	R 0(0, $0A_1$)	0001 0103	5.0088447964E−04
4	R 0(0, $0A_1$)	0001 0103	−1.2620967754E−05
5	R 0(0, $0A_1$)	0001 0103	4.7003806247E−04
6	R 0(0, $0A_1$)	0001 0103	6.4939084452E−05
7	R 0(0, $0A_1$)	0001 0103	1.7797635608E−06
8	R 0(0, $0A_1$)	0001 0111	−1.5473534628E−02
9	R 0(0, $0A_1$)	0001 0111	−3.0138555124E−04
10	R 0(0, $0A_1$)	0001 0111	−1.6398372407E−05
11	R 0(0, $0A_1$)	0001 0111	2.5471384745E−04
12	R 0(0, $0A_1$)	0001 0111	7.8534831544E−05
13	R 0(0, $0A_1$)	0001 0111	−2.0691429033E−05
14	R 0(0, $0A_1$)	0001 0111	−1.9854225634E−04
15	R 1(1, $0F_1$)	0001 0111	2.2599131901E−05
16	R 1(1, $0F_1$)	0001 0111	−3.8669830582E−05
17	R 1(1, $0F_1$)	0001 0111	9.1638928149E−07
18	R 1(1, $0F_1$)	0001 0111	−6.7549134470E−07
19	R 1(1, $0F_1$)	0001 0111	2.9523535789E−07
20	R 1(1, $0F_1$)	0001 0111	9.7740749402E−07
21	R 1(1, $0F_1$)	0001 0111	−5.7925405576E−07
22	R 1(1, $0F_1$)	0001 0111	3.8835519379E−07
23	R 1(1, $0F_1$)	0001 0111	1.2693515619E−06
24	R 1(1, $0F_1$)	0001 0111	1.1521893674E−06
25	R 1(1, $0F_1$)	0001 0111	−5.5755866620E−08
26	R 1(1, $0F_1$)	0001 0111	−4.1284363860E−07
27	R 1(1, $0F_1$)	0001 0111	−4.6669243132E−07
28	R 1(1, $0F_1$)	0001 0111	4.8599003861E−07
29	R 1(1, $0F_1$)	0001 0111	5.2493460965E−08
30	R 1(1, $0F_1$)	0001 0111	−6.2965529693E−07
31	R 1(1, $0F_1$)	0001 0111	−8.3742085981E−07
32	R 1(1, $0F_1$)	0001 0111	−7.7632490926E−07
33	R 1(1, $0F_1$)	0001 0111	1.2083069804E−06
34	R 1(1, $0F_1$)	0001 0111	−6.9909391873E−07

complete description of the infrared high-resolution spectrum of CF_4 in the region 1600–1800 cm^{-1}. The final set of effective Hamiltonian/dipole moment parameters allows to reproduce simultaneously (i) quite accurately the cold bands and (ii) in a qualitative manner the main hot band transitions. The global fit of parameters and calculation of infrared spectrum was carried out with the MIRS and SpectrAssign softwares. Assignments was made up to J_{max} = 70 and a set of 48 tensorial parameters has been adjusted. The accuracy of the final empirically optimized calculated line list is satisfactory. We have obtained a root mean square deviation RMS of about 1.590×10^{-3} cm^{-1} for 1831 cold transitions. The standard deviation for line intensities for the cold bands $\{\nu_2+2\nu_4, \nu_2+\nu_3, 4\nu_2, \nu_1+2\nu_2, 2\nu_1\}$ is of 1.1%, with respect to the *ab initio* intensities, while, for the hot bands $\{2\nu_2+2\nu_4-\nu_2, 2\nu_2+\nu_3-\nu_2\}$ and $\{\nu_2+3\nu_4-\nu_4, \nu_2+\nu_3+\nu_4-\nu_4\}$, the standard deviation is of ≈ 8% and 5%, respectively. The main objective of this study was to construct a CF_4 line list for various applications. This final list will include new assignments in the forthcoming versions of the spectroscopic HITRAN and GEISA databases. The line list for the assigned transitions is available as supplementary material to this paper. By using cold spectra (< 200 K), future works will consist

to both improve the present region and extend analysis to other spectral ranges on the basis of the present results.

Acknowledgments

The research at the V.E. Zuev Institute of Atmospheric Optics was performed under contract No 17-17-01170 with the Russian Scientific Foundation. Support from the French national LEFE/INSU CNRS program, from the academic A.D. Mendeleev program of Tomsk State University, from the French-Russian associated laboratory LIA "SAMIA" and from computing centers (ROMEO Champagne-Ardenne; IDRIS CNRS France) is acknowledged.

Supplementary material

Supplementary material associated with this article can be found, in the online version, at doi:10.1016/j.jqsrt.2019.01.018.

References

[1] Ravishankara A, Solomon S. Turnipseed a and warren r, atmospheric lifetimes of long-lived halogenated species. Science 1993;259:194–9.
[2] Morris RA, Miller TM, Viggiano A, Paulson JF, Solomon S, Reid G. Effects of electron and ion reactions on atmospheric lifetimes of fully fluorinated compounds. J Geophys Res Atmos 1995;100:1287–94.
[3] Rinsland CP, Mahieu E, Zander R, Nassar R, Bernath P, Boone C, Chiou LS. Long-term stratospheric carbon tetrafluoride CF_4 increase inferred from 1985–2004 infrared space-based solar occultation measurements. Geophys Res Lett 2006;33.
[4] Harnisch J, Höhne N. Comparison of emissions estimates derived from atmospheric measurements with national estimates of HFCs, PFCs and SF_6. Environ Sci Pollut Res 2002;9:315–19.
[5] Harnisch J, de Jager D, Gale J, Stobbe O. Halogenated compounds and climate change. Environ Sci Pollut Res 2002;9:369–74.
[6] Boudon V, J-P C, Gabard T, Pierre G, Loëte M, Wenger C. Spectroscopic tools for remote sensing of greenhouse CH_4, CF_4 and SF_6. Environ Chem Lett 2003;1:86–91.
[7] Harnisch J, Borchers R. Effect of natural tetrafluoromethane. Nature 1996;384:32.
[8] Harnisch J, Borchers R, Fabian P, Maiss M. Tropospheric trends for CF_4 and c_2f_6 since 1982 derived from SF_6 dated stratospheric air. Geophys Res Lett 1996;23:1099–102.
[9] Deeds DA, Vollmer MK, Kulongoski JT, Miller BR, Mühle J, Harth CM, Izbicki JA, Hilton DR, Weiss RF. Evidence for crustal degassing of CF_4 and SF_6 in mojave desert groundwaters. Geochim Cosmochim Acta 2008;72:999–1013.
[10] Khalil MAK, Rasmussen RA, Culbertson JA, Prins JM, Grimsrud EP, Shearer MJ. Atmospheric perfluorocarbons. Environ Sci Technol 2003;37:4358–61.
[11] Rothman LS, Gordon IE, Babikov Y, Barbe A, Benner DC, Bernath PF, Birk M, Bizzocchi L, Boudon V, Brown LR, et al. The HITRAN 2012 molecular spectroscopic database. J Quant Spectrosc Radiat Transf 2013;130:4–50.
[12] Gordon IE, Rothman LS, Hill C, Kochanov RV, Tan Y, Bernath PF, Birk M, Boudon V, Campargue A, Chance K, et al. The HITRAN 2016 molecular spectroscopic database. J Quant Spectrosc Radiat Transf 2017;203:3–69.
[13] Jacquinet-Husson N, Crepeau L, Armante R, Boutammine C, Chédin A, Scott N, Crevoisier C, Capelle V, Boone C, Poulet-Crovisier N, et al. The 2009 edition of the GEISA spectroscopic database. J Quant Spectrosc Radiat Transf 2011;112:2395–445.
[14] Jacquinet-Husson N, Armante R, Scott A, Chédin A, Crépeau L, Boutammine C, Bouhdaoui A, Crevoisier C, Capelle V, Boonne C, et al. The 2015 edition of the GEISA spectroscopic database. J Mol Spectrosc 2016;327:31–72.
[15] Gabard T, Pierre G, Takami M. Study of the ν_3 and $2\nu_4$ interacting states of $^{12}CF_4$. Mol Phys 1995;85:735–44.
[16] Boudon V, Mitchell J, Domanskaya A, Maul C, Georges R, Benidar A, Harter WG. High-resolution spectroscopy and analysis of the $\nu_3/2\nu_4$ dyad of CF_4. Mol Phys 2011;109:2273–90.
[17] Carlos M, Gruson O, Richard C, Boudon V, Rotger M, Thomas X, Maul C, Sydow C, Domanskaya A, Georges R, et al. High-resolution spectroscopy and global analysis of CF_4 rovibrational bands to model its atmospheric absorption. J Quant Spectrosc Radiat Transf 2017;201:75–93.
[18] Ba YA, Wenger C, Surleau R, Boudon V, Rotger M, Daumont L, et al. MecaSDa and ECaSDa: methane and ethene calculated spectroscopic databases for the virtual atomic and molecular data centre. J Quant Spectrosc Radiat Transf 2013;130:62–8.
[19] Rey M, Chizhmakova IS, Nikitin AV, Tyuterev Vl G. Understanding global infrared opacity and hot bands of greenhouse molecules with low vibrational modes from first-principles calculations: the case of CF_4. Phys Chem Chem Phys 2018;20:21008–33.
[20] Tyuterev Vl G, Tashkun SA, Seghir H. High-order contact transformations: general algorithm, computer implementation and triatomic tests. SPIE 2004;5311:164–76.
[21] Tyuterev Vl G, Tashkun S, Rey M, Kochanov R, Nikitin AV, Delahaye T. Accurate spectroscopic models for methane polyads derived from a potential energy surface using high-order contact transformations. J Phys Chem A 2013;117:13779–805.
[22] Plateaux J, Barbe A, Delahaigue A. Reims high resolution fourier transform spectrometer. data reduction for ozone. Spectrochim Acta A Mol Biomol Spectrosc 1995;51:1153–69.
[23] J-P C, Loëte M, Pierre G. Spherical top spectra. Spectroscopy of the Earth's atmosphere and interstellar medium; 1992. p. 339–422.
[24] Boudon V, J-P C, Gabard T, Loëte M, Michelot F, Pierre G, Rotger M, Wenger C, Rey M. Symmetry-adapted tensorial formalism to model rovibrational and rovibronic spectra of molecules pertaining to various point groups. J Mol Spectrosc 2004;228:620–34.
[25] Rey M, Nikitin AV, Babikov YL, Tyuterev Vl G. TheoreTS–an information system for theoretical spectra based on variational predictions from molecular potential energy and dipole moment surfaces. J Mol Spectrosc 2016;327:138–58.
[26] Tyuterev Vl G, J-P C, Pierre G, Perevalov V. Fourth-order invariant parameters for f_2 isolated fundamental states of tetrahedral molecules: the study of the ν_4 band of $^{12}CH_4$. J Mol Spectrosc 1984;105:113–38.
[27] Perevalov V, Tyuterev Vl G, Zhilinskii BI. Ambiguity of spectroscopic parameters in the case of accidental vibration-rotation resonances in tetrahedral molecules. r^2j and r^2j^2 terms for E-F_2 interacting states. Chem Phys Lett 1984;104:455–61.
[28] Nikitin AV, J-P C, Tyuterev Vl G. Improved algorithms for the modeling of vibrational polyads of polyatomic molecules: application to t_d, o_h, and c_{3v} molecules. J Mol Spectrosc 1997;182:72–84.
[29] Rey M, Nikitin AV, Tyuterev Vl G. Ab initio ro-vibrational hamiltonian in irreducible tensor formalism: a method for computing energy levels from potential energy surfaces for symmetric-top molecules. Mol Phys 2010;108:2121–35.
[30] J-P C. Développement complet de l'hamiltonien de vibration-rotation adapté à l'étude des interactions dans les molécules toupies sphériques. application aux bandes ν_2 et ν_4 de $^{12}CH_4$. Can J Phys 1977;55:1802–28.
[31] Wenger C, J-P C. Spherical top data system STDS software for the simulation of spherical top spectra. J Quant Spectrosc Radiat Transf 1998;59:471–80.
[32] Zhilinskii BI, Perevalov VI, Tyuterev Vl G. The method of irreducible tensor operators in the theory of molecular spectra. Novosibirsk Izdatel Nauka 1987.
[33] Moret-Bailly J. Calculation of the frequencies of the lines in a threefold degenerate fundamental band of a spherical top molecule. J Mol Spectrosc 1965;15:344–54.
[34] Zhilinskii BI. Reduction of rotational operators to standard form. Opt Spectrosc 1981;51:262–3.
[35] Rey M, Boudon V, Wenger C, Pierre G, Sartakov B. Orientation of $O(3)$ and $SU(2)\times C_i$ representations in cubic point groups (O_h, T_d) for application to molecular spectroscopy. J Mol Spectrosc 2003;219:313–25.
[36] Papousek D, Aliev MR. Molecular vibrational-rotational spectra. 1982.
[37] Nikitin AV, J-P C, Tyuterev Vl G. The MIRS computer package for modeling the rovibrational spectra of polyatomic molecules. J Quant Spectrosc Radiat Transf 2003;82:239–49.
[38] Nikitin AV, Rey M, J-P C, Tyuterev Vl G. Extension of the MIRS computer package for the modeling of molecular spectra: from effective to full ab initio ro-vibrational hamiltonians in irreducible tensor form. J Quant Spectrosc Radiat Transf 2012;113:1034–42.
[39] Rey M, Nikitin AV, Tyuterev Vl G. Accurate theoretical methane line lists in the infrared up to 3000 k and quasi-continuum absorption/emission modeling for astrophysical applications. Astrophys J 2017;847:105.

Potential Energy Surface of SF_6

Chizhmakova I.S., Nikitin A.V.

Atmospheric and Oceanic Optics, 32, (2019)

ISSN 1024-8560, Atmospheric and Oceanic Optics, 2019, Vol. 32, No. 6, pp. 613–618. © Pleiades Publishing, Ltd., 2019.
Russian Text © The Author(s), 2019, published in Optika Atmosfery i Okeana.

SPECTROSCOPY OF AMBIENT MEDIUM

Potential Energy Surface of SF_6

I. S. Chizhmakova[a, b, *] and A. V. Nikitin[a, **]

[a] *V.E. Zuev Institute of Atmospheric Optics, Siberian Branch, Russian Academy of Sciences, Tomsk, 634055 Russia*
[b] *Tomsk State University, Tomsk, 634050 Russia*
**e-mail: yschizhmakova@gmail.com*
***e-mail: avn@iao.ru*

Received April 17, 2019; revised April 17, 2019; accepted April 23, 2019

Abstract—For the first time, a 15-dimensional analytical form was obtained and the potential energy of the SF_6 molecule in the ground electronic state was found. An optimal grid of geometries was constructed, which, taking into account the full symmetry of the molecule, unambiguously determines the potential energy surface of the sixth order. Using the MP2 method with the cc-pVTZ base set, the potential energy surface of the fourth order was calculated.

Keywords: potential energy surface, SF_6, octahedral group

DOI: 10.1134/S1024856019060046

INTRODUCTION

Sulfur hexafluoride (or elegas) SF_6 has being investigated over forty years [1–3]. It is widely used in industry and medicine. Due to the strong absorption bands in the atmospheric transparency windows, SF_6 is a potent greenhouse gas, and its global warming potential (GWP500) is 29300 times higher than that of CO_2 [4]. The atmospheric concentration of SF_6 is small, but it is one of the most stable gaseous chemicals with an atmospheric lifetime of 3200 years [5]. According to Earth System Research Laboratory Global Monitoring Division data [6], the SF_6 concentration increased from 3.5 ppt (1995) to 9.5 ppt (2018). This rapid increase and long atmospheric lifetime can result in considerable accumulation of SF_6 in the troposphere and its important role in global climate change in the future.

The radiation properties of the long-lived heavy greenhouse gases, such as CF_4 or SF_6, are little studied. A common feature of these molecules is the relatively low frequency of oscillations [7] and a significant population of excited levels. Hence, the "hot bands" corresponding to transitions between excited vibrational states affect the IR absorption even at room temperature, which leads to complex vibrational spectra, where it is difficult to resolve isolated lines. Only a few vibrational bands of SF_6 were analyzed within limited spectral ranges in [8, 9]. For those molecules, the spectroscopic databases (for example, GEISA or HITRAN) contain no high-accuracy data on the spectral line parameters.

To simulate IR spectra and energy levels from first principles, ab initio, it is necessary to obtain the potential energy surface (PES) or the force field of a high order. These techniques are equivalent, but a technique based on an analytical PES is preferable for practical calculations. To derive an analytical expression for the PES, it is necessary to calculate the quantum-chemical energy for many geometries, the number of which is usually several orders of magnitude greater than the number of PES fitting parameters. In the case of a force field, the force constants are usually calculated by the finite difference method, and the validity of the resulting force field on a large geometric grid is rarely checked. To reduce the number of geometries used in the quantum-chemical calculations, it is necessary to take into account the symmetry of the molecule, which results in a more complex form of the PES. The SF_6 molecule has octahedral structure: the molecule is a cube with an S atom at the center and six F atoms at centers of each face (Fig. 1).

In this work, we discuss the calculation of the PES of the SF_6 molecule, which is to be used for calculations of the vibrational-rotation spectra with variational techniques. The equilibrium geometry of the SF_6 molecule is calculated, one-dimensional cross-sections are given, a grid of geometries is obtained, and a technique for PES construction is described.

1. EQUILIBRIUM GEOMETRY AND SYMMETRY COORDINATES

Several experimental and theoretical works were devoted to the study of the SF6 equilibrium geometry [10, 11]. In our work, all ab initio calculations were carried out with MOLPRO software [12] using the

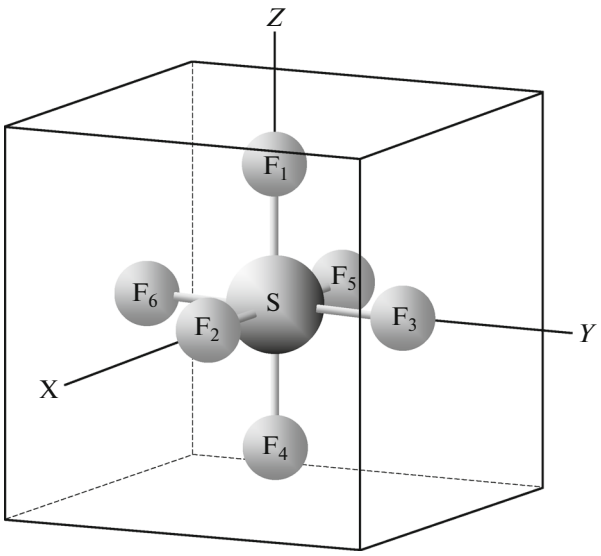

Fig. 1. Internal coordinates in the octahedral molecules.

coupled clusters (CCSD(T)) and the Meller–Plesset perturbation theory of the 2nd and 3rd orders (MP2 and MP3) [13, 14]. The CCSD(T) method successfully works for octahedral molecules [7]. This technique is based on the cluster expansion of the wave function in single and double electron excitations and takes into account a correction on the triple excited states according to perturbation theory. To calculate the equilibrium geometry, we used the correlation-consistent bases. The results obtained for optimized geometry and energy are compared in Table 1.

It is obvious that the CCSD (T)/VTZ technique overestimates the S–F bond length (5701 Å) and energy (–996.076 Hartree). Consideration of the correlation of internal electrons reduces the S–F bond length. The use of the VQZ basis improves the calculation results, which correlate with those from [16, 15], but considerably increases the PES computation time. Taking into account scalar relativistic effects, cc-pVTZ-DK does not improve the precision of description of the SF_6 equilibrium geometry. We have selected the cc-pVTZ set for further calculations as a compromise between the precision and computation time. Because of the large number of electrons, quantum-chemical methods cannot be used to obtain the SF_6 equilibrium geometry with a precision comparable with experimental measurements.

Table 1. Energies and the equilibrium lengths of the S–F bond obtained with the optimized CCSD(T) technique using different basis sets

Technique/basis set	Energy, Hartree	Equilibrium length S–F, Å
MP3/VTZ	–996.00822804	1.55952379
MP2/VTZ	–996.02881762	1.57197994
CCSD(T)/VTZ	–996.07574167	1.57015425
CCSD(T)/CVTZ	–996.79947177	1.56003654
CCSD(T)/AVTZ	–996.14253699	1.57357635
CCSD(T)/CVTZ–DK	–998.23964874	1.56042314
CCSD(T)/VQZ	–996.30894816	1.56375885
Ref. [15]		1.5647
Experimental value [16]		1.5622

Consideration of the symmetry with the use of the irreducible tensor representation lets one obtain an optimal set of atom configurations and to minimize the computation time. To calculate the 15D PES for a large grid of the equilibrium geometries, we use the geometry grid generation technique for the CH_4 molecule described in [17, 18]. This technique allows us to perform spectral-precision calculations ab initio in a wide range of energies. To parameterize all possible configurations of the SF_6 molecule, it is preferable to use polar coordinates because they are built into software packages ab initio, such as MOLPRO. The internal polar coordinates are defined in a standard way: six vectors connecting the S atom with the F atoms; six lengths of the S–F bonds $\{r_1, r_2, r_3, r_4, r_5, r_6\}$; five angles between the bonds $\{q_{12}, q_{13}, q_{14}, q_{15}, q_{16}\}$, and four torsion angles $\{t_{23}, t_{24}, t_{25}, t_{26}\}$ (see Fig. 1). The symmetry coordinates are recommended to be used for the analytical representation of PES, which are linear combinations of the internal coordinates.

A seven-atom molecule has 15 vibrational modes. However, different works report different sets of the symmetry coordinates, and most of those sets are incompatible with the method of the irreducible tensorial operators for the O_h group [19]. In this work, we use the basis elements of the O_h group (Table 2) for composing the following set of the symmetry coordinates (1)–(18).

For A_{1g} vibration:

$$S_{A_{1g}}(r) = \frac{1}{\sqrt{6}}(r_1 + r_2 + r_3 + r_4 + r_5 + r_6), \quad (1)$$

$$S_{A_{1g}}(q) = \frac{1}{\sqrt{8}}(q_{12} + q_{13} + q_{15} + q_{16} + q_{23} + q_{24} + q_{26} + q_{34} + q_{35} + q_{45} + q_{46} + q_{56}). \quad (2)$$

For E_g vibration:

$$S_{E_{ga}}(r) = \frac{1}{\sqrt{12}}(2r_1 + 2r_4 - r_2 - r_3 - r_4 - r_5), \quad (3)$$

$$S_{E_{gb}}(r) = \frac{1}{2}(r_2 - r_3 + r_5 - r_6), \quad (4)$$

$$S_{E_{ga}}(q) = \frac{1}{\sqrt{24}}(q_{12} + q_{13} + q_{15} + q_{16} + q_{24} + q_{34} + q_{45} + q_{46} - 2q_{23} - 2q_{26} - 2q_{35} - 2q_{56}), \quad (5)$$

$$S_{E_{gb}}(q) = \frac{1}{\sqrt{8}}(q_{13} + q_{16} + q_{34} + q_{46} - q_{12} - q_{15} - q_{24} - q_{45}). \quad (6)$$

Table 2. O_h group elements

Group element	C_{31}^{+}	C_{4z}^{+}	Inversion
Transformation matrix	$\begin{pmatrix}0&0&1\\1&0&0\\0&1&0\end{pmatrix}$	$\begin{pmatrix}0&-1&0\\1&0&0\\0&0&1\end{pmatrix}$	$\begin{pmatrix}-1&0&0\\0&-1&0\\0&0&-1\end{pmatrix}$
Equivalent permutations of atoms (1 to 6)	$\begin{pmatrix}1&2&3&4&5&6\\3&1&2&6&4&5\end{pmatrix}$ or (1 2 3) (4 5 6)	$\begin{pmatrix}1&2&3&4&5&6\\1&6&2&4&3&5\end{pmatrix}$ or (2 6 5 3)	$\begin{pmatrix}1&2&3&4&5&6\\4&5&6&1&2&3\end{pmatrix}$ or (14) (25) (26)

For F_{1u} vibration:

$$S_{F_{1ux}}(r) = \frac{1}{\sqrt{2}}(r_2 - r_5), \quad (7)$$

$$S_{F_{1uy}}(r) = \frac{1}{\sqrt{2}}(r_3 - r_6), \quad (8)$$

$$S_{F_{1uz}}(r) = \frac{1}{\sqrt{2}}(r_1 - r_4), \quad (9)$$

$$S_{F_{1ux}}(q) = \frac{1}{\sqrt{8}}(q_{12} + q_{23} + q_{24} + q_{26} - q_{15} - q_{35} - q_{45} - q_{56}), \quad (10)$$

$$S_{F_{1uy}}(q) = \frac{1}{\sqrt{8}}(q_{13} + q_{23} + q_{34} + q_{35} - q_{16} - q_{26} - q_{46} - q_{56}), \quad (11)$$

$$S_{F_{1uz}}(q) = \frac{1}{\sqrt{8}}(q_{12} + q_{13} + q_{15} + q_{16} - q_{24} - q_{34} - q_{45} - q_{46}). \quad (12)$$

For F_{2u} vibration:

$$S_{F_{2ux}}(q) = \frac{1}{\sqrt{8}}(q_{15} + q_{23} + q_{26} + q_{45} - q_{12} - q_{24} - q_{35} - q_{56}), \quad (13)$$

$$S_{F_{2uy}}(q) = \frac{1}{\sqrt{8}}(q_{13} + q_{26} + q_{34} + q_{56} - q_{16} - q_{23} - q_{35} - q_{46}), \quad (14)$$

$$S_{F_{2uz}}(q) = \frac{1}{\sqrt{8}}(q_{12} + q_{15} + q_{34} + q_{46} - q_{13} - q_{16} - q_{24} - q_{45}). \quad (15)$$

For F_{2g} vibration:

$$S_{F_{2gx}}(q) = \frac{1}{2}(q_{13} + q_{46} - q_{16} - q_{34}), \quad (16)$$

$$S_{F_{2gy}}(q) = \frac{1}{2}(q_{12} + q_{45} - q_{15} - q_{24}), \quad (17)$$

$$S_{F_{2gz}}(q) = \frac{1}{2}(q_{23} + q_{56} - q_{26} - q_{35}). \quad (18)$$

Radial coordinates (1), (3), (4), and (7)–(9) are compatible with those from [20]. A left-handed coordinate system is used in [21], and not all sets are given. The atomic numeration used in [22] differs from our definition in permutation (23)(56). This permutation turns the F_{1u} coordinates [22] into (7)–(12). Let S^* denote the symmetry coordinates from [22], and S, Eqs. (7)–(18). In this case, $S_x^* = S_y$, $S_y^* = S_x$, and $S_z^* = S_z$ for F_{1u}. This corresponds to the permutation of the x and y components following the permutation (23)(56). The F_{2u} and F_{2g} coordinates from [22] are connected with Eqs. (12)–(18) in the following way: $S_x^* = S_z$, $S_y^* = S_x$, and $S_z^* = S_y$. This transformation does not correspond to the permutation (23)(56). In this case, the following expressions are valid: for F_{2u} coordinates (13)–(16): (23)(56) $S_x = -S_y$, (23)(56) $S_y = -S_x$, (23)(56) $S_z = -S_z$; and for F_{2g} coordinates (16)–(17): (23)(56) $S_x = S_y$, (23)(56) $S_y = S_x$, (23)(56) $S_z = S_z$. The above-considered permutations correspond to the geometric interpretation of the coordinate axis shown in Fig. 1. On the other hand, the F_{2u} coordinates from [22] can be transformed following the rules (23)(56) $S_x^* = -S_x^*$, (23)(56) $S_y^* = S_z^*$, which does not correspond to the molecular configuration shown in Fig. 1 from [22]. Our F_{2u} coordinates (13)–(15) differ from those in [23]. The coordinates in [22, 23] form a full set of coordinates, but the use of them in the irreducible tensorial operators method [19] does not result in suitable solutions for the PES of the third order or higher.

The technique [18] has been used to define a unique set of geometries that describe the PES. It is based on the force field constants and lets us obtain an optimal set of the atomic configuration geometries sufficient for modeling the force field up to a certain order. In the first step, one-dimensional axial cross-sections are constructed (Fig. 2), and then the symmetry coordinates are found where the energy takes the following values: 1000, 2500, 4000, 7000, 10000, 12500, and 15000 cm^{-1}.

ANALYTICAL EXPRESSIONS FOR PES AND OPTIMAL GRID OF GEOMETRIES

The standard representation in terms of the irreducible tensorial operators [19] has been used to

derive analytical expressions for 15D PES. Three radial vibrational modes v_1–v_4 are transformed under the A_{1g} (774.5 cm^{-1}), E_g (643.3 cm^{-1}), and F_{1u} (948.1 cm^{-1}) representations; three bending modes v_4–v_6 are transformed under the F_{1u} (615.0 cm^{-1}), F_{2g} (524.0 cm^{-1}), and F_{2u} (347.7 cm^{-1}) representations. The potential function is written in terms of the irreducible tensorial operators:

$$V(R) = \Sigma_p F_p \Pi_{i\sigma} \left(S_{i\sigma}^{(\Gamma_i)}\right)^{p_{i\sigma}} = \Sigma_p F_p \times R_i^p(r_1, r_2, r_3, r_4, r_5, r_6, q_{12}, q_{13}, q_{14}, q_{15}, q_{16}, t_{23}, t_{24}, t_{25}, t_{26}), \quad (19)$$

where

$$R_i^p = \left(\left(\left[SR_{A_{1g}}\right]^{p_1} \times \left(\left[SR_{E_g}\right]^{p_2} \times \left[SR_{F_{1u}}\right]^{p_3}\right)^{C_{23}}\right)^{C} \times \left(\left[SR_{F_{1u}}\right]^{p_4} \times \left(\left[SR_{F_{2g}}\right]^{p_5} \times \left[SR_{F_{2u}}\right]^{p_6}\right)^{C_{56}}\right)^{C}\right)^{A_{1g}}. \quad (20)$$

Here $p = p_1 + p_2 + ... + p_6$ is the term degree; A_{1g}, E_g, F_{1u}, F_{2u}, and F_{2g} are the nondegenerate, double and triple degenerate irreducible representations of the O_h group; and F_p is the set of parameters for the PES, ab initio.

The number of the irreducible tensors of the A_{1g} symmetry up to the 4th, 5th, 6th, 7th, and 8th (included) order are 123, 406, 1334, 3924, and 10 994, respectively. For building the grid of geometries, all tensors were divided into several groups, each group included tensors of the same degrees p_1, p_2, p_3, p_4, p_5, and p_6. For each tensor group, a set of the symmetry degrees was found, which uniquely identified that group. After that, we obtained a possible set of the force field constants that uniquely define the PES up to the 6th order. From that set, we removed all points that coincide after any of 48 permutations of the F atoms. As a result, a grid of 6412 geometries was constructed that uniquely defined the PES up to the sixth order. The study confirms that the quantum-chemical energies for these geometries are different.

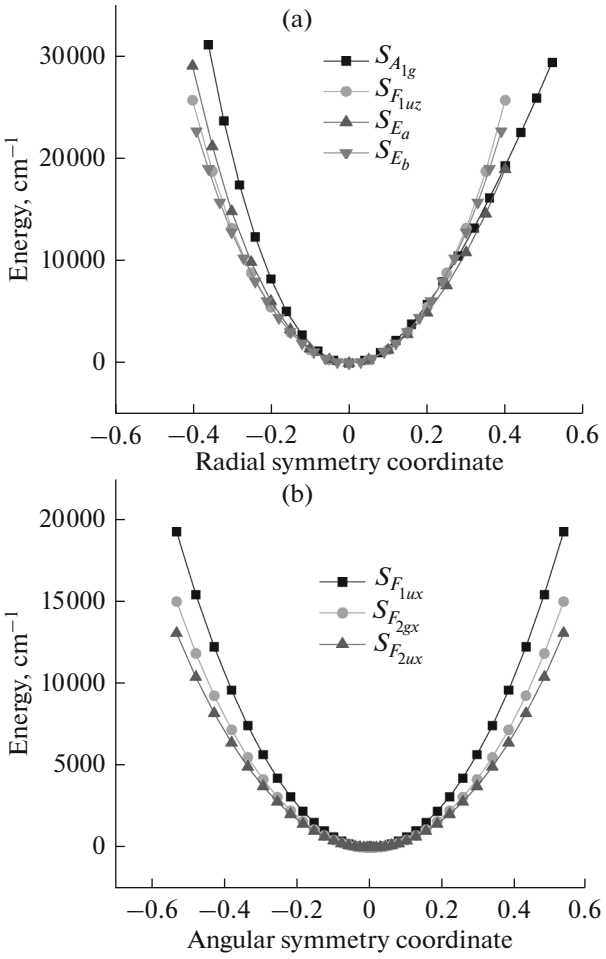

Fig. 2. One-dimensional axial cross-sections of SF_6 in the dimensionless symmetry coordinate system.

PES FITTING

The lengths r_i and the angles between bonds q_{ij} have been used as one-dimensional basis functions. As a rule, for parameterizing PES, to provide the best results using the least-squares technique, more complex one-dimensional basis functions are used. Morse functions are used for radial functions:

$$f_R(r_i) = 1 - \exp[-\alpha(r_i - r_e)], \quad (21)$$

where the parameter α depends on an approximate expression for one-dimensional radial potential

$$V_0 (1 - \exp[-\alpha(r_i - r_e)])^2; \quad (22)$$

$\alpha = 1.9$ for SF_6. The cosine function is often used for angular functions. However, by analogy with [17], the functions

$$f_A(q_{ij}) = (\cos q_{ij} - \cos q_e) + \alpha(\cos q_{ij} - \cos q_e)^2 \quad (23)$$

turned out preferable; here, $\alpha = 0.3333$. For example, the PES fitting with the hyperbolic tangent with the parameter equal to 7000 [17] as a weight function results in the following standard errors: 3.7 cm^{-1} for the cosine function and 2.3 cm^{-1} for Eq. (22). The high quality of the fourth order PES fitting proves a high rigidity of the SF_6 molecule. Figure 3 shows the dependence of the standard errors on the geometry

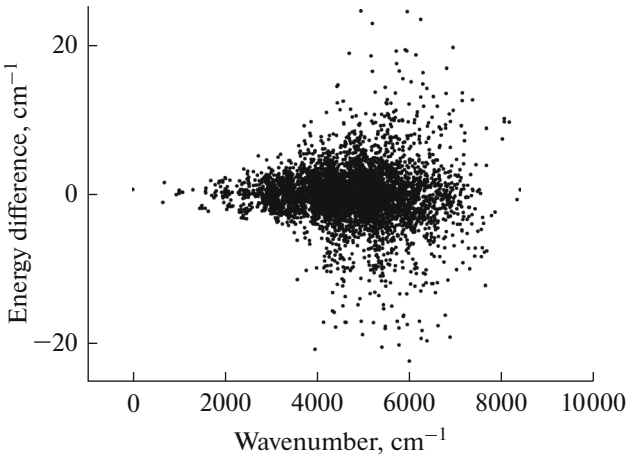

Fig. 3. Standard error of the PES fitting vs the geometry energy for SF_6, MP2/VTZ technique.

energy. We have obtained 123 PES constants using the MP2 technique with the cc-VTZ basis set.

CONCLUSIONS

In this paper, an analytical form of the SF_6 potential surface has been obtained using the VTZ basis set. This form includes 123 PES constants up to the fourth order. It is shown that the structure of one-dimensional angular functions considerably affects the PES fitting accuracy. In our further studies, we plan to calculate the PES of higher orders and improve the computation accuracy due to the use of the high-precision CCSD(T) technique with the VTZ basis set. We also plan to use the contact transformations technique [24] for modeling the PES-based effective Hamiltonian. This is to help us simplify simulation of the SF_6 spectra and include them in the information database [25].

FUNDING

The work was supported by the Russian Science Foundation (grant no. 17-17-01170).

CONFLICT OF INTEREST

The authors declare that they have no conflicts of interest.

REFERENCES

1. S. Jesse, A. J. Pedraza, and J. D. Fowlkes, "Etching-enhanced ablation and the formation of a microstructure in silicon by laser irradiation in an SF_6 atmosphere," J. Mater. Res., No. 17, 1002–1013 (2002).
2. W. M. Johnstone and W. R. Newell, "Absolute elastic differential cross sections for electron scattering from SF_6," J. Phys. B, No. 24, 473–487 (1991).
3. N. H. Malik and A. H. Qureshi, "A review of electrical breakdown in mixtures of SF_6 and other gases," IEEE Trans. Electr. Insul. **14** (1), 11–13 (1979).
4. O. Hodnebrog, M. Etminan, J. S. Fuglestvedt, G. Marston, G. Myhre, C. J. Nielsen, K. P. Shine, and T. J. Wallington, "Global warming potentials and radiative efficiencies of halocarbons and related compounds: A comprehensive review," Rev. Geophys. **51** (2), 300–378 (2013).
5. A. R. Ravishankara, S. Solomon, A. A. Turnipseed, and R. F. Warren, "Atmospheric lifetimes of long-lived halogenated species," Science **259** (5092), 194–199 (1993).
6. www.esrl.noaa.gov/?gmd/?hats/?data.html. Cited March 17, 2019.
7. M. Rey, I. S. Chizhmakova, A. V. Nikitin, and V. G. Tyuterev, "Understanding global infrared opacity and hot bands of greenhouse molecules with low vibrational modes from first-principles calculations: The case of CF_4," Phys. Chem. Chem. Phys. **20**, 21008–21033 (2018).
8. V. Boudon and D. Bermejo, "First high-resolution Raman spectrum and analysis of the ν_5," J. Mol. Spectrosc. **213**, 139–144 (2002).
9. V. Boudon, G. Pierre, and H. Burger, "High-resolution spectroscopy and analysis of the n_4 bending region of SF_6 near 615 cm^{-1}," J. Mol. Spectrosc. **205**, 304–311 (2001).
10. G. Nagarajan and D. C. Brinkley, "Statistical thermodynamics enthalpy, free energy, entropy, and heat capacity of some hexafluorides of octahedral symmetry," Z. Naturforsch., A: Phys. Sci., 1658–1665 (1971).
11. V. P. Spiridonov, Y. I. Tarasov, B. K. Novosadov, O. Y. Nikitin, and I. V. Maslov, "A practical method for diffraction analysis of equilibrium geometries molecules without refined force fields," J. Mol. Struct., 463–470 (1997).
12. H. -J. Werner, P. J. Knowles, G. Knizia, F. R. Manby, M. Schutz, P. Celani, W. Gyorffy, D. Kats, T. Korona, R. Lindh, A. Mitrushenkov, G. Rauhut, K. R. Shamasundar, T. B. Adler, R. D. Amos, S. J. Bennie, A. Bernhardsson, A. Berning, D. L. Cooper, M. J. O. Deegan, A. J. Dobbyn, F. Eckert, E. Goll, C. Hampel, A. Hesselmann, G. Hetzer, T. Hrenar, G. Jansen, C. Koppl, S. J. R. Lee, Y. Liu, A. W. Lloyd, Q. Ma, R. A. Mata, A. J. May, S. J. McNicholas, W. Meyer, T. F. III. Miller, and M. E. Mura, MOLPRO, version 2009.1, a package of *ab initio* programs. http://www.molpro.net. Cited March, 17, 2019.
13. R. J. Bartlett, "Many-body perturbation theory and coupled cluster theory for electron correlation in molecules," Ann. Rev. Phys. Chem. **32**, 359–401 (1981).
14. M. Head-Gordon, J. A. Pople, and M. J. Frisch, "MP2 energy evaluation by direct methods," Chem. Phys. Lett. **153** (6), 503–506 (1988).
15. W. Eisfeld, "Highly accurate determination of the electron affinity of SF_6 and analysis of structure and photodetachment spectrum of SF_6," J. Chem. Phys., No. 134, 054303 (2011).
16. B. R. Miller and M. Fink, "Mean amplitudes of vibration of SF_6 and intramolecular multiple scattering," J. Chem. Phys., No. 75, 5326–5328 (1981).

17. A. V. Nikitin, M. Rey, and V. G. Tyuterev, "Rotational and vibrational energy levels of methane calculated from a new potential energy surface," Chem. Phys. Lett. **501**, 179–186 (2011).
18. A. V. Nikitin, "Calculation of vibrational energy levels of symmetric molecules from potential energy surface," Opt. Atmos. Okeana **28** (5), 379–390 (2015).
19. B. I. Zhilinskii, V. I. Perevalov, and V. G. Tyuterev, *Method of Irreducible Tensorial Operators in the Theory of Molecular Spectra* (Nauka, Novosibirsk, 1987), p. 1–13 [in Russian].
20. L. Halonen and M. S. Child, "A local mode model for tetrahedral molecules," Mol. Phys. **46**, 239–255 (1982).
21. P. N. Schatz and D. F. Hornig, "Bond moments and derivatives in CF_4, SiF_4, and SF_6 from infrared intensities," J. Chem. Phys. **21** (9), 1516–1530 (1953).
22. M. Fernandez-Gomez and J. J. Lopez-Gonzalez, "Calculation of internal valence force constants for $XY_6(O_h)$ octahedral molecules," J. Mol. Struct. **220**, 287–300 (1990).
23. T. C. W. F. Pistorius, "Potential field and force constants of octahedral molecules," J. Chem. Phys. **29** (6), 1328–1332 (1958).
24. V. G. Tyuterev, S. A. Tashkun, M. Rey, R. V. Kochanov, A. V. Nikitin, and T. Delahaye, "Accurate spectroscopic models for methane polyads derived from a potential energy surface using high-order contact transformations," J. Phys. Chem. **117**, 13779–13805 (2013).
25. M. Rey, A. V. Nikitin, Y. Babikov, and V. G. Tyuterev, "TheoReTS—An information system for theoretical spectra based on variational predictions from molecular potential energy and dipole moment surfaces," J. Mol. Spectrosc. **327**, 138–158 (2016).

Translated by O. Ponomareva

First Full-Dimensional Potential Energy and Dipole Moment Surfaces of SF6

Nikitin, A.V., Rey, M., Chizhmakova, I.S., Tyuterev, V.G.

J. Phys.Chem. A, 124, (2020)

THE JOURNAL OF PHYSICAL CHEMISTRY A

pubs.acs.org/JPCA Article

First Full-Dimensional Potential Energy and Dipole Moment Surfaces of SF_6

Andrei V. Nikitin,* Michael Rey, Iana S. Chizhmakova, and Vladimir G. Tyuterev

Cite This: https://dx.doi.org/10.1021/acs.jpca.0c02733 Read Online

ABSTRACT: A 15-dimensional analytical form for the potential energy and dipole moment surfaces of the SF_6 molecule in the ground electronic state is obtained using *ab initio* methods. In order to calculate the equilibrium S−F distance, we applied the coupled cluster CCSD(T) method and several versions of the correlation-consistent basis sets from valence triple-zeta (VTZ) and augmented valence triple-zeta (AVTZ) to core-valence quadruple-zeta (CVQZ) with Douglas−Kroll (DK) relativistic corrections that provided good agreement with an empirical equilibrium value. *Ab initio* electronic energies on 15D grids of nuclear geometries are computed using the CCSD(T) method with VTZ and CVQZ-DK basis sets. The analytical representation of the potential energy surface is determined through an expansion in symmetry-adapted products of nonlinear coordinates up to the 5th order. The influence of additional redundant coordinates on the quality of the fit was investigated. Parameters of full-dimensional dipole moment surfaces are determined up to the 4th order expansion in normal mode coordinates. For validation of *ab initio* results, the fundamental vibration frequencies and absorption cross sections of the principal sulfur hexafluoride isotopologue are calculated, giving good agreement with cold (180 K) and room temperature (296 K) experimental spectra. Absorption cross sections calculated from our preliminary line list agree much better with these observations than the simulations using SF_6 line-by-line lists constructed from effective models included in currently available spectroscopic databases.

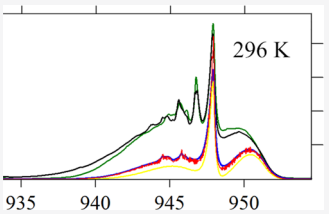

1. INTRODUCTION

Investigation of electronic structure and radiative properties of high octahedral symmetry sulfur hexafluoride (SF_6) molecule is of interest both for the theory[1−3] and for applications in many domains of industry and medicine. Because of strong absorption bands in the atmospheric transparency windows, SF_6 is a powerful greenhouse gas with the global warming potential (GWP500) 29,300 times larger than that of CO_2.[4] At present, the sulfur hexafluoride atmospheric concentration is yet small, but SF_6 is one of the most stable gaseous chemicals with an atmospheric life time of 3200 years.[5] According to the conclusions of Earth System Research Laboratory Global Monitoring Division,[6] the SF_6 concentration increased from 3.5 ppt (1995) to 9.5 ppt (2018). A rapid increase of the SF_6 concentration and its long atmospheric life time might result in a considerable accumulation of SF_6 in the troposphere. Thus, in future, sulfur hexafluoride may play an important role in the climate global changing. The radiative properties of SF_6 were insufficiently studied until now. Because of relatively low-frequency vibrations,[7] the Boltzmann population of the excited vibrational levels appears to be significant. Thus, the "hot bands" corresponded to transitions between excited vibrational states produce a considerable contribution to IR absorption even at room temperature. The ro-vibrational spectra are quite complex and crowded making it difficult to identify isolated lines in experimentally recorded absorption samples. Only few vibrational bands of SF_6 within limited spectral ranges have been studied[8−12] using the effective Hamiltonian approach. Despite many efforts, a simulation of the room-temperature SF_6 absorbance using effective spectroscopic models was not sufficiently complete. For this reason, the most advanced spectroscopic databases (as HITRAN[13] or GEISA[14]) do not contain line parameters for all necessary SF_6 bands in order to describe the absorbance at room temperature with high accuracy.

An approach based on *ab initio* potential energy surfaces (PES) and dipole moment surfaces (DMS) using variational methods for the solution of the full-dimensional nuclear motion Schrödinger equation has been successfully applied to many 4−5 atomic[7,15−22] and also to six-atomic[23−25] molecules such as C_2H_4. In[26] some calculated levels of UF_6, molecules having the same octahedral symmetry have been reported. However, high precision full-dimensional PESs and DMSs for seven-atomic molecules are still lacking in the literature.

Several works used alternative methods for the nuclear motion calculations for medium and large molecules using vibrational configuration-interaction approach or the perturbation theory (refs[27−29] and references herein). However, in most cases, the rotation states were computed for low J only and the contribution of hot bands have been neglected.

Received: March 27, 2020
Revised: July 29, 2020
Published: August 3, 2020

To compute energy levels and IR spectra beyond the harmonic oscillator approximation using *ab initio* techniques, it is necessary to obtain either the PES on a sufficiently large grid of nuclear displacements or the force field with high-order derivatives. Both techniques are often used, but for high-resolution applications, the technique based on an analytical PES determined at an extended geometrical grid has proved to produce more accurate results.[21,26,30] In the full-grid approach, the computational difficulties are related to a simultaneous account of relatively a large number of electrons (70 electrons in case of SF_6) and of a large number of degrees of freedom including representative nuclear geometries for PES and DMS parametrization. As a rule, the number of different geometries is several times bigger than the number of the fitted PES parameters. The force field technique often uses the finite difference method for calculating the force constants, and as a rule, a validity of the obtained force field could not be checked for sufficiently large nuclear displacements. To reduce the number of nuclear geometries in the electronic structure calculations, it is necessary to take into account the molecular symmetry.

This paper is devoted to first calculations of the full-dimensional PES and DMS of the SF_6 molecule and is structured as follows. Equilibrium structure at various basis sets, the coordinate choice, and the analytical model for PES and DMS surfaces are considered in Section 2, whereas *ab initio* calculations and fits are discussed in Sections 3 and 4. Calculation of the vibrational-rotation spectra using the variation techniques[31−34] shows a good agreement with experimental absorption cross sections in the range of the strongest bands of $^{32}SF_6$ and $^{34}SF_6$ isotopologues (Section 5), providing a preliminary validation of *ab initio* results.

2. EQUILIBRIUM GEOMETRY AND ANALYTICAL FORM OF PES AND DMS

The SF_6 molecule belongs to the octahedral O_h point group: at the equilibrium geometry, the molecule is a cube with the S atom at the cube center and six F atoms at centers of each edge (Figure 1). Thus, only one geometrical parameter (S−F distance) determines this equilibrium structure unambiguously. Experimental and theoretical studies of the SF_6 equilibrium geometry have been considered in.[35,36] In order to calculate the equilibrium S−F distance, we applied coupled cluster CCSD(T) method and several versions of the correlation consistent basis sets from valence triple-zeta (VTZ) and augmented valence triple-zeta (AVTZ) to core-valence quadruple-zeta (CVQZ) with Douglas−Kroll (DK) relativistic corrections. All *ab initio* calculations were carried out using MOLPRO suite of programs as implemented in the 2019.1 version.[37,38] More details concerning *ab initio* methods will be given in Section 3. A comparison of results obtained for various basis sets with some empirical values is collected in Table 1.

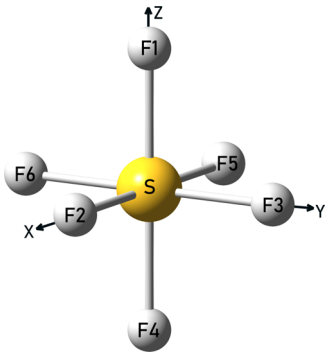

Figure 1. Equilibrium structure and the axes choice for the SF_6 molecule.

Table 1. Energies and the Equilibrium Lengths of the S−F Bound Obtained with the Optimization CCSD(T) Technique Using Various Basis Sets

method/basis set	energy, hartree	equilibrium length S−F, Å
CCSD(T)/VTZ	−996.07574167	1.57015425
CCSD(T)/CVTZ	−996.79947177	1.56003654
CCSD(T)/AVTZ	−996.14253699	1.57357635
CCSD(T)/CVTZ-DK	−998.23964874	1.56042314
CCSD(T)/VQZ	−996.30894816	1.56375885
CCSD(T)/CVQZ	−997.10132168	1.55654004
CCSD(T)/CVQZ-DK	−998.70581919	1.55702740
empirical variational[a]		1.556
ref 39		1.5647
empirical value[40]		1.5622

[a]Preliminary result of empirical optimization of S−F distance using variational calculations of rotation energies.[7,32]

Two calculations with two basis sets CVQZ and CVQZ-DK give values close to the empirical ones. In any case without additional corrections, it is impossible to calculate the equilibrium geometry with a precision better than 0.001 A°.

Various sets of the symmetry coordinates have been used in many previous works. Most of them are incompatible with our definitions of Clebsch−Gordan coefficients for the O_h group.[41,42] Here, we use the symmetric coordinates and the molecule orientation from the work.[43] Initially, we begin with linear combinations of bond lengths and bond angles, which will be further adapted using non-linear elementary morse-type and cosine-type functions as described in Section 3. At the first step, six "radial" (stretching) symmetrized coordinates were used to accommodate three irreducible representations: A_{1g}, E_g, and F_{1u}.

$$SR_{A_{1g}} = (r_1 + r_2 + r_3 + r_4 + r_5 + r_6 - 6r_e)/\sqrt{6} \quad (1)$$

$$SR_{E_g(a)} = (2r_1 + 2r_4 - r_2 - r_3 - r_5 - r_6)/\sqrt{12} \quad (2)$$

$$SR_{F_{1u}(x)} = (r_2 - r_5)/\sqrt{2} \quad (3)$$

Nine angular coordinates q_{ij} were symmetrized according to three irreducible representations: F_{1u}, F_{2g}, and F_{2u}.

$$SA_{F_{1u}(x)} = (q_{12} + q_{23} + q_{24} + q_{26} - q_{15} - q_{35} - q_{45} - q_{56})/\sqrt{8} \quad (4)$$

$$SA_{F_{2g}(x)} = (q_{13} + q_{46} - q_{16} - q_{34})/2 \quad (5)$$

$$SA_{F_{2u}(x)} = (q_{15} + q_{23} + q_{26} + q_{45} - q_{12} - q_{24} - q_{35} - q_{56})/\sqrt{8} \quad (6)$$

Some of these q_{ij} angles in Figure 1, which take $\pi/2$ values at the equilibrium, are called "adjacent" angles. Others, which take π values at the equilibrium are called "opposition" angles.

https://dx.doi.org/10.1021/acs.jpca.0c02733
J. Phys. Chem. A XXXX, XXX, XXX−XXX

The number of possible angles is bigger than the number of symmetrized angular coordinates. Hence, two types of additional symmetrized angular coordinates can be added: three coordinates S'' of symmetry A_{1g}, E_g composed of "opposition" angles q_{14}, q_{25}, and q_{36}, or three coordinates S' of the same symmetry A_{1g}, E_g from 12 "adjacent" angles

$$S''_{E_a} = (q_{25} + q_{36} - 2q_{14})/\sqrt{6}$$
$$S''_{E_b} = (q_{36} - q_{25})/\sqrt{6}$$
$$S''_{A_{1g}} = (q_{25} + q_{36} + q_{14} - 3q''_e)/\sqrt{3} \quad (7)$$

$$S'_{E_a} = (q_{12} + q_{15} + q_{34} + q_{46} + q_{13} + q_{16} + q_{24} + q_{45} - 2q_{23} - 2q_{35} - 2q_{56} - 2q_{26})/\sqrt{24}$$
$$S'_{E_b} = (q_{12} + q_{24} + q_{15} + q_{45} - q_{13} - q_{46} - q_{34} - q_{16})/\sqrt{8}$$
$$S'_{A_{1g}} = (q_{12} + q_{15} + q_{34} + q_{46} + q_{13} + q_{16} + q_{24} + q_{45} + q_{23} + q_{35} + q_{56} + q_{26} - 12q'_e)/\sqrt{12} \quad (8)$$

Here, r_e is the equilibrium values for the S−F distance and q''_e and q'_e are equilibrium values for "adjacent" or "opposite" angles. The additional angular coordinates can significantly accommodate the fit of the shape of the surface near the bottom of the potential well that will affect the energy levels and wave functions. In the case of methane, this has been shown in the ref 21.

The complete set of coordinates and the O_h group together with the matrices of irreducible representations (irrep) were reported in ref 43. As explained in ref 43, our set of internal angular coordinated is different from that of refs.[44−46] The definition of the radial symmetrized coordinates (3) coincides with that of ref 47. Matrix representation of group elements[43] (see Table 1 of Appendix 1 for matrices) coincides with that of ref 48 as given in our Table 2.

Table 2. O_h: Point Group Elements

group element	C_{31}^{+}	C_{4z}^{+}	inversion
transformation matrix	$\begin{pmatrix}0&0&1\\1&0&0\\0&1&0\end{pmatrix}$	$\begin{pmatrix}0&-1&0\\1&0&0\\0&0&1\end{pmatrix}$	$\begin{pmatrix}-1&0&0\\0&-1&0\\0&0&-1\end{pmatrix}$
equivalent permutations of F atoms (eqs 1−6)	$\begin{pmatrix}123456\\312645\end{pmatrix}$ or (132)(465)	$\begin{pmatrix}123456\\162435\end{pmatrix}$ or (2653)	$\begin{pmatrix}123456\\456123\end{pmatrix}$ or (14)(25)(26)

An account of the symmetry and the use of the irreducible tensor representation permitted obtaining an optimal non-redundant grid of nuclear geometries. One grid adapted for the analytical PES development up to the 6-th order (6412 geometries) has been constructed in the work[43] using the geometry set generation technique already applied for other symmetric molecules.[49,50] Here, we use also extended grid of 78,739 geometries that unambiguously define the PES development up to 8-th order constructed by the same technique. These two grids of geometries allowed us to carry out *ab initio* electronic energy calculations for a wide range of nuclear displacements. Initially, the grids were constructed in symmetrized coordinates (eqs 1−6), but for *ab initio* calculations both grids were recalculated in internal coordinates as in ref 43: six vectors connecting the S atom with the F atoms; six lengths of the S−F bonds $\{r_1, r_2, r_3, r_4, r_5, r_6\}$; five angles between the bonds $\{q_{12}, q_{13}, q_{14}, q_{15}, q_{16}\}$, and four torsion angles $\{t_{23}, t_{24}, t_{25}, t_{26}\}$ (see Figure 1).

In the analytical expressions for PES, it is recommended to use the symmetry coordinates that are linear combinations of the internal coordinates or of 1D elementary functions of these internal coordinates. A seven-atomic molecule has 15 vibrational degrees of freedom. The standard representation in terms of the irreducible tensor operators (ITO)[41,42] was used to obtain analytical expressions for 15-dimensional (15D) PES and DMS developments. Three stretching vibrational modes ν_1 (non-degenerate at 774.5 cm^{-1}), ν_2 (two-fold degenerate at 643.3 cm^{-1}), and ν_3 (three-fold degenerate at 948.1 cm^{-1}) transform according to the A_{1g}, E_g, and F_{1u} irreducible representations, while three triply degenerate bending modes ν_4, ν_5, and ν_6 transform under the F_{1u} (615.0 cm^{-1}), F_{2g} (524.0 cm^{-1}), and F_{2u} (347.7 cm^{-1}) representations. The analytic potential function is written in terms of the ITO

$$V(R) = \sum_{i,p} F_{ip} \boldsymbol{R}_i^{\,p}(r_1, r_2, r_3, r_4, r_5, r_6, q_{12}, q_{13}, q_{14}, q_{15}, q_{16}, t_{23}, t_{24}, t_{25}, t_{26}) \quad (9)$$

where each $\boldsymbol{R}_i^{\,p}$ tensor is obtained as an appropriate product of radial SR_Γ and angular SA_Γ non-linear symmetrized coordinates

$$\boldsymbol{R}_i^{\,p} = (([SR_{A_{1g}}]^{p_1} \times ([SR_{E_g}]^{p_2} \times [SR_{F_{1u}}]^{p_3})^{C_{23}})^{C'} \times ([SA_{F_{1u}}]^{p_4} \times ([SA_{F_{2g}}]^{p_5} \times [SA_{F_{2u}}]^{p_6})^{C_{56}})^{C''})^{C} \quad (10)$$

These non-linear radial SR_Γ and angular SA_Γ non-linear symmetrized coordinates involved in our PES model (eqs 9 and 10) were obtained by replacing the combinations (eqs 1−6) by the morse-type and cosine-type elementary functions in a similar way as was described in our works for the methane molecule.[21,49,51] We have tried several choices for an optimal fit to *ab initio* points. The final expressions of elementary functions used in the present work are given in the next Section 3. Here, p_j components of $p = \{p_1, ..., p_6\}$ correspond to powers of these coordinates, and $p = p_1 + p_2 + ... + p_6$ is the total power of the expansion term. The lower case index i corresponds to the set of symbols C_{23}, C_{56}, C, C′, and C″ in the summation (eq 9) that run over nondegenerate (A_{1g}), doubly (E_g), and triply degenerate (F_{1u}, F_{2u}, and F_{2g}) irreducible representations (irreps) of O_h point group. The C_{23} irrep results from the coupling of the symmetrized powers of the second and the third vibrational modes, whereas C′ stands for the irrep corresponding to the coupling of the latter product with the symmetrized power of the first vibrational mode. In a similar manner, the irrep C_{56} corresponds to the coupling of the fifth and sixth modes coupled with the fourth mode via C″. For the PES expansion, C′ = C″, so that only the final symmetry allowed type C of the $\boldsymbol{R}_i^{\,p}$ tensors is A_{1g}. Very similar expansion can be used for the DMS, but in this case, the final symmetry type C of the $R_i^{\,p}$ tensors is F_{1u}. Each combination of the symmetrized coordinate powers p_1, ..., p_6 and of the coupling irreps C_{23}, C_{56}, C, C′, and C″ form a "tree".[41,52] An ITO model for the PES or for the DMS

https://dx.doi.org/10.1021/acs.jpca.0c02733
J. Phys. Chem. A XXXX, XXX, XXX−XXX

expansion at a given total order p corresponds to the summation over various symmetry allowed trees[52] with the F_{ip} parameters fitted to *ab initio* values. If the "redundant" symmetrized coordinates of the type S' (8) or S'' (6) are included in the PES model,[43] then two more corresponding factors are added at the left-hand side of the ITO tree (eq 10).

The ITO formalism for the PES and DMS expansions can be also applied in terms of normal mode coordinates, as described in refs 31 and 32 This results in a similar expression to eq 10, where the symmetrized SR_j and angular SA_k coordinates are replaced by normal coordinates Q_t . In this work, we used the normal mode ITO representation for the dipole moment modeling and for intensity calculations because the matrix elements of the corresponding operators can be computed analytically. However, a sufficiently complete transformation from nonlinear symmetrized coordinates (eqs 1−6) to rectilinear normal coordinated Q_t in the case of SF_6 appears to be quite complicated. In this work, we obtained the corresponding relations $\{SR_j, SA_k\} \leftrightarrow Q_t$ numerically via the solution of the system of non-linear equations. A distribution of the RMS deviations of the fit of 15 normal coordinates to 15 internal symmetrized coordinates is shown in Figure 2. The

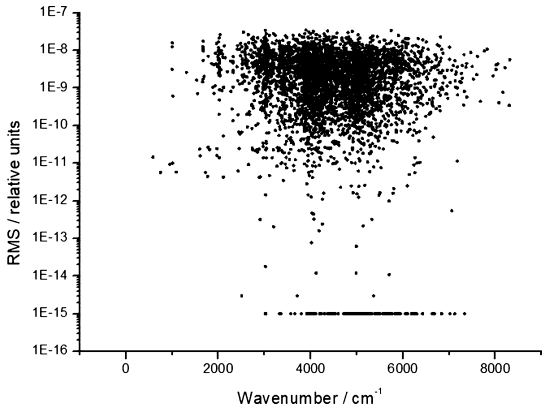

Figure 2. RMS distribution for non-linear fit of normal coordinates Q_t to internal symmetrized coordinates SR_j, SA_k.

error of the corresponding numerical solution $Q_t = Q_t(SR_j, SA_k)$ was much smaller than the precision of the fit of the analytical form (eq 10) to *ab initio* points and thus did not affect the accuracy of the final calculation of spectra.

3. PES CALCULATION

To construct the molecular PES of SF_6, we first computed a set of *ab initio* electronic energies at various molecular configurations. Equilibrium geometries and vibrational frequencies were computed with the well-established coupled cluster approach CCSD(T) with all single and double substitutions from the Hartree−Fock reference determinant augmented by a perturbative treatment of connected triple excitations.[53,54] It was found to provide a good description for the equilibrium geometry and vibrational frequencies and then used in this work to calculate the first full-dimensional PES of SF_6. We used correlation-consistent polarized valence n-tuple-zeta basis sets of Dunning, Peterson and co-workers[55−58] for the calculations and specifically adapted DK basis for calculations including relativistic effects.[59] Energies for all electronic structure calculations were converged to MOLPRO default value 10^{-10} a.u.

In order to obtain accurate calculations of vibrational and rotational energy levels from the theoretical PES useful for spectroscopic analysis, it is desirable to use high level *ab initio* methods with sufficiently large basis sets in electronic structure calculations. However, in the case of SF_6, the full-grid calculations with large basis sets (like those recently employed for methane[21,30]) are too demanding. In this work, an essential part of electronic energy calculations was performed with the CCSD(T)/VTZ ansatz at 6412 nuclear geometries of the grid optimized for the 6-th order PES. To refine the analytical PES form, the same method and the same basis set were additionally used at 2296 geometries of the 8-th order grid. In order to control the surface shape at larger nuclear displacements, we carried out supplementary MP2 calculations with VTZ atomic basis on extended grid of 85,136 geometries also optimized for the 8-th order PES.

Empirical PES corrections are often used to compensate the lack of accuracy of *ab initio* calculations. However, for an efficient application of an empirical optimization, these corrections have to be relatively small. Typically, simple empirical corrections are used to reduce calculated minus observed deviation for the fundamental vibration frequencies, but this could produce uncontrolled errors for highly excided states if the shape of the initial *ab initio* PES is not reliably established. This is an important point for a correct modeling of "hot" bands as they could produce a significant contribution to the atmospheric absorbance by heavy molecules with relatively low vibrational modes. In the case of SF_6, only a limited number of experimental vibrational frequencies are known that can be used for a validation of *ab initio* results. *Ab initio* equilibrium geometry obtained with CVQZ and CVQZ-DK basis sets was close to empirical ones (Table 1), but calculations using CCSD(T)/CVQZ-DK ansatz for a large grid of geometries are actually too demanding. For this reason, we have applied the algorithm of corrections similar to that of ref 49. First, we have computed the one-dimensional "radial" PES section using the CVQZ-DK basis set and electronic energies at 67 nuclear geometries sufficient to determine the force field up to the third order. Then, the difference between electronic energies in 67 geometries using CVQZ-DK and VTZ basis sets was fitted to an analytical function $F_{O3}(S(r,q))$ of 15 symmetrized coordinates expanded up to 3rd order. One dimensional radial correction functions $f_X(r)$ were constructed as a difference between two radial potentials calculated for X-basis and for VTZ basis

$$f_X(r) = V_X(r) - V_{VTZ}(r) - F_{O3}(S(r, r_e, r_e, ..., q_e)) \quad (11)$$

where $V_X(r)$ stands for electronic energies at the radial cut and X = CVQZ-DK or VQZ. The additional one-dimensional function $F_{O3}(r,0,0,...,0)$ was obtained from the third order correction. All other bond lengths were fixed to their equilibrium values for X and VTZ basis sets, whereas all angles were fixed to their equilibrium values. Functions $f_X(r)$ for X = CVQZ-DK is shown in Figure 3. Note that the one-dimensional radial correction (eq 11) near the equilibrium geometries of VTZ and X basis sets quite significantly depends on the analytical representation.

The number N of irreducible tensors of the total A_{1g} representation involved in the PES expansion (eqs 9 and 10) increases quite rapidly with the order. Up to the orders 2, 3, 4, 5, 6, 7, and 8, this number N is equal to 9, 31, 123, 406, 1334, 3924, and 10,994, respectively. For PES parameterization, to provide the best results using the least square technique, more

https://dx.doi.org/10.1021/acs.jpca.0c02733
J. Phys. Chem. A XXXX, XXX, XXX−XXX

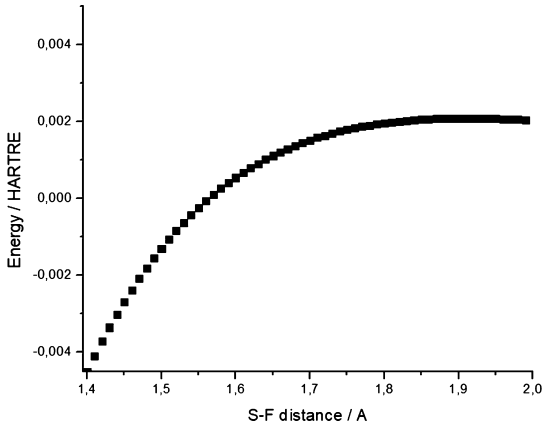

Figure 3. One-dimensional radial correction E{CCSD(T)-DK/CVQZ-DK}—E{CCSD(T)/VTZ}.

complex one-dimensional basis functions are used in (eqs 1−6). Morse-type functions are used as primitive radial functions

$$f_r(r_i) = 1 - \exp(-\alpha(r_i - r_e)) \quad (12)$$

involved in the definitions of the symmetrized SR_Γ and angular SA_Γ coordinates which are used to build our final analytical PES model. Although the function $f_r(r)^2$ for $\alpha = 2.0$ reproduces very accurately the one-dimensional potential of SF, the best choice of α in eq 12 for full-dimensional PES was $\alpha = 1.9$. Consequently, our PES model tends to the corresponding finite asymptote at large inter-nuclear distances contrary to a simple power series expansion in $(r_i - r_e)$.

The angular function was expressed in terms of the cosine function

$$f_a(q_{ij}) = \cos(q_{ij}) + \alpha \cos^2(q_{ij}) \quad (13)$$

Similar to methane PES,[49] it is preferable to use the value $\alpha = 1/3$ for angular functions.

The relevance of various analytical representation of the PES was checked by the quality of the PES fit on the 8-th order grid of 85,136 geometries using MP2/VTZ calculated energies. Various orders of the PES expansion and various forms of the angular dependence were tested. The results of the least-squares fits using weight function $w(E)$ similar to that previously employed for methane studies[49,60]

$$w(E) = \frac{\tanh(-0.0005(E - E_1) + 1.002002002)}{2.002002002} \quad (14)$$

where $E_1 = 7000$ cm^{-1}, are collected in Table 3. It is seen that the parameter value $\alpha = 1/3$ permitted a notable improvement of the standard deviation of the fit for 4-th and 5-th order of the PES expansion. The use of supplementary (redundant) coordinated, as reported in the case of methane,[21,51] could significantly change the PES near the equilibrium. In this work, we have also evaluated a possible impact of supplementary coordinates eqs 7 and 8 for SF_6. An introduction of S' coordinate in the PES expansion has somewhat larger effect on the standard deviation than that of S'', but in both cases, the improvement of the standard deviation was smaller with respect to the inclusion of $\alpha = 1/3$ in the quadratic terms of eq 13. Finally, we consider that the fifth-order PES expansion provides an acceptable quality of the fit of *ab initio* energies up to 7000 cm^{-1}.

Table 3. Result of Various PES Fits Using 85136 Electronic MP2/VTZ Energies

order	additional angular coordinates: order, type	#parameters	α	RMS cm^{-1}	STD cm^{-1}
4		123	0.	8.29	3.71
4	O3, S′	151	0.	6.77	3.16
4	O3, S″	151	0.	8.08	3.62
4		123	1/3	4.58	2.13
4	O2, S′	128	1/3	3.98	1.90
4	O2, S″	128	1/3	4.27	2.05
4	O3, S′	151	1/3	3.48	1.70
4	O3, S″	151	1/3	3.89	1.91
5		406	0.	1.96	0.79
5	O3, S′	434	0.	1.57	0.68
5	O3, S″	434	0.	1.66	0.68
5		406	1/3	0.94	0.43
5	O3, S′	434	1/3	0.58	0.28
5	O3, S″	434	1/3	0.75	0.34

The comparison of the observed fundamental band centers of $^{32}SF_6$ with our variational nuclear motion calculations using *ab initio* CCSD(T)/VTZ and CCSD(T)/CVQZ-DK surfaces is given in Table 4. For the VTZ surface defined on a large grid, vibrational and rotational energies were computed using TENSOR variational code in normal mode ITO representation. Technical details can be found in the previous works devoted to five- and six-atomic molecules.[25,32−34] For the VQZ surface defined on a small grid, we used an incremental scheme accounting for the relative difference ω_i(VQZ) − ω_i(VTZ) between the harmonic frequencies in these basis sets as described below.

The five of six fundamentals calculated with the CVQZ-DK basis set accounting for relativistic contributions show in average better agreement with observed frequencies than VTZ calculations. Note that the most significant contribution in the increase of the fundamental frequencies of angular modes ν_4, ν_5, and ν_6 when using the CVQZ-DK PES in comparison with the VTZ PES is due to the decrease of the equilibrium S−F bond length. A rough estimation of the deviations between VQZ calculations and the observed fundamental band centers (as given in column 4 of Table 4) was obtained using approximate relation ν_i(VQZ) = v_i(VTZ) + (ω_i(VQZ) − ω_i(VTZ)), where ω_i are harmonic frequencies.

The S−F bound length computed in CVQZ-DK basis set approached toward the empirical value. This could simplify in future an empirical optimization of the PES parameters. However, in order to improve the RMS deviation of the 15-dimensional PES fit with a rather small number of parameters, the slightly increased value $r_e = 1.5613$ (instead of 1.557 for CVQZ-DK) was used. The final *ab initio* PES of this work was constructed using the least-squares fit of the F_p parameters of the 5-th order expansion (eq 9) to CCSD(T)/VTZ electronic energies at 8708 geometrical nuclear configurations with the CCSD(T)/CVQZ-DK correction, as described above. In order to improve the fit accuracy near the bottom of the PES, the weighting function (eq 13) with the parameter $E_1 = 5000$ cm^{-1} was applied. This permitted obtaining RMS deviation of 0.5 cm^{-1} for 4283 geometries in the range of 5000 cm^{-1} above the potential minimum. Because the order of the PES was not very high (in comparison with best methane calculations[21]), the MP2/VTZ electronic energies were not explicitly included in

https://dx.doi.org/10.1021/acs.jpca.0c02733
J. Phys. Chem. A XXXX, XXX, XXX−XXX

Table 4. Fundamental Band Centers (cm^{-1}) for $^{32}SF_6$: Comparison of Purely *Ab Initio* Calculations Using the VTZ and CVQZ-DK PESs with Experimental Values

		Calc PES VTZ		Obs-Calc PES VQZ[a]	Calc PES CVQZ-DK	
	Obs	r_e = 1.57015	Obs-Calc VTZ	r_e = 1.57015	r_e = 1.5613	Obs-Calc CVQZ-DK
ν_1	774.5445	780.814	5.842	13.717	773.178	1.365
ν_2	643.3736	662.137	−12.113	−1.070	646.928	−3.5546
ν_3	947.9763	982.123	−25.218	−5.373	958.800	−10.824
ν_4	614.9819	613.344	5.353	11.756	620.836	−5.854
ν_5	523.449	519.258	8.766	12.495	525.897	−2.448
ν_6	347.985	347.329	3.606	7.479	351.724	−3.739

[a]These VQZ values in the fourth column were obtained from full dimensional variational nuclear motion calculation at the VTZ level corrected by the difference ω_i(VQZ) − ω_i(VTZ) between the harmonic frequencies. The values of r_e are given in Å.

the fit but were used to check the PES behavior for larger nuclear displacements.

4. *AB INITIO* DMS FIT

Several studies[8−12] have been devoted to line-by-line analyses of experimental Raman and infrared SF_6 spectra using effective Hamiltonian and effective transition moments models. An accurate determination of empirical line intensities of heavy molecules with low frequency modes is an extremely difficult task because of crowded spectra and blended lines. One of the most challenging issues is a separation of contributions of overlapping cold and hot bands with a significant impact on the uncertainty in the temperature dependence of the absorption or emission of radiation.

Advanced *ab initio* calculations of molecular PESs and DMS together with the development of variational methods for nuclear motion calculations (refs[18,61−66] and references therein) permitted constructing quite complete lines lists for triatomic,[61,67−70] four-atomic,[17,31,71−73] five-atomic,[19,22,30,34,74,75] and six-atomic[23−25,76] molecules. In some of these cases, the accuracy of *ab initio* line intensities was competitive[77−80] with best empirical determinations being more complete and reliable for the hot bands.[7,68,73,81−83] On the other hand, knowledge of the shape of *ab initio* surfaces[84,85] helped understanding issues related to molecular dynamics.

One more atom in a molecule produces three supplementary degrees of freedom in the nuclear motion resulting in a very substantial computational effort for *ab initio* predictions of high-resolution spectra for polyatomic molecules. In a brute-force approach (without symmetry considerations), there would be roughly a factor $\sim N^6$ of dimensionality between global spectra calculations of five-atomic molecule (like methane) and seven-atomic molecule such as SF_6, where N is the number of *ab initio* grid points or of basis set function for each degree of freedom.

Here, we present the first results for the full 15-dimensional SF_6 DMS components and for intensity calculations in the range of the strongest bands. A full account of symmetry permitted drastically reducing the number of redundant geometries and the number of independent DMS parameters. For the construction of the DMS, we used the corresponding irreducible tensor representation similar to the analytical expansions (eqs 9 and 10) where the symmetrized internal coordinates were replaced by normal mode coordinates. The corresponding procedure has been described in our previous works[71,86] devoted to four-atomic and five-atomic molecules. In these works, the *ab initio* DMSs were first built in molecular-fixes frames corresponding to the axes choice options of the MOLPRO code. Then, the axes were rotated to the Eckart system. As in the case of SF_6, the relations between internal and normal coordinated Q_i were found via numerical transformation, and it was easier to proceed by direct DMS fits in normal coordinates.

A progress in methane *ab initio* calculations has taken a couple of decades.[21,60,81,87,88] The line intensity accuracy in infra-red of 1−5% has been recently reported[80] using the coupled-cluster method with ACV5Z one-particle basis sets. In the case of SF_6, such calculations are presently too demanding. In this work, we used CCSD(T) method with two basis sets for the dipole moment calculations. The calculations using VTZ basis were conducted on the first grid containing 1664 nuclear geometries, which was a sub-set of the 6-th order grid relative to PES computations described above. This was then supplemented by AVTZ calculations at 500 geometries. In both cases, the optimal samples of geometries near the bottom of the PES were determined. At each geometry, three projections of the dipole moment were obtained. Dipole moments were computed as the derivative of the energy with respect to the weak external uniform electric field using the finite difference scheme with a field variation of 0.0002 a.u. around at the zero field strength.

For the DMS construction, we used here the scheme, which has been employed in our previous works for PES and DMS of four-to-six atomic molecules.[22,24,71,86] After having computed the dipole moments with AVTZ and VTZ basis sets, we fitted the corresponding 15-dimensional function $\mathrm{diff}_{2\_O3}(Q_i)$, which describes the corresponding difference DMS(AVTZ) − DMS(VTZ). This function was modeled by the third-order ITO expansion containing 61 adjustable parameters, of which 50 parameters were statistically well defined. Then, for supplementary geometries from N = 501 to N = 1664, the AVTZ calculations were lacking, and the AVTZ dipole moments were evaluated as VTZ dipole moments plus $\mathrm{diff}_{2\_O3}(Q_i)$. Finally, the forth-order parameters of the DMS power series expansion in normal coordinated were fitted to the above defined *ab initio* dipole moment values using weight function (eq 14) with E_1 = 10,000 cm^{-1}. Of 260 fourth-order DMS parameters, 194 ones were statistically well determined. This procedure was conducted to high accuracy of the fit corresponding to the RMS deviation of 1.4×10^{-5} a.u. and the weighted standard deviation of 9.9×10^{-6}. The distribution of the fit discrepancies is shown in Figure 4.

5. RESULTS AND CONCLUSIONS

Preliminary evaluation of SF_6 band intensities using algorithms of variational methods described in refs[31−34] permits to conclude that our PES and DMS provided realistic predictions of absorption spectra, at least in the range of strong bands. The

https://dx.doi.org/10.1021/acs.jpca.0c02733
J. Phys. Chem. A XXXX, XXX, XXX−XXX

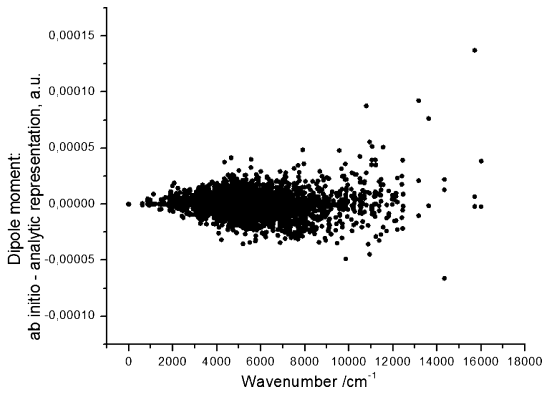

Figure 4. Deviations between fitted analytical representation of the DMS and *ab initio* dipole moment values versus energies at the corresponding nuclear geometries.

comparison of our calculated absorption cross sections with experimental SF_6 cross section[13,89] shows a very good agreement at cold temperature of 180 K, see Figure 5, lower

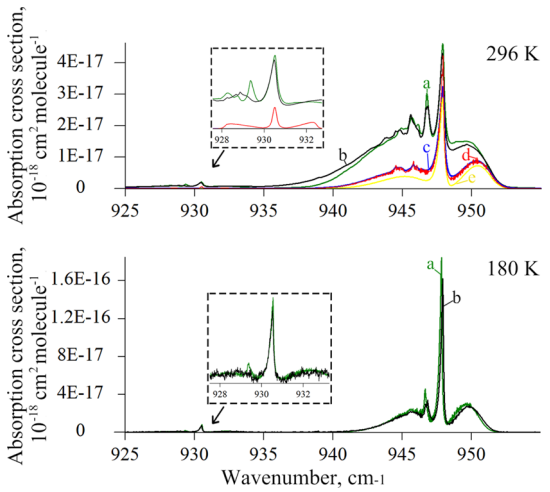

Figure 5. Comparison of cross section at a temperature of 296 K (upper panel) and of 180 K (lower panel). Upper panel: our simulation from line list of TheoReTS (green—a), the experimentally observed PNNL spectrum available in HITRAN (black—b), simulation from line list of GEISA 2015 (blue—c), the theoretical calculation of Dijon (red—d), and simulation from line list of HITRAN 2016 database (yellow—e). Lower panel: our simulation from line list of TheoReTS (green—a) and the experimental observed spectrum from HITRAN (black—b).

panel. Note that calculated band centers of $^{32}SF_6$ and $^{34}SF_6$ isotopologues in Figure 5 were shifted to empirical values (964.196 and 932.534 cm^{-1} correspondingly) available at http://vamdc.icb.cnrs.fr/PHP/SF6.php. An agreement of our calculations with experimental absorption cross sections of Sharpe et al.[90] at room temperature is also satisfactory (Figure 5, upper panel). The latter ones have been recorded at $T = 298$ K with an N_2 pressure of 760 Torr with a medium resolution of 0.112 cm^{-1} and included in HITRAN-on-line cross-section compilation.[13,90,91] The absorption feature near 930 cm^{-1} corresponds to the v3 band of the $^{34}SF_6$ isotopologue at natural abundance. Our *ab initio* cross sections agree much better with these observations than the simulations using SF_6 line-by-line lists constructed from effective models as available in HITRAN_2016,[13] GEISA_2015[14] and Dijon (SheCaS-Da)[92] databases as shown in Figure 5, upper panel. However, *ab initio* room-temperature simulations appear to be slightly less accurate than for 180 K (Figure 5, lower panel).

Calculations at room temperature require an account of more significant contributions of hot bands involving higher vibrational states. The preliminary data obtained in this work will be made available through the TheoReTS[66] (http://theorets.univ-reims.fr, http://theorets.tsu.ru) information system. A further improvement could be possibly obtained using lager vibrational basis set that is computationally very demanding. We plan to extend the computation of full line lists in future studies..

■ ASSOCIATED CONTENT

Supporting Information

The Supporting Information is available free of charge at https://pubs.acs.org/doi/10.1021/acs.jpca.0c02733.

PES in the internal coordinates and DMS in normal mode expansion in an easy-to-use explicit form for $^{32}SF_6$ (ZIP)

Short description of C program for calculation potential energy values (PDF)

■ AUTHOR INFORMATION

Corresponding Author

Andrei V. Nikitin − *V.E. Zuev Institute of Atmospheric Optics, Russian Academy of Sciences, 634055 Tomsk, Russian Federation;* orcid.org/0000-0002-4280-4096; Phone: +73822-491111 (1260); Email: avn@iao.ru

Authors

Michael Rey − *Groupe de Spectrométrie Moléculaire et Atmosphérique, UMR CNRS 6089, Université de Reims, 51687 Reims Cedex 2, France*

Iana S. Chizhmakova − *Institute of Monitoring of Climatic and Ecological Systems, Russian Academy of Sciences, 634055 Tomsk, Russian Federation; QUAMER Laboratory, Tomsk State University, 634050 Tomsk, Russian Federation*

Vladimir G. Tyuterev − *Groupe de Spectrométrie Moléculaire et Atmosphérique, UMR CNRS 6089, Université de Reims, 51687 Reims Cedex 2, France; QUAMER Laboratory, Tomsk State University, 634050 Tomsk, Russian Federation*

Complete contact information is available at: https://pubs.acs.org/10.1021/acs.jpca.0c02733

Notes

The authors declare no competing financial interest.

■ ACKNOWLEDGMENTS

The research in IOA was performed as part of the state assignment of the IOA SB RAS. V.G.T. acknowledges the support from Academic D. Mendeleev program of Tomsk State University and M.R. form LEFE CHAT CNRS program. Part of the research was performed under contract of RFBR grant (grant no. 19-03-00581).

■ REFERENCES

(1) Jesse, S.; Pedraza, A. J.; Fowlkes, J. D.; Budai, J. D. Etching-enhanced Ablation and the Formation of a Microstructure in Silicon by Laser Irradiation in an SF_6 Atmosphere. *J. Mater. Res.* **2002**, *17*, 1002.

https://dx.doi.org/10.1021/acs.jpca.0c02733
J. Phys. Chem. A XXXX, XXX, XXX−XXX

(2) Johnstone, W. M.; Newell, W. R. Absolute elastic differential cross sections for electron scattering from SF_6. *J. Phys. B: At., Mol. Opt. Phys.* **1991**, *24*, 473−487.
(3) Malik, N.; Qureshi, A. A Review of Electrical Breakdown in Mixtures of SF_6 and Other Gases. *IEEE Trans. Electr. Insul.* **1979**, *EI-14*, 1.
(4) Hodnebrog, Ø.; Etminan, M.; Fuglestvedt, J. S.; Marston, G.; Myhre, G.; Nielsen, C. J.; Shine, K. P.; Wallington, T. J. Global Warming Potentials and Radiative Efficiencies of Halocarbons and Related Compounds: a Comprehensive Review. *Rev. Geophys.* **2013**, *51*, 300−378.
(5) Ravishankara, A. R.; Solomon, S.; Turnipseed, A. A.; Warren, R. F. Atmospheric Lifetimes of Long-Lived Halogenated Species. *Science* **1993**, *259*, 194−199.
(6) Earth System Research Laboratory Global Monitoring Division. http://www.esrl.noaa.gov/gmd/hats/data.html (accessed 27.03.2020).
(7) Rey, M.; Chizhmakova, I. S.; Nikitin, A. V.; Tyuterev, V. G. Understanding global infrared opacity and hot bands of greenhouse molecules with low vibrational modes from first-principles calculations: the case of CF_4. *Phys. Chem. Chem. Phys.* **2018**, *20*, 21008−21033.
(8) Boudon, V.; Bermejo, D. First High-Resolution Raman Spectrum and Analysis of the ν_5. *J. Mol. Spectrosc.* **2002**, *213*, 139−144.
(9) Boudon, V.; Pierre, G.; Bürger, H. High-Resolution Spectroscopy and Analysis of the ν_4 Bending Region of SF_6 near 615 cm^{-1}. *J. Mol. Spectrosc.* **2001**, *205*, 304−311.
(10) Faye, M.; Boudon, V.; Loëte, M.; Roy, P.; Manceron, L. Observation and analysis of the SF_6 $\nu_2 + \nu_4 + \nu_5$ band: Improved parameters for the $\nu_5 = 1$ state. *J. Mol. Spectrosc.* **2016**, *325*, 35−41.
(11) Faye, M.; Boudon, V.; Loëte, M.; Roy, P.; Manceron, L. The high overtone and combination levels of SF_6 revisited at Doppler-limited resolution: A global effective rovibrational model for highly excited vibrational states. *J. Quant. Spectrosc. Radiat. Transfer* **2017**, *190*, 38−47.
(12) Faye, M.; Manceron, L.; Roy, P.; Boudon, V.; Loëte, M. First analysis of the $\nu_3 + \nu_5$ combination band of SF_6 observed at Doppler-limited resolution and effective model for the $\nu_3 + \nu_5 - \nu_5$ hot band. *J. Mol. Spectrosc.* **2018**, *348*, 37−42.
(13) Gordon, I. E.; Rothman, L. S.; Hill, C.; Kochanov, R. V.; Tan, Y.; Bernath, P. F.; et al. The HITRAN2016 molecular spectroscopic database. *J. Quant. Spectrosc. Radiat. Transfer* **2017**, *203*, 3−69.
(14) Jacquinet, N.; et al. The 2015 edition of the GEISA spectroscopic database. *J. Mol. Spectrosc.* **2016**, *327*, 31−72.
(15) Yurchenko, S. N.; Carvajal, M.; Thiel, W.; Jensen, P. Ab initio dipole moment and theoretical rovibrational intensities in the electronic ground state of PH_3. *J. Mol. Spectrosc.* **2006**, *239*, 71−87.
(16) Nikitin, A. V.; Holka, F.; Tyuterev, V. G.; Fremont, J. Vibration energy levels of the PH_3, PH_2D, and PHD_2 molecules calculated from high order potential energy surface. *J. Chem. Phys.* **2009**, *130*, 244312.
(17) Huang, X.; Schwenke, D. W.; Lee, T. J. Rovibrational spectra of ammonia. II. Detailed analysis, comparison, and prediction of spectroscopic assignments for $^{14}NH_3$, $^{15}NH_3$, and $^{14}ND_3$. *J. Chem. Phys.* **2011**, *134*, 044321.
(18) Yurchenko, S. N.; Tennyson, J.; Barber, R. J.; Thiel, W. Vibrational transition moments of CH_4 from first principles. *J. Mol. Spectrosc.* **2013**, *291*, 69−76.
(19) Owens, A.; Yurchenko, S. N.; Yachmenev, A.; Tennyson, J.; Thiel, W. Accurate ab initio vibrational energies of methyl chloride. *J. Chem. Phys.* **2015**, *142*, 244306.
(20) Owens, A.; Yurchenko, S. N.; Yachmenev, A.; Thiel, W. A global potential energy surface and dipole moment surface for silane. *J. Chem. Phys.* **2015**, *143*, 244317.
(21) Nikitin, A. V.; Rey, M.; Tyuterev, V. G. First fullyab initiopotential energy surface of methane with a spectroscopic accuracy. *J. Chem. Phys.* **2016**, *145*, 114309.
(22) Nikitin, A. V.; Rey, M.; Rodina, A.; Krishna, B. M.; Tyuterev, V. G. Full-Dimensional Potential Energy and Dipole Moment Surfaces of GeH_4 Molecule and Accurate First-Principle Rotationally Resolved Intensity Predictions in the Infrared. *Indian J. Chem., Sect. A: Inorg., Bio-inorg., Phys., Theor. Anal. Chem.* **2016**, *120*, 8983−8997.
(23) Delahaye, T.; Nikitin, A.; Rey, M.; Szalay, P. G.; Tyuterev, V. G. A new accurate ground-state potential energy surface of ethylene and predictions for rotational and vibrational energy levels. *J. Chem. Phys.* **2014**, *141*, 104301.
(24) Delahaye, T.; Nikitin, A. V.; Rey, M.; Szalay, P. G.; Tyuterev, V. G. Accurate 12D dipole moment surfaces of ethylene. *Chem. Phys. Lett.* **2015**, *639*, 275−282.
(25) Rey, M.; Delahaye, T.; Nikitin, A. V.; Tyuterev, V. G. First theoretical global line lists of ethylene ($^{12}C_2H_4$) spectra at various temperatures in the far-infrared range for quantification of absorption and emission in planetary atmospheres. *Astron. Astrophys.* **2016**, *594*, A47.
(26) Manzhos, S.; Carrington, T.; Laverdure, L.; Mosey, N. Mosey N Computing the Anharmonic Vibrational Spectrum of UF_6 in 15 Dimensions with an Optimized Basis Set and Rectangular Collocation. *J. Phys. Chem. A* **2015**, *119*, 9557−9567.
(27) Burcl, R.; Handy, N. C.; Carter, S. Vibrational spectra of furan, pyrrole, and thiophene from a density functional theory anharmonic force field. *Spectrochim. Acta, Part A* **2003**, *59*, 1881−1893.
(28) Wang, X.; Huang, X.; Bowman, J. M.; Lee, T. J. Anharmonic rovibrational calculations of singlet cyclic C_4 using a new ab initio potential and a quartic force field. *J. Chem. Phys.* **2013**, *139*, 224302.
(29) Pietropolli Charmet, A.; Bizzocchi, L.; Giuliano, B. M.; Caselli, P.; Craig, N. C.; Krasnoshchekov, S. V. Disentangling the IR spectra of 2,3,3,3-tetrafluoropropene using an ab initio description of vibrational polyads by means of canonical Van Vleck perturbation theory. *J. Quant. Spectrosc. Radiat. Transf.* **2019**, *239*, 106656.
(30) Owens, A.; Yurchenko, S. N.; Yachmenev, A.; Tennyson, J.; Thiel, W. A highly accurate ab initio potential energy surface for methane. *J. Chem. Phys.* **2016**, *145*, 104305.
(31) Rey, M.; Nikitin, A. V.; Tyuterev, V. G. Ab initioro-vibrational Hamiltonian in irreducible tensor formalism: a method for computing energy levels from potential energy surfaces for symmetric-top molecules. *Mol. Phys.* **2010**, *108*, 2121−2135.
(32) Rey, M.; Nikitin, A. V.; Tyuterev, V. G. Complete nuclear motion Hamiltonian in the irreducible normal mode tensor operator formalism for the methane molecule. *J. Chem. Phys.* **2012**, *136*, 244106.
(33) Rey, M.; Nikitin, A. V.; Tyuterev, V. G. First principles intensity calculations of the methane rovibrational spectra in the infrared up to 9300 cm^{-1}. *Phys. Chem. Chem. Phys.* **2013**, *15*, 10049−10061.
(34) Rey, M.; Nikitin, A. V.; Tyuterev, V. G. Convergence of normal mode variational calculations of methane spectra: Theoretical linelist in the icosad range computed from potential energy and dipole moment surfaces. *J. Quant. Spectrosc. Radiat. Transf.* **2015**, *164*, 207−220.
(35) Nagarajan, G.; Brinkley, D. C. Statistical Thermodynamics Enthalpy, Free Energy, Entropy, and Heat Capacity of Some Hexafluorides of Octahedral Symmetry. *Z. Naturforsch., A: Astrophys., Phys. Phys. Chem.* **1971**, *26*, 1658−1665.
(36) Spiridonov, V. P.; Tarasov, Y. I.; Novosadov, B. K.; Nikitin, O. Y.; Maslov, I. V. A practical method for diffraction analysis of equilibrium geometries of molecules without refined force fields. *J. Mol. Struct.* **1997**, *413−414*, 463−470.
(37) Werner, H.-J.; Knowles, P. J.; Knizia, G.; Manby, F. R.; et al. Molpro: a general-purpose quantum chemistry program package. *WIREs Comput. Mol. Sci.* **2012**, *2*, 242−253.
(38) Schütz, H.-J.; Knowles, P. J.; Lindh, R.; et al. *MOLPRO*, version 2019.1, a package of ab initio programs, http://www.molpro.net.
(39) Eisfeld, W. Highly accurate determination of the electron affinity of SF_6 and analysis of structure and photodetachment spectrum of SF_6. *J. Chem. Phys.* **2011**, *134*, 054303.
(40) Miller, B. R.; Fink, M. Mean amplitudes of vibration of SF_6 and intramolecular multiple scattering. *J. Chem. Phys.* **1981**, *75*, 5326.
(41) Champion, J.-P.; Loete, M.; Pierre, G. In *Spectroscopy of the Earth's Atmosphere and Interstellar Medium*; Rao, K. N.; Weber, A., Eds.; Academic Press: San Diego, 1992.

https://dx.doi.org/10.1021/acs.jpca.0c02733
J. Phys. Chem. A XXXX, XXX, XXX−XXX

(42) Zhilinskii, B. I.; Perevalov, V. I.; Tyuterev, V. G. *Method of Irreducible Tensorial Operators in the Theory of Molecular Spectra*; Nauka: Novosibirsk, 1987.
(43) Chizhmakova, I. S.; Nikitin, A. V. Potential Energy Surface of SF_6. *Atmos. Oceanic Opt.* **2019**, *32*, 613−618.
(44) Schatz, P. N.; Hornig, D. F. Bond Moments and Derivatives in CF_4, SiF_4, and SF_6 from Infrared Intensities. *J. Chem. Phys.* **1953**, *21*, 1516.
(45) Fernandez-Gomez, M.; Lopez-Gonzalez, J. J.; Cardenete Espinosa, A. Calculation of internal valence force constants for $XY_6(O_h)$ Octahedral molecules. *J. Mol. Struct.* **1990**, *220*, 287−300.
(46) Pistorius, C. W. F. T. Potential Field and Force Constants of Octahedral Molecules. *J. Chem. Phys.* **1958**, *29*, 1328−1332.
(47) Halonen, L.; Child, M. S. A local mode model for tetrahedral molecules. *Mol. Phys.* **1982**, *46*, 239−255.
(48) Delibas, A.; Aykan, V.; Turkkan, D.; Akkus, H. Point groups in solid state physics I: point group O_h. *Am. J. Mod. Phys.* **2013**, *2*, 81−87.
(49) Nikitin, A. V.; Rey, M.; Tyuterev, V. G. Rotational and vibrational energy levels of methane calculated from a new potential energy surface. *Chem. Phys. Lett.* **2011**, *501*, 179−186.
(50) Nikitin, A. V. Calculation of vibrational energy levels of symmetric molecules from potential energy. *Atmos. Oceanic Opt.* **2015**, *28*, 379−390.
(51) Nikitin, A. V.; Rey, M.; Tyuterev, V. G. An efficient method for energy levels calculation using full symmetry and exact kinetic energy operator: tetrahedral molecules. *J. Chem. Phys.* **2015**, *142*, 094118.
(52) Nikitin, A.; Champion, J. P.; Tyuterev, V. G. Improved algorithms for the modeling of vibrational polyads of polyatomic molecules: application to T_d, O_h, and C_{3v} molecules. *J. Mol. Spectrosc.* **1997**, *182*, 72−84.
(53) Raghavachari, K.; Trucks, G. W.; Pople, J. A.; Head-Gordon, M. A fifth-order perturbation comparison of electron correlation theories. *Chem. Phys. Lett.* **1989**, *157*, 479.
(54) Purvis, G. D.; Bartlett, R. J. A full coupled-cluster singles and doubles model: The inclusion of disconnected triples. *J. Chem. Phys.* **1982**, *76*, 1910.
(55) Woon, D. E.; Dunning, T. H. Gaussian basis sets for use in correlated molecular calculations. III. The atoms aluminum through argon. *J. Chem. Phys.* **1993**, *98*, 1358.
(56) Dunning, T. H. Gaussian basis sets for use in correlated molecular calculations. I. The atoms boron through neon and hydrogen. *J. Chem. Phys.* **1989**, *90*, 1007.
(57) Wilson, A. K.; Woon, D. E.; Peterson, K. A.; Dunning, T. H., Jr. Gaussian basis sets for use in correlated molecular calculations. IX. The atoms gallium through krypton. *J. Chem. Phys.* **1999**, *110*, 7667.
(58) DeYonker, N. J.; Peterson, K. A.; Wilson, A. K. Systematically Convergent Correlation Consistent Basis Sets for Molecular Core−Valence Correlation Effects: The Third-Row Atoms Gallium through Krypton. *J. Phys. Chem. A* **2007**, *111*, 11383−11393.
(59) de Jong, W. A.; Harrison, R. J.; Dixon, D. A. Parallel Douglas-Kroll energy and gradients in NWChem: Estimating scalar relativistic effects using Douglas-Kroll contracted basis sets. *J. Chem. Phys.* **2001**, *114*, 48.
(60) Schwenke, D. W.; Partridge, H. Vibrational energy levels for CH_4 from an ab initio potential. *Spectrochim. Acta, Part A* **2001**, *57*, 887.
(61) Partridge, H.; Schwenke, D. W. The determination of an accurate isotope dependent potential energy surface for water from extensive ab initio calculations and experimental data. *J. Chem. Phys.* **1997**, *106*, 4618−4639.
(62) Marquardt, R.; Quack, M. Global Analytical Potential Hypersurface for Large Amplitude Nuclear Motion and Reactions in Methane II. Characteristic Properties of the Potential and Comparison to Other Potentials and Experimental Information. *J. Phys. Chem. A* **2004**, *108*, 3166−3181.
(63) Huang, X.; Freedman, R. S.; Tashkun, S. A.; Schwenke, D. W.; Lee, T. J. Semiempirical $^{12}C^{16}O_2$ IR line lists for simulations up to 1500K and 20000cm^{-1}. *J. Quant. Spectrosc. Radiat. Transf.* **2013**, *130*, 134−146.
(64) Carter, S.; Sharma, A. R.; Bowman, J. M. First-principles calculations of rovibrational energies, dipole transition intensities and partition function for ethylene using MULTIMODE. *J. Chem. Phys.* **2012**, *137*, 154301.
(65) Tennyson, J.; Yurchenko, S. N.; et al. The ExoMol database: molecular line lists for exoplanet and other hot atmospheres. *J. Mol. Spectrosc.* **2016**, *327*, 73−94.
(66) Rey, M.; Nikitin, A. V.; Babikov, Y. L.; Tyuterev, V. G. TheoReTS - An information system for theoretical spectra based on variational predictions from molecular potential energy and dipole moment surfaces. *J. Mol. Spectrosc.* **2016**, *327*, 138−158.
(67) Polyansky, O. L.; Ovsyannikov, R. I.; Kyuberis, A. A.; Lodi, L.; Tennyson, J.; Zobov, N. F. Calculation of rotation-vibration energy levels of the water molecule with near-experimental accuracy based on an ab initio potential energy surface. *J. Phys. Chem. A* **2013**, *117*, 9633−9643.
(68) Polyansky, O. L.; Kyuberis, A. A.; Zobov, N. F.; Tennyson, J.; Yurchenko, S. N.; Lodi, L. ExoMol molecular line lists XXX: a complete high-accuracy line list for water. *Mon. Not. Roy. Astron. Soc.* **2018**, *480*, 2597−2608.
(69) Tyuterev, V. G.; Kochanov, R. V.; Tashkun, S. A.; Holka, F.; Szalay, P. G. New analytical model for the ozone electronic ground state potential surface and accurate ab initio vibrational predictions at high energy range. *J. Chem. Phys.* **2013**, *139*, 134307.
(70) Tyuterev, V. G.; Barbe, A.; Jacquemart, D.; Janssen, C.; Mikhailenko, S. N.; Starikova, E. N. Ab initio predictions and laboratory validation for consistent ozone intensities in the MW, 10 and 5 μm ranges. *J. Chem. Phys.* **2019**, *150*, 184303.
(71) Nikitin, A. V.; Rey, M.; Tyuterev, V. G. High order dipole moment surfaces of PH_3 and ab initio intensity predictions in the Octad range. *J. Mol. Spectrosc.* **2014**, *305*, 40−47.
(72) Yurchenko, S. N.; Barber, R. J.; Yachmenev, A.; Thiel, W.; Jensen, P.; Tennyson, J. A Variationally ComputedT= 300 K Line List for NH_3†. *J. Phys. Chem. A* **2009**, *113*, 11845−11855.
(73) Egorov, O.; Nikitin, A.; Rey, M.; Rodina, A.; Tashkun, S.; Tyuterev, V. Global modeling of NF_3 line positions and intensities from far to mid-infrared up to 2200 cm^{-1}. *J. Quant. Spectrosc. Radiat. Transf.* **2019**, *239*, 106668.
(74) Rey, M.; Nikitin, A. V.; Tyuterev, V. G. Accurate first-principles calculations for $^{12}CH_3D$ infrared spectra from isotopic and symmetry transformations. *J. Chem. Phys.* **2014**, *141*, 044316.
(75) Nikitin, A. V.; Rey, M.; Tyuterev, V. G. Rotational and vibrational energy levels of methyl fluoride calculated from a new potential energy surface. *J. Mol. Spectrosc.* **2012**, *274*, 28−34.
(76) Mant, B. P.; Yachmenev, A.; Tennyson, J.; Yurchenko, S. N. ExoMol molecular line lists − XXVII. Spectra of C_2H_4. *Mon. Not. Roy. Astron. Soc.* **2018**, *478*, 3220−3232.
(77) Birk, M.; Wagner, G.; Loos, J.; Lodi, L.; Polyansky, O. L.; Kyuberis, A. A.; Zobov, N. F.; Tennyson, J. Accurate line intensities for water transitions in the infrared: Comparison of theory and experiment. *J. Quant. Spectrosc. Radiat. Transfer* **2017**, *203*, 88−102.
(78) Zak, E. J.; Tennyson, J.; Polyansky, O. L.; Lodi, L.; Zobov, N. F.; Tashkun, S. A.; Perevalov, V. I. Room temperature line lists for CO_2 symmetric isotopologues with ab initio computed intensities. *J. Quant. Spectrosc. Radiat. Transfer* **2017**, *189*, 267−280.
(79) Tyuterev, V. G.; Kochanov, R. V.; Tashkun, S. A. Accurateab initiodipole moment surfaces of ozone: First principle intensity predictions for rotationally resolved spectra in a large range of overtone and combination bands. *J. Chem. Phys.* **2017**, *146*, 064304.
(80) Nikitin, A. V.; Rey, M.; Tyuterev, V. G. Accurate line intensities of methane from first-principles calculations. *J. Quant. Spectrosc. Radiat. Transfer* **2017**, *200*, 90−99.
(81) Yurchenko, S. N.; Tennyson, J. ExoMol line lists - IV. The rotation-vibration spectrum of methane up to 1500 K. *Mon. Not. R. Astron. Soc.* **2014**, *440*, 1649−1661.

https://dx.doi.org/10.1021/acs.jpca.0c02733
J. Phys. Chem. A XXXX, XXX, XXX−XXX

(82) Rey, M.; Nikitin, A. V.; Tyuterev, V. G. Theoretical hot methane line lists up to t = 2000 k for astrophysical applications. *Astrophys. J.* **2014**, *788*, 2.
(83) Rey, M.; Nikitin, A. V.; Tyuterev, V. G. Accurate Theoretical Methane Line Lists in the Infrared up to 3000 K and Quasi-continuum Absorption/Emission Modeling for Astrophysical Applications. *Astrophys. J.* **2017**, *847*, 105.
(84) Tyuterev, V. G.; Kochanov, R. V.; Campargue, A.; Kassi, S.; Mondelain, D.; Barbe, A. Does the ″reef structure″ at the ozone transition state towards the dissociation exist? New insight from calculations and ultrasensitive spectroscopy experiments. *Phys. Rev. Lett.* **2014**, *113*, 143002.
(85) Yuen, C. H.; Lapierre, D.; Gatti, F.; Kokoouline, V.; Tyuterev, V. G. The Role of Ozone Vibrational Resonances in the Isotope Exchange Reaction $^{16}O^{16}O+^{18}O\rightarrow{}^{18}O^{16}O+^{16}O$: The Time-Dependent Picture. *J. Chem. Phys.* **2019**, *123*, 7733−7743.
(86) Nikitin, A. V.; Rey, M.; Tyuterev, V. G. New dipole moment surfaces of methane. *Chem. Phys. Lett.* **2013**, *565*, 5−11.
(87) Lee, T. J.; Martin, J. M. L.; Taylor, P. R. An accurate ab initio quartic force field and vibrational frequencies for CH_4 and isotopomers. *J. Chem. Phys.* **1995**, *102*, 254−261.
(88) Cassam-Chenaï, P.; Liévin, J. Ab initio calculation of the rotational spectrum of methane vibrational ground state. *J. Chem. Phys.* **2012**, *136*, 174309.
(89) Varanasi, P. HITRAN (Sulfir-containing specis, SF_6). https://hitran.org/xsc/(accessed March 23, 2020).
(90) Sharpe, S. W.; Johnson, T. J.; Sams, R. L.; Chu, P. M.; Rhoderick, G. C.; Johnson, P. A. Gas-Phase Databases for Quantitative Infrared Spectroscopy. *Appl. Spectrosc.* **2004**, *58*, 1452−1461.
(91) Johnson, T. J.; Sams, R.; Sharpe, S. The PNNL Quantitative Infrared Database for Gas-Phase Sensing: A spectral Library for Environmental, Hazmat, and Public Safety Standoff Detection. *Proc. SPIE-Int. Soc. Opt. Eng.* **2004**, *5269*, 159−169.
(92) Calculated SHeCaSDa line list extraction at 296 K. http://vamdc.icb.cnrs.fr/PHP/shecasda.php (accessed 27.03.2020).

https://dx.doi.org/10.1021/acs.jpca.0c02733
J. Phys. Chem. A XXXX, XXX, XXX−XXX

Towards a complete elucidation of the ro-vibrational band structure in the SF_6 infrared spectrum from full quantum-mechanical calculations

M. Rey, I. S. Chizhmakova, A. V. Nikitin, V. G. Tyuterev

Phys. Chem. Chem. Phys., 23, (2021)

PCCP

ROYAL SOCIETY OF CHEMISTRY

PAPER

View Article Online
View Journal | View Issue

Cite this: *Phys. Chem. Chem. Phys.*, 2021, **23**, 12115

Towards a complete elucidation of the ro-vibrational band structure in the SF_6 infrared spectrum from full quantum-mechanical calculations†

Michaël Rey, *[a] Iana S. Chizhmakova,[b] Andrei V. Nikitin[c] and Vladimir G. Tyuterev[ab]

The first accurate and complete theoretical room-temperature rotationally resolved spectra in the range 300–3000 cm^{-1} are reported for the three most abundant isotopologues ($^{32}SF_6$, $^{33}SF_6$ and $^{34}SF_6$) of the sulfur hexafluoride molecule. The literature reports that SF_6 is widely used as a prototype molecule for studying the multi-photon excitation processes with powerful lasers in the infrared range. On the other hand, SF_6 is an important greenhouse molecule with a very long lifetime in the atmosphere. Because of relatively low vibrational frequencies, the hot bands of this molecule contribute significantly to the absorption infrared spectra even at room temperature. This makes the calculation of complete rovibrational line lists required for fully converged opacity modeling extremely demanding. In order to reduce the computational costs, symmetry was exploited at all stages of the first global variational nuclear motion calculations by means of irreducible tensor operators. More than 2600 new vibrational band centers were predicted using our empirically refined *ab initio* potential energy surface. Highly excited rotational states were calculated up to J = 121, resulting in 6 billion transitions computed from an *ab initio* dipole moment surface and distributed over more than 500 cold and hot bands. The final line lists are made available through the TheoReTS information system (http://theorets.univ-reims.fr, http://theorets.tsu.ru). For the first time, the major (ro)vibrational band structures in the wavenumber range corresponding to the strongest absorption in the infra-red are completely elucidated for a seven-atom molecule, providing excellent agreement with the observed spectral patterns. It is shown that the obtained results are more complete than all available line lists, permitting reliable modelling of the temperature dependence of the molecular opacity.

Received 3rd November 2020,
Accepted 3rd May 2021

DOI: 10.1039/d0cp05727d

rsc.li/pccp

1 Introduction

SF_6 is a very important greenhouse gas with a global warming potential ~29 000 times larger than that of CO_2 and its atmospheric lifetime can last up to 3200 years[1,2] since it is chemically inert. SF_6 is an important prototype molecule for infrared laser chemistry and laser isotope separation and for ultrahigh resolution spectroscopy. In particular, various problems related to the laser excitation of SF_6 in the quasi-continuum band formed by congested spectral patterns have been discussed.[3–5] As was reviewed in ref. 5, a study of the literature indicated that, in many cases, the experimental data related with multiple-photon excitation differed by factors of 2 or 3 in absolute value. This makes a more profound insight in the ro-vibrational patterns of levels and transitions of SF_6 in the infrared range. This molecule is mainly used as a gaseous dielectric insulating medium in the electrical industry[6] as well as an atmospheric[7,8] and ocean[9] tracer since its concentration is rapidly increasing in the atmosphere. Vertical profiles have been retrieved by Rinsland *et al.*[10–12] from a series of spectroscopic measurements. Though detected as a trace species, this gas plays an important role in the climate change – as recognized by the Kyoto protocol – making the need to have consistent theoretical models to monitor emissions.

SF_6 belongs to the O_h point group at the equilibrium structure and possesses 15 vibrational degrees of freedom. Due to its high octahedral symmetry, the molecule has doubly and triply degenerate vibrational modes of E and F-types. Among the 6 fundamental vibrations, three stretching modes (ν_1,ν_2,ν_3) transform according

[a] *Groupe de Spectrométrie Moléculaire et Atmosphérique, UMR CNRS 7331, BP 1039, F-51687, Reims Cedex 2, France. E-mail: michael.rey@univ-reims.fr*
[b] *Laboratory of Quantum Mechanics of Molecules and Radiative Processes, Tomsk State University, 36 Lenin Avenue, 634050 Tomsk, Russia*
[c] *V.E. Zuev Institute of Atmospheric Optics, Russian Academy of Sciences, 1, Akademichesky Avenue, 634055 Tomsk, Russian Federation*

† Electronic supplementary information (ESI) available. See DOI: 10.1039/d0cp05727d

Table 1 *Ab initio* (CCSD(T)/CVQZ(DK))[17] and optimized (this work, TW) symmetrized force constants $F_{ij} = \partial^2 V/\partial S_{i\sigma}^{(T)} \partial S_{j\sigma}^{(T)}$ (in *m*dyn, 1 dyn = 10^{-5} N) and equilibrium geometry r_e (in Å, 1 Å = 100 pm) for SF_6. The harmonic wavenumbers ω_i (in cm^{-1}) are given for $^{32}SF_6$. The values in the column "best" correspond to a final empirical optimization (see text) and were used to compute all energy levels. Here ω^{opt} and ω^{best} are the same

	Ab initio[17]	Opt. (TW)	"Best" (TW)
F_{11}	0.224671	0.220313	0.220314
F_{22}	0.151637	0.151728	0.151731
F_{33}	0.172397	0.169213	0.169213
F_{44}	0.306367	0.295676	0.295672
F_{34}	0.174623	0.163428	0.163423
F_{55}	0.226574	0.217858	0.217858
F_{66}	0.200283	0.192309	0.192034
r_e	1.557027	1.555953	1.555938
ω_1	794.8578	787.1117	—
ω_2	653.0081	653.2106	—
$\omega_3{}^a$	964.7491	963.7003	—
$\omega_4{}^a$	633.3353	621.0293	—
ω_5	539.9829	529.5244	—
ω_6	358.9892	351.5388	—

[a] $(\omega_3^{opt}, \omega_4^{opt})$ = (954.3495, 619.6474) and (945.5481, 618.2594) cm^{-1} for $^{33}SF_6$ and $^{34}SF_6$, respectively. The other ω's remain unchanged during isotopic substitutions $^xSF_6 \rightarrow {}^ySF_6$.

to the A_{1g}, E_g and F_{1u} irreducible representations and three bending modes (ν_4,ν_5,ν_6) according to F_{1u}, F_{2g} and F_{2u}. The g type modes are Raman active while ν_3 and ν_4 are infrared (IR) active; only ν_6 is inactive. A brief inspection of the harmonic vibrational modes (see Table 1) shows no simple relationships between ω_i. Consequently, the SF_6 spectrum does not exhibit a clear polyad structure, contrary to many other spherical top molecules like methane.[13] Moreover, the presence of relatively low degenerate vibrational modes, combined with a small rotational constant ($B_e \approx 0.09$ cm^{-1}), makes the rotationally resolved IR spectrum very dense and crowded, even at room temperature (RT). This particular feature gives rise to a tremendous number of degenerate and quasi-degenerate states which strongly complicate analysis of high-resolution spectra. Indeed, it can be shown that the density of lines in SF_6 spectra at T = 296 K is similar to that of small hydrocarbons like CH_4, C_2H_2, and C_2H_4[14–16] at much higher temperatures ($T \approx$ 700–1500 K). The strongest absorption region corresponds to the stretching fundamental IR band $\nu_3(F_{1u})$ detectable by remote-sensing techniques,[7,10] which is located in the atmospheric windows around 10.5 μm. However, the presence of low-lying vibrational energy levels makes the Boltzmann population of the excited states very important at RT leading to a substantial number of hot band (HB) transitions that significantly contribute to the overall opacity. For example, the HB transitions $\nu_k + \sum n_i\nu_i - \sum n_i\nu_i$ ($k = 3$ or $i \neq k$) falling in the two most congested ν_3 and ν_4 regions represent 66 and 70%, respectively, of the integrated intensity at RT. As expected, the "forbidden" mode ν_6 of lowest frequency is involved in most of the HB transitions (n_6 = 1, 2, 3,...) allowed by symmetry.

This paper is devoted to the construction of the first comprehensive, accurate and complete theoretical spectrum in the range 300–3000 cm^{-1} from variational nuclear motion calculations. To achieve this end, our recent full-dimensional *ab initio* potential energy (PES) and dipole moment (DMS) surfaces[17] were used. The quadratic force constants of the PES were empirically optimized for this work. The final aim is to fill the gap between what is available in the current spectroscopic databanks and what is really needed to properly model spectra, in particular in the 10 μm windows of atmospheric interest. The paper is structured as follows. The state-of-the art of SF_6 infrared spectroscopy as well as the main motivation for using global variational calculations is presented in Section 2. Section 3 is devoted to the construction of the Hamiltonian model, the choice of basis sets and the computation of ro-vibrational energy levels. The full calculated line lists for the three most abundant species of the sulfur hexafluoride molecule, namely $^{32}SF_6$, $^{33}SF_6$ and $^{34}SF_6$, as well as validation on raw experimental spectra are presented in Section 4.

2 Effective *versus* global variational approach

Undoubtedly, the biggest challenge concerns the modelling of all HBs, in particular those falling in the spectral windows of atmospheric interest. To this end, highly excited ro-vibrational states have to be properly modelled to predict all necessary transitions belonging to cold and hot bands, even under RT conditions. In the past four decades, a series of experimental and theoretical studies were devoted to this task to improve analysis and spectral predictions (see *e.g.* ref. 18–21). The intensities of the infrared-active fundamental vibrations have been also studied.[22,23] Recently, much effort has been made to analyse high-resolution SF_6 spectra using phenomenological effective Hamiltonians whose parameters were empirically adjusted to experimental data.[24–29] These data have been included in line list compilations like HITRAN[30] or GEISA.[31] The most extensive empirical model to date has been constructed for the main isotopologue $^{32}SF_6$ by the Dijon group for modelling the band system[28] (ν_1,ν_2,ν_3,$\nu_1 + \nu_3$,$\nu_2 + \nu_3$, $2\nu_3$,$\nu_1 + \nu_2 + \nu_3$,$3\nu_3$,$\nu_3 - \nu_1$,$\nu_3 - \nu_2$), recently updated with the set[32] ($\nu_1 + \nu_4$,$\nu_2 + \nu_6$,$\nu_5 + \nu_6$). All these combination bands and overtones are of key importance for computing some HBs falling in the strongly absorbing ν_3 and ν_4 regions. However, a purely empirical approach based on effective Hamiltonians faces several conceptual difficulties with the increasing number of atoms. First, a new analysis has to be conducted for each isotopologue, unlike global variational calculations for which all species can be predicted almost simultaneously (see *e.g.* ref. 34). Second, effective spectroscopic models are based on a line-by-line assignment procedure that suffers from the completeness issues in spectral analyses of heavy atmospheric molecules like SF_6 because of the presence of very few isolated lines in the highly congested spectra. The lack of assignments as well as ambiguities in the fits of the effective models could often lead to a poor determination of some fitted resonance coupling and empirical dipole transition moment parameters. In such cases, the ro-vibrational effective wavefunctions are not reliably determined and do not permit a correct description of the intensity borrowing effects induced by accidental resonances. In order to

partly get around the problem, the most recent analyses have been realized in a pragmatic way: all experimental spectra have been cooled down ($\sim$150 K). This permitted diminishing the density of lines by removing high-J transitions as well as many HBs. In turn, a large amount of information concerning HBs is clearly missing at 296 K. For this reason, the recent line list in the SHeCaSDa SF_6 database[32,33] as well as the closely related HITRAN[30] and GEISA[31] compilations does not contain enough line parameters to reproduce and explain the vibrational band structure at 296 K, in particular around ν_3. Completeness of rovibrational bands will be thus the key requirement for a successful modelling of the radiative transfer.

To analyse rotationally resolved SF_6 absorption spectra in the infrared, it is imperative to elucidate the vibrational structure first. As explained above, all the previous studies have been done essentially by using the empirical approach with *ad hoc* effective models which clearly showed their limits. An important drawback of a purely empirical approach was that no systematic line intensity measurements have been carried out so far for this molecule because of the difficulty in extracting non-blended lines among the highly congested spectral patterns. In this context, the present paper reports for the very first time full-dimensional, accurate and complete variational calculations in the range 300–3000 cm^{-1} – both for line positions and line intensities – for the three most abundant species of the sulfur hexafluoride molecule, namely $^{32}SF_6$ ($\sim$95%),$^{34}SF_6$ ($\sim$4%) and $^{33}SF_6$ ($\sim$0.7%). Though they may suffer from convergence issues concerning line positions, variational global calculations proved to be very efficient in accurately predicting line intensities for both cold and hot bands.[14,16,35–39] The importance of anharmonicity in the vibrational spectra of polyatomic molecules has been studied in many previous works (see *e.g.* ref. 40–45). The focus of our study is different. Here, the aim was to produce complete line lists by (i) including line-by-line intensities for a variationally converged set of spectral transitions at medium or high spectral resolution, (ii) including all hot bands and (iii) providing the temperature dependence of the global opacity. As discussed in a recent review on theoretical rotationally resolved spectral predictions,[38] only a few groups[46–48] (and see references therein) have recently developed specific tools for such applications, but for smaller molecules. In this paper, we focus on the main results permitting one to explain the complicated features in the observed SF_6 spectra. Technical details about the extension of the methods previously developed for smaller molecules[35,49–52] are beyond the scope of this paper.

3 Quantum-mechanical nuclear motion calculations

3.1 Refined potential energy surface

As a starting point, the full-dimensional *ab initio* potential and dipole moment surfaces have been computed at the CCSD(T)/CVQZ level of theory (including Douglas-Kroll relativistic corrections), as reported in ref. 17. However, the harmonic frequencies computed from the pure *ab initio* force constant matrix F^{ab} of the PES, together with the geometry-based G Wilson matrix, were off by about $\sim$1 to 10 cm^{-1}. The *ab initio* equilibrium geometry r_e^{ab} was not accurate enough to reproduce the rotational structure. In order to better match experimental fundamental band centers, the approach proposed in ref. 35 was adopted to refine the initial solutions $\{F^{ab}, r_e^{ab}\}$. A set of optimized quadratic force constants F^{opt} for each symmetry block as well as a refined value r_e^{opt} were thus obtained (see Table 1) while the high-order *ab initio* force constants were kept unchanged and fixed at the values of ref. 17. The axis convention, the atom numbering as well as the definition of the symmetry coordinates can be found in ref. 17 and 53.

3.2 Hamiltonian model and symmetry

Since SF_6 is a semirigid molecule without large amplitude vibrations, the normal mode coordinates $q_{k\sigma_k}^{(\Gamma_k)}$ were used to build the Hamiltonian in the Watson–Eckart formalism[54] implemented in the TENSOR computer code. Here, Γ_k denotes an irreducible representation and σ_k a label to distinguish the degenerate components of a vibrational mode k. Simple analytically solvable potential representations for independent vibrational modes do not permit approaching experimental accuracy in high-resolution spectra. The aim of this work was to account as fully as possible for the high-order anharmonicity of the PES and for the coupling among ro-vibrational states. To this end, we do not use perturbation theory, as often employed in the literature for polyatomic molecules, but the symmetry-adapted variational approach in 18 dimensions: 15 vibrational and 3 rotational degrees of freedom. For a full account of symmetry and to build linearly independent polynomials in q at a given order of the expansion of the complete nuclear motion Hamiltonian, the use of irreducible tensor operators (ITOs) is an optimal choice. The ITO formalism in the version proposed by Nikitin *et al.*[55] turned out to be very appropriate to describe the coupling of degenerate vibrations. Note that the ITO formalism, initially designed for effective models,[13] is extended here for the first time for global variational nuclear motion calculations of XY_6-type molecules. Concerning the construction of rotational basis functions adapted to the non-Abelian O_h point group for very high J values, the symmetrization procedure proposed by Rey *et al.*[56] was employed. In summary, all the (3+15) rotation-vibrational degrees of freedom were simultaneously taken into account to build the sum-of-product Hamiltonian in the ITO representation – including all intra-molecular coupling terms and anharmonicities at a given order – as well as the direct-product symmetry-adapted basis functions.

In the next step, a ''brute-force'' 18-dimensional variational calculation of complete rotationally resolved spectra using so many terms in the Hamiltonian up to J = 120 with standard tools and direct eigensolvers was not feasible. To overcome the first obstacle related to the large number of Hamiltonian terms, the reduction technique described in ref. 49, 51 and 52 was applied in a slightly modified form: instead of expressing the reduced tensor Hamiltonian in terms of harmonic oscillator creation and annihilation operators, this latter one was expressed directly as a function of $q_i^{(\Gamma)}$ and of conjugate momenta $p_i^{(\Gamma)} = -id/dq_i^{(\Gamma)}$. This allowed us to drastically reduce the number of

terms and thus to accelerate the calculation of all matrix elements *via* the Wigner–Eckart theorem. Briefly, the initial m-th order polynomial expansion of the Eckart–Watson Hamiltonian in $(q_i^{(\Gamma)}, p_i^{(\Gamma)})$ was reduced to a transformed polynomial of smaller order $m' < m$ without loss of accuracy of the eigenvalues. It was then converted to the ITO representation.[35] For this work, both the normal-mode, refined PES and kinetic energy part have been expanded at order $m = 9$ and reduced at order $m' = 6$. A final ITO Hamiltonian $H^{(9\rightarrow 6)}$ composed of $\sim$5600 non-zero ro-vibrational parameters was built. In the case of SF_6, such normal mode representation proved to be very efficient and allowed a fast convergence of the Hamiltonian expansion. This type of calculation inherently and systematically accounts for all intra-molecular coupling terms and for anharmonicities through a power series expansion in normal coordinates q in both the kinetic and potential parts.

3.3 Computation of vibrational energy levels

In the next step, we have solved the eigenvalue/eigenfunction problem for the full anharmonic potential with $J = 0$. The vibrational energies were obtained by the exact numerical diagonalization of the Hamiltonian matrix built in a direct-product "pruned" basis defined by a set of primitive harmonic oscillator vibrational functions such that[35]

$$F_{\mathbf{k}}(n) \Leftrightarrow \sum_{i=1}^{6} \kappa_i v_i \leq n, \qquad (1)$$

with $v_i = 0,\ldots,n$. Here, κ_i (≥ 1) are weight coefficients chosen to select an appropriate number of stretching and bending basis functions. The maximum number of quanta $v_i^{\max}$ for each mode is given by the integer part $[n/\kappa_i]$. For this work, $n = 10$ and $\kappa = \{1.05, 1, 1.05, 1, 1, 1\}$ were chosen, resulting in 32 579, 31 263, 63 824, 91 728, 93 029, 29 960, 30 640, 60 582, 94 470 and 93 775 functions for the symmetry blocks $A_{1\tau}$, $A_{2\tau}$, E_τ, $F_{1\tau}$, $F_{2\tau}$ ($\tau = g$ and u), respectively. For a given block of symmetry Γ, we have thus included in the calculations the set of eigensolutions up to $\{E_v^{\Gamma(n=10)}, \Psi_v^{\Gamma(n=10)}\}$. This compressed anharmonic vibrational basis will be used in the next step for rovibrational calculations. A comparison of our variationally computed energies with the empirical levels derived from effective models is given in Table 2 for $^{32}SF_6$. The error in the fundamental bands is below 10^{-3} cm^{-1}. A very good agreement proves the high accuracy of our refined PES, on the one hand, and validates all the theoretical "machinery" for solving the nuclear Schrödinger equation, on the other hand. However, there remain relatively large discrepancies (*e.g.* -0.4 cm^{-1} for $2\nu_1 + \nu_3$) that can be partly explained by the fact that only the quadratic force constants of the PES have been empirically refined using fundamental band origins. By doing this, we assumed that a large part of the errors was due to uncertainty in the quadratic terms ("harmonic" contribution to the PES). Higher-order terms in the PES also play a substantial role in for the modeling highly excited states but they were fixed at their *ab initio* values in this study. Consequently, though they were improved some overtones and combination bands did not reach the same accuracy as the fundamental bands.

In order to check the basis set convergence of $J = 0$ energies, we have also computed the $\Gamma = A_{1g}$ levels by using a larger set of primitive functions with the cut-off $n = 11$ in eqn (1). In comparison with $n = 10$, the convergence errors for 1-, 2-, 3-, 4-, 5- and 6-quanta levels turned out to be 0.0001, 0.0003, 0.006, 0.02, 0.15, 0.9 cm^{-1} on average. Clearly, though their contributions to the absorption spectrum are almost negligible, very highly excited vibrational levels are not fully converged as expected. Unfortunately, the use of the $F_k(11)$ basis set – composed of about twice as many basis functions than $F_k(10)$ – goes beyond our computer resources to treat all symmetry blocks. Finally, the most extensive list composed of 2686 (in comparison with

Table 2 Selected vibrational band centers (in cm^{-1}) for $^{32}SF_6$ computed from variational calculations using our refined PES (this work, TW) and from empirical effective models.[20,26–29,57] Calculated band centers for $^{33}SF_6$ and $^{34}SF_6$ as well as the isotopic shifts Δ (in cm^{-1}) with respect to $^{32}SF_6$ are also given (see text for explanation)

	$^{32}SF_6$			$^{33}SF_6$		$^{34}SF_6$	
Band	Empirical	Variational (TW)	Emp.-Var.	Variational (TW)	$\Delta(32 \rightarrow 33)$	Variational (TW)	$\Delta(32 \rightarrow 34)$
$\nu_6(F_{2u})$	347.7367	347.7366	0.0001	347.7504	−0.0137	347.7635	−0.0269
$\nu_5(F_{2g})$	523.4490	523.4494	−0.0004	523.4705	−0.0215	523.4906	−0.0412
$\nu_4(F_{1u})$	614.9819	614.9821	−0.0002	613.6757	1.3062	612.3611	2.6210
$\nu_2(E_g)$	643.3737	643.3734	0.0003	643.3908	−0.0171	643.4073	−0.0339
$\nu_1(A_{1g})$	774.5453	774.5454	−0.0001	774.5721	−0.0268	774.5968	−0.0514
$\nu_3(F_{1u})$	948.1025	948.1024	0.0001	939.0272	9.0753	930.4646	17.6378
$\nu_2 + \nu_6(F_{2u})$	989.1190	989.1653	−0.0463	989.2029	−0.0839	989.2324	−0.0671
$\nu_2 + \nu_6(F_{1u})$	991.2740	991.3071	−0.0331	991.2641	0.0099	991.2401	0.0670
$\nu_2 + \nu_4(F_{1u})$	1257.0849	1257.0190	0.0659	1255.7262	1.3587	1254.4199	2.5991
$\nu_1 + \nu_4(F_{1u})$	1388.3820	1388.3192	0.0628	1387.0563	1.3257	1385.7712	2.5480
$\nu_2 + \nu_3(F_{1u})$	1587.7173	1587.9089	−0.1916	1578.9063	8.8110	1570.3867	17.5222
$\nu_2 + \nu_3(F_{2u})$	1591.1923	1591.0909	0.1014	1582.1352	9.0571	1573.6517	17.4392
$\nu_1 + \nu_3(F_{1u})$	1719.7390	1719.8226	−0.0836	1710.8106	8.9284	1702.2811	17.5415
$2\nu_3(A_{1g})$	1889.0500	1889.3553	−0.3053	1871.3404	17.7096	1854.3259	35.0294
$2\nu_3(E_g)$	1891.6000	1892.0052	−0.4052	1873.9120	17.6880	1856.8083	35.1969
$2\nu_3(F_{2g})$	1896.5300	1896.5375	−0.0075	1878.4443	18.0857	1861.3746	35.1629
$\nu_1 + \nu_2 + \nu_4(F_{1u})$	2028.1549	2027.9459	0.2090	2026.7878	1.3671	2025.5056	2.4403
$2\nu_1 + \nu_4(F_{1u})$	2160.0257	2159.9263	0.0994	2158.3789	1.6468	2158.2626	1.6637
$2\nu_1 + \nu_3(F_{1u})$	2489.4682	2489.8765	−0.4083	2480.5044	8.9638	2473.5020	16.3745

~25 ones available in the literature) selected vibrational energy (sub)levels up to 3000 cm^{-1} is given in the ESI† S_1. Selected vibrational band centers for $^{33}SF_6$ and $^{34}SF_6$ as well as the isotopic shifts $\Delta(32 \rightarrow 33)$ and $\Delta(32 \rightarrow 34)$ are also given in Table 2. As already noted in ref. 21, "anomalous" negative frequency shifts are observed. Such a feature is generally possible when some harmonic frequencies ω_i remain unchanged during isotopic substitutions. For SF_6, anomalous shifts are thus expected for ν_1, ν_2, ν_5 and ν_6. As stated in ref. 21, "the change in the mixed-mode anharmonicity constants can lower the ground-state energy more than the excited-state energy, resulting in an increase in ν". The negative shift in ν_1 between $^{32}SF_6$ and $^{34}SF_6$ was predicted to be -0.044 cm^{-1} in ref. 21 while Volkov *et al.*[58] have observed a shift of -0.0574 cm^{-1}. In this work, the shift is given by -0.0514 cm^{-1} which is close to the observation. Similar shifts were predicted for ν_2, ν_5 and ν_6, increasing the band origins from 0.025 to 0.04 cm^{-1}. In this work, the band origins increase by 0.0269 to 0.0412 cm^{-1}. Note that a similar situation was reported in ref. 59 between $^{12}CH_4$ and $^{13}CH_4$ for $n\nu_2$ because ω_2 is unchanged during the substitution $^{12}C \rightarrow {}^{13}C$. Note that recently, $J = 0$ energy levels were reported[60] for the UF_6 molecule that belongs to the same O_h point group, by using a rectangular collocation approach and the product of harmonic basis functions but without exploiting the full symmetry.

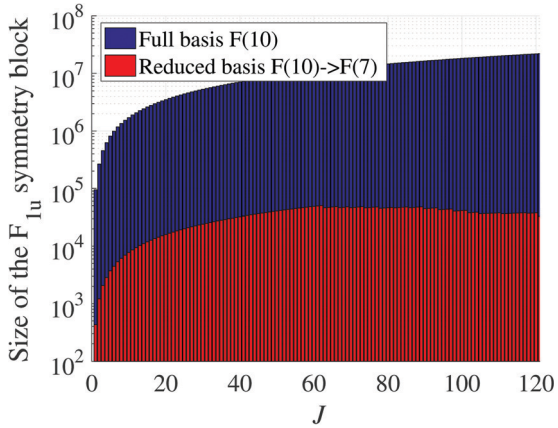

Fig. 1 Dimension of the Hamiltonian matrices to be diagonalized for the symmetry block F_{1u} as a function of J when using the full and reduced vibrational eigenfunctions $\Psi^{(10)}$ and $\Psi_v^{(10\rightarrow7)}$, respectively.

3.4 Rovibrational energy levels for high-J values

For $J > 0$, "brute-force" calculations from the direct-product basis set (1) coupled with symmetric-top wave functions are

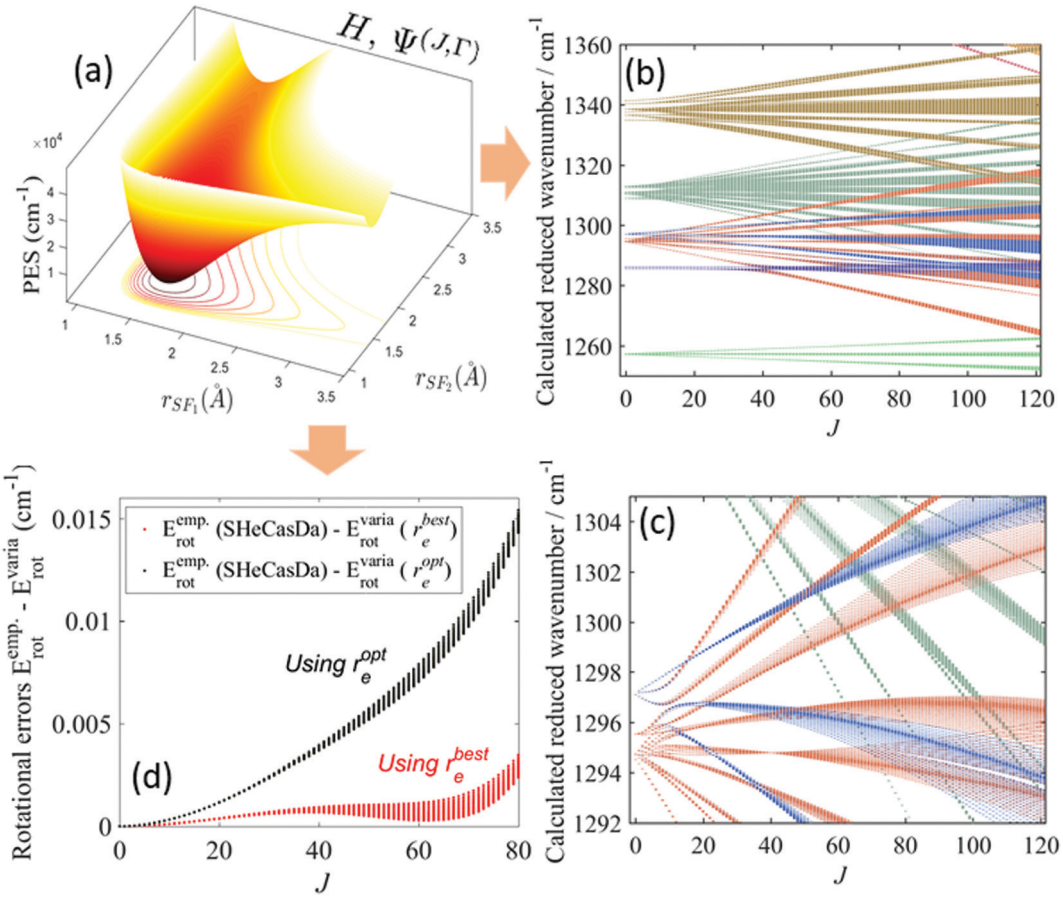

Fig. 2 (a) Cut of the SF_6 PES[17] along the S–F_1 and S–F_2 bonds. (b) Reduced upper state energy levels for $\nu_2 + \nu_4$, $2\nu_2$, $\nu_3 + \nu_6$, $\nu_1 + \nu_5$, $\nu_4 + 2\nu_6$ and $\nu_2 + \nu_6$, listed in increasing energy order. (c) Portion of reduced upper state energy levels for $\nu_3 + \nu_6$ and $\nu_1 + \nu_5$. (d) Rotational errors using our optimized (r_e^{opt}) and "best" (r_e^{best}, see text) equilibrium geometry values.

clearly proscribed using the available direct eigensolvers. Instead of considering iterative eigensolvers, as often recommended,[61] we have followed the method developed in our previous work for smaller molecules.[50] To this end, a set of reduced eigenfunctions $\Psi_v^{\Gamma(n\to m)}$ associated with a basis $F_{k^{\Gamma}}(m)$ were obtained using the projection technique onto an appropriately chosen smaller subspace with $m < n$ for which $J > 0$ calculations are feasible. For this work, rovibrational energy levels were computed up to $J_{max} = 121$ using $m = 7$. In the last step a final compression of the basis set was applied by selecting p% of eigenvectors where $p = 100$ up to $J = 61$ and then gradually decreases to $p = 33$ at $J = 121$. This strategy allows one to keep approximately the same memory requirement as J increases, bearing in mind that accurate calculations are generally not necessary for $J > 80$ since the corresponding transitions are very weak at room temperature. Note that the J_{max} value was chosen to ensure convergence of the partition function $Q(T)$ at $T = 296$ K. This gives $Q(296) = 1607253.7$ for $^{32}SF_6$, within 0.05% of error. To better illustrate the use of the reduction procedure, the maximum dimension of the eigenvector matrix for $J = 121$ is 106784×35311; without reduction it would have been (23×23) millions. Fig. 1 displays the size of the symmetry blocks F_{1u} as a function of J when using or not the reduced vibrational eigenfunctions $\Psi_v^{(10\to 7)}$. In this figure (see the red part), we clearly see that the number of rovibrational basis functions decreases beyond $J = 61$ because of reduction of the vibrational subspace which varies from 100% to 33%.

In order to validate the optimized value r_e^{opt} for the equilibrium structure (see Table 1), let us first focus on the accuracy of our variationally predicted rotational energy levels $E_{rot}^{varia.}$. To this end, we did a direct comparison with energies $E_{rot}^{emp.}$ obtained from the empirical effective Hamiltonian.[24] Fig. 2(d) displays the rotational errors $\Delta_{rot} = E_{rot}^{emp.} - E_{rot}^{varia}$ up to $J = 80$. We clearly see in this figure that the discrepancy increases with J because r_e^{opt} was optimized only for low-J values by using a small basis set during our refinement procedure. A way to improve the accuracy was to introduce an empirical correction to E_{rot}^{varia} by the term $\delta_{rot} = 1.8 \times 10^{-6} J(J+1)$ cm^{-1}. This correction is equivalent to a shift in the equilibrium geometry by $\delta_{re} = -1.5 \times 10^{-5}$ Å to give the best estimated value $r_e^{best} = r_e^{opt} + \delta_{re} = 1.555938$ Å. As a direct consequence, F^{opt} had to be slightly modified ($\equiv F^{best}$) to preserve the accuracy of the vibrational levels. Finally, both the Hamiltonian model and energy levels were recalculated using the newly optimized couple $\{F^{best}, r_e^{best}\}$ given in Table 1. This results in the improved set of rotational levels (see Fig. 2(d)) whose uncertainty does not exceed 0.0035 cm^{-1} at $J = 80$. Above this value, the extrapolation error of the effective model beyond the range of observed data also contributes to Δ_{rot}, which increases up to 0.1 cm^{-1} for $J = 120$.

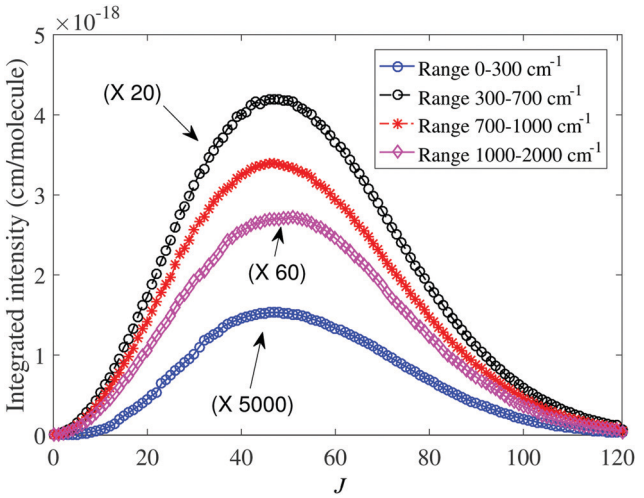

Fig. 4 Integrated intensities (in cm per molecule) for different spectral ranges at different values of the rotational angular momentum J.

Selected sets of computed rovibrational energy levels are displayed in Fig. 2(b and c) in the region of $\nu_2 + \nu_4$, $2\nu_2$, $\nu_3 + \nu_6$, $\nu_1 + \nu_5$, $\nu_4 + 2\nu_6$ and $\nu_2 + \nu_6$, listed in increasing energies. The sequence of quasi-degenerate groups of quantum levels called clusters is well known for SF_6 and was explained by semi-classical analysis.[62] The different colours give information on how the energy levels are distributed and on how the states are mixed altogether. Except for strong local resonances (*e.g.* between $\nu_3 + \nu_6$ and $\nu_1 + \nu_5$ at $J = 7$, see Fig. 2(c)), the inter-band couplings appear to be relatively weak for SF_6. As an indicator of the degree of the coupling, the average value of the absolute maximum contribution in the wavefunction decomposition for the first 100 vibrational levels is 0.922, which is close to 1. This may partly explain why the convergence of the variational

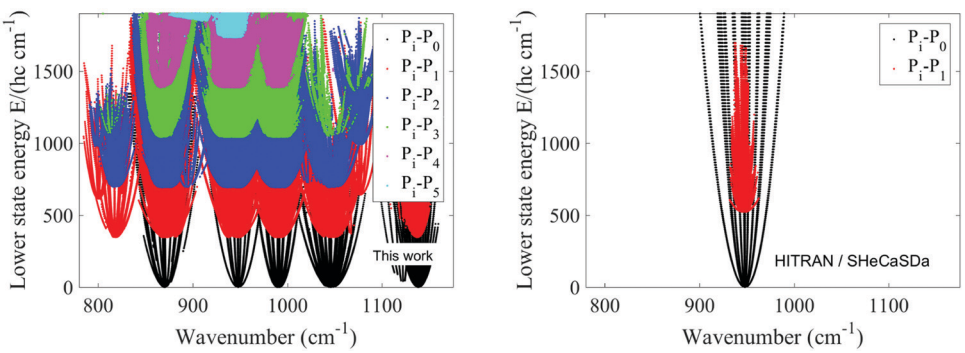

Fig. 3 Comparison of the lower state energies for transitions involved in the TheoReTS database[48] (left panel, this work) and in HITRAN[30]/SHeCaSDa[32] (right panel). The intensity cut-off was fixed at 10^{-25} cm per molecule. For the definition of $P_i - P_j$, see text.

calculation for SF_6 is rather fast compared to other molecules like methane or ethylene.

4 Construction of the line lists – validation

4.1 Methodology

The ultimate aim of this work was the construction of the room-temperature *ab initio* based line lists for $^{32}SF_6$, $^{33}SF_6$ and $^{34}SF_6$ in the range 300–3000 cm^{-1}. Here, we briefly recall the methodology obtained by the extension of the approach developed in our previous works[35,49–52] for smaller molecules.

– *Dipole moment*: the line intensities were computed using the home-made TENSOR code from the fourth order normal-mode DMS reported in ref. 17. In order to be consistent with the Hamiltonian treatment, the dipole moment component $\mu_z(q)$ which transforms as the irreducible representation F_{1u} in the molecular-fixed frame was also converted to ITOs. A set of 213 *ab initio* dipole moment parameters in the ITO representation were thus deduced algebraically and used to compute line intensities. The explicit use of symmetry considerations when building the dipole moment turns out to be of great help to deduce all the symmetry-allowed transitions $(J', C') \leftarrow (J'', C'')$ *via* the selection rules $\Delta J = 0,\pm1$ and $C' \times C'' \supset A_{1u}$. For intensity calculations, the nuclear spin statistical weights

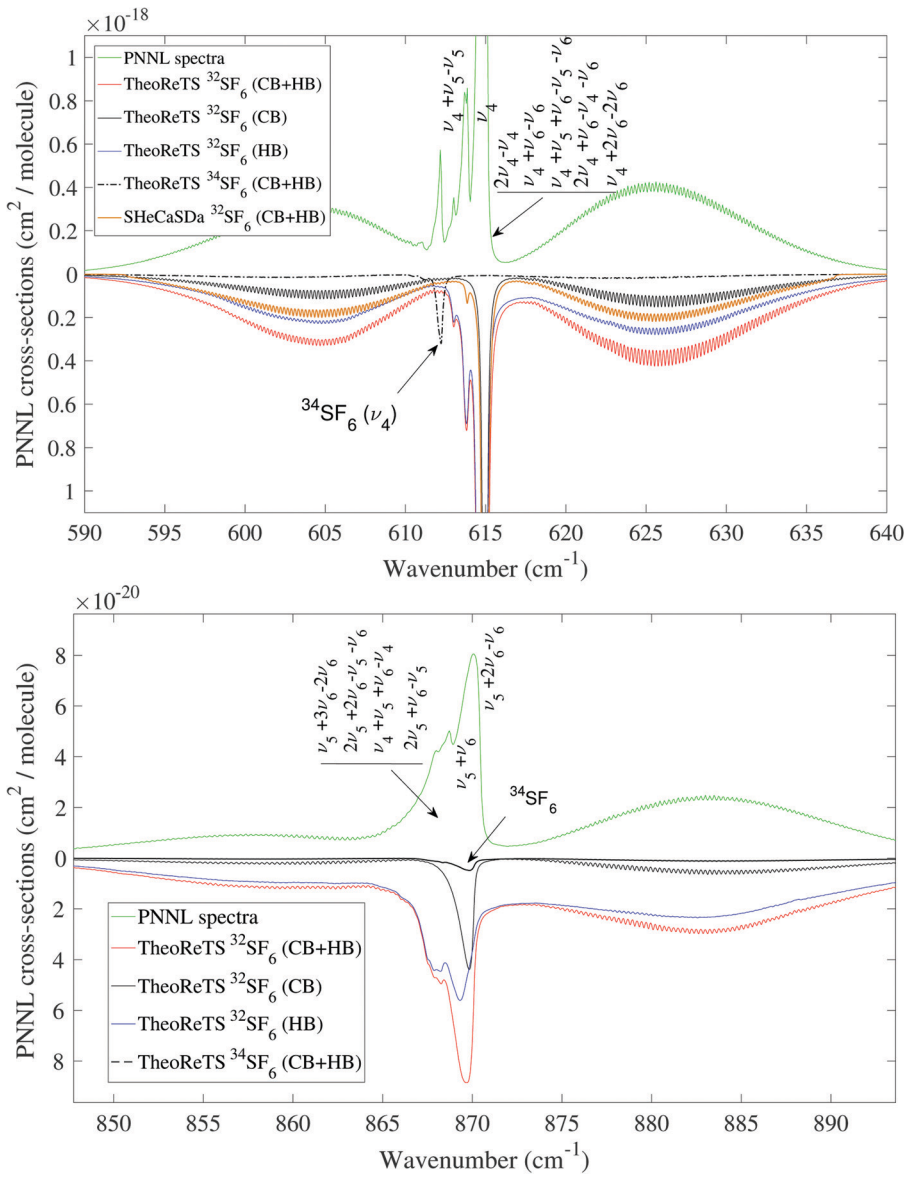

Fig. 5 Comparison of theoretical absorption spectra of $^{32}SF_6$ + $^{34}SF_6$ (red and dotted curves upside down in the lower panels) with experimental medium resolution PNNL records[63] (green curve in the upper panels) at room temperature in the range 590–895 cm^{-1}. Contribution of the cold (CB) and hot (HB) bands is plotted and the strongest bands are indicated (the complete list can be found in ESI,† S_2). A comparison with the SHeCaSDa database[32] (brown curve) is also given in the range 590–640 cm^{-1}.

for $^{32}SF_6$ and $^{34}SF_6$ are 2, 10, 8, 6, and 6 for species $A_{1\tau}$, $A_{2\tau}$, E_τ, $F_{1\tau}$ and $F_{2\tau}$ ($\tau = g, u$), respectively, while those of $^{33}SF_6$ have to be multiplied by a factor 4.

– *Completeness*: the construction of complete line lists is essential for atmospheric retrievals and opacity calculations. Completeness is controlled by two cut-off criteria, namely the lower-state energy and the intensity cut-offs. A prior in-depth study allowed us to fix the maximum lower state energy E_{low}^{max} at $[2600 + 0.09J(J+1)]$ cm^{-1} to control all necessary HBs. Fig. 3 (left) displays all lower state energies involved in rovibrational transitions around 10 μm by taking an intensity cut-off of 10^{-25} cm per molecule at 296 K. In this figure are depicted all cold band transitions ($E_{low} \equiv E_{rot}$) denoted as $P_i - P_0$ as well as all hot band transitions starting from a lower state with n quanta of excitation, denoted as $P_i - P_n$ ($n > 0$). To illustrate the gap with the literature, a comparison of the lower state energies involved in our calculations and in the currently available lists HITRAN and SHeCaSDa is shown in Fig. 3 (right).

In order to properly converge the integrated intensities using an optimal number of lines, we chose to split the whole wavenumber range W in three intervals. For each interval of $^{32}SF_6$, a specific intensity cut-off I_{cut}^{max} was defined as follows: for $300 < W \leq 910$ cm^{-1}, $I_{cut}^{max} = 5 \times 10^{-29}$ cm per molecule; for $910 < W \leq 965$ cm^{-1}, $I_{cut}^{max} = 7 \times 10^{-28}$ cm per molecule and $I_{cut}^{max} = 1 \times 10^{-29}$ cm per molecule otherwise. It is shown in Fig. 4 that the integrated intensities are nearly converged at $J_{max} = 121$

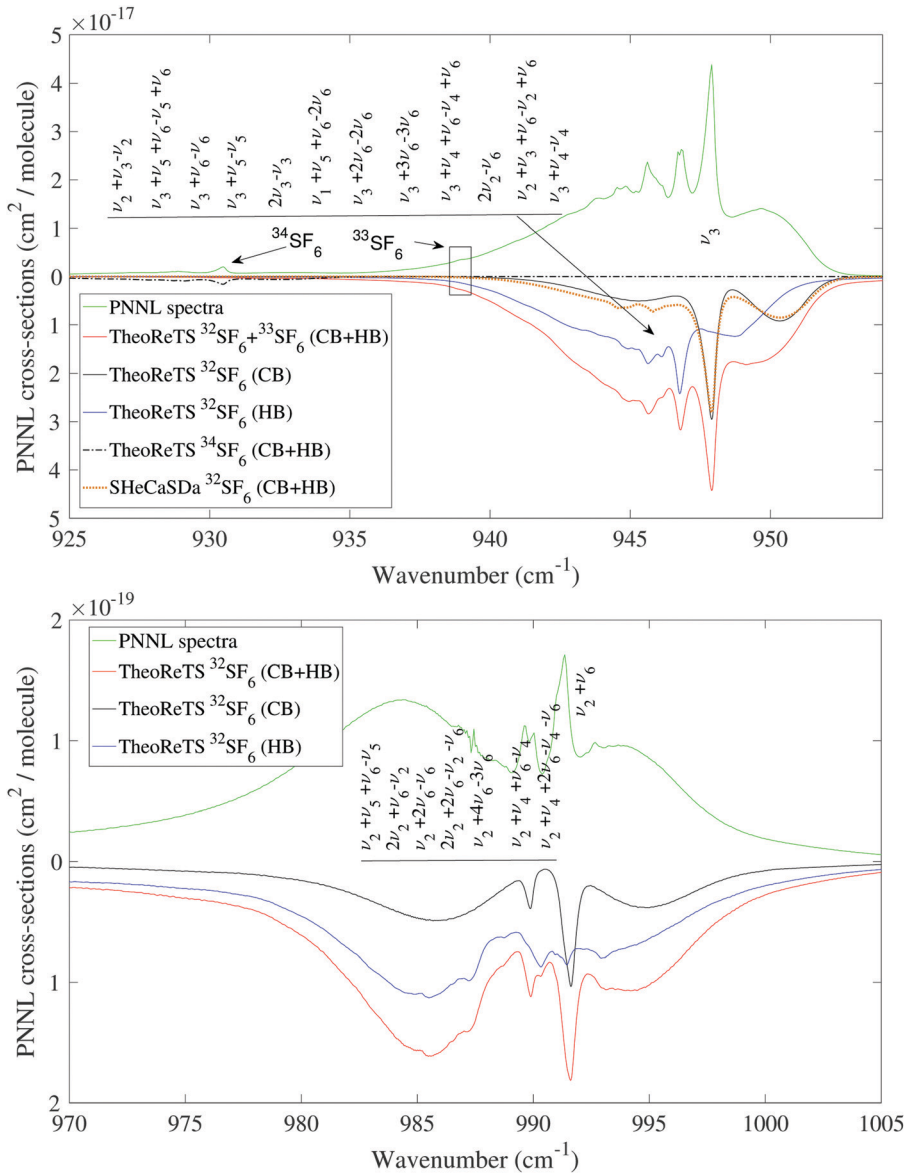

Fig. 6 Comparison of theoretical absorption spectra of $^{32}SF_6$ + $^{33}SF_6$ + $^{34}SF_6$ (red and dashed curves upside down in the lower panels) with experimental medium resolution PNNL records[63] (green curve in the upper panels) at room temperature in the range 925–1005 cm^{-1}. Contribution of the cold (CB) and hot (HB) bands is plotted and the strongest bands are indicated (the complete list can be found in ESI,† S_2). A comparison with the SHeCaSDa database[32] (brown dotted curve) is also given in the range 925–960 cm^{-1}.

using these cut-offs. Concerning $^{33}SF_6$ and $^{34}SF_6$, since only strong lines are present in the spectra with natural abundance, a constant intensity cut-off of 10^{-26} cm per molecule was applied.

– *Strong and weak lines*: at this stage, the major limitation when building the SF_6 line lists is the huge number of transitions that becomes hardly manageable for practical applications. The full line list for $^{32}SF_6$ contains 6 billion lines when using the previously defined cut-offs. To make the problem tractable for the user, we have adopted the same strategy as for CF_4[35] and hot methane.[14] This consists in extracting from the full list a smaller subset composed of strong and medium lines which are responsible for all sharp absorption features in the spectrum. In our calculations, this set of "strong" lines is composed of a few million transitions that contribute to the largest absorption in the spectra. They are selected by applying the condition $I \geq \alpha I_{\mathrm{cut}}^{\max}$ where α is a cut-off factor. For this work, the value $\alpha = 1000$ was chosen for $W \leq 300$ cm^{-1} and $\alpha = 5000$ otherwise. The remaining set is formed by an accumulation of several million (and even billions in our case) very weak overlapping lines, resulting in a smooth quasi-continuum (QC). Though the contribution of each individual weak line could be very small, the whole set plays a substantial role in the modelling of the overall opacity.

4.2 Validation and distribution

Fig. 5–7 give examples of comparison between theoretical (including the CB, HB, and total CB + HB contributions shown in different colors) and experimental PNNL raw spectra[63] which have been recently included in HITRAN as absorption cross-sections without line-by-line assignments. All simulations were made at a resolution of 0.1 cm^{-1} and a pressure of 760 Torr using a path length of 20 cm and a Voigt profile. The main absorption bands are indicated in these figures and the integrated

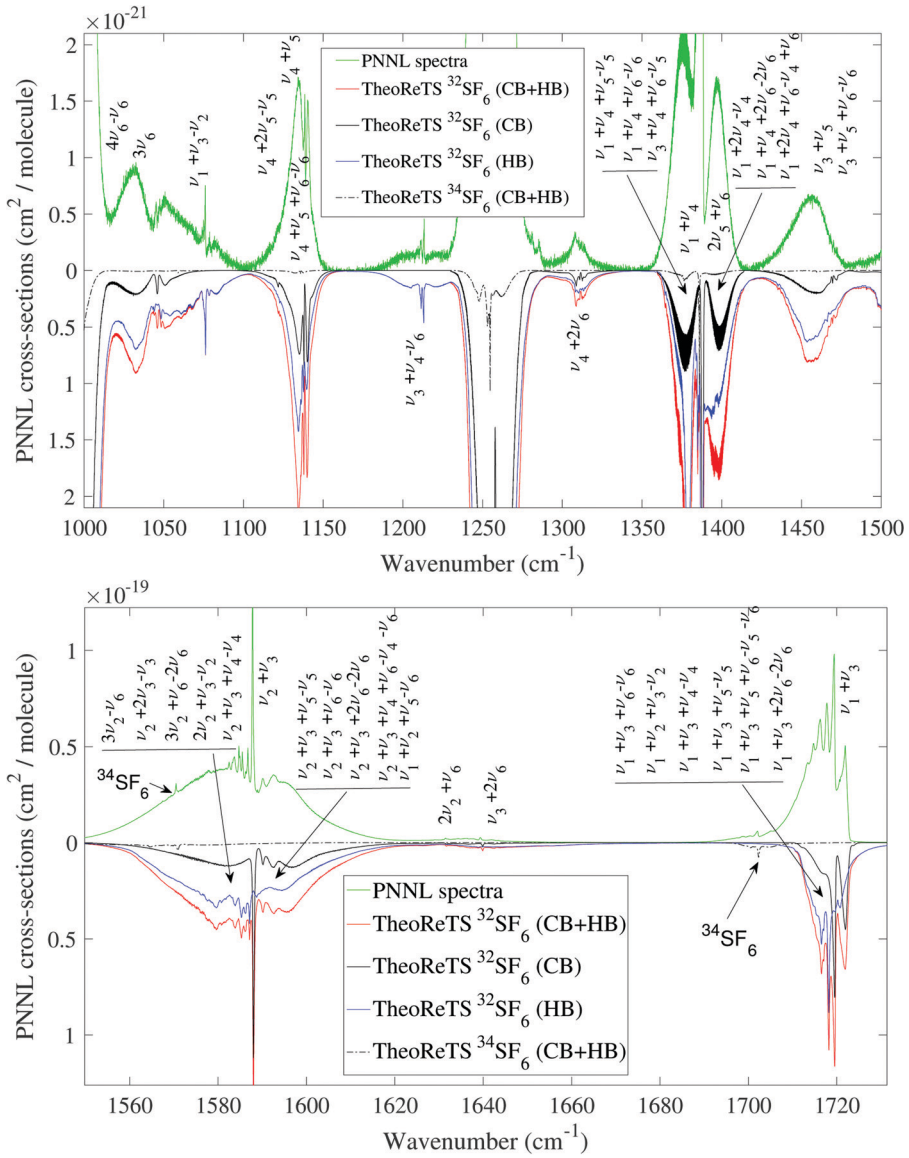

Fig. 7 Comparison of theoretical absorption spectra of $^{32}SF_6$ + $^{34}SF_6$ (red and dashed curve upside down in the lower panels) with experimental medium resolution PNNL records[63] (green curves in the upper panels) at room temperature in the range 1010–1730 cm^{-1}.

Table 3 Integrated intensities $\sum S_{ij}$ ($\times 10^{17}$ cm per molecule) for the strongest absorption bands in the ν_4 and ν_3 regions of $^{32}SF_6$ and comparison with the SHeCaSDa database[32]

ν_4 region				ν_3 region			
Center	Band	$\sum S_{ij}$ (TW)	$\sum S_{ij}$ (SHeCaSDa)	Center	Band	$\sum S_{ij}$ (TW)	$\sum S_{ij}$ (SHeCaSDa)
614.982	ν_4	0.369	0.394	948.102	ν_3	6.16	5.53
615.727	$\nu_4 + \nu_6 - \nu_6$	0.203	0.214	946.761	$\nu_3 + \nu_6 - \nu_6$	2.99	—
614.623	$\nu_4 + \nu_5 - \nu_5$	0.086	—	945.343	$\nu_3 + \nu_5 - \nu_5$	1.40	1.18
614.790	$\nu_4 + 2\nu_6 - 2\nu_6$	0.073	—	946.088	$\nu_3 + \nu_4 - \nu_4$	0.901	—
614.658	$2\nu_4 - \nu_4$	0.073	—	946.033	$\nu_3 + 2\nu_6 - 2\nu_6$	0.869	—
616.162	$\nu_4 + \nu_5 + \nu_6 - \nu_5 + \nu_6$	0.045	—	944.536	$\nu_2 + \nu_3 - \nu_2$	0.517	0.452
615.694	$2\nu_4 + \nu_6 - \nu_4 + \nu_6$	0.039	—	944.060	$\nu_3 + \nu_5 + \nu_6 - \nu_5 + \nu_6$	0.500	—
613.939	$\nu_2 + \nu_4 - \nu_2$	0.032	—	946.370	$\nu_3 + \nu_4 + \nu_6 - \nu_4 + \nu_6$	0.393	—
614.894	$\nu_4 + 3\nu_6 - 3\nu_6$	0.020	—	948.435	$2\nu_3 - \nu_3$	0.231	—
613.633	$\nu_2 + \nu_4 + \nu_6 - \nu_2 + \nu_6$	0.017	—	948.393	$\nu_2 + \nu_3 + \nu_6 - \nu_2 + \nu_6$	0.188	—
614.355	$2\nu_4 + \nu_5 - \nu_4 + \nu_5$	0.016	—	942.521	$\nu_3 + 3\nu_6 - 3\nu_6$	0.166	—

Table 4 Sum of experimental PNNL cross-sections (cm^2/molecule) for SF_6 at room temperature and comparison with simulations using the TheoReTS line list (this work) and the SHeCaSDa database[32]

Region (cm^{-1})	TheoReTS (TW)	PNNL	Error (%)
560–650	1.98×10^{-16}	2.23×10^{-16}	11.2
820–920	1.55×10^{-17}	1.63×10^{-17}	4.9
920–965	3.12×10^{-15}	3.20×10^{-15}	2.3
965–1005	4.15×10^{-17}	4.01×10^{-17}	−3.4
1005–1500	7.44×10^{-18}	7.62×10^{-18}	2.4
1550–1730	3.23×10^{-17}	3.47×10^{-17}	6.9
Region (cm^{-1})	SHeCaSDa[32]	PNNL	Error (%)
560–650	1.01×10^{-16}	2.23×10^{-16}	54.7
910–965	1.19×10^{-15}	3.20×10^{-15}	62.8

intensities for the strongest absorption bands in the ν_4 and ν_3 regions of $^{32}SF_6$ are given in Table 3. Though a good agreement can be seen in Fig. 5–7, plotting residuals between the PNNL and the TheoReTS data is quite a tricky task. On the one hand, the line positions, in particular for hot bands, may be shifted, and on the other hand, a study of PNNL line profile shapes was beyond the scope of this work, thus making a proper comparison difficult. Instead, the accuracy of the calculated patterns can be established by a direct comparison of the absorption cross-sections of SF_6 in the regions displayed in Fig. 5–7. The results are summarized in Table 4. The agreement between theory and the observed PNNL spectra in the strongest absorption region around 947 cm^{-1} is clearly confirmed as the deviation in the integrated cross-sections is only 2.3%. Assuming the value of the integrated intensity for ν_4 is consistent in SHeCaSDa (see Table 3), the first half of the 11% of error between PNNL and TheoReTS around 615 cm^{-1} can be possibly explained by a deviation (about 2.8%) of our dipole moment first derivative $\partial\mu/\partial q_4$ and the other half by line strength errors for some hot bands. The experimental uncertainty in weaker absorption intervals due to baseline issues could also significantly contribute to the deviation between PNNL and TheoReTS in Table 4. Overall, to our knowledge, such an agreement in rovibrational absorption patterns of seven-atomic molecules has not been obtained so far in previous theoretical calculations.

Spectra simulations using the SHeCaSDa line lists are also shown in Fig. 5 and 6 for the regions of ν_4 (around 600 cm^{-1}) and ν_3 (around 950 cm^{-1}). The latter ones do not reproduce the overall absorption shape of the room-temperature observed spectra due to the lack of HBs, as indicated by Tables 3 and 4 and corroborated by Table 5. Among the 500 cold and hot bands contained in the "strong" subset of our calculated line list of $^{32}SF_6$, the integrated intensities for the 260 strongest ones can be found in ESI,† S_2. For example, the most important HB $\nu_3 + \nu_6 - \nu_6$ that represents half of the ν_3 contribution to the absorption is clearly lacking in the SHeCaSDa and HITRAN line lists (see Table 3).

A detailed description of the final line lists for $^{32}SF_6$ is given in Table 5. The number of transitions in the "strong lines

Table 5 Summary of the final line lists for $^{32}SF_6$ and comparison with the SHeCaSDa database.[32] The number of strong and quasi-continuum (QC) lines (#lines) as well as the integrated intensities ($\sum$lines) are indicated. Here, CB = cold bands, HB = hot bands

	Strong lines		QC		SHeCaSDa[32]		
Range/type	#Lines	$\sum$lines	#Lines	$\sum$Lines	#Lines	$\sum$Lines	Deviations[a]
	$\times 10^6$	$\times 10^{-16}$	$\times 10^9$	$\times 10^{-16}$	$\times 10^5$	$\times 10^{-16}$	
300–910 CB	0.0426	3.828×10^{-2}	0.0005	4.273×10^{-5}	1.3165	3.942×10^{-2}	−2.8%
HB	2.7963	7.337×10^{-2}	1.6862	1.718×10^{-2}	0.3851	2.201×10^{-2}	75.6%
910–965 CB	0.0231	0.615	0.0002	3.170×10^{-4}	0.5310	0.553	10.1%
HB	2.9370	1.008	0.9543	0.253	1.6568	0.175	86.1%
965–3000 CB	0.6444	1.443×10^{-2}	0.0217	2.650×10^{-4}	—	—	—
HB	7.8830	2.254×10^{-2}	2.9239	1.213×10^{-2}	—	—	—
Total (CB + HB)	15.470	1.771	5.9991[b]	0.283	3.3584	0.789	—

[a] Relative deviations between our TheoReTs and SHeCaSDa integrated intensities computed as $\sum$(Strong + QC-SHeCaSDa)/$\sum$(Strong + QC) $\times 100$. [b] The QC line list was compressed to 1.81 millions of lines using the super-line approach.

subset''' represents 0.25% of the full line list file for $^{32}SF_6$, providing 86% of the opacity. The remaining 5.999 billion lines of the QC were compressed using our super-line approach,[14] permitting reduction of the number of lines by 3 orders of magnitude with a minimal loss of accuracy. The final compressed QC line list is composed of 1.81 million super-lines. For theoretical simulation of absorption or emission cross-sections at a given temperature, the super-lines can be treated in the same manner as the true lines contained in the ''strong line subset''. A comparison with the recent SHeCaSDa database is also given in this table. As already seen in Fig. 3 and confirmed in Table 4, the lack of opacity in the ν_4 and ν_3 regions in SHeCaSDa is due to the lack of 80% of HBs. Both the strong and QC line lists are freely downloadable from the TheoReTS information system[48] (http://theorets.univ-reims.fr, http://theorets.tsu.ru).

5 Conclusion

To summarize, we present in this work the first global theoretical predictions of infrared rotationally resolved spectra for the sulfur hexafluoride molecule. The rotation-vibration energy levels are determined from variational calculations using our refined PES obtained by the optimisation of the *ab initio* one of ref. 17. Most importantly, absolute line intensities are calculated and extensive theoretical molecular line lists are constructed for the three most abundant species $^{32}SF_6$, $^{33}SF_6$ and $^{34}SF_6$ using *ab initio* dipole moment functions. Room-temperature calculated spectra match the observed ones with unprecedented accuracy for ro-vibrational patterns of seven-atomic molecules. This is, in particular, the case of the most important range in the atmospheric windows around 10 μm where the error between the sum of experimental absorption cross-sections of PNNL and TheoReTS is 2.3%, which can be compared to the deviation of 63% between PNNL and the line lists obtained from the most recent line-by-line analyses. This work permitted one to elucidate for the first time all complicated cold and hot band structures in the rotationally resolved room-temperature SF_6 spectra in the strongly absorbing ranges. For applications requiring accurate opacity calculations and its temperature dependence, our complete theoretical line lists should thus be preferred to partial lists included in the HITRAN or SHeCaSDa databases.

Conflicts of interest

There are no conflicts to declare.

Acknowledgements

The authors acknowledge support from the Romeo computer center of Reims-Champagne-Ardenne and of French-Russian collaboration program LIA ''SAMIA''. The support of RFBR grant (Grant No. 20-35-90075) is also acknowledged.

References

1 M. Rigby, J. Mühle, B. R. Miller, R. G. Prinn, P. B. Krummel, L. P. Steele, P. J. Fraser, P. K. Salameh, C. M. Harth, R. F. Weiss, B. R. Greally, S. O'Doherty, P. G. Simmonds, M. K. Vollmer, S. Reimann, J. Kim, K. R. Kim, H. J. Wang, J. G. J. Olivier, E. J. Dlugokencky, G. S. Dutton, B. D. Hall and J. W. Elkins, *Atmos. Chem. Phys.*, 2010, **10**, 10305–10320.
2 T. Kovács, W. Feng, A. Totterdill, J. M. C. Plane, S. Dhomse, J. C. Gómez-Martín, G. P. Stiller, F. J. Haenel, C. Smith, P. M. Forster, R. R. García, D. R. Marsh and M. P. Chipperfield, *Atmos. Chem. Phys.*, 2017, **17**, 883–898.
3 V. I. Zakharov and V. G. Tyuterev, *Sov. J. Quantum Electron.*, 1984, **14**, 70–74.
4 S. S. Alimpiev, N. V. Karlov, E. M. Khokhlov, S. M. Nikiforov, A. M. Prokhorov, B. G. Sartakov and A. L. Shtarkov, Excitation Spectrum of SF_6 Irradiated by an Intense IR Laser Field, In *Multiple-Photon Excitation and Dissociation of Polyatomic Molecules. Topics in Current Physics*, ed. C. D. Cantrell, Springer, Berlin, Heidelberg, 1986, vol 35.
5 J. L. Lyman, G. P. Quigley and O. P. Judd, Single-Infrared-Frequency Studies of Multiple-Photon Excitation and Dissociation of Polyatomic Molecules, in *Multiple-Photon Excitation and Dissociation of Polyatomic Molecules. Topics in Current Physics*, ed. C. D. Cantrell, Springer, Berlin, Heidelberg, 1986, vol 35.
6 C. T. Dervos and P. Vassiliou, *J. Air Waste Manage. Assoc.*, 2000, **50**, 137–141.
7 P. Varanasi, A. Gopalan and J. F. Brannon Jr., *J. Quant. Spectrosc. Radiat. Transf.*, 1992, **48**, 141–145.
8 M. Maiss, L. P. Steele, R. Francey, P. J. Fraser, R. L. Langenfelds, N. B. A. Trivett and I. Levin, *Atmos. Environ.*, 1996, **30**, 1621–1629.
9 R. A. Fine, CFCs and SF_6 as tracers of ocean processes, *Encyclopedia of Ocean Sciences*, Elsevier, 2019, pp. 228–234.
10 C. P. Rinsland, M. R. Gunson, M. C. Abrams, L. L. Lowes, R. Zander and E. Mahieu, *J. Geophys. Res.*, 1993, **98**, 20491–20494.
11 R. Zander, C. P. Rinsland and P. Demoulin, *J. Geophys. Res.*, 1991, **96**, 15447–15454.
12 C. P. Rinsland, A. Goldman, T. M. Stephen, L. S. Chiou, E. Mahieu and R. Zander, *J. Quant. Spectrosc. Radiat. Transf.*, 2003, **78**, 41–53.
13 J. P. Champion, M. Loëte and G. Pierre, *Spherical Top Spectra*, ed. K. N. Rao and A. Weber, Academic Press, San Diago, 1992.
14 M. Rey, A. V. Nikitin and V. G. Tyuterev, *ApJ*, 2017, **847**, 1.
15 K. L. Chubb, J. Tennyson and S. N. Yurchenko, *Mon. Not. R. Astron. Soc.*, 2020, **493**, 1531–1545.
16 M. Rey, T. Delahaye, A. V. Nikitin and V. G. Tyuterev, *A&A*, 2016, **594**, A47.
17 A. V. Nikitin, M. Rey, I. S. Chizhmakova and V. G. Tyuterev, *J. Phys. Chem. A*, 2020, **124**, 7014–7023.
18 R. S. McDowell, H. W. Galbraith, C. D. Cantrell and N. G. Nereson, *Opt. Lett.*, 1978, **2**, 97–99.
19 C. W. Patterson, R. S. McDowell, P. F. Moulton and A. Mooradian, *Opt. Lett.*, 1981, **6**, 93–95.
20 R. S. McDowell, B. J. Krohn, H. Flicker and M. C. Vasquez, *Spectrochim. Acta, Part A*, 1986, **42**, 351–369.

21 R. S. McDowell and B. J. Krohn, *Spectrochim. Acta, Part A*, 1986, **42**, 371–385.
22 W. B. Person and J. Overend, *J. Chem. Phys.*, 1976, **66**, 1442–1448.
23 K. Kim, R. S. McDowell and W. T. King, *J. Chem. Phys.*, 1980, **73**, 36–41.
24 V. Boudon, M. Hepp, M. Herman, I. Pak and G. Pierre, *J. Mol. Spectrosc.*, 1998, **192**, 359–367.
25 D. Bermejo, R. Z. Martínez, E. Loubignac, V. Boudon and G. Pierre, *J. Mol. Spectrosc.*, 2000, **201**, 164–171.
26 M. Faye, A. Le Ven, V. Boudon, L. Manceron, P. Asselin, P. Soulard, F. wabia-Tchana and P. Roy, *Mol. Phys.*, 2014, **112**, 2504–2514.
27 M. Faye, V. Boudon, M. Loëte, P. Roy and L. Manceron, *J. Mol. Spectrosc.*, 2016, **325**, 35–41.
28 M. Faye, V. Boudon, M. Loëte, P. Roy and L. Manceron, *J. Quant. Spectrosc. Radiat. Transf.*, 2017, **190**, 38–47.
29 M. Faye, L. Manceron, P. Roy, V. Boudon and M. Loëte, *J. Mol. Spectrosc.*, 2018, **348**, 37–42.
30 I. E. Gordon, L. S. Rothman, C. Hill, R. V. Kochanov, Y. Tan and P. F. Bernath, *et al.*, *J. Quant. Spectrosc. Radiat. Transfer*, 2017, **203**, 3–69.
31 N. Jacquinet-Husson, R. Armante, N. A. Scott, A. Chédin, L. Crepeau, C. Boutammine and A. Bouhdaoui, *et al.*, *J. Mol. Spectrosc.*, 2016, **327**, 31–72.
32 H. Ke, V. Boudon, C. Richard, V. Madhur, M. Faye and L. Manceron, *J. Mol. Spectrosc.*, 2020, **368**, 111251.
33 D. Albert, B. K. Antony, Y. A. Ba, Y. L. Babikov, P. Bollard and V. Boudon, *et al.*, *Atoms*, 2020, **8**, 76.
34 D. Viglaska-Aflalo, M. Rey, A. V. Nikitin and T. Delahaye, *Phys. Chem. Chem. Phys.*, 2020, **22**, 3204–3216.
35 M. Rey, I. S. Chizhmakova, A. V. Nikitin and V. G. Tyuterev, *Phys. Chem. Chem. Phys.*, 2018, **20**, 21008–21033.
36 O. Egorov, A. V. Nikitin, M. Rey, A. A. Rodina, S. A. Tashkun and V. G. Tyuterev, *J. Quant. Spectrosc. Radiat. Transf.*, 2019, **239**, 106668.
37 S. N. Yurchenko, D. S. Amundsen, J. Tennyson and I. P. Waldmann, *A&A*, 2017, **8605**, A95.
38 J. Tennyson and S. N. Yurchenko, *Mol. Astrophys.*, 2017, **8**, 1–18.
39 B. P. Mant, A. Yachmenev, J. Tennyson and S. N. Yurchenko, *Mon. Not. R. Astron. Soc.*, 2018, **478**, 3220–3232.
40 P. Carbonnière, T. Lucca, C. Pouchan, N. Rega and V. Barone, *J. Comput. Chem.*, 2005, **26**, 384–388.
41 P. Carbonnière, A. Dargelos and C. Pouchan, *Theor. Chem. Acc.*, 2010, **125**, 543–554.
42 M. Sibaev and D. L. Crittenden, *Comput. Phys. Commun.*, 2016, **203**, 290–297.
43 E. L. Sibert, D. P. Tabor, N. M. Kidwell, J. C. Dean and T. S. Zwier, *J. Phys. Chem. A*, 2014, **118**, 11272–11281.
44 S. V. Krasnoshchekov, R. S. Schutski, N. C. Craig, M. Sibaev and D. L. Crittenden, *J. Chem. Phys.*, 2018, **148**, 084102.
45 A. Dargelos, P. Karamanis and C. Pouchan, *Chem. Phys. Lett.*, 2019, **723**, 155–159.
46 J. Tennyson and S. N. Yurchenko, *Proc. Int. Astron. Union*, 2014, **9**, 330–338.
47 X. Huang, D. W. Schwenke and T. J. Lee, *J. Chem. Phys.*, 2014, **140**, 114311.
48 M. Rey, A. V. Nikitin, Y. L. Babikov and V. G. Tyuterev, *J. Mol. Spectrosc.*, 2016, **327**, 138–158.
49 M. Rey, A. V. Nikitin and V. G. Tyuterev, *J. Chem. Phys.*, 2012, **136**, 244106.
50 M. Rey, A. V. Nikitin and V. G. Tyuterev, *Phys. Chem. Chem. Phys.*, 2013, **15**, 10049–10061.
51 M. Rey, A. V. Nikitin and V. G. Tyuterev, *J. Chem. Phys.*, 2014, **141**, 044316.
52 M. Rey, A. V. Nikitin and V. G. Tyuterev, *J. Phys. Chem. A*, 2015, **119**, 4763–4779.
53 I. S. Chizhmakova and A. V. Nikitin, *Atmos. Oceanic Opt.*, 2019, **32**, 613–618.
54 J. K. G. Watson, *Mol. Phys.*, 1968, **15**, 479–490.
55 A. V. Nikitin, J. P. Champion and V. G. Tyuterev, *J. Mol. Spectrosc.*, 1997, **182**, 72–84.
56 M. Rey, V. Boudon, C. Wenger, G. Pierre and B. Sartakov, *J. Mol. Spectrosc.*, 2003, **219**, 313–325.
57 V. Boudon, L. Manceron, F. Kwabia Tchana, M. Loëte, L. Lago and P. Roy, *Phys. Chem. Chem. Phys.*, 2014, **16**, 1415–1423.
58 S. Y. Volkov, D. N. Kozlov, M. R. Malikov, E. A. Otlivanchik and V. V. Smirnov, *Sov. J. Quantum Elektron.*, 1984, **14**, 1240.
59 M. Rey, A. V. Nikitin and V. G. Tyuterev, *J. Mol. Spectrosc.*, 2013, **291**, 85–97.
60 S. Manzhos, T. Carrington, L. Laverdure and N. Mosey, *J. Phys. Chem. A*, 2015, **119**, 9557–9567.
61 T. Carrington, *J. Chem. Phys.*, 2017, **146**, 120902.
62 W. G. Harter and C. W. Patterson, *J. Chem. Phys.*, 1984, **80**, 4241–4261.
63 T. J. Johnson, R. L. Sams and S. W. Sharpe, *Proc. SPIE*, 2004, **5269**, 159–167.

